UNIVERSIDADE FEDERAL DE MINAS GERAIS
Instituto de Geociências
Programa de Pós-Graduação em Geologia

Marcelo de Almeida Freimann

SIGNIFICADO TECTÔNICO DAS SEQUÊNCIAS METAVULCANOSSEDIMENTARES PRÉ-ESTATERIANAS DA SERRA DO ESPINHAÇO EM MINAS GERAIS

Belo Horizonte
30/05/22

Nº60

Marcelo de Almeida Freimann

SIGNIFICADO TECTÔNICO DAS SEQUÊNCIAS METAVULCANOSSEDIMENTARES PRÉ-ESTATERIANAS DA SERRA DO ESPINHAÇO EM MINAS GERAIS

Versão final

Tese apresentada ao Programa de Pós-Graduação em Geologia da Universidade Federal de Minas Gerais como requisito parcial para obtenção do título de Doutor em Geologia.

Área de concentração: Geologia Regional

Orientador: Prof. Dr. Luiz Guilherme Knauer

Coorientador: Prof. Dr. Matheus Henrique Kuchenbecker do Amaral

Belo Horizonte

2022

F865s
2022

Freimann, Marcelo de Almeida.

Significado tectônico das sequências metavulcanossedimentares pré-estaterianas da Serra do Espinhaço em Minas Gerais [manuscrito] / Marcelo de Almeida Freimann. – 2022.

142 f., enc. il. (principalmente color.)

Orientador: Luiz Guilherme Knauer.

Coorientador: Matheus Henrique Kuchenbecker do Amaral.

Tese (doutorado) – Universidade Federal de Minas Gerais, Instituto de Geociências, 2022.

Área de concentração: Geologia Regional.

Bibliografia: f. 96-119.

Inclui apêndices e anexo.

1. Tempo geológico – Teses. 2. Espinhaço, Serra do (MG e BA) – Teses. 3. Cianita – Teses. I. Knauer, Luiz Guilherme. II. Kuchenbecker, Matheus. III. Universidade Federal de Minas Gerais. Instituto de Geociências. IV. Título.

CDU: 550.93(815.1+813.8)

Ficha catalográfica elaborada por Elisabete Quatrini Vieira – CRB6 2210

Biblioteca “Vitória Pedersoli”, Instituto de Geociências da UFMG

UNIVERSIDADE FEDERAL DE MINAS GERAIS

PROGRAMA DE PÓS-GRADUAÇÃO EM GEOLOGIA DO IGC-UFMG

FOLHA DE APROVAÇÃO

Significado tectônico das sequências metavulcanossedimentares pré-estaterianas da Serra do Espinhaço em Minas Gerais

MARCELO DE ALMEIDA FREIMANN

Tese submetida à Banca Examinadora designada pelo Colegiado do Programa de Pós-Graduação em GEOLOGIA, como requisito para obtenção do grau de Doutor em GEOLOGIA, área de concentração GEOLOGIA REGIONAL, pelo Programa de Pós-graduação em Geologia do Instituto de Geociências da Universidade Federal de Minas Gerais.

Aprovada em 30 de maio de 2022, pela banca constituída pelos membros:

Prof. Luiz Guilherme Knauer - Orientador
UFMG

Jorge G. Roncato Jr.
Prof. Jorge Geraldo Roncato Júnior
UFMG

Danielle Piuzana
Profa. Danielle Piuzana Mucida
UFVJM

Profa. Lúcia Maria Fantinel

gov.br
Documento assinado digitalmente
PEDRO ANGELO ALMEIDA ABREU
Data: 16/06/2022 11:59:40-0300
Verifique em https://verificador.iti.br

Prof. Pedro Angelo Almeida Abreu
UFVJM

Belo Horizonte, 30 de maio de 2022.

À minha maior inspiração, Helena, e aos meus pais, Ordália e Guilherme, meus alicerces.

AGRADECIMENTOS

Tão difícil quanto escrever esta tese é conseguir, de forma justa, agradecer a todas as pessoas que de alguma forma participaram dessa longa caminhada. Com enorme gratidão, agradeço:

Aos meus pais e irmãos, por tanto apoio e confiança. Sem vocês este trabalho definitivamente não seria possível. À minha filha Helena, por ser minha alegria, minha luz guia. À Bruna.

Aos membros da banca de avaliação desta tese, por aceitarem o convite e disporem de seu tempo;

Ao meu orientador Guilherme Knauer: por toda a sabedoria do Espinhaço e, abertamente, por quase tudo o que sei sobre geologia; por abrir tantas portas que, só agora já transpassadas, percebo o valor imensurável; pelos importantíssimos conselhos pessoais e profissionais sem os quais este Marcelo eu não seria; pelas agradáveis e construtivas conversas em sala e em campo; pela cultura, especialmente por suas listas musicais formidáveis e de tão refinado gosto; pelo exemplo; e em especial pela sua grande virtude de ser tão humano, empático aos aflitos;

Ao meu coorientador Matheus Kuchenbecker, por todo o apoio irrestrito despendido na realização do trabalho, pelas enriquecedoras conversas geológicas, pela solicitude e disponibilidade e por todo o conhecimento transferido;

Aos caros amigos, geólogos Borgatti, Caju e Miguilim, pelos bons momentos, pela amizade, conselhos e apoio para a realização do trabalho;

Aos companheiros de jornada da pós-graduação: Anderson Victória, Tati Dias, Chico Villela, Márcio, Raíssa Santiago, Ana, Gabi, Zangão, Carol Deluca, Tobias Fonteboa, Fernando, Alex, Christopher Rezende, Cristina, Paula Serrano e Lorena Martins;

Aos técnicos do CPMTC, em especial Carlos, Denise e Johnny;

Ao grupo de gordos, pela companhia de almoço: Guilherme, Bidu, Eliane, André, Valdir e Karin.

Ao Programa de pós-graduação em Geologia do Istituto de Geociências da UFMG;

À Pró-reitoria de Pós-graduação (PRPg) da UFMG;

Ao Centro de Geologia Eschwege;

À FAPEMIG pela bolsa de doutorado concedida;

Ao CNPq, pelo apoio ao projeto temático “Bacias riacianas/orosirianas da Serra do Espinhaço: tectônica e proveniência sedimentar” (Processo # 205254/2016-4), e ao NGU-UFMG.

E ao laboratório de geocronologia da Universidade de Campinas, em especial ao Professor Elson Oliveira, bem como ao laboratório de geocronologia da UFOP.

A geologia destroça as certezas dos mais convictos e, impiedosa, assombra as noites das mentes inférteis. Aos frugais, permite que contemplem, por uma fenda, a dinâmica dança de algumas das possibilidades do passado da Terra.

RESUMO

As sequências vulcanossedimentares são de grande importância para a compreensão da dinâmica da crosta, uma vez que representam o registro sedimentar resultante da interação entre placas tectônicas, hidrosfera e atmosfera. Na Serra do Espinhaço Meridional, duas sequências têm sido alvo de estudos nas últimas décadas: as sequências metavulcanossedimentares Pedro Pereira e Costa Sena. Apesar dos esforços, muitas questões ainda permanecem abertas, em parte devido à complexidade da geologia fragmentada e policíclica às quais foram submetidas. Afim de contribuir com relação ao posicionamento das sequencias no tempo geológico e avançar na proposição de um modelo evolutivo, essas sequências foram revisitadas nesta tese de doutoramento. Zircões extraídos de metariolito intercalado em formação ferrífera bandada do Grupo Pedro Pereira definem a idade de cristalização da rocha vulcânica em 2.77 Ga, idade coincidente com aquelas encontradas para os greenstone belts Rio da Velhas e Pitangui, no Quadrilátero Ferrífero. Analises geoquímicas das formações ferríferas bandadas associadas ao metariolito indicam a existência de bolsões oxigenados locais já no início da era Neoarqueano, mais de 250 Ma antes do GOE. Resultados semelhantes foram encontrados no greenstonebelt Pitangui. Desta forma, a região sudeste do Cráton do São Francisco registra algumas das evidências mais antigas do início da oxigenação dos oceanos. Análises geocronológicas e geoquímicas também foram realizadas na sequência metavulcanossedimentar Costa Sena. Os espectros de idades concordantes de zircões detríticos de xisto e parametaconglomerado foram levantados e, em conjunto com os dados geoquímicos, sugerem deposição em em ambiente geotectônico colisional, em uma bacia de antepaís, entre 2.0 e 2.2 Ga. As assinaturas geoquímicas de parte dos xistos indicam contribuição de fontes extremamente enriquecidas em ETR leves, compatíveis com valores para rochas calci-alcalinas. Outros xistos tem assinatura de ETR compatíveis com os valores do embasamento local, o leucogranito de Gouveia, sua provável fonte dominante. Xistos com níveis ricos em cianita, que podem chegar a constituir verdadeiros cianititos, representariam o metamorfismo sobre paleossolos gerados durante os frequentes episódios de exposição sub aérea da região forebulge da bacia em condições de clima quente e úmido, com provável precipitação de evaporitos ricos em boro e fósforo. Os dados isotópicos de zircão detrítico da amostra de metabrecha da Formação Bandeirinha em sua área-tipo produziram pico estatístico mais novo em 2093 ± 9 Ma (n=98), sendo que a idade do spot mais novo foi 2000 ± 40 Ma. Estes dados, compatíveis com a definição original, fortalecem a concepção de origem paleoproterozoica da sequência e sugerem a manutenção da Formação Bandeirinha dentro do Grupo Costa Sena.

Palavras-chave: Serra do Espinhaço Meridional; sequência metavulcanossedimentar; Grupo Costa Sena; Grupo Pedro Pereira; BIF; Paleoproterozoico; Arqueano; cianita.

ABSTRACT

Vulcanosedimentary sequences are of great importance for understanding the dynamics of the crust since they represent the sedimentary record resulting from the interaction between tectonic plates, hydrosphere, and atmosphere. In the Southern Espinhaço Ridge, two sequences have been the subject of studies in recent decades: the metavulcanosedimentary sequences Pedro Pereira and Costa Sena. Despite efforts, many questions remain open, to some extent due to the complexity of the fragmented and polycyclic geology to which they were subjected. To contribute to the positioning of sequences in geological time and an evolutionary model, these sequences were revisited in this doctoral thesis. Zircons extracted from metariolite interlayered in a banded iron formation of the Pedro Pereira Group define the crystallization age of the volcanic rock in 2.77 Ga, an age coincident with those found for the greenstone belts Rio da Velhas and Pitangui, in the Quadrilátero Ferrífero. Geochemical analyses of the banded iron formation associated with metariolite imply the existence of locally oxygenated pockets as early as the beginning of the Neoarchean era, more than 250 Ma before the GOE. Similar results were found in the Pitangui greenstone belt. Thus, the southeastern region of the San Francisco Craton records some of the oldest evidence of the onset of ocean oxygenation. Geochronological and geochemical analyses were also performed in the Costa Sena metavulcanosedimentary sequence. The concordant age spectra of detritic zircons for schist and parametaconglomerate were collected and, jointly with geochemical data, suggest deposition in a collisional geotectonic environment, in a foreland basin, between 2.0 and 2.2 Ga. The geochemical signatures of part of the schists indicate a contribution from sources extremely enriched in light ETR, compatible with values for calc-alkaline rocks. Other schists have ETR signatures compatible with the values of the local basement, Gouveia leucogranite, its most likely dominant source. Schists with kyanite-rich levels, which may constitute true kyanitites, would represent the metamorphism of paleosols generated during the frequent episodes of subaerial exposure of the forebulge region of the basin in hot and humid climate conditions, together with precipitation of evaporites rich in boron and phosphorus. The isotopic data of detritic zircon from the metabreccia sample of the Bandeirinha Formation in its type-area produced a younger statistical peak at 2093 ± 9 Ma (n=98), given that the age of the youngest spot was 2000 ± 40 Ma. These data, compatible with the originally defined positioning of the unit, strengthen the Paleoproterozoic origin conception of the sequence and suggest the maintenance of the Bandeirinha Formation within the Costa Sena Group.

Keywords: Southern Espinhaço Ridge; metavulcanosedimentary sequence; Costa Sena Group; Pedro Pereira Group; BIF; Paleoproterozoic; Archean; Kyanite; Foreland.

LISTA DE FIGURAS

Figura 1.**1** - Localização áreas estudadas em Minas Gerais. CSF-Cráton São Francisco. 21

Figura 2.**1** - Sequências metavulcanossedimentares riacianas/orosirianas (em azul) potencialmente correlacionáveis à amalgamação do paleocontinente São Francisco-Congo. Modificado de Alkmim et al. (2006). 23

Figura 2.**2** - Mapa geológico regional da porção meridional da Serra do Espinhaço com destaque para as unidades do embasamento cristalino e sequências supracrustais paleoproterozoicas e arqueanas (modificado de Heineck *et al.*, 2003) 26

Figura 2.**3** - Mapa geológico mostrando a distribuição espacial da sequência metavulcanossedimentar Riacho dos Machados, no centro do bloco Porteirinha (Leal *et al.*, 2021). No canto superior, à esquerda, mapa esquemático do craton São Francisco com domínios arqueanos/paleoproterozoicos em destaque e localização do mapa. 28

Figura 2.**4** - Complexo Limoeiro (em azul), entre as folhas Monte azul, a sul, e Espinosa, a norte (modificado de Knauer *et al.*, 2007)...30

Fig. 3.**1**- Simplified domains map of the São Francisco craton and Araçuaí orogen region highlighting the Archean-Paleoproterozoic nuclei, Paleoproterozoic orogenic belts, and greenstone belts (modified from Barbosa and Dominguez, 1996; Heilbron *et al.*, 2016; Pinto and Silva, 2014; Silva *et al.*, 2005; Vieira *et al.*, 2018). West Gondwana miniature (after Pedrosa-Soares *et al.*, 2007): A – Amazonian craton; P,LA,RP – Paranapanema, Luis Alves and Rio de la Plata cratons; SF – São Francisco craton; WC, SL – West Africa and São Luiz cratons; C – Congo craton; K – Kalahari craton; and T – Tanzania craton. Greenstone belts: 1-Piumhi; 2-Pitangui; 3-Rio das Velhas; 4-Rio Mata Cavalo; 5-Serro; 6-Pedro Pereira; 7-Riacho dos Machados; 8-Riacho de Santana; 9-Umburanas; 10-Mundo Novo; 11-Rio Itapicuru. 37

Fig. 3.**2** (a) Geologic map of Pedro Pereira region (adapted from Carvalho, 1982; Knauer and Grossi-Sad, 1997), Datum WGS84, zone 23S; (b) regional map enclosing the northern portion of the Gouveia anticlinorium (adapted from Fogaça, 1997; Knauer and Grossi-Sad, 1997)..38

Fig. 3.**3** The general aspect of the PPMS rocks. a) common aspect of the BIF outcrops, often as in-situ loose blocks; b) tight fold hinge zone in BIF; c) sheared BIF; d) section of a BIF hand specimen showing milli- to centimetric alternation of quartz/hematite-rich bands; e) tectonic contact between metagranite of the Gouveia Complex (lower right) and BIF (upper left); f) weathered chlorite schist, which often interleaves the BIF; g) pinkish to greenish sheared porphyritic metarhyolite; h) photomicrograph of metarhyolite showing the main mineral phases, quartz phenocrysts and related dynamic recrystallization, and the anastomosed foliation; and i) quartz phenocryst highlighting a lobate re-entrant that resembles a dissolution

feature. Mineral abbreviation: Qtz-quartz; Chl-chlorite; Ms – muscovite; Op – opaque mineral; and Ser – sericite..40

Fig. 3**.4** The microscopic aspect of the metavolcanics and BIFs from PPMS. a) photomicrograph of the metarhyolite highlighting the abundance of phenocrysts in a very fine sericitic groundmass; b) photomicrograph of metavolcaniclastic rock showing the angular nature of the poorly sorted broken quartz crystals in a fine-grained groundmass (fine ash), suggesting the fragmental character of the rock; c) photomicrograph of metaultramafic and its mineral assemblage; d) iron formation photomicrograph (crossed polarizers) emphasizing the presence of muscovite; e) photomicrograph of massive iron formation texture showing advanced metasomatism (parallel polarizers); and f) photomicrograph of banded iron formation showing micro-scale hematite-quartz bands and granoblastic texture. Mineral abbreviation: Qtz-quartz; Ms – muscovite; Op – opaque mineral; Hem – hematite; and Ser – sericite. 41

Fig. 3**.5** PAAS normalized REE+Y patterns. a) group 1 (grey), group 2 (red), and MIF (green) PPMS patterns. b) field representation of 1,2, and MIF defined groups, the interleaved metarhyolite REE chemistry, and PPMS BIF samples from Chaves et al. (2012) for comparison. 44

Fig. 3**.6** Plot of CeSN /CeSN* and PrSN/PrSN* for PPMS and worldwide iron formations, discriminating La induced false negative Ce anomalies from the true ones (after Bau and Dulski, 1996). Data sources: [a]Planavsky et al. (Planavsky *et al.*, 2010); [b]Spier et al. (2007); [c]Chaves et al. (2012); [d]Araújo and Lobato (2019); [e]Nutman et al. (2019); [f]Brando Soares et al. (2017);[g]Kato et al.(2002); and [h]this study. The dotted red line represents the power curve fit of this work samples (y = 0.6621x-2.5 R^2 = 0.9181)..45

Fig 3**.7** a) Wetherill-type Concordia diagram for the metarhyolite from PPMS.; b) Concordia age of an eleven-spot cluster. 47

Fig. 3**.8** Cathodoluminescence (CL) images of all dated zircon grains from the acid metavolcanite and the spot location with the respective U-Pb ages (207Pb/206Pb age; 2σ error), percentual of discordances, and Th/U ratios. 47

Fig. 3**.9**. Graph of REE+Y concentration sum vs. Ce_{SN}/Ce_{SN}^* ratio from Pedro Pereira IF samples. 52

Fig. 3**.10**. Graph of Th concentration vs. Th/U ratio from Pedro Pereira IF samples. The dashed line represents the Th/U average value for the upper continental crust (UCC; Rudnick and Gao, 2003; Taylor and McLennan, 1995). 54

Figure 4.1 Geological map framing the spatial distribution of the Costa Sena metavolcanosedimentary sequence, highlighting the main areas of occurrence (after Fogaça, 1997; Heineck *et al.*, 2003; Knauer and Grossi-Sad, 1997). 62

Figure 4.2 General aspects of the Costa Sena metavolcanosedimentary sequence rocks. a) Most common outcrop style of the schists from Costa Sena sequence; b) oligomitic metaconglomerates from Fazenda Formação area; c) angular unconformity at the Fazenda Casa de Telha area, between the Bandeirinha Formation quartzites (west) and the Espinhaço Supergroup (east); d) sample of banded iron formation from in situ loose blocks layer from Fazenda Bandeirinha area; e) and f) metaconglomerate with sparse banded iron formation pebbles in a ky-qtz-mus schist matrix; g) coarse-grained ky-ms-qtz schist with porphyroclastic pinkish quartz grains; h) stratified quartzite and BIF clasts inside ky-mus-qtz schist (the matrix of the metabreccia); i) and j) fine-grained ky-qtz-mus schist showing compositional variation layering in Gouveia and Cachimbo areas, respectively; k) kyanite-bearing schist with pinkish quartz porphyroclasts; i) laminated muscovite quartzite with very fine tourmaline layers. 63

Figure 4.3 General aspects of the Costa Sena metavolcanosedimentary sequence rocks. a) weathered mus-ky-qtz schist with up to 3 cm tabular crystals in prominence; b) and c) massive aggregates of lazulite/augelite from the Barão do Guaicuí schists; d) massive chloritoid + quartz vein sample that crosscuts the schists; e) levels of chloritoid in the Barão do Guaicuí schist; f) radial kyanite/pyrophyllite + quartz vein crosscutting a schist; g) another angular unconformity between Bandeirinha Formation quartzites (west) and Supergrupo Espinhaço (east) at the Fazenda Bandeirinha area; h) pinkish ortho-metaconglomerate of the Bandeirinha Formation; and i) pinkish intraformational metabreccia of the Bandeirinha Formation. 66

Figure 4.4 Spidergrams with CI chondrite normalized (Anders and Grevesse, 1989) REE values of the Costa Sena sequence groups and field patterns from possible sources. a) Porphyroclastic schist/lazulite bearing schist (the red circles represent the lazulite bearing ones); b) and c) Type I schist; d) Type II schist; e) High SiO2 metasedimentary rock; f) Highly weathered (laterized) schist. a(Chaves *et al.*, 2014);b(Grochowski, 2019);c(Dussin and Chemale Jr, 2012);d(Freimann *et al.*, 2021) ;e(Chaves and Coelho, 2013). 72

Figure 4.5 Spidergrams with upper continental crust normalized (Taylor and McLennan, 1995) major oxide and trace element values of the Costa Sena sequence groups and field patterns from possible sources. a) Porphyroclastic schist/lazulite bearing schist b) High SiO2 metasedimentary rock; c) and d) Type I schist; e) and f) Type II schist; g) Highly weathered (laterized) schist). a(Chaves *et al.*, 2014);b(Grochowski, 2019);e(Chaves and Coelho, 2013). 73

Figure 4.6 A-CN-K ternary plot for the Costa Sena sequence samples (Nesbitt and Young, 1984). The arrowed line refers to the ideal weathering trend, while de dotted arrowed line to the advanced weathering trend. 74

Figure 4.7 La/Th-Hf diagram (Floyd and Leveridge, 1987). Grey fields indicate the compositions of sedimentary rocks deposited in different tectonic settings. Colored dashed lines represent the fields from the possible sources. [a](Chaves *et al.*, 2014);[b](Grochowski, 2019);[c](Chaves and Coelho, 2013). 75

Figure 4.8 Plot of the Costa Sena sequence samples within a major element discrimination diagram (Bhatia, 1983a) for tectonitc settings; [a](Fogaça *et al.*, 1984). 75

Figure 4.9 Major element provenance discriminant function plot (Roser and Korsch, 1988) for Costa Sena sequence rocks. Stars: UCC – average upper continental crust; BA, AN, DA, RD, and RH – average basalt, andesite, dacite, rhyodacite, and rhyolite, as plotted by Roser and Korsch (1988) 76

Figure 4.10 Wetherill-type Concordia diagram for the Barão do Guaicuí schist sample. 77

Figure 4.11 Frequency histogram (gray bars), probability density plot (PDP, black line), and kernel density estimation (KDE, red) for the Barão do Guaicuí Formation schist CSOV-08. Numerical analysis based on Vermeesch (2012). 78

Figure 4.12 Frequency histogram (gray bars), probability density plot (PDP, black line), and kernel density estimation (KDE, red) for the Bandeirinha Formation sample. Numerical analysis based on Vermeesch (2012). 79

Figure 4.13 Cathodoluminescence (CL) images for representative detrital zircon grains from Bandeirinha Formation metabreccia. 79

Figure 4.14 A summary plot of the general fields for convergent (A: red field), collisional foreland (B: blue field), and extensional basins (C: green field) as in Cawood et al. (2012). Pink solid line: Bandeirinha Formation; purple solid line: Barão do Guaicuí Formation. Note the similarity between the cumulative curves of Bandeirinha and Barão do Guaicuí formations indicating similar age sources, as well as the proportion of them in the zircon population. 83

Figure 4.15 Gains and losses for the alteration from alkali-granite (Gouveia leucogranite) to the porphyroclastic schist (Barão do Guaicuí Formation) based on Isocon method of Grant (2005, 1986). The red bar encompasses the losses, while the yellow and green, the immobile elements and the gains, respectively. 88

Figure 4.16 Schematic block diagram of the Costa Sena foreland basin and its depositional environments. 91

SUMÁRIO

1 INTRODUÇÃO **18**
1.1 Estrutura da tese 18
1.2 Prefácio 19
1.3 Objetivos 20
1.4 Localização das áreas estudadas e trabalho de campo 20
2 CONTEXTO GEOLÓGICO **22**
2.1 Complexos arqueanos 23
2.2 Unidades metassedimentares arqueanas/paleoproterozoicas 25
2.2.1 Grupo Costa Sena 25
2.2.2 Grupo Riacho dos Machados 27
2.2.3 Complexo Limoeiro 29
3 ARTIGO I: NEW GEOCHRONOLOGIC AND GEOCHEMICAL CONSTRAINTS FOR THE PEDRO PEREIRA METAVOLCANOSEDIMENTARY SEQUENCE: EVIDENCE FOR A 2.77 GA OXYGEN OASIS RECORD IN THE SÃO FRANCISCO-CONGO PALEOCONTINENT **31**
3.1 Introduction 32
3.2 Geological settings 33
3.3 Geology of the Gouveia domain 34
3.4 The Pedro Pereira metavolcanosedimentary sequence 38
3.5 Analytical methods 41
3.5.1 Sampling 41
3.5.2 Geochemistry 41
3.5.3 U-Pb geochronology 42
3.6 Analytical results 42
3.6.1 Geochemistry of the PPMS iron formations 42
3.6.2 Metarhyolite lithochemistry 45
3.6.3 U-Pb geochronology 46
3.7 Discussion 48
3.7.1 Age of the PPMS and tectonic implications 48
3.7.2 Iron formation geochemistry 49
3.7.3 . Detrital input in the BIFs 50

3.7.4 Pedro Pereira iron formation, a Neoarchean oasis? 54
3.7.5 Hydrothermal vent input? 54
3.8 Conclusion 55
3.9 Declaration of interest statement 56
3.10 Acknowledgments 56
4 ARTIGO II: THE SYN-OROGENIC RHYACIAN/OROSIRIAN COSTA SENA BASIN, SOUTHEASTERN BRAZIL 57
4.1 Introduction 58
4.2 Geological setting 59
4.3 A Costa Sena metavolcanosedimentary sequence overview 60
4.3.1 Fazenda Formação and Fazenda Casa de Telha (areas 1 and 2) 60
4.3.2 Guinda (area 3) 61
4.3.3 Fazenda Braúnas/Barão do Guaicuí (area 4) 63
4.3.4 Cunha/Padre Matias (area 5) 64
4.3.5 Gouveia/Morro do Juá/ Janela de Pedra (area 6) 64
4.3.6 Cuiabá (area 7) 65
4.3.7 West Flank of the Gouveia anticlinorium (areas 8,9, and 14) 66
4.3.8 Pedro Pereira and Cachimbo (areas 10 and 11) 67
4.3.9 Costa Sena (area 12) 67
4.3.10 Capitão Felizardo (area 13) 68
4.4 Analytical methods 69
4.4.1 Sampling 69
4.4.2 Whole-rock geochemistry 69
4.4.3 U-Pb Geochronology 69
4.5 Analytical results 70
4.5.1 Geochemistry of the Costa Sena Group schists 70
4.6 Geochronology 77
4.6.1 Sample CSO*V*-06A 77
4.6.2 CSO*V*-08 77
4.6.3 Bandeirinha Formation (sample CSOV-07) 78
4.7 Discussion 80

4.7.1 Does Barão do Guaicuí Formation exist? 80
4.7.2 The high kyanite content 80
4.7.3 The absence of feldspar grains 82
4.7.4 Geochronology and geotectonic settings 82
4.7.5 An attempt at facies differentiation 84
4.7.6 Mass transfer calculations 87
4.7.7 The “Gouveia Anticlinorium” 88
4.7.8 Neoproterozoic Shearing (Brasiliano event) 89
4.8 Conclusion 92
4.9 Declaration of interest statement 92
4.10 Acknowledgements 92
5 CONCLUSÕES 93
6 REFERÊNCIAS 96
APÊNDICE A 120
APÊNDICE B 121
APÊNDICE C 123
APÊNDICE D 125
APÊNDICE E 127
APÊNDICE F 133
APÊNDICE G 136
APÊNDICE H 140
ANEXO 142

1 INTRODUÇÃO

1.1 Estrutura da tese

A tese é apresentada na forma de capítulos compilados e artigos científicos, conforme a seguinte disposição:

Capítulo 1 (Introdução) – Introdução geral ao tema da pesquisa, seus objetivos principais e localização das áreas estudadas.

Capítulo 2 (Geologia regional) – Uma introdução geológica às unidades pré-estaterianas com foco nos domínios tectônicos estudados.

Capítulo 3 (Artigo I - New geochronologic and geochemical constraints for the Pedro Pereira metavolcanosedimentary sequence: Evidence for a 2.77 Ga oxygen oásis record in the São Francisco-Congo paleocontinent) – por Marcelo Freimann, Luiz Guilherme Knauer e Matheus Kuchenbecker, um manuscrito publicado na revista Journal of South American Earth Sciences.

Capítulo 4 (Artigo II - The syn-orogenic Rhyacian/Orosirian Costa Sena basin, southeastern Brazil – por Marcelo Freimann, Luiz Guilherme Knauer, Matheus Kuchenbecker e Francisco J. Rios. *Manuscrito submetido para a* revista *Journal of South American Earth Sciences.*

Capítulo 5 (Conclusões gerais) – Este capítulo é dedicado às conclusões gerais levantadas nesta tese.

Apêndice – Apresenta tabelas suplementares de ambos manuscritos (capítulos 3 e 4).

Anexos – Documentos externos ao trabalho.

1.2 Prefácio

Ao longo da Serra do Espinhaço afloram rochas mais antigas que o Supergrupo Espinhaço em diversas regiões e, na maior parte das ocorrências, predominam rochas graníticas e gnáissicas, integrantes de diversos complexos arqueanos e/ou paleoproterozoicos. Ocorrem também, em menor expressão geográfica, sequências supracrustais pré-estaterianas. Alinhadas em um *trend* NNE ao longo da Serra do Espinhaço, estas sequências metavulcanossedimentares afloram como *basement inliers,* inseridas no contexto geotectônico do Orógeno Araçuaí, em sua borda oeste, no Cinturão de Dobras e Falhas/Zonas de cisalhamento da Serra do Espinhaço. Estas sequências registram uma série de bacias, pouco estudadas até o presente momento. Este grupo de bacias, potencialmente correlacionáveis do ponto de vista tectônico, pode ter sua gênese associada a complexos processos orogenéticos riacianos/orosirianos que culminaram na edificação de extensa(s) cadeia(s) de montanhas entre o bloco Gavião/Guanambi-Correntina e Bloco Gabão (*e.g.* Alkmim, 2004; Barbosa *et al.*, 2020)

Apesar de obliterados pelos processos tectônicos subsequentes (em especial pela orogenia Brasiliana e múltiplas tafrogêneses paleo- a neoproterozoicas), são reconhecíveis componentes tectônicos deste antigo orógeno. Os segmentos poupados da orogênese neoproterozoica ocorrem no interior do Cráton do São Francisco sendo representados pelo Orógeno Itabuna-Salvador-Curaçá/Arco Magmático Caraíba e o Arco Magmático do Oeste da Bahia a norte (*e.g.* Barbosa and Sabaté, 2004; Cruz *et al.*, 2016; Martins de Sousa *et al.*, 2020), e Cinturão Mineiro, a sul (Alkmim and Teixeira, 2017; Teixeira *et al.*, 2000). Os segmentos alóctones que ocorrem no interior do Orógeno Araçuaí são representados pelos complexos Mantiqueira, Juiz de Fora, Pocrane (*e.g.* Heilbron *et al.*, 2010; Noce *et al.*, 2007; Novo *et al.*, 2013), bloco Piedade (Bruno *et al.*, 2020b) e, na Faixa Oeste Congolesa, pelas unidades Complexo Eburneano e Grupo Zadiniano (*e.g.* Lerouge *et al.*, 2006; Tack *et al.*, 2001; Vicat and Pouclet, 2000). Também foram envolvidos no processo orogenético paleoproterozoico os blocos Serrinha e Jequié (possíveis microcontinentes – Barbosa and Sabaté, 2004).

Na Serra do Espinhaço, as principais unidades metavulcanossedimentares de possível/provável idade riaciana/orosiriana são os grupos Costa Sena, Riacho dos Machados e o Complexo Limoeiro. Outra unidade de grande importante frente a questão e que tem sido alvo de controvérsia é o Grupo Pedro Pereira. A sequência metavulcanossedimentar, pioneiramente posicionada no Mesoarqueano (Machado *et al.*, 1989), teve sua idade contestada e considerada paleoproterozoica (*e.g.* Chaves *et al.*, 2013, 2012; M. C. R. Silva *et al.*, 2015). Estas unidades estão dispostas ao longo da possível borda desta faixa orogênica paleoproterozoica, nos domínios dos blocos a oeste.

Neste contexto esta tese tem como objetivo principal realizar estudos que permitam sugerir interpretações geológicas a luz de novos dados geocronológicos e geoquímicos sobre sequências metavulcanossedimentares potencialmente correlacionáveis ao evento Paleoproterozoico na Serra do Espinhaço Meridional. A pesquisa conta com recursos do NGU-CPMTC, bem como do projeto temático do CNPq “Bacias riacianas/orosirianas da Serra do Espinhaço: tectônica e proveniência sedimentar” (Processo # 205254/2016-4)”.

Os dados produzidos durante o desenvolvimento desta tese estão expostos na forma de artigos científicos nos capítulos 3 e 4.

1.3 Objetivos

Os principais objetivos dessa tese são contribuir para o entendimento do significado tectônico das sequências metavulcanossedimentares pré-estaterianas que ocorrem ao longo da Serra do Espinhaço Meridional e avaliar possíveis correlações tectônicas as sequências da Serra do Espinhaço Central, em especial o Grupo Riacho dos Machados.

Os objetivos específicos são:

a) Reavaliar o posicionamento da sequência metavulcanossedimentar Pedro Pereira através de geocronologia e caracterização geoquímica de suas formações ferríferas;
b) Revisitar o Grupo Costa Sena à luz da geocronologia e geoquímica para:
    i. investigar o significado das rochas que compõem a Formação Barão do Guaicuí;
    ii. reavaliar o posicionamento da Formação Bandeirinha em sua área-tipo;
    iii. propor um modelo evolutivo para o grupo;

1.4 Localização das áreas estudadas e trabalho de campo

As áreas em estudo se situam na região central e norte do Estado de Minas Gerais, entre os meridianos 43°25’W e 42°47’W, e paralelos 15°S e 19°S. No domínio fisiográfico da Serra do Espinhaço Meridional, precisamente entre as cidades Conceição do Mato Dentro e Diamantina, ocorrem as rochas do Grupo Costa Sena. De caráter mais local, na região de Gouveia, afloram as rochas da sequência metavulcanossedimentar Pedro Pereira (ou Grupo Pedro Pereira). As rochas das sequências metavulcanossedimentares Riacho dos Machados e

Complexo Limoeiro afloram domínio da Serra do Espinhaço Central, próximo às cidades Riacho dos Machados e Monte Azul, respectivamente. As rotas de acesso a partir de Belo Horizonte podem ser consultadas na Figura 1.1. Interessante ressaltar que as rodovias partem do interior do sul do Cráton do São Francisco em direção à faixa orogenética Araçuaí.

A primeira etapa do trabalho de campo foi dedicada à realização de perfis estratégicos para caracterização e coleta de amostras dos grupos Costa Sena e Pedro Pereira, dividida em 4 campanhas de 10 dias. Em seguida, concomitante à coorientação de Trabalho de Graduação Final (Araújo and Leal, 2017), foi realizado o mapeamento da área de ocorrência do Grupo Riacho dos Machados e posterior coleta de amostras, em 20 dias. Por fim, foi realizado 10 dias de trabalho de campo no Complexo Limoeiro para a realização de perfis estratégicos e coleta de amostra, fechando um total de 70 dias de campo para realização desta tese de doutoramento.

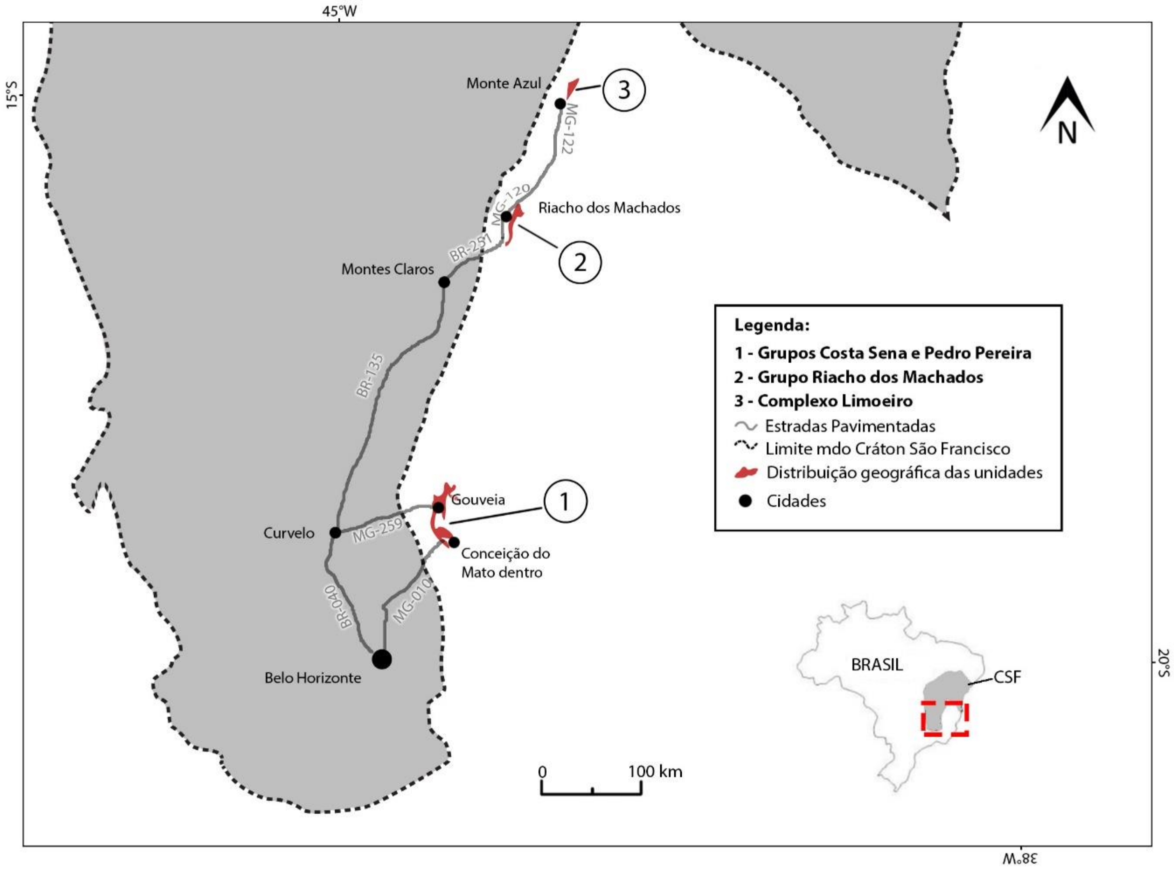

Figura 1.1 - Localização áreas estudadas em Minas Gerais. CSF-Cráton São Francisco.

2 CONTEXTO GEOLÓGICO

A rede paleoproterozoica de cinturões orogenéticos está registrada em quase todos os continentes atuais. Na América do Sul e África são vastos os registros da orogênese Riaciana/Orosiriana (também conhecida como Transamazônica ou Eburneana) que originou o paleocontinente São Francisco-Congo, a partir da colisão diacrônica de vários continentes arqueanos e arcos de ilhas entre 2.2 e 1.9 Ga (*e.g.* Aguilar *et al.*, 2017; Alkmim, 2004; Almeida, 1981; Barbosa and Sabaté, 2004; Barbosa *et al.*, 2020; Heilbron *et al.*, 2010). O PCSC foi um dos vários continentes envolvidos na amalgamação de Gondwana Oeste (e.g. Kalarari, Rio de la Plata, Amazônico, Oeste-africano, Leste-antártica). Seus fragmentos permanecem preservados no interior do cráton São Francisco-Congo e também como basement inliers nas faixas móveis neoproterozoicas que o circundam, tanto na América do Sul quanto na África.

A complexidade de sua amalgamação, o retrabalhamento de parte de seu domínio não cratônico pelas faixas móveis brasilianas e as coberturas proterozoicas dificultam o entendimento sobre o paleocontinente e muitas questões permanecem abertas/controversas. A título de exemplo, especula-se se o PCSC foi parte de uma enorme massa continental (supercontinente Columbia – ou Atlântica, seu precursor; Rogers and Santosh, 2004) ou um continente a parte de Columbia (Bloco Central Africano; D'Agrella-Filho and Cordani, 2017); se foi fragmentado por rifteamentos proterozoicos e, por conseguinte, partes que um dia o compuseram foram espalhadas e acrescidas em outros continentes (*e.g.* Craton do Norte da China; Cederberg *et al.*, 2016; Chaves *et al.*, 2019; Fu *et al.*, 2015; Peng *et al.*, 2011; Teixeira *et al.*, 2016); qual seria sua extensão em sua origem; se seriam os blocos Gabão, Kasai e Angola uma unidade no momento da colagem paleoproterozoica ou blocos separados que se colidiram (Crosby *et al.*, 2010; Fernandez-Alonso *et al.*, 2011; Pasyanos and Nyblade, 2007; Priestley *et al.*, 2008).

Na parte sul-americana, os núcleos arqueanos que compõem o PCSC são representados principalmente por rochas gnáissicas/migmatíticas de médio a alto grau, suítes TTG, granitoides alcalinos e associações tipo granito-greenstone belt. Sobre os blocos arqueanos, encontram-se uma série de sequências metavulcanossedimentares ou que já foram confirmadas riacianas/orosirianas ou que são potencialmente desta faixa de idade (Figura 2.1). Esta tese tratará, em especial, daquelas alinhadas sobre a Serra do Espinhaço meridional e central.

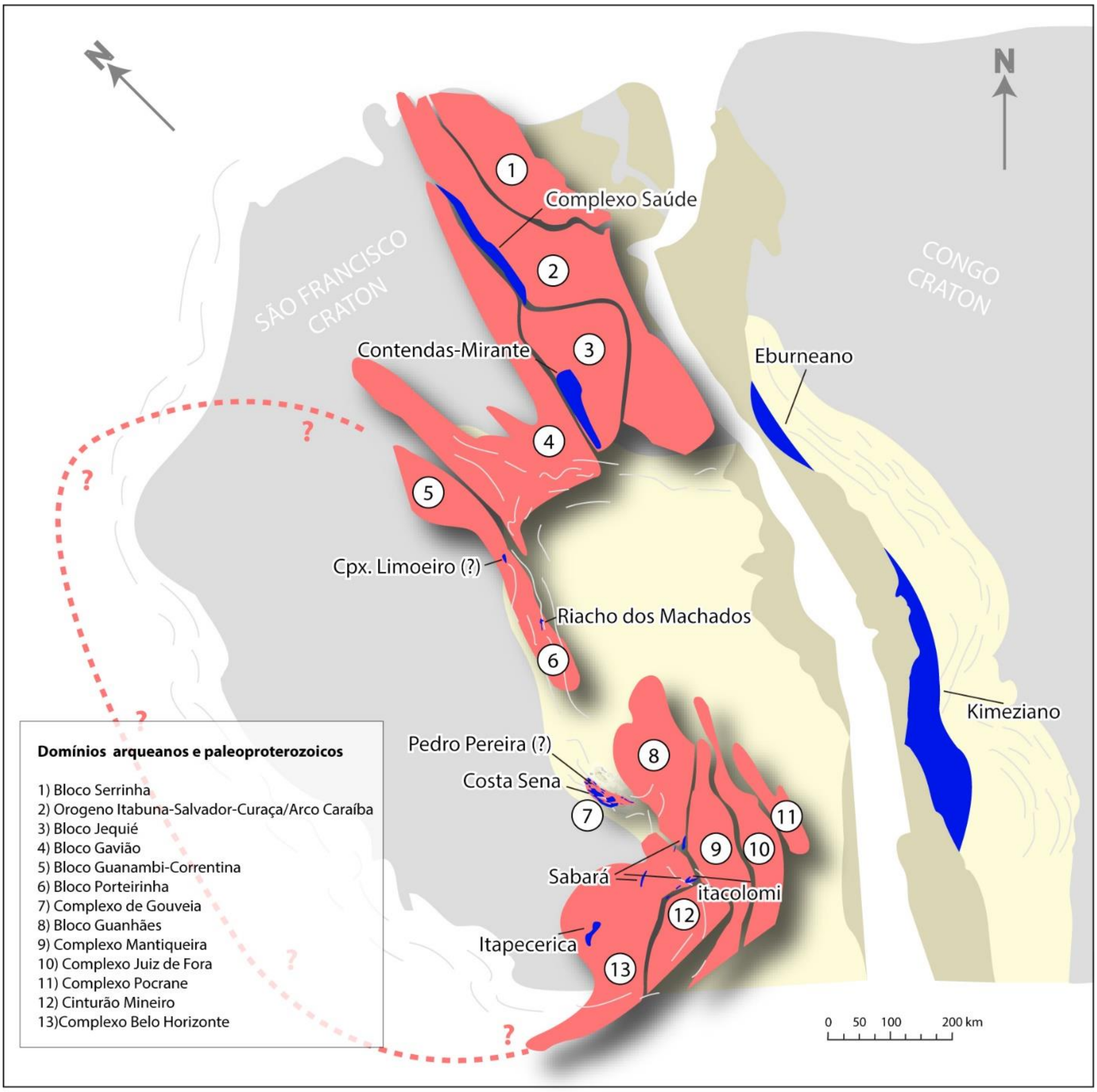

Figura 2.1 - Sequências metavulcanossedimentares riacianas/orosirianas (em azul) potencialmente correlacionáveis à amalgamação do paleocontinente São Francisco-Congo. Modificado de Alkmim et al. (2006).

2.1 Complexos arqueanos

Na Serra do Espinhaço Meridional, o Eon Arqueano é registrado em complexos graníticos/gnáissicos/migmatíticos, restritos corpos anfibolíticos e pequenas injeções pegmatíticas (Schöll and Fogaça, 1979) agrupados no designado Complexo de Gouveia (Knauer, 1990), na região central, e pelo denominado Complexo Basal, na borda leste. Uma amostra de gnaisse da região de Gouveia foi datada em 2828 ± 43 Ma (Santos, 2015), enquanto amostras de granitoides da mesma região forneceram discórdia com intercepto superior em 2839 ± 14 M.a. (U/Pb em zircão Machado *et al.*, 1989). Sob a denominação de Sequência

Vulcano-sedimentar Pedro Pereira (Carvalho, 1982), agrupam-se sericita-quartzo xistos intercalados à cherts ferruginosos e itabirito, metariolito, talco xisto, metabásicas e metaultrabásicas, rochas consideradas relictas de um *greenstone belt* (Fogaça *et al.*, 1984). Para esta unidade, metavulcanitos ácidos da região de Pedro Pereira forneceram idade de 2971 ± 16 M.a. (U/Pb em zircão Machado *et al.*, 1989). No entanto, esta idade tem sido contestada por alguns autores (Chaves *et al.*, 2013, 2012; M. C. R. Silva *et al.*, 2015), os quais acreditam que a rocha datada da região de Pedro Pereira era um granitoide milonitizado do embasamento que foi confundido com metariolito. Rosière et al. (2019) também refuta esta idade devido ao posicionamento obscuro da amostra analisada e levanta a possibilidade de que as rochas do Grupo Pedro Pereira façam parte de uma ampla bacia pós-riaciana com fluidos enriquecidos em Fe. Chaves et al. (2012) conduziram estudos de geoquímica nas formações ferríferas bandadas da região de Pedro Pereira e caracterizaram-nas como tipo Lago-Superior e atribuíram-nas ao eon Proterozoico baseado em assinaturas de ETR com acentuadas anomalias de Eu e Ce.

Na Serra do Espinhaço central, as rochas arqueanas são agrupadas nos complexos Córrego do Tingui, Porteirinha e Córrego do Cedro, aflorantes no contexto do denominado Bloco Porteirinha, um *basement inlier* interno ao orógeno Araçuaí. O primeiro complexo corresponde a rochas graníticas gnaissificadas, localmente afetadas por graus variáveis de milonitização. São comuns corpos de anfibolitos escuros concordantes e discordantes ao bandamento gnáissico (Knauer *et al.*, 2007). O Complexo Porteirinha engloba gnaisses/migmatitos de coloração acinzentada, também com corpos anfibolíticos concordantes ou discordantes. Encraves estirados de composição diorítica até mais básica estão presentes, bem como corpos graníticos intrusivos e diques aplíticos (Knauer *et al.*, 2007). O Complexo Porteirinha é intrudido por vários plutons com intervalo de cristalização entre 2.38 e 1.85 Ga (Cruz *et al.*, 2016) agrupados no Arco Magmático do Oeste da Bahia. Na região de Riacho dos Machados (MG), o Complexo Córrego do Cedro aflora no Anticlinal de Itacambira e inclui rochas granito-gnaissicas. Segundo Siga Jr. (1986), esses gnaisses sofreram retrabalhamento ca. 2700 M.a., confirmando sua idade arqueana.

2.2 Unidades metassedimentares arqueanas/paleoproterozoicas

2.2.1 Grupo Costa Sena

Sob a denominação de Grupo Costa Sena (Fogaça *et al.*, 1984), a sequência aflora na Serra do Espinhaço Merdional (Figura 2.2) ora recobrindo o embasamento ora na forma de cunhas tectônicas circundadas pelo embasamento granito-gnaissico. São agrupadas, na base, rochas predominantemente epiclásticas com raras contribuições vulcânicas de ocorrência mais expressiva nos arredores do distrito homônimo. A Formação Barão do Guaicuí, com empilhamentos que podem chegar a 1000 m de espessura (Fogaça *et al.*, op. cit.), é composta em sua maioria por quartzo-muscovita xistos, cianita-muscovita-quartzo xistos, sericita-quartzo xistos e hematita-quartzo-muscovita xistos, com raras intercalações de vulcânicas básicas e félsicas. Minoritariamente, é constituída por quartzo xistos com horizontes lenticulares de quartzito. Uma pequena parte dos cianita xistos podem conter massas e veios de lazulita/dumortierita (e.g. a oeste da Serra da Miúda ou a norte da Serra Matriculada). Comumente intercalados nos quartzo-mica xistos, ocorrem horizontes pouco espessos (~10 cm) de “xistos verdes” com origem controversa. Fogaça et al. (1984) cita a ocorrência de metaconglomerados monomíticos até polimíticos, escassos, em forma de lentes métricas, sobretudo nas proximidades dos contatos com a Formação Bandeirinha.

Os autores (Fogaça *et al.*, op. cit.) identificaram também a ocorrência local de xistos finos com níveis delgados de mica verde (fuchsita) na Serra do Paraúna, a oeste do povoado de Costa Sena. Machado et al. (1989) dataram metavulcanito ácido (U/Pb em zircões) representante dessa formação na região de Ouro Fino, que produziu uma discórdia com intercepto superior em 2049 +3/-2 Ma. O contato basal pode se dar com o embasamento granítico ou com o Grupo Pedro Pereira, na forma de inversão tectônica ou pseudoconformidade tectônica. São descritos em sua base, de ocorrência restrita, níveis metaconglomeráticos delgados a norte de Gouveia e a oeste da faz. Formação. Os contatos superiores com a Formação Bandeirinha são gradativos ou tectonizados. Quando em contato direto com o Supergrupo Espinhaço, se dá por discordância angular e erosiva ou por contato tectônico por falhamentos/zonas de cisalhamento dúcteis.

A Formação Bandeirinha é caracterizada por pacotes de até 200 m de espessura, estruturados em uma faixa irregular que se estende a sudoeste e ao sul de Guinda, podendo ser encontrado em locais restritos como ao sul de Diamantina e também nas imediações do Córrego do Amarelo, a sudoeste de Costa Sena (Fogaça, 1982), ou ao norte da Serra Matriculada. Em sua porção basal, a Formação Bandeirinha é constituída por quartzitos finos, mineralogicamente puros ou micáceos (até 20 %), com variações laterais parta quartzo-muscovita/sericita xistos finos. Nas porções média e superior são frequentes os quartzitos de granulação fina a média e coloração rósea com grãos envoltos por fina película de óxidos de ferro (Schöll and Fogaça, 1981), interpretado como red beds por Almeida-Abreu (1993) ou de cores mais claras, com bandamento ferruginoso. Nessa porção também se intercalam horizontes conglomeráticos (clastos de até 30 cm) que podem ser considerados como produto de retrabalhamento intraformacional. Subordinadamente são encontrados clastos (tamanho seixo) de quartzo leitoso, formação ferrífera, jaspilito e quartzito ferruginoso. As estruturas mais frequentes são as estratificações cruzadas tabulares de médio porte e baixo ângulo (< 10°) e tangenciais à base dos estratos. A Formação Bandeirinha recobre concordantemente a Formação Barão do Guaicuí, sendo frequentemente gradacional, por vezes brusco ou tectônico. Simplicio e Basilici (2015) interpretam a unidade como tendo sido depositada em ambiente eólico dominante intercalado com episódios fluviais efêmeros, com fases climáticas alternadamente secas e úmidas. O contato superior com o Supergrupo Espinhaço se dá por discordância angular e erosiva.

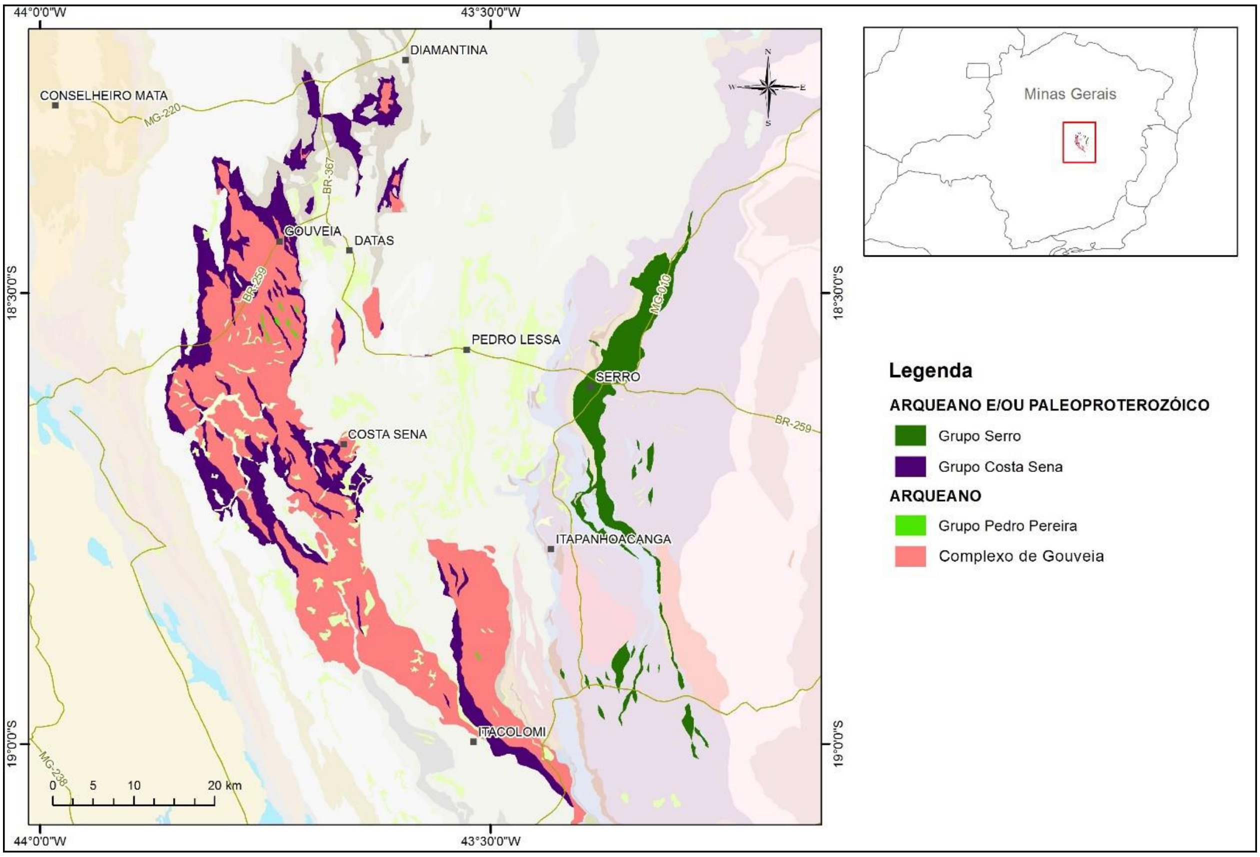

Figura 2.2 - Mapa geológico regional da porção meridional da Serra do Espinhaço com destaque para as unidades do embasamento cristalino e sequências supracrustais paleoproterozoicas e arqueanas (modificado de Heineck *et al.*, 2003)

2.2.2 Grupo Riacho dos Machados

Situado no segmento central da Serra do Espinhaço, o Grupo Riacho dos Machados ocorre no Bloco Itacambira-Monte Azul (BIMA, Figura 2.3) bordejando o Bloco Porteirinha, onde afloram rochas arqueanas e paleoproterozoicas. O grupo corresponde a uma pilha de xistos, predominantemente metapelíticos, principalmente representados por quartzo-biorita xisto, com porções variáveis de plagioclásio, granada, estaurolita e cianita. Destacam-se, localmente associados aos mica xistos, lentes de formação ferrífera. Xistos quartzo-feldspáticos, quartzo-actinolita xistos, quartzo-tremolita xistos, tremolita xistos anfibolitos e xistos máficos/ultramáficos são potenciais registros de atividade magmática relacionada à unidade (Fonseca et al., 1997, Mourão et al., 1997). No que tange ao contexto geotectônico, as rochas que compõem o Grupo Riacho dos Machados já foram objeto de diversas interpretações. Inda et al. (1984) consideram que a unidade represente uma sequência do tipo greenstone belt, enquanto Fonseca (op. cit.) e Guimarães et al. (1997) postulam deposição relacionada a um arco vulcânico continental. Por sua vez, Abreu & Belo de Oliveira (1998) e Crocco et al. (2006) consideram que a unidade tenha se depositado em contexto extensional, em bacia do tipo rifte. Até 2020 não existiam dados geocronológicos diretos sobre as rochas do Grupo Riacho dos Machados e sua idade permanecia especulativa. Recentemente, Leal et al. (2021) dataram hornblendito da sequência que produziu uma idade de cristalização em 2071 ± 9 Ma, atestando idade riaciana para a unidade. Através de análises geoquímicas em ultramafitos, eles concluem também que a sequência metavulcanossedimentar se desenvolveu em uma bacia intracontinental *back-arc.* Estes dados implicam que o bloco Porteirinha se encontrava em estágio acrescionário ao final do Riaciano. A unidade hospeda importantes depósitos de ouro (e.g. mina Riacho dos Machados, CVRD e RDM), zinco e chumbo (depósito de Salobro, companhia Zinco do Brasil), alvo de exploração desde 1970. Vale destacar que este doutorando é coautor do artigo publicado supracitado (Anexo), tendo participado ativamente da etapa de concepção e campo, até sua elaboração e publicação.

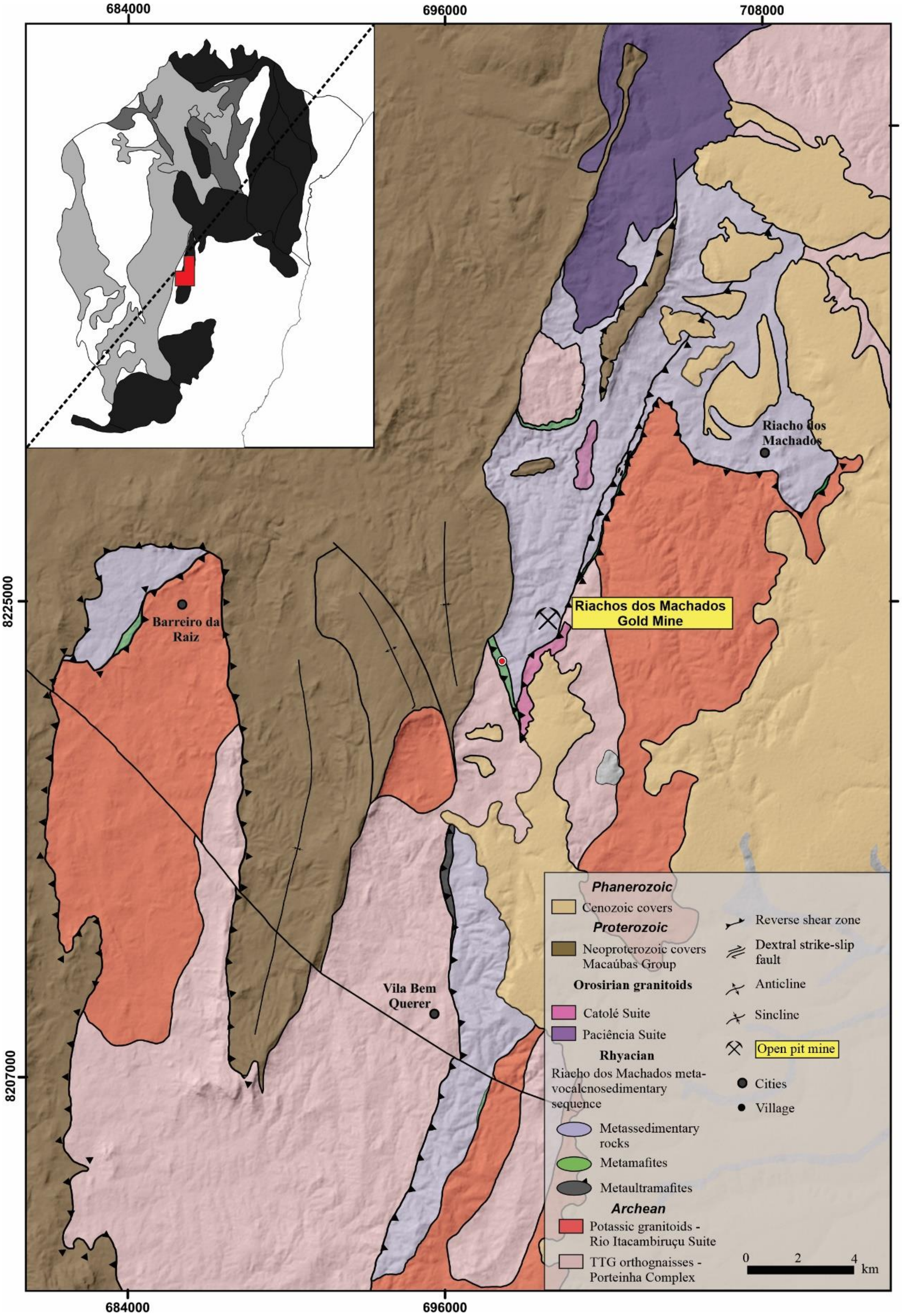

Figura 2.3 - Mapa geológico mostrando a distribuição espacial da sequência metavulcanossedimentar Riacho dos Machados, no centro do bloco Porteirinha (Leal *et al.*, 2021). No canto superior, à esquerda, mapa esquemático do craton São Francisco com domínios arqueanos/paleoproterozoicos em destaque e localização do mapa.

2.2.3 Complexo Limoeiro

Ainda no setor central da Serra do Espinhaço, e também no contexto do Bloco Porteirinha (ou Bloco Itacambira-Monte Azul), ocorre uma sequência metavulcanossedimentar na região de Monte Azul (MG), composta por quartzo-clorita xistos, clorita-quartzo-turmalina-pirita xistos, quartzo-muscovita xistos, raros quartzitos feldspáticos e localmente, corpos lenticulares de barita contidos em xistos miloníticos, quartzitos, gnaisses paraderivados intercalados à marmores e rochas calcissilicáticas, de arranjo espacial complexo (Figura 2.4). Estas rochas foram integradas por Knauer et al. (2007) no Complexo Limoeiro, nomenclatura proposta em substituição à antiga “Sequência Limoeiro”, de Penha e Sabóia (1995). Apesar de não existirem dados geocronológicos disponíveis sobre as rochas do Complexo Limoeiro, Knauer et al. (2007) postulam para a unidade uma idade riaciana/orosiriana, tendo como base nas relações de contato com o Supergrupo Espinhaço e o embasamento Arqueano, levantando a possível correlação com as rochas dos grupos Costa Sena e Riacho dos Machados.

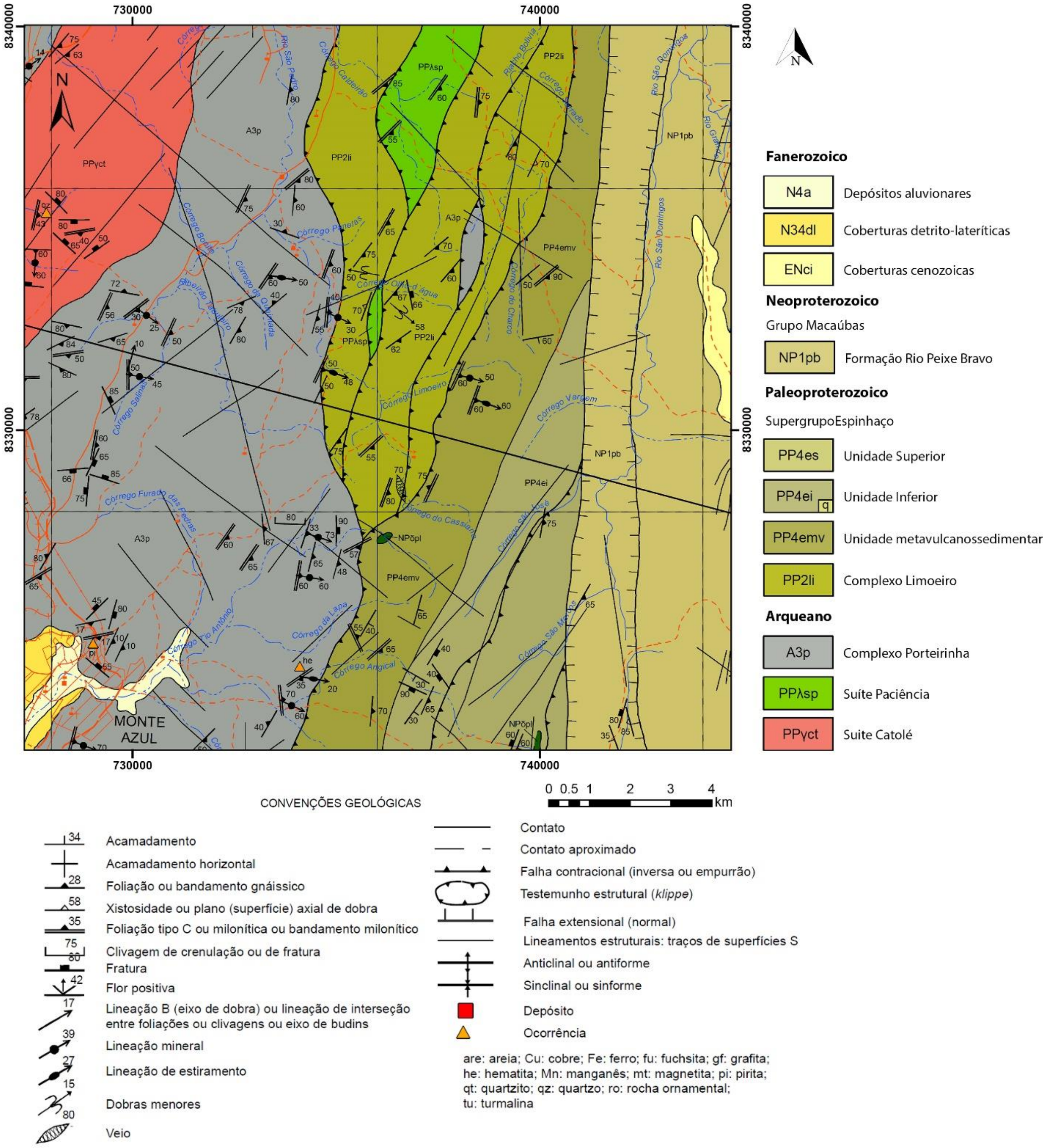

Figura 2.4 - Complexo Limoeiro (em azul), entre as folhas Monte azul, a sul, e Espinosa, a norte (modificado de Knauer *et al.*, 2007).

3 ARTIGO I: NEW GEOCHRONOLOGIC AND GEOCHEMICAL CONSTRAINTS FOR THE PEDRO PEREIRA METAVOLCANOSEDIMENTARY SEQUENCE: EVIDENCE FOR A 2.77 GA OXYGEN OASIS RECORD IN THE SÃO FRANCISCO-CONGO PALEOCONTINENT

Marcelo A. Freimann[a,b], Luiz Guilherme Knauer[a,b], Matheus Kuchenbecker[a,b,c]

[a]Programa de Pós-Graduação em Geologia, Universidade Federal de Minas Gerais, Belo Horizonte (MG), Brazil

[b]Centro de Pesquisas Professor Manoel Teixeira da Costa, Instituto de Geociências, Universidade Federal de Minas Gerais, Campus Pampulha, Belo Horizonte (MG), Brazil

[c]Laboratório de Estudos Tectônicos, Centro de Estudos em Geociências, Instituto de Ciência e Tecnologia, Universidade Federal dos Vales do Jequitinhonha e Mucuri, Diamantina (MG), Brazil

Abstract

Exposed within the reworked basement of the Araçuaí orogen, eastern Brazil, the Pedro Pereira metavolcanosedimentary sequence (PPMS) comprises a lower unit dominated by metaultramafic/mafic rocks, a intermediate unit dominated by metarhyolites and a predominant upper unit of acid metavolcanites associated with chemical and clastic metasedimentary rocks. This sequence has been defined and investigated in the ’80s when it was considered as a Mesoarchean greenstone belt. Since then, few studies have addressed these rocks, and due to the lack of reliable geochronological data a Paleoproterozoic age has also been suggested for the sequence. To reevaluate the age and evolution of the unit, new whole-rock geochemical and zircon U-Pb (LA-ICPMS) geochronologic data were obtained for the iron formation and acid metavolcanic rocks, respectively. When normalized to post-Archean Australian Shale standard, BIF samples can be divided into three groups. Group 1 BIF samples are marked by significant enrichment of the LREE, very high ∑REE+Y, positive La anomaly, extreme negative Ce anomaly, negative Eu anomaly, and subchondritic Y/Ho ratio. In contrast, Group 2 BIFs are marked by the enrichment of HREE, low ∑REE+Y, positive La anomaly, negative Eu anomaly, slight negative Ce anomaly, and predominantly super- and subchondritic Y/Ho ratios. The massive iron formation (MIF) group shows very high middle-to-heavy REE+Y enrichment, strong negative Ce anomaly, negative Eu anomaly, very high ∑REE+Y, and variable Y/Ho ratios. The modification of the iron formation by post-depositional hydrothermal alteration might have disturbed the original basin water signature. However, Group 2 is more compatible with pure chemical precipitates and its slight negative anomalies suggest an oxic environment. A PPMS metarhyolite from the upper portion of the sequence interlayered with the BIFs yielded the Concordia Age of 2771±8.4 Ma. This age rules out a Paleoproterozoic origin for the PPMS, as suggested/considered by recent papers. The results imply that PPMS possibly represents one of the oldest records of oxygenation previous to the GOE in the geologic archives and could provide information to understand the early evolution of localized pockets of oxygen before the Great Oxidation Event.

Keywords: Pedro Pereira; São Francisco-Congo paleocontinent; oasis; iron formation; greenstone belt;

3.1 Introduction

Nearly a third of the Earth's evolution occurred during the Archean Eon. A challenge for the geologists, however, is that a large amount of crust has been recycled back into the mantle through subduction zones and lower crustal delamination (Spencer *et al.*, 2017) and therefore, the geological record of the early Earth is scarce and discontinuous. As ancient granite-greenstone terranes can hold valuable clues of the deep past, their study has been crucial in the understanding of a variety of Earth's system spheres. While their igneous rocks assist in the understanding of the early lithosphere's nature, the sedimentary (especially chemical precipitates as iron formations) shed light on the early Earth atmosphere, hydrosphere, and biosphere (Anhaeusser, 2014). Beyond the academic value, greenstone belts are well known for hosting massive gold and base metals deposits and, therefore, are of great interest to the mineral exploration sector.

As parts of the intricate São Francisco-Congo paleocontinent, at least a dozen greenstone belts are mapped in its Brazillian extension (see Fig. 3.1). While some of them were vastly studied (*e.g.* Rio das Velhas and Pitangui greenstone belts), others have been overlooked (e.g. Pedro Pereira, Rio Mata Cavalo, and Serro greenstone belts). In this sense, the main contribution of this work is to investigate where does Pedro Pereira metavolcanosedimentary sequence fit in time and geotectonic setting concerning the São Francisco-Congo paleocontinent.

The São Francisco-Congo paleocontinent (hereinafter referred to as "SFCP") was one of the continents involved in the assembly of Gondwana, whose rocks remain preserved within the Neoproterozoic cratons and also in basement inliers of their surrounding orogens, both in South America and Africa (*e.g.* Alkmim *et al.*, 2017; Heilbron *et al.*, 2017)

Exposed within the reworked basement of the Araçuaí orogen (Pedrosa-Soares *et al.*, 2001) eastern Brazil, Pedro Pereira metavolcanosedimentary sequence (hereinafter referred to as “PPMS”; Carvalho, 1982; Fogaça *et al.*, 1984; Knauer, 2007; Knauer and Grossi-Sad, 1997) contains metaultramafic/mafic rocks and metarhyolite associated with chemical and clastic metasedimentary rocks. This greenstone belt sequence was studied in the ’80s, being positioned in the Mesoarchean by Machado *et al.* (1989). More recently, due to the lack of reliable geochronological data and based on chemical features of its banded iron formations, researchers postulate a Paleoproterozoic age for the PPMS (Chaves *et al.*, 2013, *e.g.* 2012; Rosière *et al.*, 2019; M. C. R. Silva *et al.*, 2015), impacting the envisaged tectonic evolution of the SFCP.

In this paper we revisit the PPMS, presenting an up-to-date review of the literature about the unit and reporting new geochronological (zircon U-Pb, LA-ICP-MS) and geochemical data from an acid metavolcanite, as well as a complete geochemical characterization of its associated banded iron formation. This dataset allows us to discuss the age and tectonic significance of PPMS and also assess the reliability of inferring paleoenvironmental conditions from their banded iron formation. Grounded on modern analytical data, we intend to contribute to the collaborative effort in understanding the tectonic evolution of the SFCP, which was deeply dismembered by the Neoproterozoic orogenic belts in South America.

3.2 Geological settings

The São Francisco-Congo paleocontinent represents a long-lived and relatively stable continent involved in the assembly of Gondwana by the end of the Neoproterozoic, whose remnants now represent the São Francisco (South America) and Congo (Africa) cratons, two key pieces in the world’s Precambrian scenario. The SFCP evolved from the collision between several smaller Archean continents and island arcs (Aguilar *et al.*, 2017; Alkmim, 2004; Almeida, 1981; Barbosa and Sabaté, 2004; Barbosa *et al.*, 2020; Cruz *et al.*, 2016; Heilbron *et al.*, 2010), in a diachronous and complex orogenic process occurred between 2.2 and 1.9 Ga. Whether the PSFC has been part of a larger landmass (e.g. Central African Block and Columbia supercontinents) or comprised other parts now resting elsewhere in the world (e.g. North China craton) is still a theme of intense debate and a hot research topic (*e.g.* Alkmim and Teixeira, 2017; Cederberg *et al.*, 2016; Chaves *et al.*, 2019; Cordani *et al.*, 2013; D’Agrella-Filho and Cordani, 2017; Fu *et al.*, 2015; Lin *et al.*, 2016; Peng *et al.*, 2011; Rogers and Santosh, 2004; *e.g.* Teixeira *et al.*, 2017b)

Due to this intricate tectonic history, the Archean record of the SFCP encompasses quite distinct units in its different areas of occurrence. In the Brazilian portion, these Archean nuclei are chiefly represented by medium- to high-grade gneissic-migmatitic rocks, TTG suites, alkaline granitoids, and granite-greenstone associations (Barbosa and Sabaté, 2004; Barbosa *et al.*, 2020; Noce *et al.*, 2007; L. C. da Silva *et al.*, 2015; Silva *et al.*, 2002a; Teixeira *et al.*, 2017a). These Archean greenstone belts include the Piumhi (*e.g.* Chiarini, 2001; Fritzsons Jr *et al.*, 1980), Rio das Velhas (*e.g.* Machado *et al.*, 1992; Noce *et al.*, 2005), Pitangui (*e.g.* Brando Soares *et al.*, 2017; Verma *et al.*, 2017), Rio Mata Cavalo (probably Archean; *e.g.* Angeli *et al.*, 2011; Dossin *et al.*, 1985), Pedro Pereira (*e.g.* Carvalho, 1982; this work), Umburanas (*e.g.* Cunha and Fróes, 1994; Menezes Leal *et al.*, 2015), and Mundo Novo sequences (*e.g.* Mascarenhas and Silva, 1994; Spreafico *et al.*, 2019; Zincone *et al.*, 2017). Some of these units host major economic deposits, such as the Rio das Velhas (*e.g.* Araújo and Lobato, 2019; Baltazar and Zucchetti, 2007; Kresse *et al.*, 2020; Lobato *et al.*, 2001; Vitorino *et al.*, 2020) and Pitangui (Bosco-Santos *et al.*, 2020; Brando Soares *et al.*, 2018; Cabral and Corrêa Neto, 2015; *e.g.* Fabricio-Silva *et al.*, 2019; Tassinari *et al.*, 2015) gold and iron deposits.

At the Ediacaran-Cambrian, the SFCP was deeply affected by the evolution of the Brasiliano-Pan African orogenetic system that welded West Gondwana (*e.g.* Alkmim *et al.*, 2017; Brito Neves *et al.*, 2014). The inner portions of the continent were relatively preserved within São Francisco and Congo cratons, while their borders were intensely reworked and dismembered, lying now as basement inliers within the various Neoproterozoic orogenic belts that surround these cratonic areas (Borges *et al.*, 2020; Degler *et al.*, 2018; Leal *et al.*, 2021; Martins-Ferreira *et al.*, 2020; Noce *et al.*, 2007; Santos *et al.*, 2015).

The Araçuaí orogen, which bounds the eastern São Francisco craton, is a confined orogen that evolved from the closure of a partially oceanized gulf in the Ediacaran-Cambrian transition (*e.g.* Alkmim *et al.*, 2017; Pedrosa-Soares *et al.*, 2020). Within the orogen, several basement inliers present Archean and Paleoproterozoic rocks that host key information to understanding the evolution of the SFCP (Degler *et al.*, 2018; Grochowski, 2019; Leal *et al.*, 2021; Noce *et al.*, 2007). Among these basement inliers, we highlight the Gouveia domain, which hosts the metavolcanosedimentary sequence that is the object of this investigation.

3.3 Geology of the Gouveia domain

The Gouveia domain (Fig. 3.1) is a basement inlier within the Southern Espinhaço ridge, an important geomorphological expression of the external Araçuaí orogen, where Archean and Paleoproterozoic rocks crop out in the core of a regional N-trending anticlinorium (Simone C.P. Cruz *et al.*, 2005). The Archean is represented by granite-gneiss-migmatite complexes, with uncommon amphibolitic bodies and minor pegmatitic injections grouped in the Gouveia

Complex (Hoffmann, 1983a; Knauer, 1990; Schöll and Fogaça, 1979). A gneiss from the Gouveia Complex was dated at 2828 ± 43 Ma (zircon U/Pb; Santos, 2015).

A pioneering study (Carvalho, 1982) identified NNW-SSE oriented tectonic slivers inserted in the Gouveia Complex, composed of strained sericite-quartz schists intercalated with ferruginous cherts and iron formations, meta-acid, metabasic, and metaultrabasic schistified rocks. These rocks, grouped under the denomination of "Pedro Pereira Volcanic-sedimentary Sequence" has been considered as greenstone belt remnant (*e.g.* Fogaça *et al.*, 1984; Hoffmann, 1983a). Although the volcanogenic nature of the ultramafic rocks is uncertain due to the intense shearing, the close stratigraphic relationship with acid metavolcanic and banded iron formation was considered by these authors as an indication of subaqueous extrusion.

An abstract briefly reports preliminary results of zircon U-Pb assay on an acid metavolcanite sample from Pedro Pereira region. The sample yielded upper intercept age of 2971 ± 16 Ma (Machado *et al.*, 1989). Some authors (Chaves *et al.*, 2013, 2012; M. C. R. Silva *et al.*, 2015) challenge this age and believe that the acid metavolcanite sample dated from Pedro Pereira region is a mylonitized basement granitoid mistaken as a metarhyolite. Therefore, the acquired age would represent an older basement unit that hosts Gouveia Granite intrusion. Rosière et al. (2019) also challenge this data due to the unclear geological positioning of the analyzed sample and raise the possibility of PPMS rocks being part of a larger post-Rhyacian basin with Fe-rich hydrothermal fluids.

Recently, Chaves et al. (2012) carried out geochemical studies on banded iron formation from Pedro Pereira region. The authors characterized the BIFs as Lake Superior-type and ascribe them to the Proterozoic eon based on REE signatures with strong negative europium and cerium anomalies.

The early Proterozoic is represented in the Gouveia anticlinorium by the Costa Sena Group, subdivided into a basal unit composed of schists and metavolcanic rocks (Barão do Guaicuí Formation) and an upper unit made of quartzites and metaconglomerates (Bandeirinha Formation, Fogaça *et al.*, 1984; Lopes-Silva and Knauer, 2011). Due to an iron oxide coating in the quartz grains, the Bandeirinha Formation quartzites frequently show pink coloration and are interpreted as red beds (Almeida-Abreu, 1993). Santos (2015) constrained the maximum depositional age of Barão do Guaicuí Formation at 2114 ± 13 through U/Pb detrital zircons. A metarhyolite sample from the Costa Sena Group was dated at 2049 ± 3 Ma (U-Pb zircon, Machado *et al.*, 1989).

These older rocks in the core of the Gouveia anticlinorium (Fig. 3.2b) are bordered by metasedimentary units of the Espinhaço Supergroup, which record successive aborted rifting events that affected the SFCP between 1.7 and 1.2 Ga (*e.g.* Chemale Jr *et al.*, 2012; Knauer, 2007; Kuchenbecker *et al.*, 2015; Martins-neto, 2000; Santos *et al.*, 2015; Schöll and Fogaça, 1979). All mentioned units are cut by Tonian metabasic dike swarm of the Pedro Lessa Metaigneous Suite (Biondi *et al.*, 1978; Knauer, 1990).

Major shear zones, related to the evolution of the Araçuaí orogen, affect the basement rocks at the core of the Gouveia anticlinorium (Simone C.P. Cruz *et al.*, 2005), controlling the spatial distribution of the Pedro Pereira metavolcanosedimentary sequence (Fig. 3.2). The metasedimentary units of the Costa Sena Group and Espinhaço Supergroup are also affected by such shear zones but accommodate part of the strain in multiscaled folds and interlayer shear zones as well (*e.g.* Kuchenbecker and Sanglard, 2018; Rolim, 1992).

The Gouveia domain Archean nucleus record upper amphibolite facies metamorphism in the granitic rocks of the Gouveia Complex, that were generated by anatexis at estimated temperature and pressure of 660 °C and 3.5-4.0 kb, respectively (Hoffmann, 1983a; Knauer and Grossi-Sad, 1997). This metamorphism took place at the Mesoarchean, marked by the age of the granite (Machado *et al.*, 1989; Neves *et al.*, 1979). The Gouveia Complex also records superposed greenschist facies metamorphism associated with non-coaxial shortening that occurred in the Paleoproterozoic and/or Neoproterozoic. The PPMS is metamorphosed at greenschist facies and also records superposed Paleoproterozoic and/or Neoproterozoic metamorphic phases (Carvalho, 1982; Fogaça *et al.*, 1984).

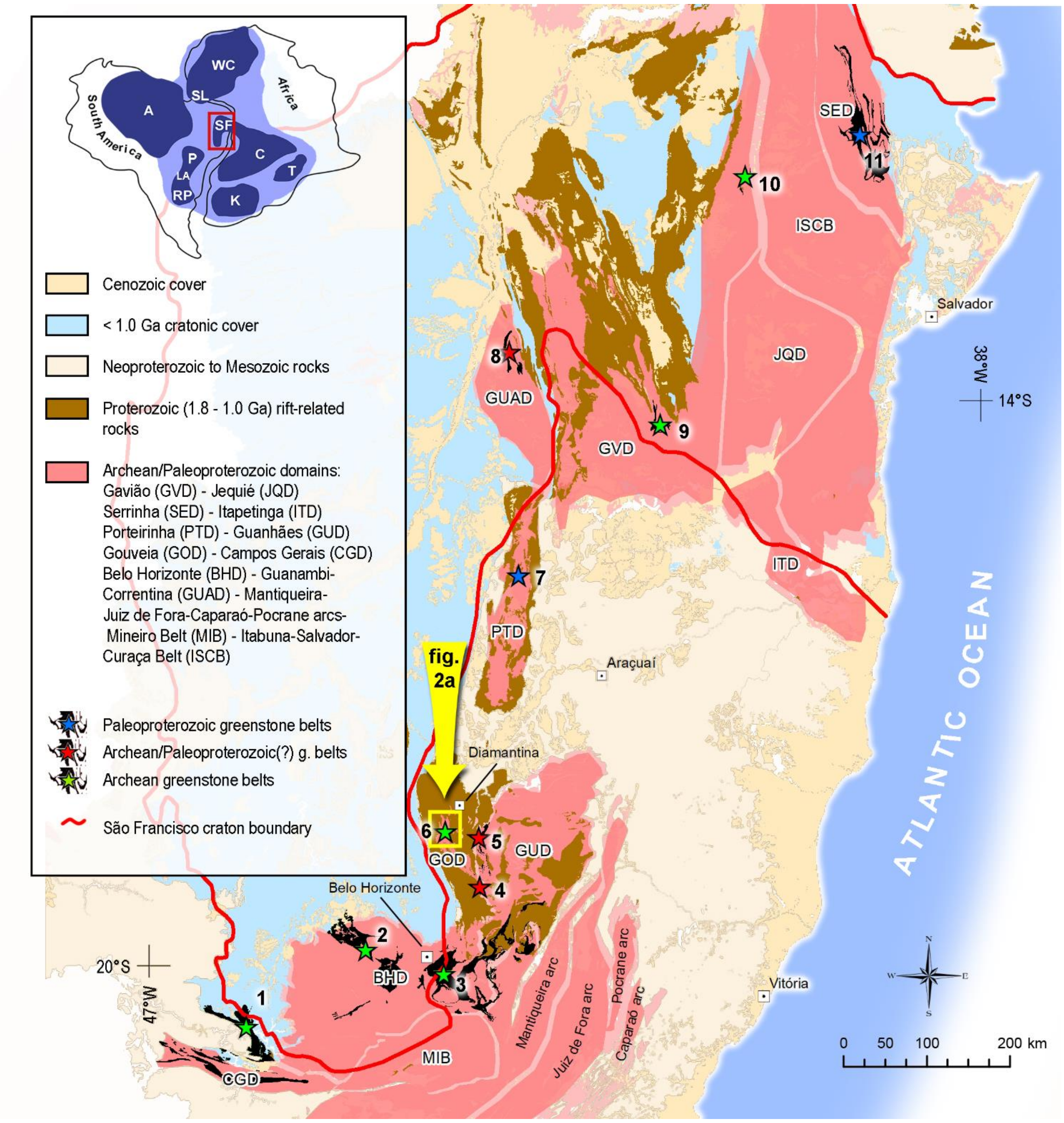

Fig. 3.1- Simplified domains map of the São Francisco craton and Araçuaí orogen region highlighting the Archean-Paleoproterozoic nuclei, Paleoproterozoic orogenic belts, and greenstone belts (modified from Barbosa and Dominguez, 1996; Heilbron *et al.*, 2016; Pinto and Silva, 2014; Silva *et al.*, 2005; Vieira *et al.*, 2018). West Gondwana miniature (after Pedrosa-Soares *et al.*, 2007): A – Amazonian craton; P,LA,RP – Paranapanema, Luis Alves and Rio de la Plata cratons; SF – São Francisco craton; WC, SL – West Africa and São Luiz cratons; C – Congo craton; K – Kalahari craton; and T – Tanzania craton. Greenstone belts: 1-Piumhi; 2-Pitangui; 3-Rio das Velhas; 4-Rio Mata Cavalo; 5-Serro; 6-Pedro Pereira; 7-Riacho dos Machados; 8-Riacho de Santana; 9-Umburanas; 10-Mundo Novo; 11-Rio Itapicuru.

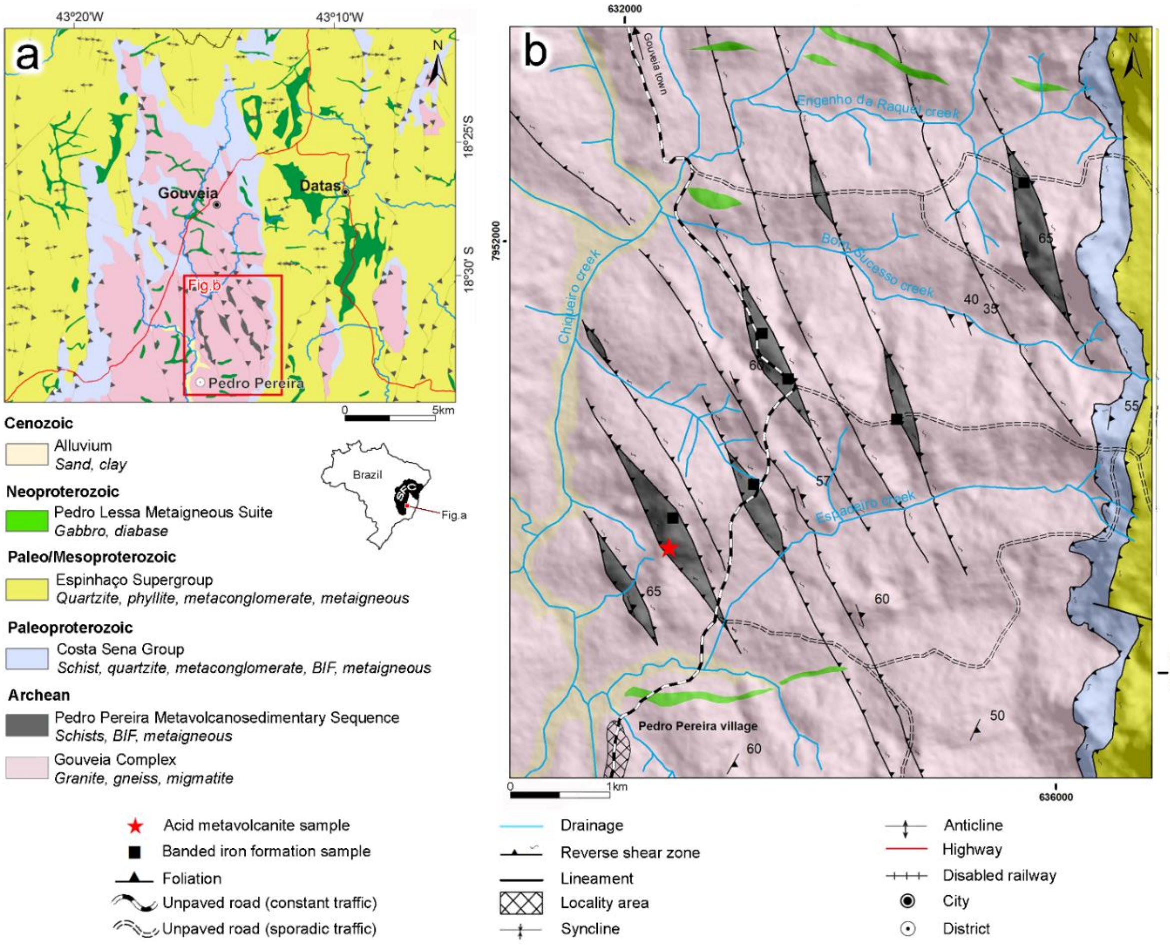

Fig. 3.2 (a) Geologic map of Pedro Pereira region (adapted from Carvalho, 1982; Knauer and Grossi-Sad, 1997), Datum WGS84, zone 23S; (b) regional map enclosing the northern portion of the Gouveia anticlinorium (adapted from Fogaça, 1997; Knauer and Grossi-Sad, 1997).

3.4 The Pedro Pereira metavolcanosedimentary sequence

The type-area of the PPMS is the vicinity of the Pedro Pereira, in the eastern border of the Gouveia anticlinorium (Fig. 3.2a, b). The PPMS comprises metabasic/metaultrabasic schists, banded iron formation, ferruginous chert, and chlorite-sericite-quartz schist (metarhyolite), which occur as isolated bodies tectonically emplaced in the Gouveia Complex. These bodies have tectonic contact (Fig. 3.3e) with the Gouveia Complex and display lens geometry. The sequence shows strong foliation, with modal to 070/40 with isoclinal folding axis in the same direction.

Due to intense shearing, tight folding, limited exposure, and intense weathering, it is not possible to establish a reliable stratigraphy for the whole unit. However, some generalizations can be made based on the internal stratigraphic array of the bodies. Although the bodies are not physically connected, many of them show an internal sequence with a basal, intermediate, and an upper unit. Considering that, it is reasonable to infer this persistent relation between the layers as the original stratigraphy. The relative ages between the layers were taken from the general stratigraphy of greenstone belts.

The PPMS is approximately 50 m thick and comprises a basal ultramafic and mafic unit (first quarter), which encompasses dark green serpentinites, magnetite-bearing chlorite-talc schist (10%; Fig. 3.4c), and green to brown chlorite schist (90%). Stratigraphically lying above it, metarhyolite composes the second quarter of the sequence. The upper unit of the sequence presents intercalated layers of banded iron formation, ferruginous chert, metarhyolite, metavolcaniclastic (Fig. 3.3f, Fig. 3.4b), and mafic schists.

The metarhyolites are represented by pinkish- to greenish porphyritic schists with euhedral quartz crystals and quartz-rich pods enveloped by an anastomosed foliation (Fig. 3.3g). In thin-sections, they show a fine-grained, well-foliated matrix composed dominantly of sericite and chlorite, with dispersed quartz phenocrysts up to 3mm long (Fig. 3.3h, i, and Fig. 3.4a). Quartz phenocrysts vary from elliptical- to round-shaped and can exhibit undulatory extinction, deformation lamellae, and subgrains while others are subhedral to euhedral with little evidence of internal strain. Rarely, some of them show either circular or lobate re-entrants of fine-grained matrix material, which suggest primary volcanic embayments (Fig. 3.3i).

The associated metavolcaniclastic rock has poorly-sorted, fine ash groundmass composed of quartz (60%), sericite (39%), and subordinated opaque mineral, epidote, and tourmaline. The quartz grains are light purple, poorly sorted broken crystals that show sharp angle edges that can be up to 2 orders of magnitude larger than the matrix. Lenses of sericite aggregates are common and resemble feldspar pseudomorphs.

The banded iron formations (BIF) occur as loose blocks (Fig. 3.3a,b) or in situ exposures (Fig. 3.3e), frequently deeply weathered. They range from a few centimeters (when intercalated with chlorite-sericite-quartz schist) to 20 m-thick, commonly exhibiting tight to isoclinal folds (Fig. 3.3c and 3d). The alternated hematitic and silicic bands vary from <1 to 100 mm-thick (Fig. 3.3b, 3c, 3d, and Fig. 3.4f), and the hematite is often predominant over the quartz. It is worth mentioning the common presence of muscovite (<1%; Fig. 3.4d) and goethite (<5%). Occurrences of massive iron formations (MIF) are rare, such as those found nearby Capitão Felizardo village (Fig. 3.4e).

The metamafic rocks occur as highly weathered green to brown chlorite schists, frequently with magnetite blasts, weathered carbonate grains, and quartz. In contrast to the low- to unstrained Pedro Lessa Metaigneous Suite metabasic rocks, the PPMS ones are ubiquitously sheared. The metaultramafic schists are subordinated and composed of talc, serpentine, magnetite, and chlorite (Fig. 3.4c).

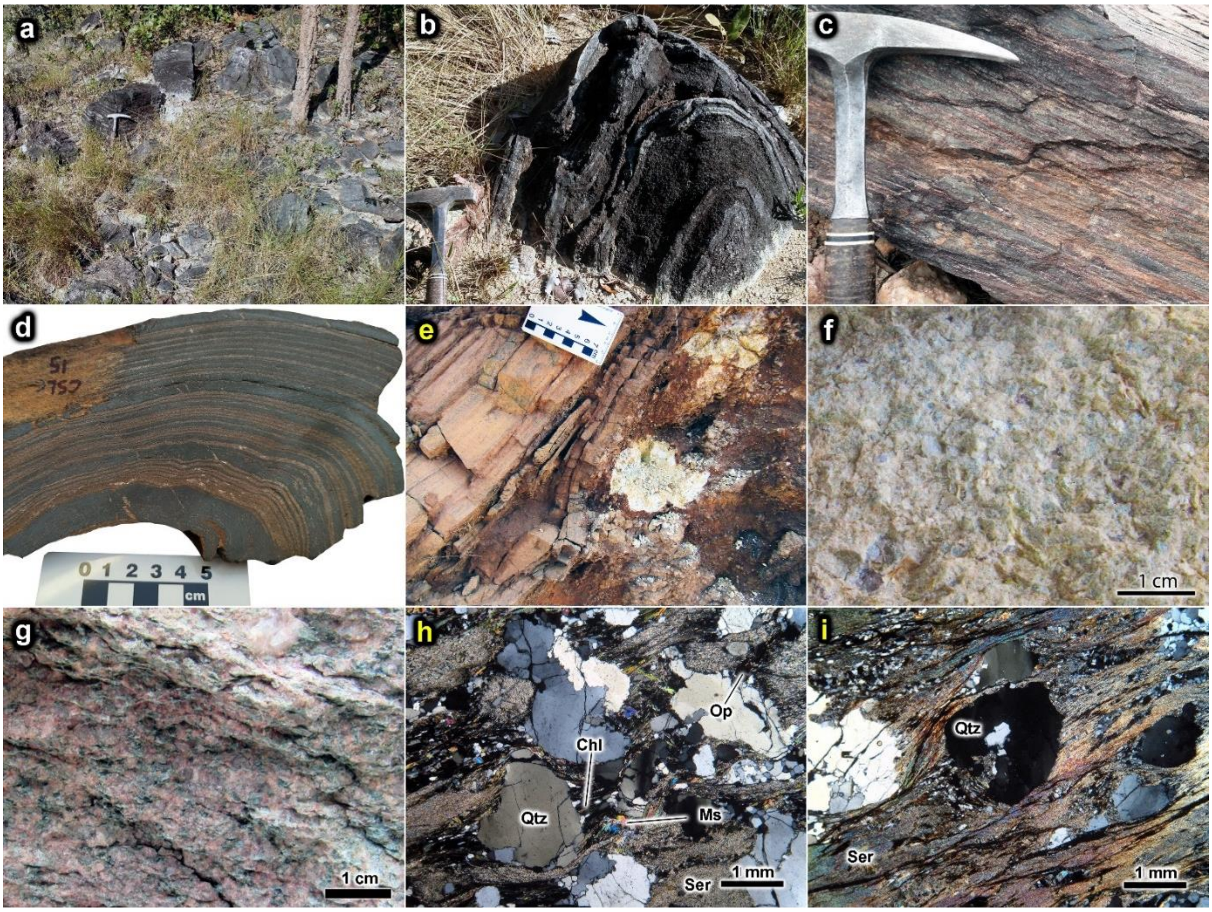

Fig. 3.3 The general aspect of the PPMS rocks. a) common aspect of the BIF outcrops, often as in-situ loose blocks; b) tight fold hinge zone in BIF; c) sheared BIF; d) section of a BIF hand specimen showing milli- to centimetric alternation of quartz/hematite-rich bands; e) tectonic contact between metagranite of the Gouveia Complex (lower right) and BIF (upper left); f) weathered chlorite schist, which often interleaves the BIF; g) pinkish to greenish sheared porphyritic metarhyolite; h) photomicrograph of metarhyolite showing the main mineral phases, quartz phenocrysts and related dynamic recrystallization, and the anastomosed foliation; and i) quartz phenocryst highlighting a lobate re-entrant that resembles a dissolution feature. Mineral abbreviation: Qtz-quartz; Chl-chlorite; Ms – muscovite; Op – opaque mineral; and Ser – sericite.

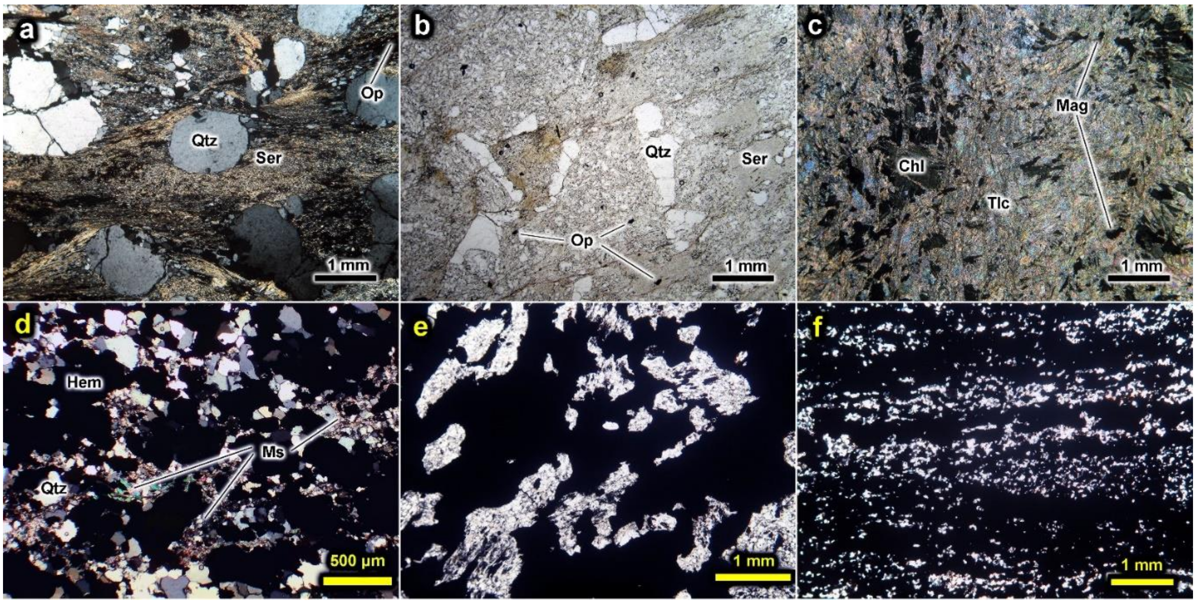

Fig. 3.4 The microscopic aspect of the metavolcanics and BIFs from PPMS. a) photomicrograph of the metarhyolite highlighting the abundance of phenocrysts in a very fine sericitic groundmass; b) photomicrograph of metavolcaniclastic rock showing the angular nature of the poorly sorted broken quartz crystals in a fine-grained groundmass (fine ash), suggesting the fragmental character of the rock; c) photomicrograph of metaultramafic and its mineral assemblage; d) iron formation photomicrograph (crossed polarizers) emphasizing the presence of muscovite; e) photomicrograph of massive iron formation texture showing advanced metasomatism (parallel polarizers); and f) photomicrograph of banded iron formation showing micro-scale hematite-quartz bands and granoblastic texture. Mineral abbreviation: Qtz-quartz; Ms – muscovite; Op – opaque mineral; Hem – hematite; and Ser – sericite.

3.5 Analytical methods

3.5.1 Sampling

More than thirty representative samples distributed over the PPMS bodies were collected, with the sampling location highly dependent on the availability of suitable outcrops. Twenty thin sections were prepared for microscopic investigation. Based on fieldwork data and detailed microscopic examination, eleven samples free of surface weathering alteration were selected for whole-rock chemical analysis, with a metarhyolite sample from the upper unit selected for zircon age dating. This metarhyolite is intercalated to banded iron formation, and spatially associated to ferruginous chert, other metarhyolite layers, and metavolcaniclastics.

3.5.2 Geochemistry

Whole-rock analyses of major, minor, trace, and rare earth elements were undertaken at Bureau Veritas Commodities Canada Ltd. and SGS GEOSOL, Brazil. The samples were pulverized (agate mill), homogenized, quartered, and then submitted to lithium tetraborate fusion, after which they were analyzed through ICP-OS (major, minor, and some trace elements) and ICP-MS (trace and REE).

3.5.3 U-Pb geochronology

Ten kilograms of fresh samples of a metarhyolite from PPMS were processed for zircon U-Pb analysis. Zircon concentrates were extracted from rock samples by crushing, grinding, magnetic (Frantz isodynamic separator), and gravimetric standard techniques for geochronological analysis. The final separation of zircon grains was achieved by handpicking. Grains were mounted in epoxy disks and polished to expose their centers. Morphological features and internal structures of zircon grains were revealed by backscattered electron (BSE) and cathodoluminescence (CL) images.

U-Pb isotopic analysis was performed by using the Laser Ablation Sector Field Inductively Coupled Plasma Mass Spectrometry (LA-SF-ICP-MS, Thermo Scientific ELEMENT 2 with a coupled 213 nm Cetac laser) equipment of the geochronological laboratory of Federal University of Ouro Preto (LOPAG, Brazil). Rock samples were prepared for analysis in the laboratory of the Federal University of Minas Gerais (SEPURA, Brazil).

Blueberry (564 Ma; Santos *et al.*, 2017), Plešovice (338 Ma; Sláma *et al.*, 2008), and GJ-1 (605 Ma; Jackson *et al.*, 2004) standard zircons were used in the analytical routines. Data reduction used Glitter software (Van Achterbergh *et al.*, 2001). Analytical spots avoided grain areas with inclusions, fractures, and metamict structures. The data from each spot were evaluated taking into account the common Pb contents, errors of isotopic ratios, percentages of discordance, and Th/U ratios. From the selected spots, only those between 99.0 and 100 % of concordance were considered in Concordia Age calculations. They were plotted in Concordia diagram obtained with the software Isoplot/Ex (Ludwig, 2003).

3.6 Analytical results

3.6.1 Geochemistry of the PPMS iron formations

To obtain a broad view of the chemical signature of the PPMS iron formations, we present a complete compilation of the few data available in the literature (Chaves *et al.*, 2012; Fogaça *et al.*, 1984; Knauer and Grossi-Sad, 1997), together with the results of eleven new analyses of major oxides, trace elements, and REE+Y (Apêndice B, supplementary material).

The PPMS banded iron formations are characterized by variable content of SiO2 (38-49 wt. %) and Fe2O3 (47-57 wt. %), but these two oxides always correspond to more than 90 wt. % (average 95,6 wt. %), while the other oxides show concentrations <1.3 wt. % (except for the Al2O3 in sample PP14**, 3.08 wt. %). The massive iron formations show lower SiO2 (14-19 wt. %) and higher Fe2O3 (75-80 wt. %) contents, and even lower concentrations of the other oxides (<0.5 wt. %). Among the transition metals, vanadium has higher consistent concentrations between the samples (<8-52 ppm), with copper and zinc important in some of them (<5-87 and 11-85 ppm, respectively). Cobalt content ranges from 1.4 to 27 ppm and nickel from <5 to 18 ppm. In terms of incompatible elements, hafnium and thorium have an average concentration of 0.3 and 2.5 ppm, respectively. Zirconium concentration ranges from 4.6 to 25.7 ppm, although half of the samples show concentrations below the detection limit. Yttrium has an average concentration of 16.1 ppm (2.3-60.8 ppm).

As the element Y has properties very similar to Ho, it is included in this assessment. For the purpose of this study, the group REE is subdivided into light REE (LREE, La-Nd), middle REE (MREE, Sm-Ho), and heavy REE (HREE, Er-Lu). When normalized to PAAS (Post Archean Australian Shale average - Taylor and McLennan, 1995), the IF samples group into three slightly different patterns. Group 1 is marked by very high ∑REE (min=50 ppm; max=245 ppm; average=120 ppm), significant enrichment of the LREE (PrSN/YbSN ratios values ranging from 2.54 to 6.42; average=3.58), positive La anomaly, strong negative Ce anomaly, and negative Eu and Y anomalies. In contrast, Group 2 is marked by lower ∑REE (min=14 ppm; max=85 ppm; average=45 ppm), enrichment of HREE (PrSN/YbSN ratios ranging from 0.36 to 0.34; average=0.35), and minor and variable La, Ce, Eu, and Y anomalies. The MIF samples show a coherent pattern, with very high middle-to-heavy REE enrichment (PrSN/YbSN ratios are 0.60 and 0.77), high ∑REE (average=188 ppm), strong negative Ce anomalies, negative Eu anomalies, and variable mild Y anomalies (Fig. 3.5a).

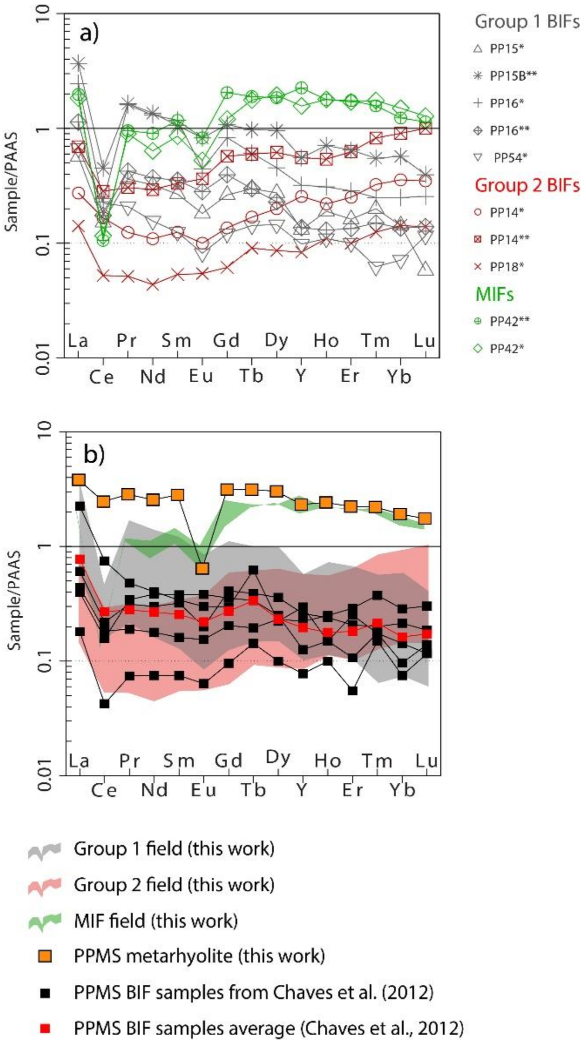

Fig. 3.5 PAAS normalized REE+Y patterns. a) group 1 (grey), group 2 (red), and MIF (green) PPMS patterns. b) field representation of 1,2, and MIF defined groups, the interleaved metarhyolite REE chemistry, and PPMS BIF samples from Chaves et al. (2012) for comparison.

In order to clarify the presence of a true negative Ce anomaly and distinguish it from possible La anomalies, the ratios of $Ce/Ce^{*}=Ce_{SN}/(0.5Pr_{SN}+0.5La_{SN})$ and $Pr/Pr^{*}=Pr_{SN}/(0.5Ce_{SN}+0.5Nd_{SN})$ were calculated and plotted in a binary graph (after Bau and Dulski, 1996, Fig. 3.6). True negative Ce anomalies are defined when $Ce/Ce^{*}<1$ and $Pr/Pr^{*}>1$. Except for sample PP14*, true negative Ce anomalies are consistent for all samples. Calculating Ce/Ce* ratio using the relationship $Ce_{SN}/(2Pr_{SN}-1Nd_{SN})$ by extrapolating from Pr and Nd (Bolhar *et al.*, 2004), values are persistently <1 and range from 0.10 to 1.19, with an average of 0.51. Group 1 and MIF clearly show stronger negative Ce anomalies than Group 2. Positive La anomalies are true for all samples and were calculated as $La/La^{*}=La_{SN}/(3Pr_{SN}-2Nd_{SN})$ by extrapolating from Pr and Nd (Bolhar *et al.*, 2004).

Eu/Eu* ratios were calculated as $Eu_{SN}/(0.66Sm_{SN}+0.33Tb_{SN})$ because seawater can have a slight positive Gd anomaly (De Baar *et al.*, 1985). All samples show negative Eu anomalies with Eu/Eu* ratios ranging from 0.45 to 0.87, with an average of 0.69.

Except for samples PP14* ($Y_{SN}/Y_{SN}*=1.22$), the BIFs show negative Y anomalies with $Y_{SN}/Y_{SN}*$ ratios ranging from 0.57 to 0.96 and an average of 0.77. The MIFs show both negative and positive Y anomalies (0.84 and 1,24, respectively). Y/Ho ratios are dominantly chondritic to sub-chondritic, ranging from 18.74 to 28.46 and an average of 24.05 (samples PP14*=31.41 and PP42**=34.16 not included).

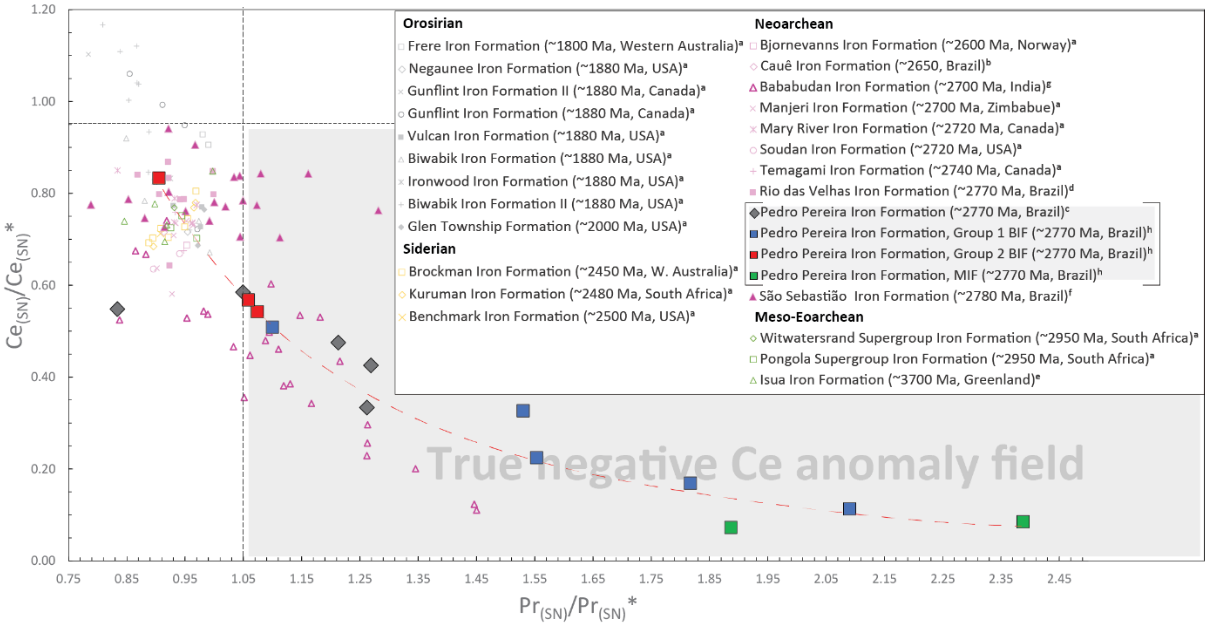

Fig. 3.6 Plot of CeSN /CeSN* and PrSN/PrSN* for PPMS and worldwide iron formations, discriminating La induced false negative Ce anomalies from the true ones (after Bau and Dulski, 1996). Data sources: ᵃPlanavsky et al. (Planavsky *et al.*, 2010); ᵇSpier et al. (2007); ᶜChaves et al. (2012); ᵈAraújo and Lobato (2019); ᵉNutman et al. (2019); ᶠBrando Soares et al. (2017);ᵍKato et al.(2002); and ʰthis study. The dotted red line represents the power curve fit of this work samples ($y = 0.6621x^{-2.5}$ $R^2 = 0.9181$).

3.6.2 Metarhyolite lithochemistry

Major, trace, and REE geochemical data of the dated metarhyolite are presented in Apêndice B (supplementary material). The sample showed enriched values of Fe_2O_3 and MgO and depleted values of K_2O, Na_2O, and CaO.

The sample plot in the rhyolite field in the TAS diagram (Le Bas *et al.*, 1986), show high-K calc-alkaline/shoshonitic signature (Co vs. Th diagram from Hastie *et al.*, 2007; Ta/Yb vs Th/Yb diagram from Pearce, 1982) and is related to intra-continent magmatic settings in most geotectonic classification diagrams (Cabanis and Lecolle, 1989; Harris *et al.*, 1986; Pearce *et al.*, 1984).

3.6.3 U-Pb geochronology

Twenty-seven grains recovered from the PPMS metarhyolite were analyzed (Fig. 3.8 and Apêndice C – Supplementary material). The grains are euhedral to subhedral, with pyramidal, flat, or rounded crystal terminations, and they range from 235 to 410 µm-long, with length:width ratios between 2:1 and 4:1. In CL images the crystals present typical igneous oscillatory zoning (Pidgeon, 1992) and can show rounded dark cores (Fig. 3.8). From the 31 analyzed spots, 28 are concordant (21 with less than 10% of discordance). They belong to a single population of zircons which align to define a Discordia with the upper intercept at 2785 ± 12 Ma (MSWD = 8.0, 2σ error; Fig 3.7a). A cluster of 11 oscillatory-zoned domains of zircon crystals with highly concordant isotopic ratios yielded the Concordia Age of 2771 ± 8.4 Ma (MSWD=0.51 with 0.48 of probability of concordance; 2σ error; Fig 3.7b). This age is, therefore, considered the best crystallization age for the PPMS metarhyolite.

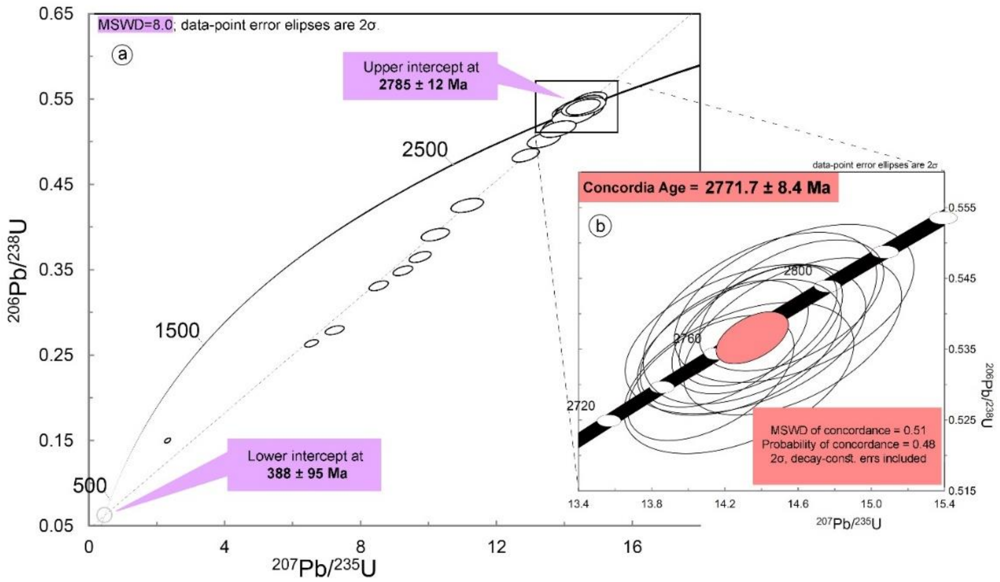

Fig 3.7 a) Wetherill-type Concordia diagram for the metarhyolite from PPMS.; b) Concordia age of an eleven-spot cluster.

Fig. 3.8 Cathodoluminescence (CL) images of all dated zircon grains from the acid metavolcanite and the spot location with the respective U-Pb ages (207Pb/206Pb age; 2σ error), percentual of discordances, and Th/U ratios.

3.7 Discussion

3.7.1 Age of the PPMS and tectonic implications

The yielded Concordia age of 2772 ± 8 Ma positions the unit at the Neoarchean, as a supracrustal sequence of an Archean nucleus of the São Francisco-Congo paleocontinent. Many greenstone belts are present within the São Francisco craton and inside basement inliers in the Araçuaí orogen (Fig. 3.1). The oldest among them compose the various Archean-Siderian nuclei that form the São Francisco-Congo paleocontinent building blocks, while the youngers are, by and large, components of the Paleoproterozoic orogenic system that welded these blocks throughout the Rhyacian and Orosirian periods.

The Rio das Velhas and the associated Pitangui greenstone belts are contemporaneous to the Pedro Pereira greenstone belt. Their metasedimentary and metavolcanic rocks show U-Pb zircon ages between 2.9 and 2.7 Ga (Brando Soares *et al.*, 2017; Machado *et al.*, 1996, 1992; Melo-Silva *et al.*, 2020; Noce *et al.*, 2005; Sepulveda *et al.*, 2021), recording expressive volcanic activity at 2776 Ma. The Pedro Pereira greenstone belt is located 200 km to the north of Rio das Velhas greenstone belt and, halfway in the same direction, lies the Rio Mata Cavalo greenstone belt, which is potentially relatable to PPMS. The question then arises as to whether these greenstone belts were part of the same terrain and share linked origins or were brought together by the Rhyacian-Orosirian orogeny and have disconnected roots. Were they part of related basins with coeval volcanic activity related to Fe-rich fluids, although deposited in diverse geographical positions? Were they environmentally unrelated, but connected by the same heat source, like a mantle plume upwelling? Are they related to a common subduction setting? Further petrogenetic study on the mafic/ultramafic rocks from PPMS is recommended to investigate a possible correlation between these greenstone belts.

The acquired metarhyolite age significantly differs from the first data reported by Machado et al. (1989), which is about 200 Ma older. The 2.97 Ga age is problematic since (i) it is older than the age acquired for the basement where it is inserted; (ii) the greenstone sequence has no features that would be expected if it had been intruded by granitic magma like dykes, aplitic veins, or contact metamorphism; (iii) with this age older than the basement, the PPMS metaigneous rocks could not be an instrusion into the basement and should be therefore dispersed xenoliths inside the basement younger plutonics; and (iv) the greenstone sequence bodies are highly unlikely to be xenoliths brought by a magma since they occur concentrated in a single location, with the same orientation disposed over a shear zone. The Neoarchean age yielded for the PPMS metarhyolite rules out a Paleoproterozoic age for the PPMS as suggested/considered by recent papers (*e.g.* Chaves *et al.*, 2013, 2012; Rosière *et al.*, 2019; M. C. R. Silva *et al.*, 2015).

Another interesting question to explore is to which Archean paleocontinent the PPMS belonged. Two distinct tectonic scenarios of the Paleoproterozoic orogen in the context of the São Francisco craton and Araçuaí orogen have been hypothesized. The first (*e.g.* Aguilar *et al.*, 2017; Alkmim and Marshak, 1998) suggest the collision between two Archean nuclei and traces the suture as continuous from the south to the north. The suture is positioned between the Mantiqueira continental arc and the Juiz de Fora island arc in the south and is connected to the suture in the northeastern portion of the São Francisco craton, between the eastern Gavião block and the Jequié microcontinent and Itabuna-Salvador-Curaça belt (see Fig. 3.1 for referencing). In this scenario, the PPMS would be positioned in the same Archean paleocontinent where the Gavião block was inserted.

More recently, Barbosa et al. (2020) suggest that the northern portion of the São Francisco craton shows a different tectonic setting. For those authors, the Guanambi-Correntina and the Gavião blocks represent two Archean terranes amalgamated during a Paleoproterozoic collisional event in an outward dipping double-sided subduction setting. Instead of just one orogenic belt uplifted in the Paleoproterozoic era connecting the Mantiqueira continental arc to the east of Gavião block, perhaps two major subparallel orogenic belts operated. In this scenario, the PPMS would be positioned in the same Archean paleocontinent of the Guanambi-Correntina block.

3.7.2 Iron formation geochemistry

The PAAS normalized REE+Y patterns from Group 1 Pedro Pereira BIF (Fig. 5a) samples are quite unusual when compared to world-wide Archean to Paleoproterozoic iron formation patterns. Group 1 BIFs display conspicuous negative Eu anomalies, singular extreme negative Ce anomalies, significant LREE enrichment, and chondritic to subchondritic Y/Ho ratios. Chaves et al. (2012) described similar patterns, and interpreted them as a distinctive signature of oxic seawater conditions, so claiming a younger, post-GOE age for PPMS. However, the metarhyolite age acquired in this work (2772 ± 8 Ma) disqualifies a Paleoproterozoic deposition. Further, the operation of some processes like detrital input and post-depositional alteration/metamorphism could modify the original geochemical composition.

3.7.3 Detrital input in the BIFs

The contamination of chemical sediments with siliciclastic and volcanic-clastic materials, exhalative insoluble materials, and volcanic ashes and glass significantly disturb seawater signatures of banded iron formations because the contaminants commonly have higher REE, LILE, HSFE, and transition element contents (*e.g.* Bau, 1993; Bau and Alexander, 2009; Bolhar *et al.*, 2004; Viehmann *et al.*, 2015). Broadly speaking, HSFE, Al^{3+}, and Ti^{4+} are insoluble in aqueous solutions (Andrews *et al.*, 2004; Martin and Whitfield, 1983) and concentrated in weathering-resistant minerals such as zircon and some aluminous and titaniferous phases and clay minerals.

According to some researchers (*e.g.* Bau, 1993; Bau and Alexander, 2009; Bolhar *et al.*, 2004; Viehmann *et al.*, 2015), particle-reactive trace elements such as Ti, Nb, Y, Sr, Zr, Hf, and Th are good indicators of detrital aluminosilicate contamination. Since clastic detritus REE concentrations may be more than 2 orders in magnitude higher than precipitates, the presence of only 1% of clastic material would be enough to dominate the REE distribution of chemical sediments (Bau, 1993). The studied IF samples show a low concentration of this indicators and no strong correlation between them, which would point to no important detrital contribution.

Y and Ho share a trivalent oxidation state and similar ionic radii and are not fractionated in magmatic systems (Bau, 1996; Nozaki *et al.*, 1997). However, Ho is preferentially scavenged by suspended particles relative to Y in aqueous systems. Modern and ancient seawaters consistently show super-chondritic Y/Ho ratios (Bau, 1996; Bolhar *et al.*, 2005), low light-to-heavy REE ratio, and low ∑REE+Y (Bolhar *et al.*, 2004; Fryer, 1983, 1977). While seawater and associated chemical sediments have superchondritic Y/Ho ratios, volcanic and clastic materials have almost chondritic values (ca. 26 - Alibo and Nozaki, 1999; Bau, 1996; Bolhar *et al.*, 2005; Nozaki *et al.*, 1997). In a magmatic system, which is characterized by "CHARAC" (CHarge-and RAdius-Controlled), the twin pair elements display extremely coherent behavior and retain the chondritic-like ratio. More recently, researchers (Konhauser *et al.*, 2017; Planavsky *et al.*, 2010) demonstrated that this is true for Archean and early Paleoproterozoic iron formations, but not necessarily for those of the late Paleoproterozoic, when the ocean got significantly redox stratified due to the rise of atmospheric oxygen ca. 2.4 Ga (Holland, 2006). They argue that with this ocean structure, Mn and Ce oxides particulates from shallow oxic waters will be transported for deeper anoxic waters and redissolved below the redoxcline. This would lower the Y/Ho ratio, raise the light-to-heavy REE ratio, and increase Ce concentration relative to its REEs neighbors in deep anoxic water columns.

The BIFs from Pedro Pereira show predominant chondritic to sub-chondritic Y/Ho ratios and high ∑REE+Y. Also, Group 1 samples show LREE and MREE enrichment relative to HREE. The redissolution of Mn and Ce oxides in stratified ocean deep anoxic waters could explain the greater than 1 light-to-heavy REE ratio and chondritic to sub-chondritic Y/Ho ratios, however, could not explain the high ∑REE+Y, neither the negative Ce anomalies.

The possibility that Pedro Pereira Group 1 BIFs REE+Y patterns have been modified is patent and must be considered. Hydrothermal alteration can depress the Y/Ho ratios and raises ∑REE+Y and light-to-heavy REE ratios of chemical sediments.

However, even though the water signal of Group 1 and MIF samples has probably been modified, the general shape of shale-normalized REE+Y patterns of Group 2 samples show LREE/HREE<1, low ∑REE+Y, and also superchondritic Y/Ho ratio (only PP14*) which indicates that they represent those with lower/none alteration.

3.7.3.1 Post-depositional hydrothermal REE mobilization

If the detrital input in the PPMS iron formations is not the main process that is controlling the REE scattering of Group 1 samples, post-depositional REE mobilization could be the cause. Hensler *et al.* (2015) and Sampaio *et al.* (2018) understand variations between true negative and positive Ce anomalies together with chondritic-like Y/Ho rations in pure BIFs as produced by post-depositional fluid-rock interaction. Hydrothermal fluids have been equilibrated with country rocks that have low Y/Ho ratios and remobilized the HREE. In the southern Serra do Espinhaço, Cabral *et al.* (2012) also decribed fluid-rock interaction of brines derived from metamorphic dewatering. Chetty and Gutzmer (2012) analyzed ore samples from Kalahari Manganese Deposit ranging from least to advanced hydrothermally altered conditions. Samples show a larger range and relative increase in total REE contents on those with the advanced alteration. They observed dispersion of Ce anomalies towards both positive and negative fields when plotted on the Bau and Dulski (1996) diagram, which describes a power curve trend. Therefore, from a given material, it is possible to predict its power curve with just a few samples. They interpreted this behavior as a conservative system that was predominantly protolith-buffered.

The PPMS IF Group 1 and MIF samples display chondritic-like Y/Ho ratios and show variations between true negative and positive Ce anomalies, which also plot as a power curve on the Bau and Dulski (1996) diagram (Fig. 3.6; $y=0.6621x^{-2.5}$; $R^2 = 0.9181$). Besides, Group 1 BIF samples show relative HREE depletion, while the MIF samples, which are the most hydrothermally altered ones, show the highest ∑REE+Y content and HREE enrichment (see Fig. 3.9). These features are compatible with a hydrothermal explanation. Silva *et al.* (2015)

studied BIF clasts from the diamantiferous Sopa-Brumadinho Formation metaconglomerates. Based on REE geochemical signature similarities, they selected the PPMS BIFs as the most likely source rock where the clasts came from. Considering that the deposition of the conglomerate occurred at the Statherian, this period may be considered as the minimum age for the hypothesized fluid-rock interaction.

3.7.3.2 Redox-sensitive elements

Negative Ce anomalies in banded iron formations have been used to infer prevailing oxic conditions in a marine environment. In oxic seawater, soluble trivalent Ce^{3+} is converted Ce^{4+}. The oxidation of Ce^{3+} greatly reduces Ce solubility, resulting in Ce^{4+} scavenging by clay minerals, organic matter, and Mn-Fe oxyhydroxides (Byrne and Sholkovitz, 1996; Planavsky *et al.*, 2010).

Based on the assumption that hydrothermal alteration is the only processes that mask seawater patterns, and that Group 2 samples are those without hydrothermal alteration, it could thus be suggested that these samples are the best to infer about paleoenvironmental conditions. In this regard, Group 2 slight negative Ce anomalies point out to a mildly oxic to anoxic environment.

As shown in Fig. 3.9, there seems to exist a relationship between the ∑REE+Y and the negative Ce anomalies for all samples. The higher ∑REE+Y values, the lower Ce_{SN}/Ce_{SN}^* ratios. This relationship could be controlled by fluid/rock interaction, where an advanced alteration would result in a relative increase of the total REE content and a relative negative Ce anomaly.

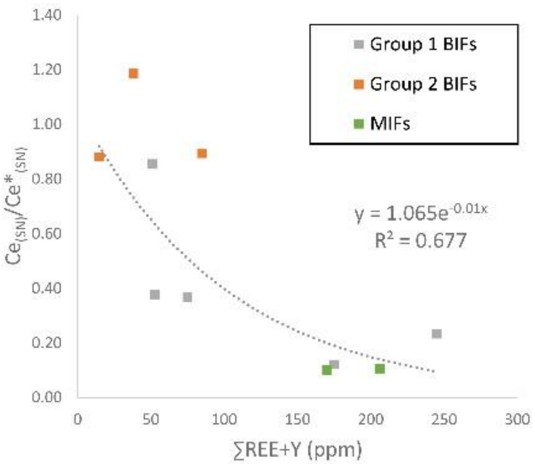

Fig. 3.9. Graph of REE+Y concentration sum vs. Ce_{SN}/Ce_{SN}^* ratio from Pedro Pereira IF samples.

A considerable amount of literature describes the fractionation of U from Th as a result of preferential dissolution of U over Th during oxidative weathering in oxygenated fluvial waters. The conversion of immobile U^{4+} to mobile U^{6+} enriches fluvial waters with diluted U whereas Th is almost insoluble and transported by small detrital particles (*e.g.* Andersson *et al.*, 1995; Bau and Alexander, 2009; Cabral *et al.*, 2016; Collerson and Kamber, 1999). The swift deposition of these suspended particles in estuaries leads to a low Th/U ratio in oxic seawaters (Nozaki *et al.*, 1997). In contrast, anoxic seawaters are depleted in dissolved U. This removal is attributed to the reduction of U^{4+} back to insoluble U^{3+} and trapping onto Mn oxyhydroxides (Andersson *et al.*, 1995). Hence, Archean chemical sediments usually show high Th/U ratios, although exceptions have been reported (*e.g.* Alexander *et al.*, 2008; Bau and Alexander, 2009; Cabral *et al.*, 2016).

All samples from Pedro Pereira IFs but PP16* display Th/U ratios values consistently below the average ratio for the upper continental crust (Fig. 3.10), which is 3.9 (*e.g.* Condie, 1993; Rudnick and Gao, 2003; Taylor and McLennan, 1995). Different from the negative Ce anomalies, there is no relationship between Th/U values and ∑REE+Y concentrations. This means that the low Th/U ratios were not affected by the input of clastic material or hydrothermal alteration. Therefore, the U enrichment is more likely to be another type of post-depositional alteration and an ancient seawater signature interpretation can be ruled out.

In acidic pH, ferric oxyhydroxide (amorphous and goethite) and hematite are capable of adsorbing UO_2^{2+} (*e.g.* Hsi and Langmur, 1985; Spier *et al.*, 2019; Yuan *et al.*, 2017). Therefore, the low Th/U ratios could be a result of U adsorption onto hematite and ferric oxyhydroxides in the weathered IF. Oxic solutions could have transport hexavalent U from the nearby rocks to the IFs, causing the U enrichment and consequently low Th/U ratios. Granitic rock fits as a potential local source of U considering that PPMS is surrounded by TTG complexes with high U content (average of 30 ppm; Chaves and Coelho, 2013).

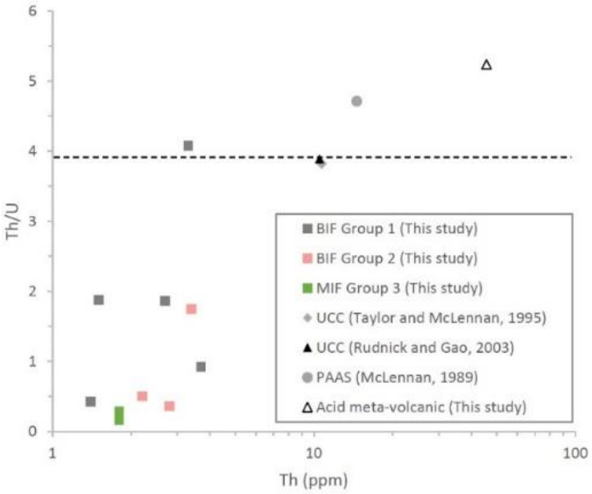

Fig. 3.10. Graph of Th concentration vs. Th/U ratio from Pedro Pereira IF samples. The dashed line represents the Th/U average value for the upper continental crust (UCC; Rudnick and Gao, 2003; Taylor and McLennan, 1995).

3.7.4 Pedro Pereira iron formation, a Neoarchean oasis?

Based on the abundance of redox-sensitive elements, as well as on sulfur, nitrogen, carbon, molybdenum isotopes (Olson *et al.*, 2013 and references therein), it has been proposed the existence of local oxygen concentration in surface-ocean environments before the great oxidation event (GOE; ~2.4 Ga), at least since 2.7 Ga (*e.g.* Koehler *et al.*, 2018; Ossa *et al.*, 2019). True negative Ce anomalies in Archean/early Paleoproterozoic iron formations seems to be an uncommon feature in IFs all around the world (Fig. 3.6), since there are just a few cases reported in the literature (*e.g.* Pitangui greenstone belt in Brazil and Bababudan BIF in south India, Bosco-Santos *et al.*, 2020; Brando Soares *et al.*, 2017; Kato *et al.*, 2006, 2002). The acquired Neoarchean age for the PPMS and its negative Ce anomalies in Group 2 samples support the interpretation of a local oxygenated environment before the GOE in the São Francisco-Congo paleocontinent. Furthermore, it is possible to hypothesize that this oxygenation was a more spread feature at the paleocontinent São Francisco-Congo instead of a singular occurrence since PPMS is potentially relatable to the Pitangui greenstone belt. This reinforces the São Francisco-Congo paleocontinent as a potential starting region where Earth's hydrosphere and atmosphere oxygenation process have begun.

3.7.5 Hydrothermal vent input?

Strong positive Eu_{SN} and Eu_{CN} anomalies in marine chemical sediments are usually attributed to the presence of >200°C hydrothermal fluids in ambient seawater during their precipitation (*e.g.* Danielson *et al.*, 1992; Fryer, 1983; Michard and Albarède, 1986).

Plagioclase is specially enriched in Eu relative to the other REE during magma crystallization. The breakdown of volcanic rocks plagioclase that underwent water-rock interaction linked to hydrothermal vents enriches the fluids with soluble Eu^{2+}, causing the positive anomaly (*e.g.* Fryer, 1983).

Kato *et al.* (2006) argue that secular variation of Eu anomalies in BIFs shows that pre-2.7 Ga BIFs (mostly Algoma-type) have significantly positive Eu anomalies and that a change in Eu/Eu* ratios of BIFs occur ca. 2.7 Ga, presenting negative Eu anomalies. However, researchers re-analyzed important worldwide IF with modern analytical methods and showed that, although after 2.7 Ga a progressive decrease in Eu/Eu* ratios occurs, it remained greater than 1 from the Archean to the late Paleoproterozoic. (Bekker *et al.*, 2012, 2010; Konhauser *et al.*, 2017; Planavsky *et al.*, 2012, 2010).

PPMS IF samples display $Eu_{SN}/Eu^*_{SN} < 1$, which could point to low interference from hydrothermal vents in the Pedro Pereira basin and match the secular variation described by Kato *et al.* (2006). However, those negative Eu anomalies must be interpreted with caution, since hydrothermally altered samples (Group 1 and MIF) show much stronger negative Eu anomalies than those of Group 2. This behavior reinforces the interpretation of hydrothermal alteration modification.

3.8 Conclusion

Uncertainties about the Pedro Pereira metavolcanosedimentary sequence (PPMS) age and geochemical data from its iron formations have raised hot debate regarding its geotectonic context and related paleoenvironmental conditions. Recent literature suggests a Paleoproterozoic age based on BIF negative Ce anomalies and regional correlation. However, the reported findings assign a Neoarchean age for the PPMS, and its banded iron formations possibly record local oxygenation. Zircon U/Pb dating on metarhyolite yielded a crystallization age of 2.77 Ga, and geochemistry of iron formations that are associated with the metarhyolite allowed the identification of three groups with distinct geochemical features that reflect variable degrees of hydrothermal alteration. The negative Ce anomalies of least altered banded iron formation samples suggest evidence of an oxygenated environment during precipitation. The results imply that PPMS perhaps represents one of the oldest records of oxygenation previous to the GOE in the geologic archives. As a Neoarchen greenstone belt relict of São Francisco-Congo paleocontinent (SCPC) basement, it is potentially relatable to the nearby important Neoarchean greenstone belts. Detailed studies focusing on PPMS's igneous rocks are recommended since the greenstone belt has the potential to shed light on the early Earth atmosphere and SCPC evolutions.

3.9 Declaration of interest statement

The authors declare that they have no known competing financial interests or personal relationships that could have appeared to influence the work reported in this paper.

3.10 Acknowledgments

This work was financially supported by Conselho Nacional de Desenvolvimento Científico e Tecnológico (CNPq; grant # 205254/2016-4) and NGU/CPMTC-UFMG. The first author thanks FAPEMIG for providing the Ph.D. scholarship. M.K. is a fellow of the Brazilian Research Council and acknowledges its support (grant # 309106/2017–6).

4 ARTIGO II: THE SYN-OROGENIC RHYACIAN/OROSIRIAN COSTA SENA BASIN, SOUTHEASTERN BRAZIL

Marcelo A. Freimann[a,b], Luiz Guilherme Knauer[a,b], Matheus Kuchenbecker[a,b,c], Francisco Javier Rios[a,d]

[a]Programa de Pós-Graduação em Geologia, Universidade Federal de Minas Gerais, Belo Horizonte (MG), Brazil

[b]Centro de Pesquisas Professor Manoel Teixeira da Costa, Instituto de Geociências, Universidade Federal de Minas Gerais, Campus Pampulha, Belo Horizonte (MG), Brazil

[c]Laboratório de Estudos Tectônicos, Centro de Estudos em Geociências, Instituto de Ciência e Tecnologia, Universidade Federal dos Vales do Jequitinhonha e Mucuri, Diamantina (MG), Brazil

[d]Centro de Desenvolvimento da Tecnologia Nuclear, Universidade Federal de Minas Gerais (UFMG), Campus Pampulha, Belo Horizonte-MG, Brazil

Abstract

The Costa Sena metavolcanosedimentary sequence occurs as a basement inlier within the Araçuaí fold-and-thrust belt, Minas Gerais State, Brazil. Its origin and evolution are still controversial. New whole-rock geochemical analyses and zircon U-Pb (LA-ICPMS) geochronological data were obtained for schists from the base of the sequence, as well as for metabreccia from the top. The schists are chemically classified as (i) porphyroclastic schists, with or without lazulite, that show the same REE signature as the Archean basement; (ii) schists from a dominantly alkaline source; (iii) schists from a dominantly leucogranite source. Macroscopically, the schists can be (iv) fine grained and banded; and (v) kyanite and/or tourmaline rich. Together with the alkaline nature of the samples, detrital zircon age spectra for the Barão do Guaicuí schists and Bandeirinha metabreccia suggest that the sequence was deposited in a foreland basin, in a collisional tectonic setting. The Bandeirinha metabreccia sample yielded a maximum depositional age peak at 2093 ± 9 Ma (25%), with an important contribution peak at 2656 Ma (52%). The youngest zircon spot of the population (n=98) yielded an age of 2000 ± 40 Ma. Therefore, as originally defined, we suggest the maintenance of the Bandeirinha Formation as part of the Costa Sena metavolcanosedimentary sequence, representing a change to arid environmental conditions after epicontinental water regression.

The concordant detrital zircon data from a schist (sample CSOV-08) of the Barão do Guaicuí Formation shows a latest population peak at 2112 ± 7 Ma, although schist sample CSOV-06A shows a younger population at 2070 ± 23 Ma (Discordia line age). As foreland basins are the sedimentary record of orogenetic processes, this work contributes to the understanding of the Paleoproterozoic evolution of the São Francisco-Congo Paleocontinent.

4.1 Introduction

Orogenesis-related basins usually show elongate to curved shape, are driven fundamentally by flexure, and are found on continental lithosphere at continent-continent and continent-ocean collision zones (Allen and Allen, 2005). Foreland basins are genetically connected to such orogens and their internal features are strongly driven by their settings. They archive in their sedimentary record most of the history of the mountain building, including the interactions between orogenic and climatic processes (DeCelles, 2012), and life evolution. For instance, the explosion of life may have occurred due to the building of major mountain chains that fed the oceans with nutrients during the assembly of Gondwana (Ganade De Araujo *et al.*, 2014); and the current most important orographic climate gradients are controlled by giant thrust belts as the Andes and Himalaya (Bookhagen and Strecker, 2008; Grujic *et al.*, 2006). Foreland basins may record important information about changing climate and exhumation patterns through contained organic matter, paleosols, and mineral detritus (DeCelles, 2012).

Orogenic foreland basins are recognised throughout Earth's tectonic history, from the Archean until nowadays, distributed all over the world *e.g.* the Pyrenees (Burbank *et al.*, 1992), the European Alps (Allen *et al.*, 1991), the Himalayas (Burbank *et al.*, 1996), Zagros (Pirouz *et al.*, 2011), Sicily (Gugliotta, 2012), Andes (Strecker *et al.*, 2007), Witwatersrand basin (Burke *et al.*, 1986), and São Francisco basin (Reis *et al.*, 2017).

The São Francisco-Congo paleocontinent (SFCP) was one of the continents involved in the assembly of Gondwana, whose remains are preserved within the eponymous craton and also as basement inliers in surrounding orogens, both in South America and Africa (*e.g.* Alkmim and Teixeira, 2017; Heilbron *et al.*, 2017). Recently, great advances have been made in the understanding of the Paleoproterozoic orogeny that assembled the SCPC, particularly regarding its igneous and sedimentary record. (*e.g.* Bersan *et al.*, 2020; Bruno *et al.*, 2020a; Cruz *et al.*, 2016; Duque *et al.*, 2020; Grochowski *et al.*, 2021; Leal *et al.*, 2021; Miranda *et al.*, 2020; Teixeira *et al.*, 2017b; Zincone *et al.*, 2017; Zincone and Oliveira, 2017).

Exposed within the reworked basement of the Araçuaí orogen (Neoproterozoic, Pedrosa-Soares *et al.*, 2001), eastern Brazil, the Costa Sena metavolcanosedimentary sequence crops out as a basement inlier (Figure 4.1). It occurs within the Araçuaí fold-and-thrust belt, flanking a 20 km wide anticline with Archean basement toward the center (Alkmim, 1995; Pflug, 1965). The sequence, which was first detailed and formalized by Hoffmann (1983b), then scrutinized by Fogaça et al. (1984). Since then, the metavolcanosedimentary sequence geotectonic setting, positioning in geological time, and even its existence as a sedimentary sequence have been objects of controversy (which is better explained in the Discussion section).

In this paper we revisit the Costa Sena metavolcanosedimentary sequence, presenting a full review of its typical occurrences. We also report new geochronological (zircon U-Pb, LA-ICP-MS) and geochemical characterization of both Barão do Guaicuí and Bandeirinha formations, which allow us to discuss their nature, geotectonic environment, and geochemical processes that acted changing their composition, as well as the positioning of the units throughout geological time. Grounded on modern analytical data, we intend to contribute to understanding of the Paleoproterozoic evolution of the São Francisco-Congo Paleocontinent, which was dismembered by Neoproterozoic orogenic belts.

4.2 Geological setting

In the Southern Espinhaço Ridge (Figure 4.1), the Archean basement is represented by granite-gneiss/migmatite complexes, rare amphibolitic bodies, and minor pegmatitic injections (Schöll and Fogaça, 1979). These rocks are grouped in the so-called Gouveia Complex at the central region and in the "Basal Complex" at the eastern border (Knauer, 1990). A granitoid sample from the Gouveia region yielded an upper intercept age at 2839 ± 14 Ma (zircon U/Pb; Machado *et al.*, 1989). Inserted in the Gouveia Complex, NNW-SSE oriented tectonic lenses composed of strained sericite-quartz schists intercalated to ferruginous cherts and iron formations, metarhyolite, talc schist, quartzites, metabasic, and metaultrabasic rocks are grouped under the denomination "Pedro Pereira Volcanic-sedimentary Sequence" (Carvalho, 1982). Recent study carried out on a metarhyolite from the upper portion of this sequence interlayered with the BIFs yielded the Concordia Age of 2771 ± 8.4 Ma (Freimann *et al.*, 2021). For some authors (*e.g.* Fogaça *et al.*, 1984; Hoffmann, 1983) this unit represents a greenstone belt relict.

The early Proterozoic is represented by the Costa Sena Group, subdivided into the basal Barão do Guaicuí Formation and the overlying Bandeirinha Formation (Fogaça *et al.*, 1984). An acid metarhyolite sample of the Costa Sena Group from Ouro Fino region yielded an age of 2049 ± 3 Ma (Machado *et al.*, 1989). The basal contacts of the former with the Archean units are ubiquitously tectonic and rarely unconformable. The upper contacts with the Bandeirinha

Formation are frequently graded, although they can also be tectonic. When the contact is direct with the Statherian Espinhaço Supergroup rocks, it shows clear nonconformity. The Barão do Guaicuí Formation is mostly composed of quartz-muscovite schists, kyanite-muscovite-quartz schist, sericite-quartz schists, and hematite-quartz-muscovite schists with rare felsic and mafic volcanic intercalation. Less frequently, quartz schists and quartzite lenses occur at the top of the sequence. The Bandeirinha Formation is characterized by a 200 m sequence of fine-grained quartzites, mineralogically pure or micaceous (up to 20 %), with subordinated horizons of metaconglomerate and metabreccia. This unit frequently shows pink coloration, interpreted by Almeida-Abreu (1995, 1993) as redbeds.

4.3 A Costa Sena metavolcanosedimentary sequence overview

A sequence of dominant schists and quartzites crops out in the Southern Espinhaço Ridge under the denomination of Costa Sena Group (Fogaça *et al.*, 1984). Its geographical distribution follows a NNW-SSE trend over 90km, from Conceição do Mato Dentro to Diamantina (Minas Gerais state) and has 20 km width, in the core of an anticlinorium (Gouveia Anticlinorium) together with the underlying basement.

4.3.1 Fazenda Formação and Fazenda Casa de Telha (areas 1 and 2)

The “Fazenda Formação” and “Fazenda Casa de Telha” areas (1 and 2 in Figure 4.1) are the northeastern occurrences of the unit, in a basement high. In these areas, sequences of approximately 200 m thickness outcrops. Medium-grained kyanite-muscovite-quartz schist and kyanite-quartz-muscovite schist are predominant at the base, and kyanite rich metaconglomerate (Figure 4.2**a,b**) and dumortierite quartzite occur to the top. The sequence has a very subordinate intercalation of chlorite schist with the local occurrence of blastic pyrite in the mica-quartz schists and deep blue lazulite crystals in quartz veins. Noteworthy is the dissemination of tourmaline in the “Fazenda Casa de Telha” area. Millimetric crystals appear both disseminated syn- to post-kinematically, and curiously as pure microcrystalline centimetric levels (up to 5 cm) parallel to the mylonitic schistosity. In this same region, at the top of the sequence, Bandeirinha Formation quartzites are in angular unconformity with the Espinhaço Supergroup rocks (Figure 4.2c).

4.3.2 Guinda (area 3)

A 500 m thickness sequence crops out in the Guinda area (3, Figure 4.1). The first 100 m of the sequence is composed of medium-grained kyanite-muscovite-quartz schist with localized banded iron formation (cropping out as *in situ* pebbles and cobbles; see hand-specimen in Figure 4.2d). Lateral variation to very coarse-grained kyanite-muscovite-quartz schist with porphyroclasts of up to 8 mm pink quartz were found (Figure 4.2g). Above, the schist has a metric level of matrix-supported metaconglomerate with rounded pebbles of quartzite and banded iron formation in the same kyanite-muscovite-quartz schist matrix (Figure 4.2e,f). This metaconglomerate is overlain by a 50 m thick matrix-supported metasedimentary breccia with sparse angular to sub-angular clasts (pebble and cobble) of stratified white quartzite, grey phyllite, and banded iron formation in a medium- to coarse-grained kyanite-muscovite-quartz schist matrix (Figure 4.2h). The top 150 m comprises variations of fine- and coarse-grained muscovite-quartz schists, with and without kyanite, intercalated with subordinated centimetric levels of chlorite schist and fine-grained gray quartzite. The contact with the pinkish quartzites of the Bandeirinha Formation in this area is transitional to the south in which quartz content increases towards the top, while mica content decreases. To the north, this contact can also be lateral, with abrupt contact of the schist with the pink quartzites. The Bandeirinha Formation is approximately 200 m thick and is composed of frequently micaceous quartzites with or without kyanite. It shows remarkably planar parallel sand sheets with low-angle tabular cross-bedding (<10°), symmetric and asymmetric ripple marks, interbedded with metamorphosed orthoconglomerate and orthobreccia (Figure 4.3h,i). The contact with Espinhaço Supergroup rocks is also characterized by an angular unconformity (Figure 4.3g). While Banderinha Formation has modal bedding of 060/35, the Espinhaço Supergroup has modal bedding orientation of 090/15 in this area.

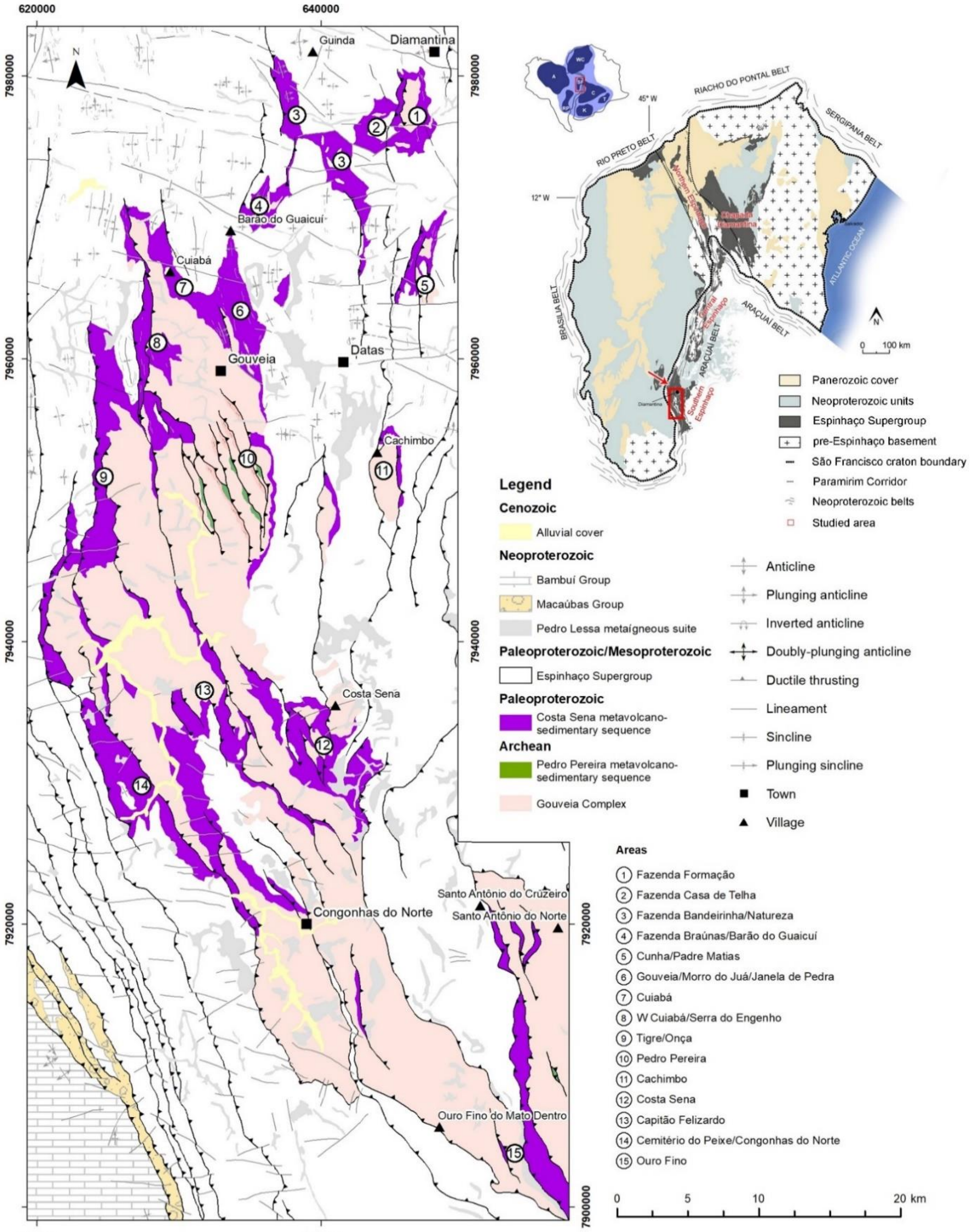

Figure 4.1 Geological map framing the spatial distribution of the Costa Sena metavolcanosedimentary sequence, highlighting the main areas of occurrence (after Fogaça, 1997; Heineck *et al.*, 2003; Knauer and Grossi-Sad, 1997).

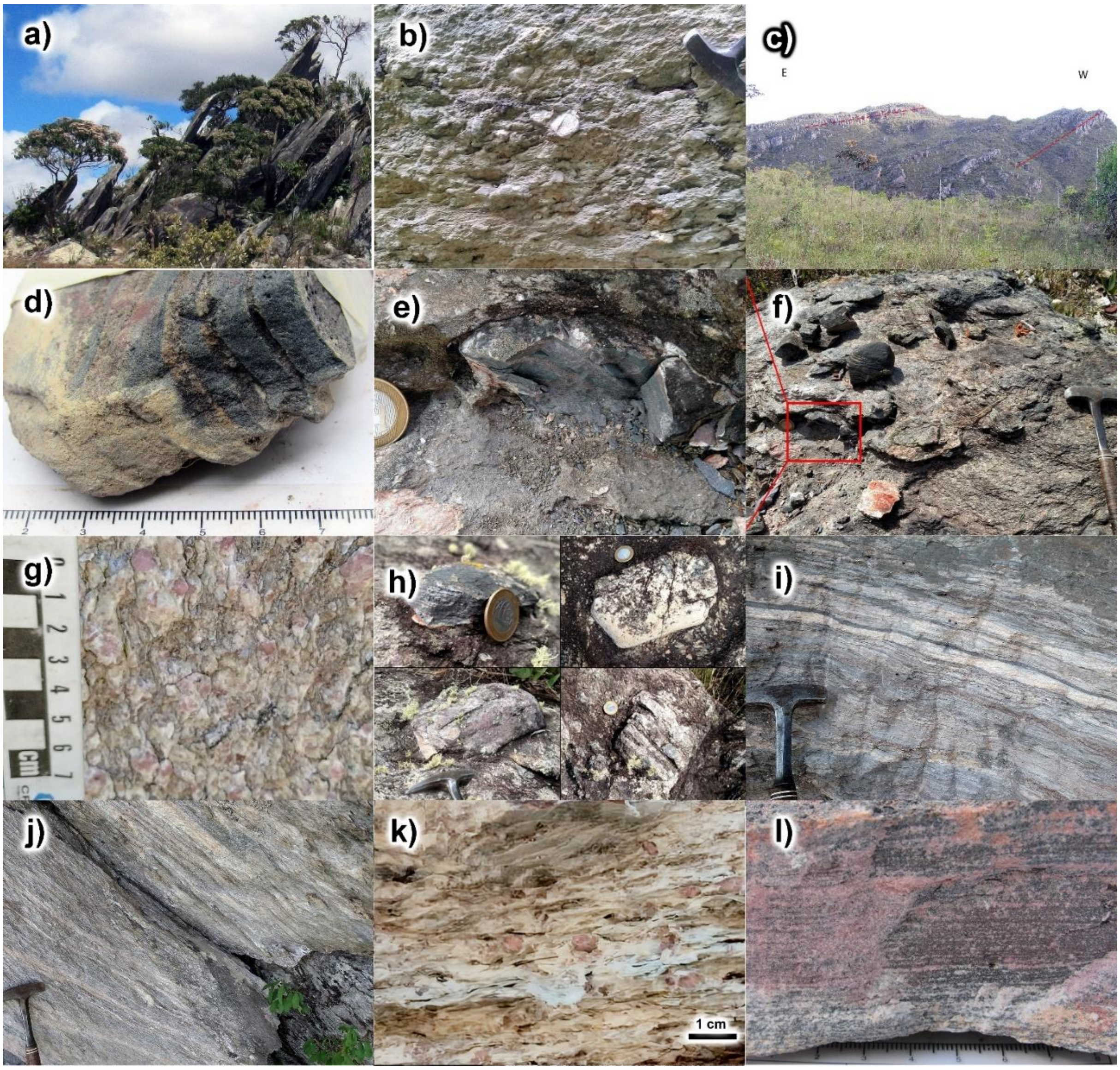

Figure 4.2 General aspects of the Costa Sena metavolcanosedimentary sequence rocks. a) Most common outcrop style of the schists from Costa Sena sequence; b) oligomitic metaconglomerates from Fazenda Formação area; c) angular unconformity at the Fazenda Casa de Telha area, between the Bandeirinha Formation quartzites (west) and the Espinhaço Supergroup (east); d) sample of banded iron formation from in situ loose blocks layer from Fazenda Bandeirinha area; e) and f) metaconglomerate with sparse banded iron formation pebbles in a ky-qtz-mus schist matrix; g) coarse-grained ky-ms-qtz schist with porphyroclastic pinkish quartz grains; h) stratified quartzite and BIF clasts inside ky-mus-qtz schist (the matrix of the metabreccia); i) and j) fine-grained ky-qtz-mus schist showing compositional variation layering in Gouveia and Cachimbo areas, respectively; k) kyanite-bearing schist with pinkish quartz porphyroclasts; i) laminated muscovite quartzite with very fine tourmaline layers.

4.3.3 Fazenda Braúnas/Barão do Guaicuí (area 4)

Area 4 (Figure 4.1) comprises the region east and northeast of Barão do Guaicuí village. At the northeastern portion, to the west of “Serra da Miúda”, the Barão do Guaicuí Formation crops out as a 100 m thick mylonitic tectonic sliver positioned within the Supergroup Espinhaço basal rocks. It consists of mylonitized medium- to coarse-grained kyanite-muscovite-quartz schist with millimetric syn- to post-kinematic tourmaline crystals and a distinct ~1 m level rich in fine-grained lazulite/augelite masses (Figure 4.3b,c). Close to Barão do Guaicuí village, the sequence lies directly over the Gouveia Complex granite and is mainly composed of mylonitized medium- to coarse-grained kyanite-muscovite-quartz schist, quartz-sericite schist, and transitions between these rocks.

4.3.4 Cunha/Padre Matias (area 5)

In the Padre Matias region (area 5, Figure 4.2), the landscape draws attention to the structural framework, with numerous slivers juxtaposed by shear zones that define a remarkably thick-skin tectonic imbrication system embracing the Gouveia Complex, Costa Sena Group, and Espinhaço Supergroup. The lenses have a maximum thickness of 300 m and intercalate mylonitic schists, quartzites, metabreccia, and granitoid mylonites. Due to the intense deformation, it is not possible to define a reliable stratigraphic order. However, worthwhile information can be gained inside the lenses. The Costa Sena Group lenses are composed of medium- to coarse-grained muscovite-quartz schist, quartz-sericite schist, and transitional units, with or without kyanite and recurrent blastic magnetite as a consequence of iron-rich fluid percolation near the shear zone areas. Concentrated in a 2 m thickness level, parallel to the mylonitic foliation, centi- to decimetric stretched and fine-grained lazulite/augelite masses occur inside kyanite-muscovite-quartz schist, as in area 4. Bandeirinha Formation pink quartzite also occurs, though very subordinate, as a tectonically emplaced lens between the Barão do Guaicuí schists. Noteworthy is the occurrence of localized euhedral sub-millimetric beryl crystal in the schist. Also noteworthy is the presence of fine- to medium-grained kyanite-sericite-quartz schist with centimetric greenish chloritoid bands (Figure 4.3e). The chloritoid also occurs in the same site as fine-grained aggregates in decimetric veins, together with milky quartz (Figure 4.3d). In this area, not all the mylonitized schists are of volcano-sedimentary origin.

4.3.5 Gouveia/Morro do Juá/ Janela de Pedra (area 6)

In the northern part of area 6 (Figure 4.1), to the south of Barão do Guaicuí town, the base of the Costa Sena Group sequence is remarkably aluminous. Medium- to coarse-grained muscovite-kyanite-quartz schist predominate. The kyanite crystals can locally compose 30% of the volume, reach up to 2.5 cm, and are dispersed through the rock, being syn- to post-kinematic (Figure 4.3a). Thin chlorite schist levels are intercalated. Above this, the sequence gets coarser and changes to fine-grained micaceous quartzite and fine-grained quartzites with gray to pink quartz porphyroclasts (up to 2 mm). To the top, coarse-grained micaceous quartzite is interbedded with coarse-grained muscovite-quartz schist with up to 8mm purple quartz porphyroclasts, that grades to well-sorted, fine- to medium-grained pink quartzite. As in the northern portion, the center of area 6 (northwest of the Morro do Juá doubly-plunging syncline) has muscovite-kyanite-quartz schists which are composed of up to 30% of kyanite, cut by centimetric veins composed also of kyanite, pyrophyllite, and milky quartz. To the south of Morro do Juá, the Barão do Guaicuí schists are tectonically placed over the Gouveia Complex rocks. At the base of the sequence, a 20 m weathered chlorite schist passes into a 300 m thick metasedimentary set composed of medium- to coarse-grained mylonitized kyanite-muscovite-quartz schist cut by tension gashes perpendicular to the mylonitic foliation filled by milky quartz, kyanite, and pyrophyllite (Figure 4.3f). In the upper third of the set, the same schist grades to fine-grained and records rare well-preserved centimetric sedimentary bedding, marking a plane-parallel stratification alternating beige and gray colors (Figure 4.2i). At the top, a blueish millimetric euhedral beryl crystal was described. The top contact is marked by a nonconformity with the Supergroup Espinhaço rocks.

4.3.6 Cuiabá (area 7)

The Cuiabá region (area 7, Figure 4.1), to the southwest of Barão do Guaicuí town, reveals itself potentially important to the comprehension of the Costa Sena Group due to the possible presence of meta-volcanic rocks. To the north of Cuiabá town, a thicker metavolcano-sedimentary set (600 m) crops out. At the base, for the first third of the sequence, medium-grained light grey muscovite-quartz schist with frequent veins of quartz, tourmaline, and decussed muscovite predominate. At the top of this schist, there is a thin lens (20 m thick and 1200 m in extension) of highly weathered red chlorite schist with sparse residual euhedral quartz crystals up to 1mm diameter. The second third comprises 60 m of medium-grained quartz-muscovite schist with up to 2mm porphyroclastic smoky quartz grading to coarser muscovite-quartz schist. Above this, 3 m of fine-grained quartz-sericite schist with euhedral smoky quartz crops out. Finally, there is a 40 m thick intercalation of quartz-sericite schist and sericite-quartz schist with a variable content (<5%) of milli- to sub-millimetric tourmaline that occurs as disseminated post-kinematic blasts or as milli- to centimetric bands concordant to the mylonitic foliation (Figure 4.2l).

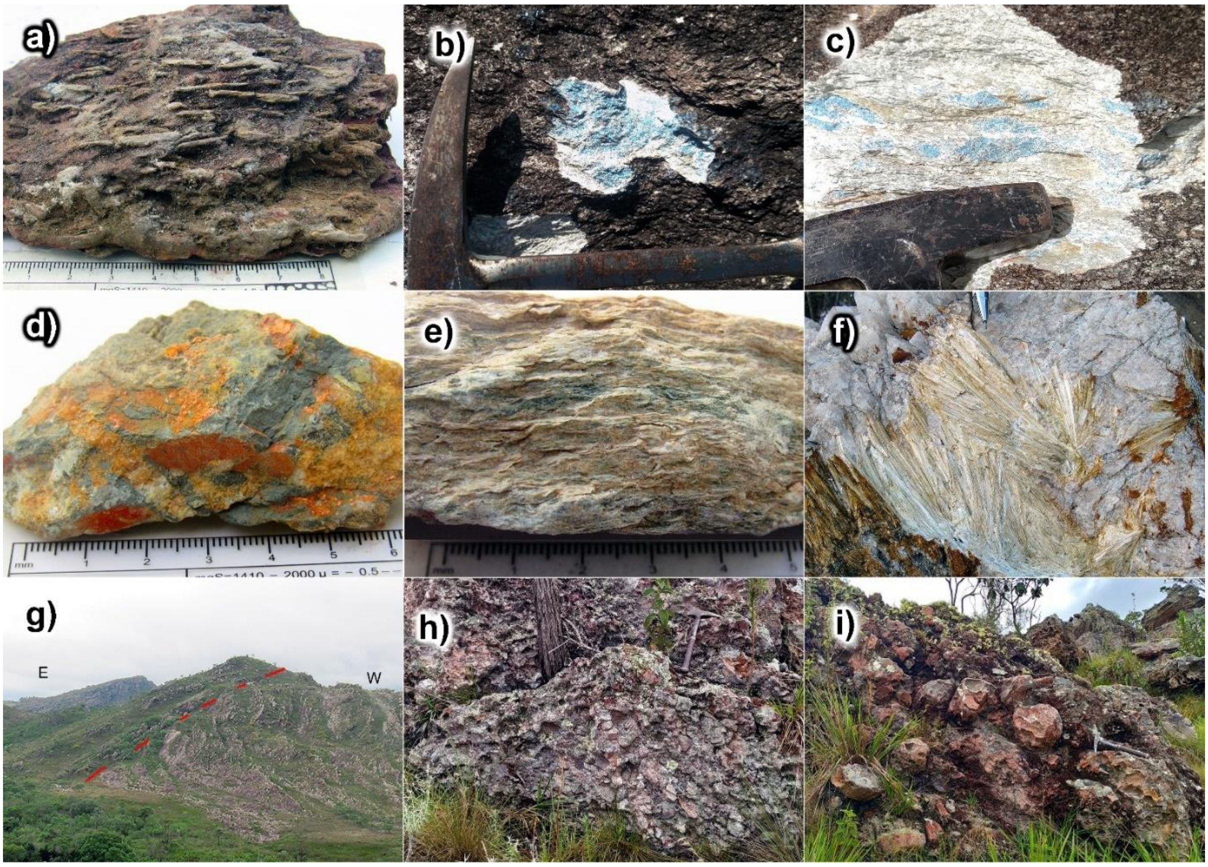

Figure 4.3 General aspects of the Costa Sena metavolcanosedimentary sequence rocks. a) weathered mus-ky-qtz schist with up to 3 cm tabular crystals in prominence; b) and c) massive aggregates of lazulite/augelite from the Barão do Guaicuí schists; d) massive chloritoid + quartz vein sample that crosscuts the schists; e) levels of chloritoid in the Barão do Guaicuí schist; f) radial kyanite/pyrophyllite + quartz vein crosscutting a schist; g) another angular unconformity between Bandeirinha Formation quartzites (west) and Supergrupo Espinhaço (east) at the Fazenda Bandeirinha area; h) pinkish ortho-metaconglomerate of the Bandeirinha Formation; and i) pinkish intraformational metabreccia of the Bandeirinha Formation.

The remainder of the sequence is medium-grained muscovite-quartz schist, highly sheared, with stretched quartz veins that locally give to the rock a pseudo-conglomeratic aspect. Lastly, these schists switch to a 20 m thickness weathered red phyllite in tectonic contact with the Espinhaço Supergroup rocks. Notably, kyanite is conspicuously not present as an important mineralogical constituent of the schists in this area (Cuiabá, area 7).

4.3.7 West Flank of the Gouveia anticlinorium (areas 8,9, and 14)

Areas 8, 9, and 14 are located in the west flank of the Gouveia Anticlinorium where the Costa Sena Group occurs over the Espinhaço Supergroup through major N-S shear zones, dipping moderately to the east. Close to the shear zones, mylonitized fine- to coarse-grained kyanite-quartz-sericite schists frequently grade to ultramylonites, especially in area 9. To the north of Serra do Engenho (in the center of area 8) a 400 m intercalation of fine- to coarse-grained muscovite-quartz schist and quartz-muscovite schist crops out. In the upper third portion, a level of fine-grained quartz-sericite schist with sparse 3mm euhedral blueish/pinkish quartz eyes seems to represent the product of a mylonitized metavolcanic/volcaniclastic (?). In the same area, to the northwest of Cuiabá town, a 70 m set of medium-grained kyanite-muscovite-quartz schist resemble those kyanite-rich schists from area 6. The Cemitério do Peixe region (area 14, Figure 4.1) is also in the west flank of the Gouveia Anticlinorium. The basal contact of the Costa Sena Group is tectonic, through NNW-SSE major shear zones that dip moderately to east place the sequence over the Galho do Miguel Formation quartzites. The eastern top contact with the Gouveia Complex granite is also tectonic. The sequence is composed of approximately 500 m of intercalated fine-to medium-grained muscovite-quartz schist, with or without kyanite, subordinate weathered chlorite schists, and fine-grained micaceous quartzite. Noteworthy is a local occurrence of a talc-serpentine-chlorite schist with millimetric blastic magnetite body emplaced inside the Gouveia Complex granite in Cemitério do Peixe town.

4.3.8 Pedro Pereira and Cachimbo (areas 10 and 11)

In the eastern part of area 10, there is a thin sequence (50 m) that crops out between the Gouveia Complex and Espinhaço Supergroup. Its first third is composed of light greenish to pinkish fine-grained chlorite-sericite-quartz schist that changes to a fine-grained chlorite quartzite in the middle of the set. The upper third is composed of a coarse-grained light green chlorite-muscovite-quartz schist.

The Cachimbo region (area 11, Figure 4.1) exposes 150 m of fine-grained banded kyanite-sericite-quartz schist. The bands mark the bedding beige sericite-rich layers alternate with gray kyanite-rich layers (Figure 4.2j). The sequence is sheared and shows mylonitic foliation and centimetric folds verging to the west.

4.3.9 Costa Sena (area 12)

The Costa Sena region (area 12, Figure 4.1) is the type-area of occurrence and one of the best exposed. The Serra do Paraúna range is the geomorphological expression of a nearly 800 m thick sequence of predominantly metasedimentary and possible metavolcanic rocks. The basal contact with the Gouveia Complex granite is tectonic. The base of the sequence starts with 50 m of weathered fine-grained sericite-chlorite schists intercalated with chlorite-quartz schists that change to quartz-muscovite schist, sericite schists with 2 mm quartz-eyes and tourmaline, and weathered chlorite schist. The next 700 m of the sequence is even more heterogeneous. In the first 250 m, fine-grained quartz-mica schist is predominant, although kyanite-quartz-mica schist, ferruginous and microconglomeratic levels occur subordinately. Above this, quartz becomes important, and pinkish muscovite-quartz schist, with and without up to 4 mm pale pink and blue quartz porphyroclasts, predominates. Granulation variation is frequent from fine- to coarse-grained, and subordinated lenses of white and pinkish quartzite occur. In the last 50 m of the sequence, pinkish two sericite-quartz schists with purple quartz porphyry from Cuiabá region.

4.3.10 Capitão Felizardo (area 13)

In Capitão Felizardo region (area 13, Figure 4.1) there is a 400 m sequence to the east of the eponymous town. The western contact with the Gouveia Complex granite is tectonic. The base of the sequence (first 100 m) is composed of banded tourmaline quartzite, tourmaline-quartz schist with blastic magnetite, and intrafolial quartz veins. The whole sequence is mylonitized and the tourmaline quartzite shows boudinage. The remaining 300 m of the sequence is composed of very fine-grained laminated schist alternating white and reddish millimetric bands interbedded with coarse-grained chlorite-quartz schist with up to 6 mm quartz porphyroclasts and subordinated chlorite schist. An isolated decametric body of iron formation crops out 2.5 km to the southwest of Capitão Felizardo. This shows no quartz bands but some sparse relict thin quartz lines resemble bedding. It is composed almost totally of massive hematite (~85 %) and minor amounts of quartz (~15 %). The suggestive banding and the high hematitic content suggest that metasomatic alteration of a banded iron formation leached out Si and concentrated Fe.

A 500 m thickness sequence outcrops in Ouro Fino region (area 15, Figure 4.1). Its basal contact is with a metabasic intrusion between the Gouveia Complex rocks and the sequence itself. The first third of the set is composed predominantly of fine-grained sericite schists with variable content of quartz, locally with kyanite, tourmaline, and rare pale blue quartz-eyes. The middle is composed of pure fine-grained laminated light yellow quartzites with minor intercalations of sericite-quartz schist and ferruginous quartzite horizons. The last third of the sequence is mainly composed of sericite-muscovite-quartz phyllite with millimetric blastic magnetite overlaid by metric levels of coarse-grained micaceous quartzite and greenish chlorite schist.

4.4 Analytical methods

4.4.1 Sampling

A total of 75 samples were selected for thin-section petrography and 21 fresh samples were carefully chosen for geochemical assessment. From these, 4 samples were collected for geochronological investigation (CSOV-04; CSOV-06A; CSOV-07; CSOV-08). The UTM coordinates for each analyzed sample is provided in the Appendix D, and the geochronological data are provided in the Appendix E, F, G, and H**Erro! Fonte de referência não encontrada.**. For the Bandeirinha Formation, the quartzitic matrix of an intraformational metabreccia was sampled in its type-area for dating purposes. For the Barão do Guaicuí Formation, 3 outcrops were sampled: a metaconglomerate matrix from Fazenda Formação area and two sericite-quartz schists with purple quartz porphyroblasts from Cuiabá region.

4.4.2 Whole-rock geochemistry

Major and trace element concentrations of the selected samples are reported in Appendix D. Whole-rock analyses of major, trace, and rare earth elements were undertaken in SGS GEOSOL laboratory. The samples were pulverized, homogenized, quartered, and then submitted to lithium tetraborate fusion, after which they were analyzed by ICP-OS (Inductively Coupled Plasma Optical Spectrometry - major and some trace elements) and ICP-MS (Inductively Coupled Plasma Mass Spectrometry - trace and REE).

4.4.3 U-Pb Geochronology

U-Pb isotopic analysis was performed by using the Laser Ablation Sector Field Inductively Coupled Plasma Mass Spectrometry (LA-SF-ICP-MS, Thermo Scientific ELEMENT 2 with a coupled 213 nm Cetac laser) at the geochronological laboratory of Federal University of Ouro Preto (LOPAG, Brazil). Rock samples were prepared for analysis in the laboratory of the Federal University of Minas Gerais (SEPURA, Brazil).

Ten kilograms of each sample were processed for zircon U-Pb analysis in order to obtain age distribution and maximum depositional age. Zircon concentrates were prepared using crushing, grinding, magnetic (Frantz isodynamic separator), and gravimetric techniques. The final separation of zircon grains was achieved by handpicking. Grains were mounted in epoxy disks and polished to expose their centers. Morphological features and internal structures of zircon grains were revealed by backscattered electron (BSE) and cathodoluminescence (CL) images obtained through SEM (JEOL, model JSM-6510 coupled with a Centaurus detector).

Blueberry (564 Ma; Santos *et al.*, 2017), Plešovice (338 Ma; Sláma *et al.*, 2008), and GJ-1 (605 Ma; Jackson *et al.*, 2004) standard zircons were used in the analytical routines. Data reduction used Glitter software (Van Achterbergh et al., 2001). Grain areas with inclusions, fractures, and metamict structures were avoided. The data from each spot were evaluated taking into account the common Pb contents, errors of isotopic ratios, percentages of discordance, and Th/U ratios. From the selected spots, only those with less than 10% of discordance were considered for the age distribution plots. They were plotted in frequency histograms and/or Concordia diagram, using Isoplot/Ex (Ludwig, 2003).

4.5 Analytical results

Based on petrographic, field-related features, and geochemistry, the dataset was subdivided into 5 groups: (i) Porphyroclastic schist; (ii) Type I schist; (iii) Type II schist; (iv) High SiO_2 metasedimentary rock; and (v) Laterized schist. This grouping is considered to simplify data description and investigation. Data for samples PE-BD-88, PE-SM-04, PE-BD-87, and PE-GO-01 are from Dussin and Chemale Jr. (2012) and were re-compiled for this assessment.

4.5.1 Geochemistry of the Costa Sena Group schists

The porphyroclastic schist group has a restricted compositional range and consists primarily of SiO_2 (72-82 wt%), Al_2O_3 (12-17 wt%), and K_2O (1-6 wt%). Contents of Fe_2O_3 (total iron) and MgO are low, between 1.3 and 3.1 wt%, and between 0.01 and 1.11 wt%, respectively. This group shows strong depletion in CaO, MnO, and Na_2O, with values <0.18 wt%. Concentrations of trace elements are also low for Cs, Ba, Nb-Ta, Sr, P, and Ti, and show strong negative anomalies when normalized to Upper Continental Crust values from Taylor and McLennan (1995) as shown in Figure 4.5a. REE are enriched in relation to Cl chondrite (Anders and Grevesse, 1989; average ∑REE = 187.4, ranging from 85.4 to 362.6). LREE are fractionated and show an inclined pattern (La_{CN}/Sm_{CN}=4.70), whilst HREEs show a flat pattern (Gd_{CN}/Lu_{CN}=0.97). Europium shows strong negative anomalies (Eu_{CN}/Eu^*_{CN}=0.37) in all samples (Figure 4.4a). Although all samples show similar REE patterns, it is noteworthy that sample MSC004 has higher HREE contents.

By and large, Type I and II schist groups have similar compositions of major oxides with small differences. Considering both groups, SiO_2 content ranges from 51 to 80 wt%, Al_2O_3 (9-25 wt%), K_2O (1.1-7.6 wt%), Fe_2O_3 (2.1-11.3 wt%) and MgO (0.02-3.04 wt%). CaO, MnO, and Na_2O are strongly depleted, with average values <0.6 wt%. Trace elements show negative anomalies for Nb and Sr (UCC normalized, Figure 4.5c,e), though they are stronger in the Type I schist group. Type I schists also show a strong negative anomaly for Ba, which does not occur in the Type II schist group. REEs are enriched in relation to Cl chondrite for both groups, although they have higher values in the Type I schist group (average ∑REE = 526.8 ppm, ranging from 236.3 to 856.7 whereas Type II schist group have average ∑REE = 133.5 ppm, ranging from 68.1 to 200.25). REE are fractionated in both groups (Type I schist $La_{CN}/Yb_{CN}=31.9$; Type II schist $La_{CN}/Yb_{CN}=14.7$ Figure 4.4b,d), being stronger in Type I schist. Europium anomaly is present in Type I schist ($Eu_{CN}/Eu^*_{CN}=0.64$) and less pronounced in Type II schist ($Eu_{CN}/Eu^*_{CN}=0.75$).

The High SiO_2 metasedimentary rock group has a restricted compositional range and consists primarily of SiO_2 (95-96 wt%), Al_2O_3 (2.05-3.4 wt%), and Fe_2O_3 (total iron, 0.4-1.3 wt%). All the other oxides are strongly depleted, with values <0.1 wt%. This group has Cs, Rb, Nb, Sr, and P negative anomalies when normalized to UCC (Figure 4.5b) and show much lower REE contents than the other groups (∑REE average = 55.6). LREE are fractionated (average $La_{CN}/Sm_{CN}=6.33$), whilst HREEs show a flatter pattern (average $Gd_{CN}/Lu_{CN}=1.2$). Europium shows strong negative anomalies ($Eu_{CN}/Eu_{CN}=0.44$) in all samples (Figure 4.5e)

The deeply laterized sample show strong enrichment of Al_2O_3, Fe_2O_3 (22 and 31 wt%, respectively), and SiO_2 depletion. The other major oxides show negligible values (>0.1 wt%), or almost (TiO_2 = 0.44 wt%). U and Th are relatively enriched while Sr is strongly depleted; Nb, Ta, Zr, and HREE behaved as resistive elements.

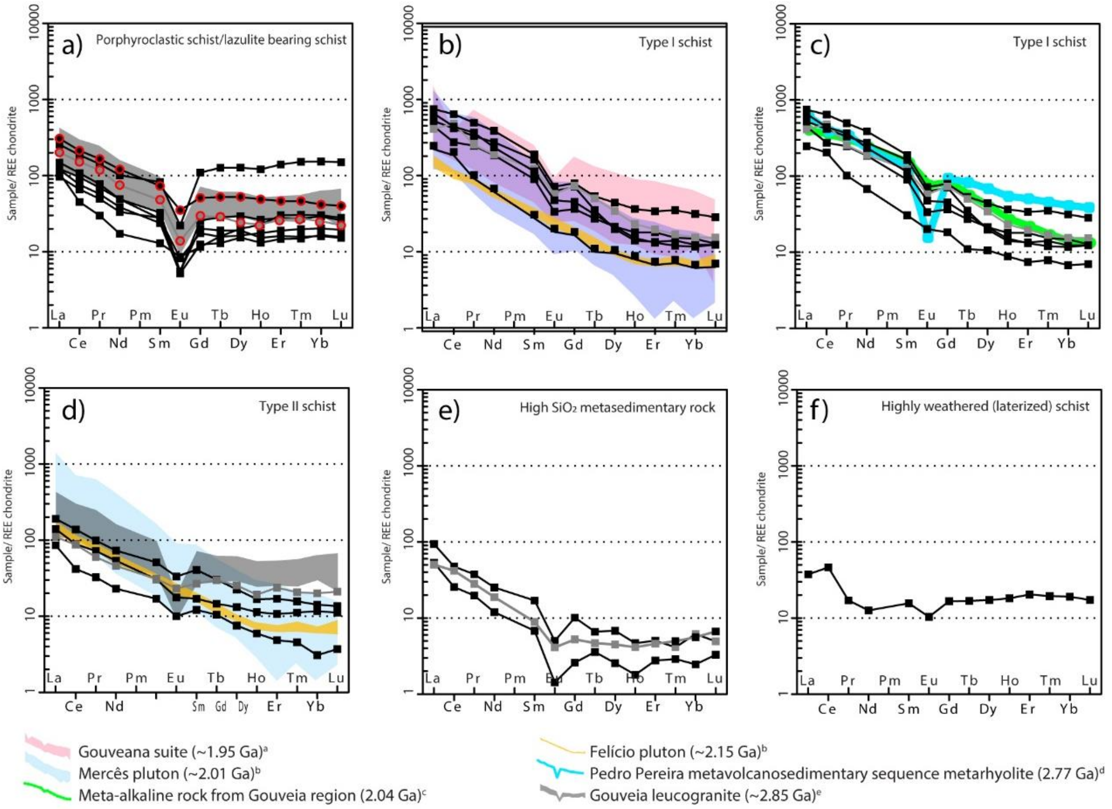

Figure 4.4 Spidergrams with CI chondrite normalized (Anders and Grevesse, 1989) REE values of the Costa Sena sequence groups and field patterns from possible sources. a) Porphyroclastic schist/lazulite bearing schist (the red circles represent the lazulite bearing ones); b) and c) Type I schist; d) Type II schist; e) High SiO2 metasedimentary rock; f) Highly weathered (laterized) schist. a(Chaves *et al.*, 2014);b(Grochowski, 2019);c(Dussin and Chemale Jr, 2012);d(Freimann *et al.*, 2021) ;e(Chaves and Coelho, 2013).

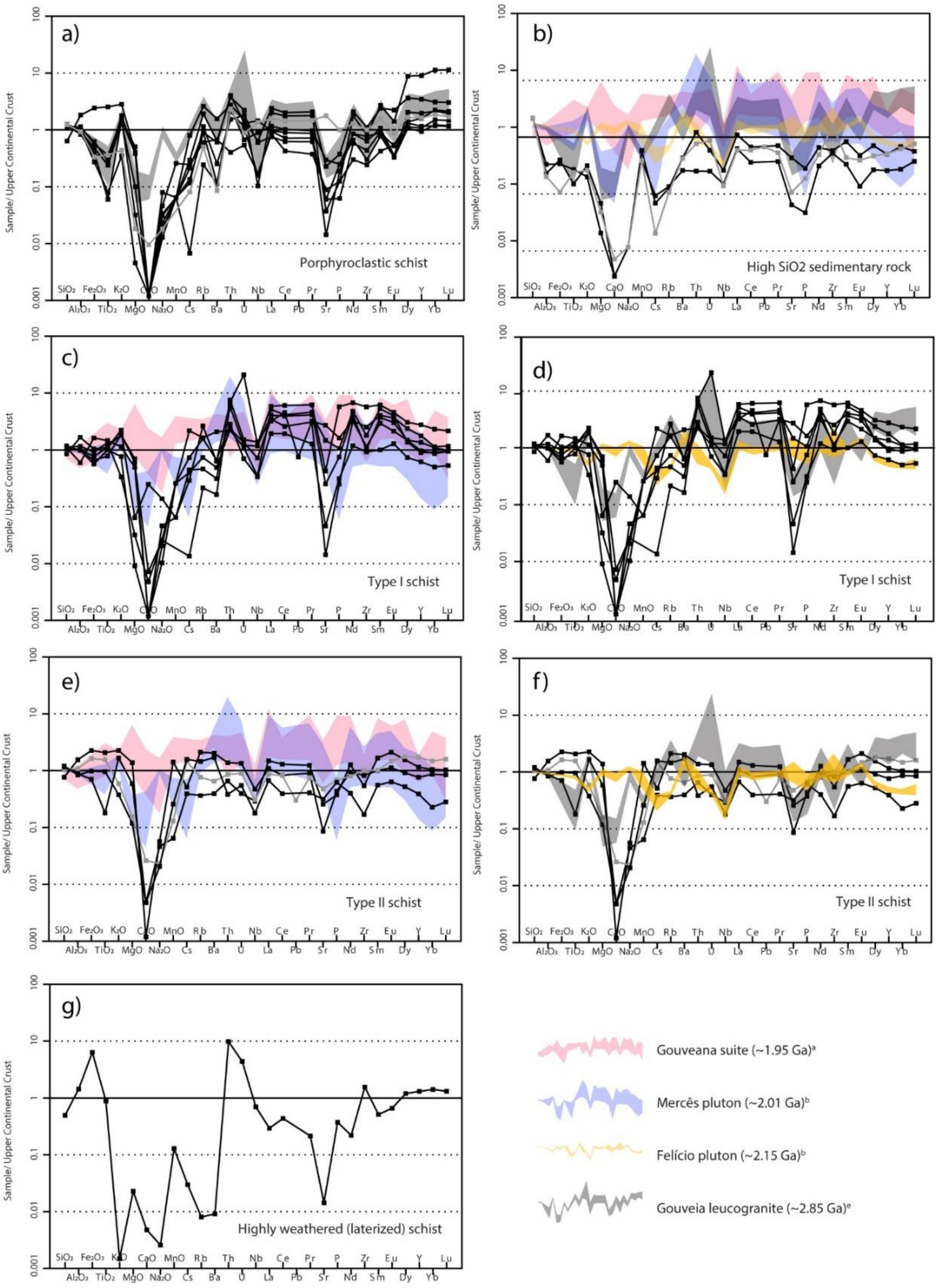

Figure 4.5 Spidergrams with upper continental crust normalized (Taylor and McLennan, 1995) major oxide and trace element values of the Costa Sena sequence groups and field patterns from possible sources. a) Porphyroclastic schist/lazulite bearing schist b) High SiO2 metasedimentary rock; c) and d) Type I schist; e) and f) Type II schist; g) Highly weathered (laterized) schist). a(Chaves *et al.*, 2014);b(Grochowski, 2019);e(Chaves and Coelho, 2013).

Although samples were selected carefully, avoiding those altered by currently weathering processes, they all show strong depletion of CaO, Na_2O, MnO, Sr, and slightly so for K_2O and MgO. When plotted in the (Na_2O+CaO) – Al_2O_3 – K_2O diagram of Nesbitt and Young (1984), all samples plot in the advanced weathering trend (Figure 4.6). Values for the Chemical Index of Alteration (CIA - Nesbitt and Young, 1982), Chemical Index of Weathering (CIW - Harnois, 1988), and Advanced Argillic Alteration Index (AAAI - Williams and Davidson, 2004), are between 100-70, 100-94, and 99-70, respectively. Therefore, any attempt to use major oxide diagrams that involve those depleted elements will probably lead to wrong interpretation. In order to see through the weathering processes, diagrams based on less mobile trace elements (or on multi-elemental functions) were preferred over those based on mobile oxides. All groups are plotted in each of the graphs presented below.

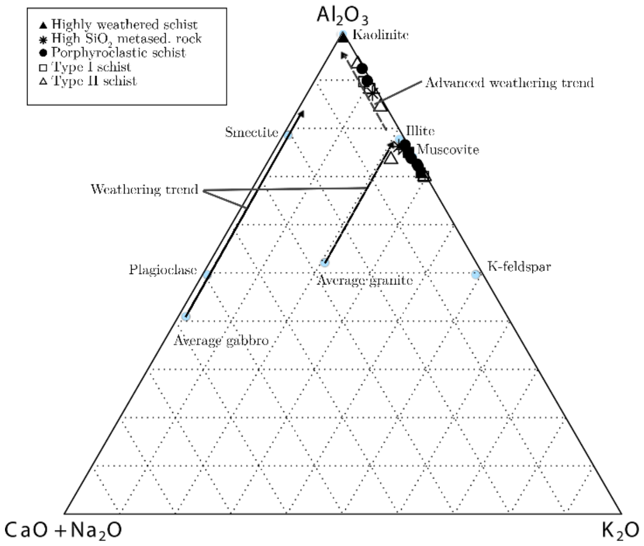

Figure 4.6 A-CN-K ternary plot for the Costa Sena sequence samples (Nesbitt and Young, 1984). The arrowed line refers to the ideal weathering trend, while de dotted arrowed line to the advanced weathering trend.

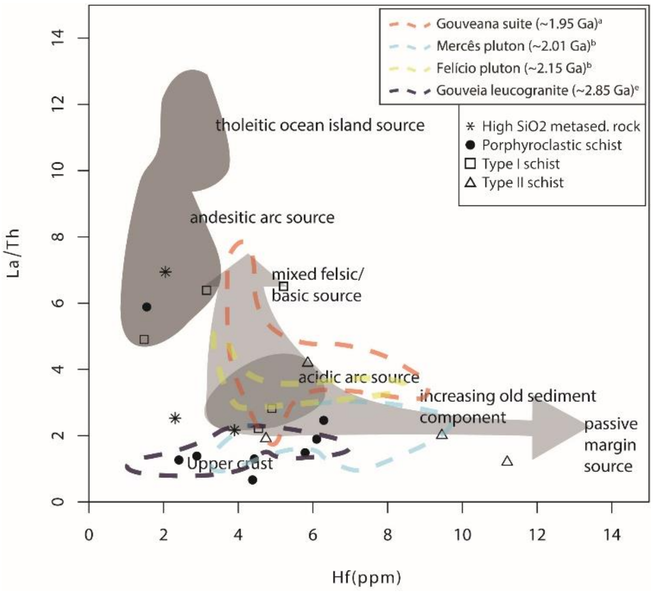

Figure 4.7 La/Th-Hf diagram (Floyd and Leveridge, 1987). Grey fields indicate the compositions of sedimentary rocks deposited in different tectonic settings. Colored dashed lines represent the fields from the possible sources. a(Chaves *et al.*, 2014);b(Grochowski, 2019);c(Chaves and Coelho, 2013).

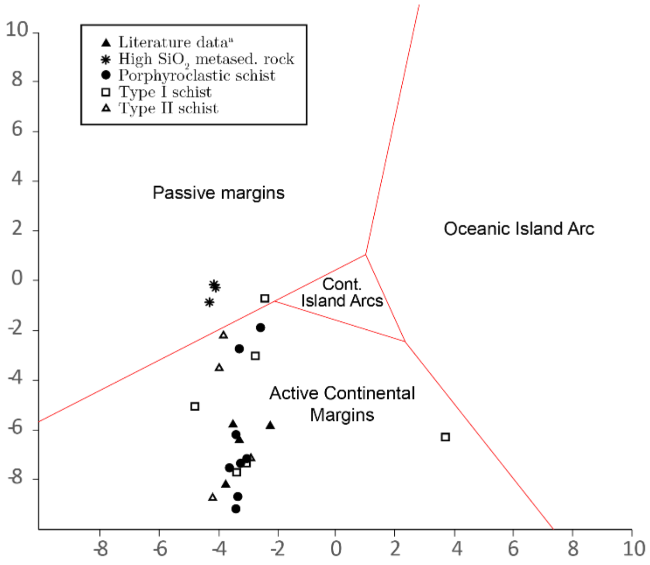

Figure 4.8 Plot of the Costa Sena sequence samples within a major element discrimination diagram (Bhatia, 1983a) for tectonitc settings; a(Fogaça *et al.*, 1984).

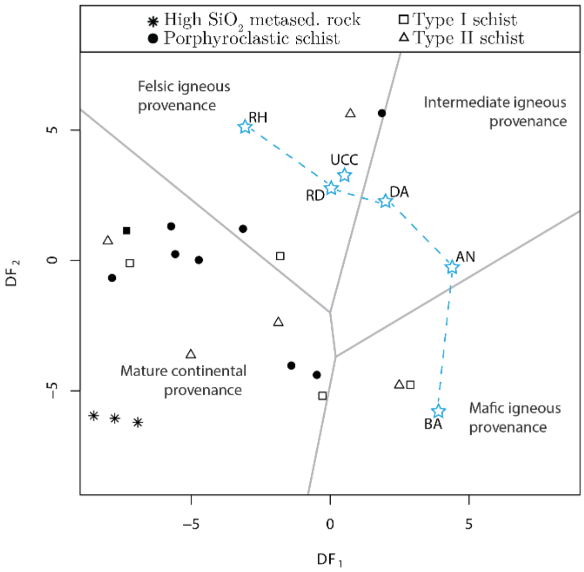

Figure 4.9 Major element provenance discriminant function plot (Roser and Korsch, 1988) for Costa Sena sequence rocks. Stars: UCC – average upper continental crust; BA, AN, DA, RD, and RH – average basalt, andesite, dacite, rhyodacite, and rhyolite, as plotted by Roser and Korsch (1988)

At least some of the results (Type I schists) point to a source with very high values of LREE (Figure 4.4). Possibilities include the Gouveiana Suite (although this may be too young to be a source – crops out as a 5km^2 body in area 6), the Mercês pluton (crops out as a 300 km^2 body, 75km NE), the meta-alkaline from Gouveia region (unknow extent, area 6), and the Pedro Pereira metavulcanosedimentary sequence, which is situated 10 km to the south of Gouveia city comprising a total of 6 km^2 tectonic lenses (see Figure 4.4 and Figure 4.5). The porphyroclastic schist REEs (with or without lazulite) seem to correspond almost exactly to the Gouveia leucogranite REEs.

In the La/Th-Hf diagram (Figure 4.7), the porphyroclastic schist samples cluster consistently in the Gouveia leucogranite limits. Type II schist samples point to contribution of mature sources, while Type I schists point toward an andesitic source. Almost all samples fall within “Active Continental Margins” field in the multi-element diagram of Bhatia (1983b), except the mature quartz-rich metasedimentary rocks (Figure 4.8). The major element provenance discriminant function plot of Roser and Korsch (1988) did not produced conclusive classification maybe because it uses many mobile elements to differentiate the fields (Figure 4.9).

4.6 Geochronology

4.6.1 Sample CSO*V*-06A

Forty-four grains recovered from the sericite-quartz schist were analyzed. The grains are subhedral to anhedral, with pyramidal, flat, or rounded crystal terminations, and they range from 70 to 320 µm-long, with axial ratios between 1:1 and 3:1. The BSE images show mostly fractured grains. After data reduction, 19 spots could be used for age calculations (Appendix F). Two populations of zircon were found, yielding Discordia lines with upper intercepts at 2070 ± 23 Ma and 2466 ± 22 Ma. The lower intercepts are at 384 ± 23 Ma and 371 ± 9 Ma, respectively (Figure 4.10).

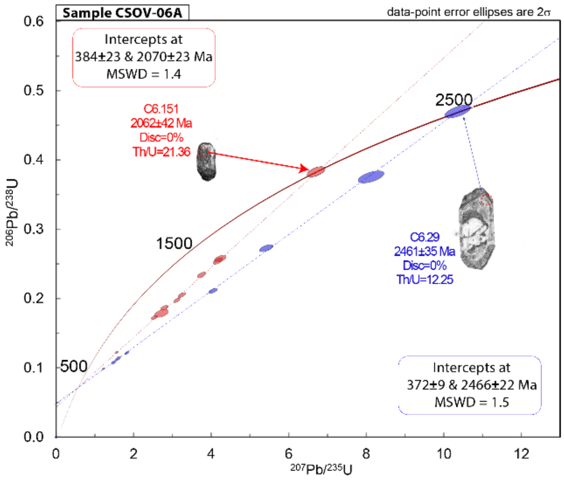

Figure 4.10 Wetherill-type Concordia diagram for the Barão do Guaicuí schist sample.

4.6.2 CSO*V*-08

From the 173 grains recovered from kyanite-bearing metaconglomerate, 70 were analyzed (Apêndice G). The grains range from 80 to 395 µm-long, with axal ratios between 1:1 and 5:1, although predominantly 2:1 (70%). The grains are mostly fractured and corroded and are translucent to opaque with light to deep yellow colors. Only 12 grains yielded ages within 10 % of discordance. Santos (2015) reports detrital zircon analyses from kyanite-muscovite-quartz schist (sample PE-GO-01) collected 3 km NE from Gouveia city in our study area which are included in our compilation to enhance the understanding of our new data (Figure 4.11). The majority of zircon grains from the Barão do Guaicuí schist composite range from 2.6 to 3.0 Ga. Statistical analysis using the criteria of Vermeesch (2012) yielded an older peak at 2927 ± 3 Ma (32% of the results). The second most important peak (30%) remains in the same interval, at 2698 ± 5 Ma. Minor Archean ages also point to sources around 2811 Ma. The youngest zircon population indicates maximum depositional age for the Barão do Guaicuí Formation rocks of 2112 ± 7 Ma.

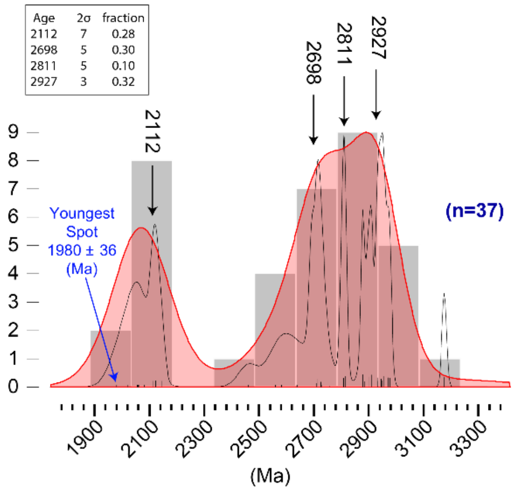

Figure 4.11 Frequency histogram (gray bars), probability density plot (PDP, black line), and kernel density estimation (KDE, red) for the Barão do Guaicuí Formation schist CSOV-08. Numerical analysis based on Vermeesch (2012).

4.6.3 Bandeirinha Formation (sample CSOV-07)

From the 200 recovered grains from the intraformational metabreccia matrix, 133 spots were analyzed (Apêndice E). Only those within 10% of discordance were used (98 spots). The grains are heterogeneous, subhedral to anhedral, with dominantly rounded terminations. They range from 69 to 381 µm-long, with axial ratios between 1:2 and 4:1 (Figure 4.13).

Most zircon grains (52 %) from sample CSOV-07 yielded a main peak around 2656 ± 5 Ma, representing an age interval of 2570-2720 Ma. Minor Archean ages point to sources around 2810- Ma and 3240 Ma. The second most important probability peak represents the zircon population dated from 2000 Ma to 2130 Ma (25 %). This population indicates maximum depositional age at 2093 ± 9 Ma for the Bandeirinha Formation intraformational metabreccia (Figure 4.12).

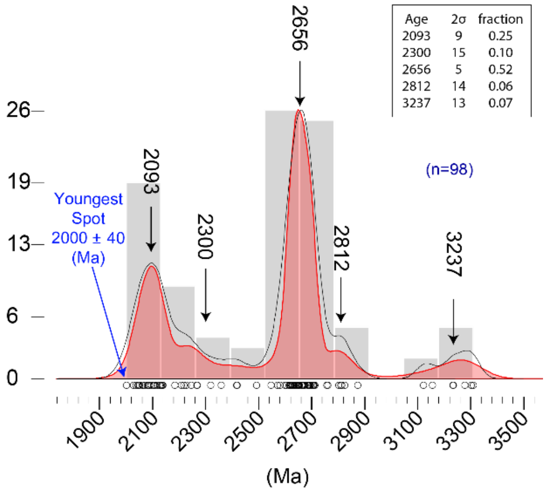

Figure 4.12 Frequency histogram (gray bars), probability density plot (PDP, black line), and kernel density estimation (KDE, red) for the Bandeirinha Formation sample. Numerical analysis based on Vermeesch (2012).

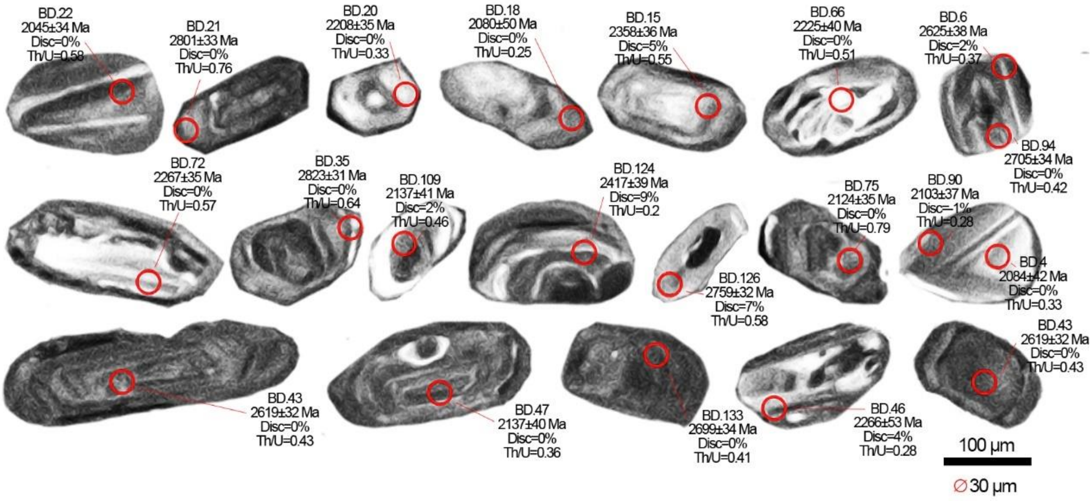

Figure 4.13 Cathodoluminescence (CL) images for representative detrital zircon grains from Bandeirinha Formation metabreccia.

4.7 Discussion

4.7.1 Does Barão do Guaicuí Formation exist?

Prior studies have questioned the real existence of the Barão do Guaicuí Formation as a metamorphosed volcanic-sedimentary sequence. Uhlein (1991) claims that the kyanite-bearing mylonitic schists are the sheared contact between the basement and the supracrustal rocks. Other authors argue that the schists are partially (Dossin *et al.*, 1990) or entirely (Silva, 1995) a product of basement granite mylonitization. A serious weakness with these arguments is that it is impossible to explain the lithological heterogeneity of the sequence by the mylonitization process. The Barão do Guaicuí Formation schists hold quartzite intercalations, metaconglomerates and banded iron formation lenses, and chlorite schist horizons. Also, these arguments do not take into account the high mineralogical content of kyanite in the schists. The mylonitization of the Gouveia Complex has already been carefully characterized. Cruz et al. (2005) demonstrated that to the center of shear zones in unambiguous granites of the Gouveia Complex, there is a progressive decrease of the plagioclase, K-feldspar, and quartz, whilst biotite and chlorite contents increase. No kyanite-bearing mylonite of the Gouveia granite was observed in this study. Another question that needs to be asked is the absence of feldspars in the Barão do Guaicuí Formation schists. Most of these schists are coarse-grained proto-mylonites, whereas phyllonites only occur locally. As the proto-mylonites have experienced limited grain-size reduction and recrystallization, one would expect relict feldspars grains and porphyroclasts with preserved igneous texture in thin-section if they were, in fact, the direct mylonitization of originally granitic rocks. Therefore, this study supports previous researchers (e.g Fogaça *et al.*, 1984; Hoffmann, 1983b; Knauer, 1999, 1990) and justifies the integrity of the Barão do Guaicuí Formation as a metamorphosed volcanosedimentary sequence.

4.7.2 The high kyanite content

The Costa Sena Group shows only limited evidence of its origins from fieldwork or petrography perspective, considering its complex polycyclic deformational and metamorphic background. Therefore, geochemistry seems to be a useful tool to contribute to the unraveling of the unit’s history. The kyanite-bearing schists of Barão do Guaicuí Formation have a particular composition of predominantly SiO_2 and Al_2O_3, with extremely low values for some alkalis and alkali earths. This composition deviates from common Al_2SiO_5 mineral-bearing rocks, which are usually metapelites, and is atypical for volcanic and other general sedimentary and metamorphic rocks. It is somewhat surprising that the analyzed samples show ubiquitous strong depletion of CaO, Na_2O, MnO, Sr, and slightly of K_2O and MgO, even in carefully selected fresh samples.

According to Nesbitt and Young (1984, 1982), this homogeneous depletion is characteristic of weathering leaching. During the initial stages of weathering, sodium, calcium, and strontium decrease quickly in comparison with potassium in rocks. The main reason for this is the early dissolution of plagioclase, which is much less stable than K-feldspar or biotite, the major potassic minerals. As weathering progresses, kaolinisation takes place, and vermiculite and illite join the clay mineral assemblage influencing the loss or retention of cations. As pH increases, the charge balance in interlayer sites and on surfaces in clays is satisfied by large cations (K^+, Rb^+, Cs^+, and Ba^{2+}). The smaller cations (Ca^{2+}, Na^+, and Sr^{2+}) are less readily accepted in interlayer sites and so are removed in groundwater and surface runoff. As vermiculite has a small structural site, it can accommodate Mg^{2+}, which can be retained in the soil/sediments.

The strong homogeneous leaching of calcium, sodium, and strontium, even for fresh samples, suggests that this weathering process is not recent and probably took place during basin filling. As a consequence, the aluminum content was proportionally concentrated, reflected in the high Al_2O_3 content for all schist samples. Since kyanite frequently composes the essential mineralogy, reaching up to 30% of the modal composition in some cases, it is reasonable to assume that this relative aluminum enrichment occurred at least before the last metamorphic event at the Neoproterozoic Era.

Inside de Barão do Guaicuí schists sequence, kyanite content varies drastically. Some horizons show almost pure kyanite levels, or localized chloritoid-rich levels, whilst others show no kyanite, not even as an accessory mineral. Since all the sequences underwent the same regional greenschist facies conditions, it is reasonable to infer that the presence of kyanite and/or chloritoid was controlled by aluminum excess in the protolith rather than metamorphic heterogeneity. It is reasonable to infer that at least some of the kyanite-rich schist levels record variable degrees of supergene alteration.

These findings indicate that the controversial high kyanite content in the Barão do Guaicuí schists is chiefly a result of metamorphism of previously weathered rocks, as formerly suggested by Knauer (1999). The homogeneity of this depletion throughout the wide geographic extent of the Costa Sena Group rocks rules out any hydrothermal alteration explanation since this type of process is usually localized and heterogeneous. Although a minor influence, another factor that can contribute to the loss of calcium, sodium, potassium, and silica is the progression of the mylonitization process.

4.7.3 The absence of feldspar grains

As mentioned before in the text, the absence of feldspar in the schist sequence has been the cause of controversy about the rock protolith and its origin. Whether the product of mylonitization of granites, acid-volcanites or arkosic sediments derived from them we would expect to find relict feldspar grains in the schists, at least locally, especially in those coarse-grained schists with low transportation and mechanical sorting. As mentioned before, the whole-rock geochemical analyses indicate that the protoliths underwent advanced weathering processes. It is therefore likely that the parent feldspar grains were largely altered to clay minerals in the basin (or/and in the source site), which is coherent with the explanation for the high kyanite content. Metamorphism together with dynamic recrystallization would be a final blow over any remnant unaltered feldspar grains, transforming them into fine quartz and muscovite crystals.

4.7.4 Geochronology and geotectonic settings

Previous detrital zircon data for the Bandeirinha Formation (Santos *et al.*, 2013) do not show the spectral pattern nor the maximum depositional age obtained here (Figure 4.11 and Figure 4.12). Considering the depositional age of the Costa Sena Group as the metarhyolite age from by Machado et al. (1989), and the detrital zircon ages from Barão do Guaicuí Formation schists and Bandeirinha Formation quartzites, it is possible to construct the [cumulative proportion] vs. [Crystallization Age – Depositional Age] plot from Cawood et al. (2012), which can constrain tectonic settings even where the original nature of the basin is no longer preserved (Figure 4.14). Both populations fall mainly in the foreland collisional field, with ages close to the depositional age of the sample, as well as significant input from older sources.

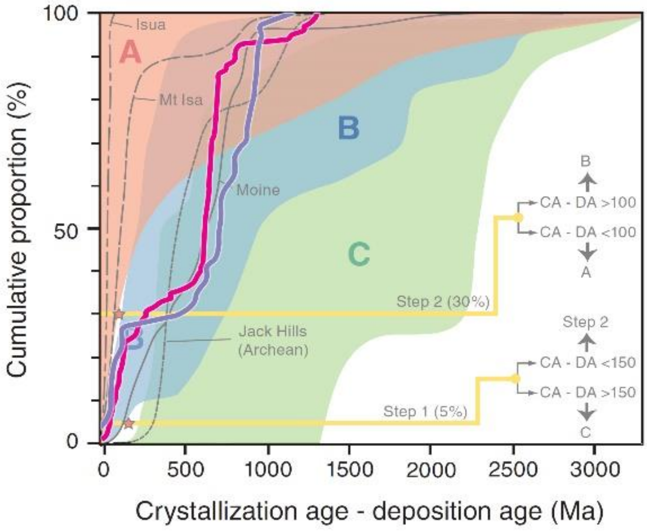

Figure 4.14 A summary plot of the general fields for convergent (A: red field), collisional foreland (B: blue field), and extensional basins (C: green field) as in Cawood et al. (2012). Pink solid line: Bandeirinha Formation; purple solid line: Barão do Guaicuí Formation. Note the similarity between the cumulative curves of Bandeirinha and Barão do Guaicuí formations indicating similar age sources, as well as the proportion of them in the zircon population.

The basal schists of the Barão do Guaicuí Formation show Paleoproterozoic and Neoarchean detrital zircon age peaks (2.7 - 2.9 Ga), while the Bandeirinha Formation show Paleo-Mesoarchean peak in addition to the Neoarquean and Paleoproterozoic ones.

Possible nearby Paleo-Mesoarquean detrital zircon from primary sources are the Santa Barbara complex (~3.2 Ga; Lana *et al.*, 2013), the Porteirinha Complex (3.3-3.4 Ga; L. C. da Silva *et al.*, 2015) and the Guanhães Complex (3.15 Ga; Kuchenbecker and Barbuena, 2023; Silva *et al.*, 2002b). The erosion of the metasediments from Rio das Velhas and Minas basins (Nova Lima Group and Minas Supergroup from the Quadrilátero Ferrífero; Martínez Dopico *et al.*, 2017) could also work as a Paleo-Mesoarquean detrital zircons supply source.

The Gouveia Complex is the closest Mesoarchean source (2839 ± 14 Ma; Machado *et al.*, 1989) for the Costa Sena Group, and it composes the majority of the Costa Sena basin basement, outcropping as an approximately 800 km^2 body nearby the sequence. The Pedro Pereira metavolcanosedimentary sequence also suits as a local sedimentary Neoarchean supply source (2771 ± 8 Ma; Freimann *et al.*, 2021). The Rio das Velhas II and Mamonas Events recorded in the Quadrilátero Ferrífero Minas and Rio das Velhas basin likewise produced Neoarchean zircons that could be the source (e.g Farina *et al.*, 2016).

Approximately 40 km ENE of the city of Diamantina, there is a granitic batholith named Rio Itanguá (*e.g.* Gorlt, 1972; Grossi-Sad *et al.*, 1997; Hettich, 1973; Souza and Grossi-Sad, 1997; Toloczyki, 1982). Hagedorn (2004) carried out the first isotope measurements in this batholith and suggested a Paleoproterozoic crystallization age. This batholith is positioned in the northwestern portion of the Guanhães block, which is a basement inlier in the Araçuaí orogen (Noce *et al.*, 2007). Petrological, geochemical, and geochronological studies in this batholith were recently undertaken by Grochowski (2021; 2019), who subdivided it into the granodioritic Felício pluton and the monzogranitic to syenogranitic Mercês pluton. Both plutons show strong subduction-zone geochemical composition with an emplacement age of 2151 ± 12 Ma for the Felício pluton and 2014 ± 11 Ma for the Mercês pluton. They were interpreted as related to the Paleoproterozoic orogenic event that assembled the São Francisco-Congo paleocontinent, the older belonging to the arc stage, whilst the younger records late to post-collisional magmatism that marks the end of the orogeny.

The maximum depositional age yielded for the basal schists of the Costa Sena sequence (2112 ± 7 Ma) confirm that the Felício pluton could be Paleoproterozoic sedimentary supply source for the foreland basin. The youngest zircon found in our study (1980 ± 36 Ma) overlaps that of the Orosirian Mercês pluton and also of the alkaline intrusion from Gouveia (2043 ± 40 Ma; Dussin and Chemale Jr, 2012). The same is true for the Bandeirinha sample (maximum depositional age = 2093 ± 9 Ma; youngest zircon = 2000 ± 40 Ma).

4.7.5 An attempt at facies differentiation

Since the Costa Sena Group underwent chemical alteration and shearing of variable intensities, identifying the facies of the sequence is a challenge. We believe that the predominant preserved portion of the metavolcanosedimentary sequence is the record of the forebulge domains of the basin (see Figure 4.16). This may explain why the Costa Sena Group sequence is composed chiefly of metasedimentary rocks (ca. 99 %) with very subordinate meta-volcanites since the magmatic arc would have been on the other side of the basin.

4.7.5.1 The coarse-grained porphyroclastic facies

The coarse-grained porphyroclastic facies is composed of usually fragmented quartz porphyroclasts up to 1 cm that can be pale pink, gray, or colorless. The matrix is composed predominantly of fine- to coarse-grained recrystallized quartz and muscovite, with or without lazulite, kyanite, and tourmaline blasts.

The geochemical results of trace elements and REE show that the kyanite/lazulite-bearing schists with quartz porphyroclasts have UCC and Cl chondrite normalized patterns consistently akin to those of the Gouveia leucogranite (Figure 4.4), except for the depleted values of CaO, Na_20, MgO, MnO. It suggests that these schists facies may be the result of metamorphism of mainly chemically leached granite sediments that underwent minor or no transportation and mechanical sorting: *i.e.* a residual and/or alluvial/colluvial paleosol.

According to (DeCelles, 2012), nonmarine forebulges are characterized by zones of intense pedogenesis, karstification (if carbonatic), and fluvial erosion. The basement is expected to be faulted and fractured due to flexure on the foreland lithosphere, which can speed up weathering processes. If aggradation occurs on the forebulge crest, the rates of accumulation are very slow and sediments are likewise intensely weathered and condensed (Crampton and Allen, 1995; DeCelles, 2012).

Also, due to the low topographic gradient between the forebulge and foredeep, small variations on the base level can lead to the precipitation of evaporites in a tropical climate. Morteani et al. (2001) carried out a study of aluminophosphates from the Costa Sena sequence and conclude that the lazulite/augelite bearing layers were probably phosphorus- and boron-rich clay-bearing sandstone deposited in an alkaline sabkha-like environment.

In the Barão do Guaicuí Formation sequence, tourmaline is found (i) dispersed in the rock, oriented or not, following the schistosity; (ii) as porphyroblasts, disseminated throughout the rock; (iii) as stratiform fine-grained tourmalinite layers; (iv) in very fine laminated bedding; and (v) in veins crosscutting the rocks. Tourmaline group minerals are perhaps the most important repository for boron in the earth’s crust. With a wide stability range, tourmaline can be found from low P-T environments (<150°C, 1Mpa) to high-T (>850°C) and ultra-high pressure conditions (4 GPa; Henry and Dutrow, 2018). Therefore, it is found in a broad variety of rocks. As many elements can enter into complex structure of tourmaline, it can inherit the environmental signature of where it crystallized (if undeformed) and has been used as a petrogenetic indicator (*e.g.* Henry and Dutrow, 1996; Van Hinsberg and Schumacher, 2011; Von Goerne *et al.*, 1999). Monteiro et al. (2019) studied tourmaline from the Costa Sena Group region and identified species from X-site vacant and alkalic groups (dravite and Mg-foitite) associated with REE-rich phosphate (Ce-florencite). They found a tourmaline signature identical to that of the meta-evaporitic derived Gurumanas tourmalinites of Namibia (Henry *et al.*, 2008). The literature on stratiform tourmalinites points to origin mainly related to pre-metamorphic evaporitic and exalative hydrothermal systems (*e.g.* Henry *et al.*, 2008; Henry and Dutrow, 2018; Pesquera and Velasco, 1997).

Another intriguing question is from where does the pink quartz come from? The supposed Gouveia leucogranite protolith does not have such quartz, neither does any other known lithology in the region except for the Bandeirinha quartzites. In the latter, however, the color does not come from the quartz itself, but from an iron oxide coating that wraps the grains. There are a number of mechanisms that could impart color to pure quartz of the leucogranite, such as (i) the formation of hole centers due to defects in crystal lattice; (ii) element substitution;

(iii) IVTC (intervalence charge transfer); (iv) submicroscopic inclusion of a separate mineral phase (dumortierite-related) within the quartz; (v) and trace elements occupying open spaces in the structure (Clifford, 2012). This situation seems to be a great opportunity to study the unclear rose quartz issue since both the product and the protolith can be found naturally, and the most likely driven processes are known (chemical weathering and/or the mylonitization).

4.7.5.2 Type I schist facies (distal forebulge)

Schists without porphyroclasts would represent those facies where the transportation and mechanical sorting played a more important role, representing deposition sites farther from the source(s). The dominantly fine-grained and mica-rich schists would represent deposition in deeper portions of the basin, whilst the coarse-grained quartz-rich schists, quartzites, and metaconglomerates would represent products of deposition in shallow water, transitional, and continental environments. Although the sources of the sediments could be many, it is reasonable to assume that the underlying basement rocks and the contemporaneous plutonics/volcanites were significantly predominant.

The geochemical results of trace element and REE analysis of schists without porphyroclasts and with similar proportions of quartz and mica allow a preliminary differentiation between two types (and the transition between them). The first, named as “Type I schist”, shows strong REE with high La_{CN}/Lu_{CN} ratios and high LREE content. Since the REE patterns and contents resemble those of the Mercês pluton, or the alkaline intrusion from Gouveia region and the Gouveana suite, it is more likely that Type I schists have a dominantly Paleoproterozoic contribution (LREE-rich) from basement rocks, although the metarhyolites from the Pedro Pereira metavolcanosedimentary sequence (also basement) may have likewise contributed.

4.7.5.3 Type II schist facies (proximal forebulge)

On the other hand, “Type II” schists show weaker REE fractionation, with moderate La_{CN}/Lu_{CN} ratios that are akin to the Gouveia leucogranite ratios. Also, the HREE show a tendency to flattened patterns, just like the granitic patterns. It is, therefore, reasonable to assume that they represent a dominant basement contribution (closer to the forebulge) instead of Rhyacian/Orosirian rocks from the volcanic front. The slightly lower REE contents may be explained by the quartz dilution effect (Taylor and McLennan, 1985).

4.7.5.4 Banded iron formation (BIF)

Though scarce, BIFs have been reported from foreland basins (*e.g.* Bontognali *et al.*, 2013; Cotter and Link, 1993; Li and Kusky, 2007). Barão do Guaicuí *stricto sensu* BIFs are erratic and are locally found in the Guinda and Costa Sena areas (Figure 4.1), although millimetric hematite-rich levels are a common feature of the Barão do Guaicuí schists. The forebulge-foredeep transition is the most likely environment for iron precipitation due to a condensing sedimentary regime. The sediment starved facies is characterized by low sediment accumulation rates and silica authigenesis on the basin floor (Föllmi, 2016); BIF would be deposited during times of decreased clastic sediment supply. The BIF could not have been formed in the foredeep, because its associated rocks are too immature for a flysch-like deposit, nor at the wedge-top due to the high energy of the system.

4.7.5.5 Meta-ruditic facies

The texturally and mineralogically imature metaconglomerates and coarse-grained metarenites would represent facies of high energy and low transportation of sediments, which are compatible with common fault-driven syn-tectonic debris flows that occur in the very proximal regions of the basin, in the deformation front (top-wedge basin).

4.7.5.6 Fine banded schist

The banded medium to fine-grained schists rich in muscovite and fine quartz grains with variable amount of kyanite would represent facies of low energy and episodic sedimentation, compatible to the region of transition to foredeep facies.

4.7.6 Mass transfer calculations

We used the Isocon method (Grant, 2005, 1986) to illustrate the Gresens's mass transfer equation (Gresens, 1967) and visualize the quantified gains and losses of elements, as a result of the Gouveia alkali-granite alteration to the porphyroclastic schist using the equation

$$C_i^0 = \frac{M^0}{M^A} \times \left(C_i^A + \Delta C_i\right)$$

where C_i is the concentration of species i, and A and O stand for the altered and original rocks, respectively. M^A and M^O are the equivalent masses before and after alteration, and ΔC_i is the variation of species i concentration.

Considering $\Delta C_i = 0$ for immobile elements, which show no gain or loss of mass, the equation simplifies to

$$C_i^0 = \left(\frac{M^0}{M^A}\right) \times C_i^A$$

which is the Isocon line equation. Using immobile elements such REE and traces we can define the slope (M^O/M^A) and calculate/visualize gains and losses of the mobile elements. The average of the Gouveia alkali-granite (data from Chaves and Coelho, 2013) was taken as the original rock, while the average of the porphyroclastic schists was taken as the altered product. An Isocon with a slope of 1.06 (regression index = 0.999226) was defined by cluster slopes between 1.02 and 0.99 from Sn, Zr, Hf, SiO_2 Yb, Er, and Ho.

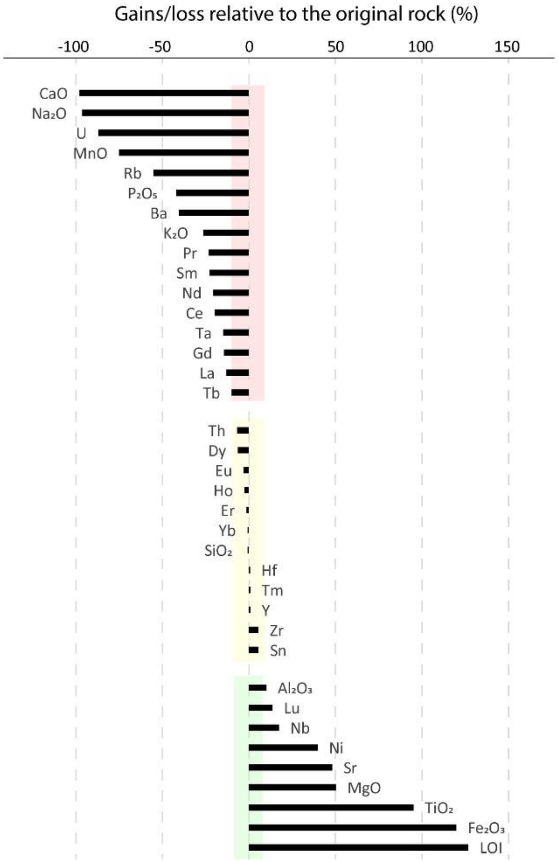

Figure 4.15 Gains and losses for the alteration from alkali-granite (Gouveia leucogranite) to the porphyroclastic schist (Barão do Guaicuí Formation) based on Isocon method of Grant (2005, 1986). The red bar encompasses the losses, while the yellow and green, the immobile elements and the gains, respectively.

Figure 4.15 synthesizes the estimated element gains and losses quantitatively obtained through the mass transfer calculations. The alkali and alkaline earth elements (with the exception of magnesium and strontium) are strongly depleted, showing losses between 30 % and 100 %. The increase of the LOI value (larger than 100 %) may reflect primary alteration when hydrous minerals are formed. Elements such as Ti, Nb, and Al, which are usually considered to be immobile in fluids close to pure water show concentration increase towards the alteration product. Ti and Nb are accommodated by rutile in the alteration product.

4.7.7 The “Gouveia Anticlinorium”

The Gouveia Anticlinorium, first described by Pflug (1965), is a regional scale antiform that has in its core the Archean basement and supracrustal rocks of the Costa Sena Group, bordered by the Espinhaço Supergroup rocks. Cruz et al. (2005) assign the nucleation of this structure to the Neoproterozoic Brasiliano event. They studied N-S direction reverse shear zones with 60° dip within the Gouveia Anticlinorium. As this angle is unusual for thrusts, they attributed this to the foliation of the Gouveia leucogranite, which has approximately the same orientation as the high dip-angle shear zones. However, an alternative hypothesis for both the nucleation of the Gouveia Anticlinorium and the shear zones would involve a Paleoproterozoic perspective. The Costa Sena Group facies point to deposition mainly in the forebulge sector of a foreland basin. As the sequence crops out in both eastern and western flanks of the Gouveia Anticlinorium (Figure 4.1), it is possible to conjecture that the regional fold is the forebulge itself (assuming the unit as autochthonous). This could explain why the basement is so high in that region, in particular. Multiple cases show that tensional settings commonly control forebulge domains, leading to the development of normal fault systems concurrently with uplift (Bradley and Kidd, 1991; DeCelles and Giles, 1996; Reis *et al.*, 2017). So, maybe the high angle dip shear zones are Paleoproterozoic faults reactivated during the Neoproterozoic compression, which could uplift even more the bulge structure (see Figure 4.16 for a view of Paleoproterozoic settings).

4.7.8 Neoproterozoic Shearing (Brasiliano event)

The Archean granitoids from the Gouveia Complex and the quartzites from the Espinhaço Supergroup commonly develop highly heterogeneous deformation in response to stress, centered in relatively thin shear bands. The Barão do Guaicuí schists also accommodate deformation heterogeneously, particularly in detachment zones where the mechanical contrast with the Gouveia Complex rocks is clear. As this sheared basement-cover contact is regional in scale, shear features are common at the borders of the Gouveia anticlinorium (Simone Cerqueira Pereira Cruz *et al.*, 2005; Kuchenbecker and Sanglard, 2018).

However, the mylonitic character of the Barão do Guaicuí schists is very pervasive and indicates deformation that is, to a certain point, homogeneous, especially in the coarse-grained schists, far from the effect of the localized shear bands. By and large, the rocks exhibit blastomylonitic texture with quartz grains frequently stretched, in a lepidoblastic matrix of muscovite and/or sericite, and with aggregates of dynamically recrystallized quartz subgrains. The anastomosed foliation wraps the quartz grains (which often display pressure shadows) in a sigmoidal shape that consistently indicates top movement to the west with down-dip to slightly oblique lineation easily found in almost all outcrops.

These features indicate that the whole sequence underwent non-coaxial deformation of a roughly similar intensity. The most likely mechanism that could cause such deformation is shearing of the entire sequence between the more competent granitic basement and the quartzitic rocks of the Espinhaço Supergroup. The competent rocks transferred strain dissipation to the schists, which following Tapponier and Molnar (1976) greatly reduced the energy necessary to uplift the Espinhaço Meridional sector of the Araçuaí fold and thrust belt, offsetting the competent quartzite layers instead of internally deforming them. In this model, the pervasive mylonitic foliation of the shists cannot have been formed by the Paleoproterozoic event, but during the Neoproterozoic event.

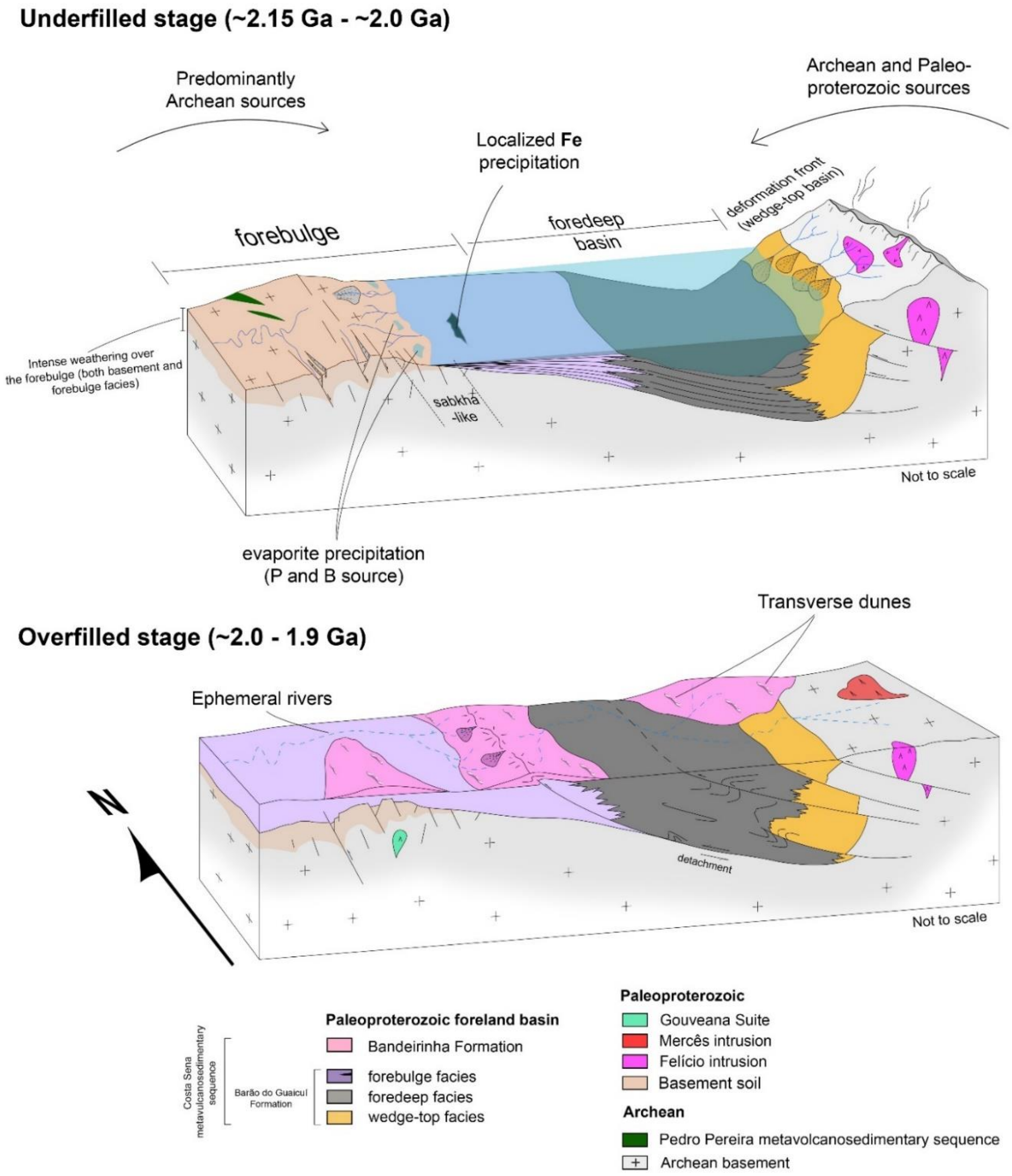

Figure 4.16 Schematic block diagram of the Costa Sena foreland basin and its depositional environments.

4.8 Conclusion

Questions have been raised about the Costa Sena metavolcanosedimentary sequence origin. Our geochronologic and geochemical data suggest that the sequence was deposited around 2.06 Ga under a collisional setting, in a foreland basin related to Paleoproterozoic orogenesis. The findings also suggest that kyanite-rich schists in part of the sequence result from metamorphism of previously altered basement saprolite/soil. The remaining schists are metamorphic products of sediments from varied facies of a foreland basin, with contribution from the Gouveia leucogranite and alkaline sources. Geochronological data from Bandeirinha Formation metabreccia from the place where the unit was defined showed a maximum depositional age peak of 2093 ± 9 Ma, which confirms its assignment to the Costa Sena Group as originally interpreted.

4.9 Declaration of interest statement

The authors declare that they have no known competing financial interests or personal relationships that could have appeared to influence the work reported in this paper.

4.10 Acknowledgements

This work was financially supported by Conselho Nacional de Desenvolvimento Científico e Tecnológico (CNPq; grant # 205254/2016-4) and NGU/CPMTC-UFMG. The first author thanks FAPEMIG for providing the Ph.D. scholarship. M.K. is a fellow of the Brazilian Research Council and acknowledges its support (grant # 309106/2017–6).

5 CONCLUSÕES

No contexto da geologia da Serra do Espinhaço, as sequências pré-estaterianas são frequentemente alvo de controvérsias, em parte devido à complexidade geológica envolvida nos poucos registros fragmentados, comumente sobrepostos por eventos deformacionais diversos. Nas últimas duas décadas, com a facilitação do acesso a ferramentas robustas como a geocronologia e geoquímica, trabalhos envolvendo a geologia pré-estateriana nas regiões Nordeste e Sudeste do Brasil ganharam novo fôlego, intensificando a disponibilidade de dados e interpretações acerca do tema.

Uma das questões levantada nos últimos anos diz respeito ao Grupo Pedro Pereira. Inicialmente definido como uma sequência ultramáfica arqueana, foi recentemente imaginado como membro de um sistema paleoproterozoico de deposição de ferro (Rosière *et al.*, 2019). Entretanto, zircões extraídos de metariolito intercalado em BIF do G. Pedro Pereira produziram idade de cristalização em 2.77 Ga, coincidente com aquelas idades encontradas para os greenstone belts Rio das Velhas (*e.g.* Machado *et al.*, 1992; Noce *et al.*, 2005) e Pitangui (*e.g.* Brando Soares *et al.*, 2017; Verma *et al.*, 2017). Em adição, as análises geoquímicas apontam para um ambiente de precipitação localmente oxigenado, coincidente com situação descrita no greenstone belt de Pitangui. Assim, o cráton do São Francisco registra algumas das evidências mais antigas do início da oxigenação dos oceanos, mais de 250 milhões de anos anteriormente ao Grande Evento de Oxidação.

O Grupo Costa Sena também tem sido alvo de diversas controvérsias nas últimas décadas. Os xistos da Formação Barão do Guaicuí possuem conspícua textura milonítica que pode ser vista em praticamente todos os afloramentos, frequentemente associada à uma lineação de estiramento mineral com caimento para E. Posicionado usualmente entre rochas reologicamente mais competentes (sotoposto por granito e sobreposto por quartzitos), os xistos da Fm. Barão do Guaicuí parecem ter funcionado como uma grande superfície de cisalhamento que absorveu considerável parte da deformação durante o evento compressivo Brasiliano, tendo todo o pacote sofrido deformação não-coaxial, da base ao topo. Essa deformação, além de obliterar as estruturas primárias, conferiu à rocha a textura milonítica relativamente homogênea que dificulta a discriminação entre as variações de xistos em campo.

Para suplementar as observações de campo, espectros de idades de zircões detríticos de xisto e parametaconglomerado foram levantados e, em conjunto com os dados geoquímicos, sugerem que a sequência metavulcanossedimentar Costa Sena foi depositada em ambiente geotectônico colisional, em uma bacia de antepaís. As assinaturas geoquímicas de parte dos xistos indicam contribuição de fontes extremamente enriquecidas em ETR leves, compatíveis com valores para rochas calci-alcalinas. Outros xistos tem assinatura de ETR compatíveis com os valores do embasamento local, o leucogranito de Gouveia, sua provável fonte dominante. Ainda com base em geoquímica de variados litotipos da Formação Barão do Guaicuí e de rochas de outras unidades do mesmo contexto geológico, esta tese propõe uma diferenciação: (i) os xistos porfiroclásticos, com grãos pórfiros de quartzo rosa, roxo ou incolor, além da variada quantidade de cianita, representaria o metamorfismo sobre produtos de alteração do embasamento que teriam sofrido pouquíssimo ou nenhum transporte (arcóseos eluviais alterados ou/e saprólitos); (ii) os xistos com níveis ricos em cianita, que podem chegar a constituir verdadeiros cianititos, representariam o metamorfismo sobre paleossolos de frequentes episódios de exposição sub aérea da região *forebulge* da bacia em condições de clima quente e úmido, região de provável precipitação de evaporitos ricos em boro; (iii) os xistos de granulação fina com bandas de coloração alternadas representariam termos transicionais entre a região *forebulge* e *foredeep* da bacia, local de baixa energia também propício para a precipitação de formações ferríferas locais. Para o topo, os metassedimentos quartzosos, por vezes rudíticos, representariam a progradação e avanço do front deformacional sobre o espaço de acomodação, até a colmatação da bacia. As amostras de xisto e metaparaconglomerado da Fm. Barão do Guaicuí têm população de zircões mais nova em 2070 ± 23 Ma (idade discórdia) e 2112 ± 7 Ma (pico estatístico de probabilidade, n=37), respectivamente, definindo uma idade máxima de deposição em 2070 Ma. Os dados isotópicos de zircão detrítico da amostra de metabrecha da Formação Bandeirinha em sua área-tipo produziram pico estatístico mais novo em 2093 ± 9 Ma (n=98), sendo que a idade do spot mais novo foi 2000 ± 40 Ma. Estes dados, compatíveis com a definição original de (Fogaça *et al.*, 1984), fortalecem a concepção de origem paleoproterozoica da sequência e sugerem a manutenção da Formação Bandeirinha dentro do Grupo Costa Sena.

Mais ao norte, na Serra do Espinhaço Central, aflora a sequência metavulcanossedimentar Riacho dos Machados. A idade da unidade foi adquirida em zircões de hornblendito, que definem idade de cristalização em 2070 Ma (Leal *et al.*, 2021). A geoquímica das rochas da unidade indica que a sequência foi depositada um bacia back-arc. Apesar do caráter geotectônico inicialmente extensional, ambas as sequências Riacho dos Machados e Costa Sena são consequência de uma zona de subducção de mesma idade (~2.07 Ga), com placa subductante mergulhando sentido oeste atual, com linha de sutura direção N-S, inferida a partir da estruturação de ambas unidades. Este grupo de bacias, potencialmente correlacionáveis do ponto de vista tectônico, apresentam-se como registros sedimentares de complexos processos orogenéticos riacianos/orosirianos que culminaram na edificação de extensa(s) cadeia(s) de montanhas entre os blocos Gavião/Guanambi-Correntina e Bloco Gabão (*e.g.* Alkmim, 2004; Barbosa *et al.*, 2020).

6 REFERÊNCIAS

Aguilar, C., Alkmim, F.F., Lana, C., Farina, F., 2017. Palaeoproterozoic assembly of the São Francisco craton, SE Brazil: New insights from U–Pb titanite and monazite dating. Precambrian Res. 289, 95–115. https://doi.org/10.1016/j.precamres.2016.12.001

Alexander, B.W., Bau, M., Andersson, P.S., Dulski, P., 2008. Continentally-derived solutes in shallow Archean seawater: Rare earth element and Nd isotope evidence in iron formation from the 2.9 Ga Pongola Supergroup, South Africa. Geochim. Cosmochim. Acta 72, 378–394. https://doi.org/10.1016/j.gca.2007.10.028

Alibo, D.S., Nozaki, Y., 1999. Rare earth elements in seawater: Particle association, shale-normalization, and Ce oxidation. Geochim. Cosmochim. Acta 63, 363–372. https://doi.org/10.1016/S0016-7037(98)00279-8

Alkmim, F.F. de, 2004. O que faz de um cráton um cráton? O cráton do São Francisco e as revelações almeidianas ao delimitá-lo, in: Geologia Do Continente Sul-Americano: Evolução e Obra de Fernando Flávio Marques de Almeida. pp. 17–35.

Alkmim, F.F. de, Teixeira, W., 2017. The Paleoproterozoic Mineiro Belt and the Quadrilátero Ferrífero, in: São Francisco Craton, Eastern Brazil: Tectonic Genealogy of a Miniature Continent. pp. 71–94. https://doi.org/10.1007/978-3-319-01715-0

Alkmim, F.F., 1995. O Anticlinório de Gouveia: exemplo de culminação antiformal nucleada pelo embasamento. SIMPÓSIO Geol. MINAS GERAIS 8, 1–2.

Alkmim, F.F., Kuchenbecker, M., Reis, H.L.S., Pedrosa-Soares, A.C., 2017. The Araçuaí Belt, in: Heilbron, M., Cordani, U.G., Alkmim, F.F. (Eds.), São Francisco Craton, Eastern Brazil: Tectonic Genealogy of a Miniature Continent. Springer International Publishing, Cham, pp. 255–276. https://doi.org/10.1007/978-3-319-01715-0_14

Alkmim, F.F., Marshak, S., 1998. Transamazonian Orogeny in the Southern São Francisco Craton Region, Minas Gerais, Brazil: Evidence for Paleoproterozoic collision and collapse in the Quadrilátero Ferrífero. Precambrian Res. 90, 29–58.

Alkmim, F.F., Marshak, S., Pedrosa-Soares, A.C., Peres, G.G., Cruz, S.C.P., Whittington, A., 2006. Kinematic evolution of the Araçuaí-West Congo orogen in Brazil and Africa: Nutcracker tectonics during the Neoproterozoic assembly of Gondwana. Precambrian Res. 149, 43–64. https://doi.org/10.1016/j.precamres.2006.06.007

Allen, J.R., Allen, P.A., 2005. Basin Analysis: Principles and Application, Second. ed, Blackwell Publishing. Blackwell Publishing.

Allen, P.A., Crampton, S.L., Sinclair, H.D., 1991. The inception and early evolution of the north Alpine foreland basin, Switzerland. Basin Res. 3, 143–163. https://doi.org/10.1111/j.1365-2117.1991.tb00124.x

Almeida-Abreu, P.Â., 1993. A evolução geodinâmica da Serra do Espinhaço Meridional, Minas Gerais, Brasil. Freiburg University.

Almeida-Abreu, P.Â., 1995. O Supergrupo Espinhaço Da Serra Do Espinhaço Meridi-Onal (Minas Gerais): O Rifte , a Bacia E O Orógeno. Geonomos 3, 1–18.

Almeida, F.F.M., 1981. O Craton do Paramirim e suas relações com o do São Francisco, in: Anais Do Simpósio Sobre o Cráton Do São Francisco e Suas Faixas Marginais. pp. 1–10.

Anders, E., Grevesse, N., 1989. Abundances of the elements: Meteoritic and solar. Geochim. Cosmochim. Acta 53, 197–214. https://doi.org/10.1016/0016-7037(89)90286-X

Andersson, P.S., Wasserburg, G.J., Chen, J.H., Papanastassiou, D.A., Ingri, J., 1995. 238U234U and 232Th230Th in the Baltic Sea and in river water. Earth Planet. Sci. Lett. 130, 217–234. https://doi.org/10.1016/0012-821X(94)00262-W

Andrews, J.E., Brimblecombe, P., Jickells, T.D., Liss, P.S., Reid, B., 2004. An Introduction to Environmental Chemistry, Second edi. ed, Journal of Environment Quality. Blackwell Science, Malden, USA.

Angeli, N., Penha, U.C., Knauer, L.G., Ito, G.M., 2011. The Rio Mata Cavalo Group : the gold mineralization and its origin 301–310.

Anhaeusser, C.R., 2014. Archaean greenstone belts and associated granitic rocks - A review. J. African Earth Sci. 100, 684–732. https://doi.org/10.1016/j.jafrearsci.2014.07.019

Araújo, J.C.S., Lobato, L.M., 2019. Depositional model for banded iron formation host to gold in the Archean Rio das Velhas greenstone belt, Brazil, based on geochemistry and LA-ICP-MS magnetite analyses. J. South Am. Earth Sci. 94, 102205. https://doi.org/10.1016/j.jsames.2019.05.021

Araújo, R.G., Leal, V.L.S., 2017. Mapeamento Geológico em Escala 1 : 25 . 000 da Região Oeste do Município de Riacho dos Machados – MG. Belo Horizonte.

Baltazar, O.F., Zucchetti, M., 2007. Lithofacies associations and structural evolution of the Archean Rio das Velhas greenstone belt, Quadrilátero Ferrífero, Brazil: A review of the setting of gold deposits. Ore Geol. Rev. 32, 471–499. https://doi.org/10.1016/j.oregeorev.2005.03.021

Barbosa, J.S.F., Dominguez, J.M.L., 1996. Geologia da Bahia: texto explicativo para o mapa geológico ao milionésimo. Salvador Secr. da Indústria, Comércio e Mineração. Supt. Geol. e Recur. Minerais.

Barbosa, J.S.F., Sabaté, P., 2004. Archean and Paleoproterozoic crust of the São Francisco Craton, Bahia, Brazil: Geodynamic features. Precambrian Res. 133, 1–27. https://doi.org/10.1016/j.precamres.2004.03.001

Barbosa, N., Menezes Leal, A.B., Debruyne, D., Bastos Leal, L.R., Barbosa, N.S., Marinho, M., Mercês, L., Barbosa, J.S., Koproski, L.M., 2020. Paleoarchean to Paleoproterozoic crustal evolution in the Guanambi-Correntina block (GCB), north São Francisco Craton, Brazil, unraveled by U-Pb Geochronology, Nd-Sr isotopes and geochemical constraints. Precambrian Res. 340, 105614. https://doi.org/10.1016/j.precamres.2020.105614

Bau, M., 1993. Effects of syn- and post-depositional processes on the rare-earth element distribution in Precambrian iron-formations. Eur. J. Mineral. 5, 257–268. https://doi.org/10.1127/ejm/5/2/0257

Bau, M., 1996. Controls on the fractionation of isovalent trace elements in magmatic and aqueous systems: Evidence from Y/Ho, Zr/Hf, and lanthanide tetrad effect. Contrib. to Mineral. Petrol. 123, 323–333. https://doi.org/10.1007/s004100050159

Bau, M., Alexander, B.W., 2009. Distribution of high field strength elements (Y, Zr, REE, Hf, Ta, Th, U) in adjacent magnetite and chert bands and in reference standards FeR-3 and FeR-4 from the Temagami iron-formation, Canada, and the redox level of the Neoarchean ocean. Precambrian Res. 174, 337–346. https://doi.org/10.1016/j.precamres.2009.08.007

Bau, M., Dulski, P., 1996. Distribution of yttrium and rare-earth elements in the Penge and Kuruman iron-formations, Transvaal Supergroup, South Africa. Precambrian Res. 79, 37–55. https://doi.org/10.1016/0301-9268(95)00087-9

Bekker, A., Krapež, B., Slack, J.F., Planavsky, N., Hofmann, A., Konhauser, K.O., Rouxel, O.J., 2012. Iron formation: The sedimentary product of a complex interplay among mantle, tectonic, oceanic, and biospheric processes-a reply. Econ. Geol. 107, 379–380. https://doi.org/10.2113/econgeo.107.2.379

Bekker, A., Slack, J.F., Planavsky, N., Krapež, B., Hofmann, A., Konhauser, K.O., Rouxel, O.J., 2010. Iron formation: The sedimentary product of a complex interplay among mantle, tectonic, oceanic, and biospheric processes. Econ. Geol. 105, 467–508. https://doi.org/10.2113/gsecongeo.105.3.467

Bersan, S.M., de Oliveira Costa, A.F., Danderfer, A., de Abreu, F.R., Lana, C., Queiroga, G., Storey, C., Moreira, H., 2020. Paleoproterozoic juvenile magmatism within the northeastern sector of the São Francisco paleocontinent: Insights from the shoshonitic high Ba–Sr Montezuma granitoids. Geosci. Front. 11, 1821–1840. https://doi.org/10.1016/j.gsf.2020.01.017

Bhatia, M.R., 1983a. Plate Tectonics and Geochemical Composition of Sandstones. J. Geol. 91, 611–627. https://doi.org/10.1086/628815

Bhatia, M.R., 1983b. Plate Tectonics and Geochemical Composition of Sandstones. J. Geol. 91, 611–627. https://doi.org/10.1086/628815

Biondi, J.C., Schrank, A., Pinheiro, J.C. de F., 1978. Basitos e ultrabasitos do Espinhaço Meridional e região sul de Minas Gerais, in: Anais Do XXX Congresso Brasileiro de Geologia. Recife.

Bolhar, R., Kamber, B.S., Moorbath, S., Fedo, C.M., Whitehouse, M.J., 2004. Characterisation of early Archaean chemical sediments by trace element signatures. Earth Planet. Sci. Lett. 222, 43–60. https://doi.org/10.1016/j.epsl.2004.02.016

Bolhar, R., Van Kranendonk, M.J., Kamber, B.S., 2005. A trace element study of siderite-jasper banded iron formation in the 3.45 Ga Warrawoona Group, Pilbara Craton - Formation from hydrothermal fluids and shallow seawater. Precambrian Res. 137, 93–114. https://doi.org/10.1016/j.precamres.2005.02.001

Bontognali, T.R.R., Fischer, W.W., Föllmi, K.B., 2013. Siliciclastic associated banded iron formation from the 3.2Ga Moodies Group, Barberton Greenstone Belt, South Africa. Precambrian Res. 226, 116–124. https://doi.org/10.1016/j.precamres.2012.12.003

Bookhagen, B., Strecker, M.R., 2008. Orographic barriers, high-resolution TRMM rainfall, and relief variations along the eastern Andes. Geophys. Res. Lett. 35, 1–6. https://doi.org/10.1029/2007GL032011

Borges, C.C.A., Toledo, C.L.B., Silva, A.M., Chemale, F., dos Santos, B.A., Figueiredo, F.L., Zacchi, É.N.P., 2020. Unraveling a hidden Rhyacian magmatic arc through provenance of metasedimentary rocks of the Crixás greenstone belt, Central Brazil. Precambrian Res. 353, 106022. https://doi.org/10.1016/j.precamres.2020.106022

Bosco-Santos, A., Gilhooly, W.P., Fouskas, F., Fabricio-Silva, W., Oliveira, E.P., 2020. Euxinia in the Neoarchean: The starting point for early oxygenation in a Brazilian Craton. Precambrian Res. 341, 105655. https://doi.org/10.1016/j.precamres.2020.105655

Bradley, D.C., Kidd, W.S.F., 1991. Flexural extension of the upper continental crust in collisional foredeeps. Geol. Soc. Am. Bull. 103, 1416–1438. https://doi.org/10.1130/0016-7606(1991)103<1416:FEOTUC>2.3.CO;2

Brando Soares, M., Corrêa Neto, A.V., Bertolino, L.C., Alves, F.E.A., de Almeida, A.M., Montenegro da Silva, P.H., Mabub, R.O. de A., Manduca, L.G., Araújo, I.M.C. de P., 2018. Multistage mineralization at the hypozonal São Sebastião gold deposit, Pitangui greenstone belt, Minas Gerais, Brazil. Ore Geol. Rev. 102, 618–638. https://doi.org/10.1016/j.oregeorev.2018.09.028

Brando Soares, M., Corrêa Neto, A.V., Zeh, A., Cabral, A.R., Pereira, L.F., Prado, M.G.B. do, Almeida, A.M. de, Manduca, L.G., Silva, P.H.M. da, Mabub, R.O. de A., Schlichta, T.M., 2017. Geology of the Pitangui greenstone belt, Minas Gerais, Brazil: Stratigraphy, geochronology and BIF geochemistry. Precambrian Res. 291, 17–41. https://doi.org/10.1016/j.precamres.2017.01.008

Brito Neves, B.B. de, Fuck, R.A., Pimentel, M.M., 2014. The Brasiliano collage in South America: A review. Brazilian J. Geol. 44, 493–518. https://doi.org/10.5327/Z2317-4889201400030010

Bruno, H., Elizeu, V., Heilbron, M., de Morisson Valeriano, C., Strachan, R., Fowler, M., Bersan, S., Moreira, H., Dussin, I., Guilherme do Eirado Silva, L., Tupinambá, M., Almeida, J., Neto, C., Storey, C., 2020a. Neoarchean and Rhyacian TTG-Sanukitoid suites in the southern São Francisco Paleocontinent, Brazil: Evidence for diachronous change towards modern tectonics. Geosci. Front. 11, 1763–1787. https://doi.org/10.1016/j.gsf.2020.01.015

Bruno, H., Heilbron, M., de Morisson Valeriano, C., Strachan, R., Fowler, M., Bersan, S., Moreira, H., Motta, R., Almeida, J., Almeida, R., Carvalho, M., Storey, C., 2020b. Evidence for a complex accretionary history preceding the amalgamation of Columbia: The Rhyacian Minas-Bahia Orogen, southern São Francisco Paleocontinent, Brazil. Gondwana Res. 92. https://doi.org/10.1016/j.gr.2020.12.019

Burbank, D.W., Beck, R.A., Mulder, T., 1996. The Himalayan foreland basin. World Reg. Geol. 149–190.

Burbank, D.W., Puigdefabregas, C., Anton Munoz, J., 1992. The chronology of the Eocene tectonic and stratigraphic development of the eastern Pyrenean foreland basin, northeast Spain. Geol. Soc. Am. Bull. 104, 1101–1120. https://doi.org/10.1130/0016-7606(1992)104<1101:TCOTET>2.3.CO;2

Burke, K., Kidd, W.S.F., Kusky, T.M., 1986. Archean Foreland Basin tectonics in the Witwatersrand, South Africa. Tectonics 5, 439–456. https://doi.org/10.1029/TC005i003p00439

Byrne, R.H., Sholkovitz, E.R., 1996. Chapter 158 Marine chemistry and geochemistry of the lanthanides. pp. 497–593. https://doi.org/10.1016/S0168-1273(96)23009-0

Cabanis, B., Lecolle, M., 1989. Le diagramme La/10-Y/15-Nb/8: un outil pour la discrimination des séries volcaniques et la mise en évidence des processus de mélange et/ou de contamination crustale. Comptes rendus l'Académie des Sci. Série 2, Mécanique, Phys. Chim. Sci. l'univers, Sci. la Terre 309, 2023–2029.

Cabral, A.R., Corrêa Neto, A.V., 2015. Empirical Bi8Te3 and Bi2Te from the São Sebastião Gold Deposit, Brazil: Implications for lode-gold mineralization in Minas Gerais. Can. Mineral. 53, 1061–1072. https://doi.org/10.3749/canmin.1500066

Cabral, A.R., Lehmann, B., Gomes, A.A.S., Pašava, J., 2016. Episodic negative anomalies of cerium at the depositional onset of the 2.65-Ga Itabira iron formation, Quadrilátero Ferrífero of Minas Gerais, Brazil. Precambrian Res. 276, 101–109. https://doi.org/10.1016/j.precamres.2016.01.031

Cabral, A.R., Wiedenbeck, M., Koglin, N., Lehmann, B., De Abreu, F.R., 2012. Boron-isotopic constraints on the petrogenesis of hematitic phyllite in the southern Serra do Espinhaço, Minas Gerais, Brazil. Lithos 140–141, 224–233. https://doi.org/10.1016/j.lithos.2012.01.011

Carvalho, A. de S., 1982. Geologia e gênese das mineralizações de quartzo no Espinhaço Meridional, Minas Gerais - Brasil. Universidade de Brasília.

Cawood, P.A., Hawkesworth, C.J., Dhuime, B., 2012. Detrital zircon record and tectonic setting. Geology 40, 875–878. https://doi.org/10.1130/G32945.1

Cederberg, J., Söderlund, U., Oliveira, E.P., Ernst, R.E., Pisarevsky, S.A., 2016. U-Pb baddeleyite dating of the Proterozoic Pará de Minas dyke swarm in the São Francisco craton (Brazil) – implications for tectonic correlation with the Siberian, Congo and North China cratons. Gff 138, 219–240. https://doi.org/10.1080/11035897.2015.1093543

Chaves, A. de O., Coelho, R.M., 2013. Petrografia, Geoquímica E Geocronologia Do Leucogranito Peraluminoso Do Complexo De Gouveia-Mg. Geonomos 21, 1–12. https://doi.org/10.18285/geonomos.v21i2.267

Chaves, A. de O., Coelho, R.M., Renger, F.E., Dussin, T.M., Azevedo, M. do R.M. de A., Ribeiro, S.M., 2014. Petrografia e Litoquímica do Magmatismo Tardi-orogênico Toleítico Alto-K e da Suíte Pós-colisional Alcalina Saturada em Sílica de Gouveia (MG). Geochim. Bras. 28, 117–130. https://doi.org/10.5327/Z0102-9800201400020001

Chaves, A. de O., Ernst, R.E., Söderlund, U., Wang, X., Naeraa, T., 2019. The 920–900 Ma Bahia-Gangila LIP of the São Francisco and Congo cratons and link with Dashigou-Chulan LIP of North China craton: New insights from U-Pb geochronology and geochemistry. Precambrian Res. 329, 124–137. https://doi.org/10.1016/j.precamres.2018.08.023

Chaves, M.L.D.S.C., Silva, M.C.R. Da, Chaves, A. de O., Dussin, T.M., 2012. Formações ferríferas bandadas no grupo Costa Sena (Gouveia: Minas Gerais, Brasil), in: Para Conhecer a Terra: Memórias e Notícias de Geociências No Espaço Lusófono. Imprensa da Universidade de Coimbra, pp. 251–260. https://doi.org/10.14195/978-989-26-0534-0_26

Chaves, M.L.D.S.C., Silva, M.C.R. Da, Scholz, R., Babinski, M., 2013. Grenvillian age magmatism in the Southern Espinhaço Range (Minas Gerais): evidence from U-Pb zircon ages. Brazilian J. Geol. 43, 477–486. https://doi.org/10.5327/Z2317-48892013000300005

Chemale Jr, F., Dussin, I.A., Alkmim, F.F., Martins, M.S., Queiroga, G., Armstrong, R., Santos, M.N. Dos, 2012. Unravelling a Proterozoic basin history through detrital zircon geochronology: The case of the Espinhaço Supergroup, Minas Gerais, Brazil. Gondwana Res. 22, 200–206. https://doi.org/10.1016/j.gr.2011.08.016

Chetty, D., Gutzmer, J., 2012. REE redistribution during hydrothermal alteration of ores of the Kalahari Manganese Deposit. Ore Geol. Rev. 47, 126–135. https://doi.org/10.1016/j.oregeorev.2011.06.001

Chiarini, A.P., 2001. Geologia da porção basal do "Greenstone Belt" de Piumhi-MG. Universidade de São Paulo, São Paulo. https://doi.org/10.11606/D.44.2001.tde-16072015-101156

Clifford, J.H., 2012. Connoisseur's Choice: Rose (Pink) Quartz Lavra da Pitorra, Laranjeiras, Galiléia Minas Gerais, Brazil. Rocks Miner. 87, 530–539. https://doi.org/10.1080/00357529.2012.728892

Collerson, K.D., Kamber, B.S., 1999. Evolution of the continents and the atmosphere inferred from Th-U-Nb systematics of the depleted mantle. Science (80-.). 283, 1519–1522. https://doi.org/10.1126/science.283.5407.1519

Condie, K.C., 1993. Chemical Composition and Evolution of the Upper Continental Crust : Contrasting Results from Surface and Shales. Chem. Geol. 104, 1–37. https://doi.org/10.1016/0009-2541(93)90140-E

Cordani, U.G., Pimentel, M.M., Araújo, C.*E.G.* de, Fuck, R.A., 2013. The significance of the -Transbrasiliano-Kandi tectonic corridor for the amalgamation of West Gondwana. Brazilian J. Geol. 43, 583–597. https://doi.org/10.5327/Z2317-48892013000300012

Cotter, E., Link, J.E., 1993. Deposition and diagenesis of Clinton ironstones (Silurian) in the Appalachian Foreland Basin of Pennsylvania. Geol. Soc. Am. Bull. 105, 911–922. https://doi.org/10.1130/0016-7606(1993)105<0911:DADOCI>2.3.CO;2

Crampton, S.L., Allen, P.A., 1995. Recognition of forebulge unconformities associated with early stage foreland basin development: example from the north Alpine foreland basin. Am. Assoc. Pet. Geol. Bull. 79, 1495–1514. https://doi.org/10.1306/7834da1c-1721-11d7-8645000102c1865d

Crosby, A.G., Fishwick, S., White, N., 2010. Structure and evolution of the intracratonic Congo Basin. Geochemistry, Geophys. Geosystems 11, 1–20. https://doi.org/10.1029/2009GC003014

Cruz, Simone C.P., Alkmim, F.F., Lagoeiro, L.E., 2005. Zona De Cisalhamento Do Núcleo Do Anticlinório De Gouveia , Processos Deformacionais. Rev. Bras. Geociências 35, 441–452.

Cruz, Simone Cerqueira Pereira, Alkmim, F.F., Lagoeiro, L.E., 2005. Zona de cisalhamento do núcleo do anticlinório de Gouveia, cordilheira do Espinhaço, MG: geometria, cinemática e processos deformacionais. Rev. Bras. Geociências 441–452. https://doi.org/10.25249/0375-7536.2005i441452

Cruz, S.C.P., Figueiredo Barbosa, J.S., Pinto, M.S., Peucat, J.J., Paquette, J.L., Santos de Souza, J., de Souza Martins, V., Júnior, F.C., Carneiro, M.A., 2016. The Siderian-Orosirian magmatism in the Gavião Paleoplate, Brazil: U–Pb geochronology, geochemistry and tectonic implications. J. South Am. Earth Sci. 69, 43–79. https://doi.org/10.1016/j.jsames.2016.02.007

Cunha, J.C., Fróes, R.J.B., 1994. Komati{\i}tos com textura spinifex do Greenstone belt de Umburanas, Bahia. Salvador. Série Arq. Abertos, Cia. Baiana Pesqui. Miner. 29p.

D'Agrella-Filho, M.S., Cordani, U.G., 2017. The Paleomagnetic Record of the São Francisco-Congo Craton, in: Heilbron, M., Cordani, U.G., Alkmim, F.F. de (Eds.), São Francisco Craton, Eastern Brazil: Tectonic Genealogy of a Miniature Continent. Springer International Publishing, pp. 305–320.

Danielson, A., Möller, P., Dulski, P., 1992. The europium anomalies in banded iron formations and the thermal history of the oceanic crust. Chem. Geol. 97, 89–100. https://doi.org/10.1016/0009-2541(92)90137-T

De Baar, H.J.W., Brewer, P.G., Bacon, M.P., 1985. Anomalies in rare earth distributions in seawater: Gd and Tb. Geochim. Cosmochim. Acta 49, 1961–1969. https://doi.org/10.1016/0016-7037(85)90090-0

DeCelles, P.G., 2012. Foreland Basin Systems Revisited: Variations in Response to Tectonic Settings, in: Tectonics of Sedimentary Basins. John Wiley & Sons, Ltd, Chichester, UK, pp. 405–426. https://doi.org/https://doi.org/10.1130/0016-7606

DeCelles, P.G., Giles, K.A., 1996. Foreland basin systems. Basin Res. 8, 105–123. https://doi.org/10.1046/j.1365-2117.1996.01491.x

Degler, R., Pedrosa-Soares, A.C., Novo, T., Tedeschi, M., Silva, L.C., Dussin, I., Lana, C., 2018. Rhyacian-Orosirian isotopic records from the basement of the Araçuaí-Ribeira orogenic system (SE Brazil): Links in the Congo-São Francisco palaeocontinent. Precambrian Res. 317, 179–195. https://doi.org/10.1016/j.precamres.2018.08.018

Dossin, I.A., Chaves, M.L.D.S.C., Uhlein, A., 1985. Geologia e depósitos diamantíferos da região de Sopa, Diamantina, MG, in: Anais Do III Simpósio de Geologia de Minas Gerais. Belo Horizonte.

Dossin, I.A., Dossin, T.M., Chaves, M.L.D.S.C., 1990. Compartimentação estratigráfica do supergrupo Espinhaço em Minas Gerais - os grupos Diamantina e Conselheiro Mata. Rev. Bras. Geociências 20, 178–186.

Duque, T.R.F., Alkmim, F.F., Lana, C.D.C., 2020. Grãos detríticos de zircão do Grupo Itacolomi em sua área tipo, Quadrilátero Ferrífero, Minas Gerais: idades, proveniência e significado tectônico. Geol. USP. Série Científica 20, 101–123. https://doi.org/10.11606/issn.2316-9095.v20-151397

Dussin, I.A., Chemale Jr, F., 2012. Geologia estrutural e estratigrafia do Sistema Espinhaço-Chapada Diamantina e sua aplicação nas bacias mesocenozoicas da margem passiva brasileira, Authors ed. ed. Belo Horizonte.

Fabricio-Silva, W., Rosière, C.A., Bühn, B., 2019. The shear zone-related gold mineralization at the Turmalina deposit, Quadrilátero Ferrífero, Brazil: structural evolution and the two stages of mineralization. Miner. Depos. 54, 347–368. https://doi.org/10.1007/s00126-018-0811-7

Farina, F., Albert, C., Martínez Dopico, C., Aguilar Gil, C., Moreira, H., Hippertt, J.P., Cutts, K., Alkmim, F.F., Lana, C., 2016. The Archean–Paleoproterozoic evolution of the Quadrilátero Ferrífero (Brasil): Current models and open questions. J. South Am. Earth Sci. 68, 4–21. https://doi.org/10.1016/j.jsames.2015.10.015

Fernandez-Alonso, M., Tack, L., Tahon, A., De Waele, B., 2011. The Proterozoic history of the proto-Congo craton of central Africa, in: 23rd Colloquium of African Geology (CAG23). Johannesburg, p. 142.

Floyd, P.A., Leveridge, B.E., 1987. Tectonic environment of the Devonian Gramscatho basin, south Cornwall: framework mode and geochemical evidence from turbiditic sandstones. J. Geol. Soc. London. 144, 531–542. https://doi.org/10.1144/gsjgs.144.4.0531

Fogaça, A.C.C., 1982. Geologia e mineralizações auríeras da região de Costa Sena (Minas Gerais), UnB, Rel. Int. Brasília.

Fogaça, A.C.C., 1997. Geologia da Folha Diamantina, in: Projeto Espinhaço Em CD-ROM (Textos, Mapas e Anexos). pp. 1575–1665.

Fogaça, A.C.C., Almeida-Abreu, P.Â., Schorscher, H.D., 1984. Estratigrafia da sequência supracrustal arqueana na porção mediana-central da Serra do Espinhaço, MG, in: Anais Do XXXIII Congresso Brasileiro de Geologia. pp. 2654–2667.

Föllmi, K.B., 2016. Sedimentary condensation. Earth-Science Rev. 152, 143–180. https://doi.org/10.1016/j.earscirev.2015.11.016

Freimann, M.A., Knauer, L.G., Kuchenbecker, M., 2021. New geochronologic and geochemical constraints for the Pedro Pereira metavolcanosedimentary sequence: Evidence for a 2.77 Ga oxygen oasis record in the São Francisco-Congo paleocontinent. J. South Am. Earth Sci. 112, 103613. https://doi.org/10.1016/j.jsames.2021.103613

Fritzsons Jr, O., Biondi, J.C., Chaban, N., 1980. Geologia da região de Piumhi (MG), in: CONGRESSO BRASILEIRO DE GEOLOGIA. pp. 2906–2917.

Fryer, B.J., 1977. Rare earth evidence in iron-formations for changing Precambrian oxidation states. Geochim. Cosmochim. Acta 41, 361–367. https://doi.org/10.1016/0016-7037(77)90263-0

Fryer, B.J., 1983. Chapter 8 Part B. Rare Earth Elements in Iron-Formation, in: Iron-Formation Facts and Problems. pp. 345–358. https://doi.org/10.1016/S0166-2635(08)70048-3

Fu, X., Zhang, S., Li, Haiyan, Ding, J., Li, Huaikun, Yang, T., Wu, H., Yuan, H., Lv, J., 2015. New paleomagnetic results from the Huaibei Group and Neoproterozoic mafic sills in the North China Craton and their paleogeographic implications. Precambrian Res. 269, 90–106. https://doi.org/10.1016/j.precamres.2015.08.013

Ganade De Araujo, C.E., Rubatto, D., Hermann, J., Cordani, U.G., Caby, R., Basei, M.A.S., 2014. Ediacaran 2,500-km-long synchronous deep continental subduction in the West Gondwana Orogen. Nat. Commun. 5. https://doi.org/10.1038/ncomms6198

Gorlt, G., 1972. Fazieswechsel und Metamorphose in der weslichen Serra Negra (Espinhaço Zone, Minas Gerais, Brasilien). Geol. Rundschau 61, 166–201.

Grant, J.A., 1986. The isocon diagram-a simple solution to Gresens' equation for metasomatic alteration. Econ. Geol. 81, 1976–1982. https://doi.org/10.2113/gsecongeo.81.8.1976

Grant, J.A., 2005. Isocon analysis: A brief review of the method and applications. Phys. Chem. Earth 30, 997–1004. https://doi.org/10.1016/j.pce.2004.11.003

Gresens, R.L., 1967. Composition-volume relationships of metasomatism. Chem. Geol. 2, 47–65. https://doi.org/10.1016/0009-2541(67)90004-6

Grochowski, J., Kuchenbecker, M., Barbuena, D., Novo, T., 2021. Disclosing Rhyacian/Orosirian orogenic magmatism within the Guanhães basement inlier, Araçuaí

Orogen, Brazil: A new piece on the assembly of the São Francisco-Congo paleocontinent. Precambrian Res. 363, 106329. https://doi.org/10.1016/j.precamres.2021.106329

Grochowski, J.D., 2019. Os plútons Felício e Mercês: registros da orogênese riaciana/orosiriana no Bloco Guanhães. Universidade Federal dos Vales do Jequitinhonha e Mucurí.

Grossi-Sad, J.H., Roque, N.C., Knauer, L.G., Noce, C.M., Fonseca, E., 1997. Geologia da Folha Carbonita, in: Grossi-Sad, J.H., Lobato, L.M., Pedrosa-Soares, A.C., Soares-Filho, B.S. (Eds.), Projeto Espinhaço Em Cd-Rom (Textos, Mapas e Anexos). COMIG, Belo Horizonte, pp. 1251–1371.

Grujic, D., Coutand, I., Bookhagen, B., Bonnet, S., Blythe, A., Duncan, C., 2006. Climatic forcing of erosion, landscape, and tectonics in the Bhutan Himalayas. Geology 34, 801–804. https://doi.org/10.1130/G22648.1

Gugliotta, C., 2012. Inner vs. outer wedge-top depozone “ sequences” in the Late Miocene (late Tortonian-early Messinian) Sicilian Foreland Basin System; new data from the Terravecchia Formation of NW Sicily. J. Geodyn. 55, 41–55. https://doi.org/10.1016/j.jog.2011.11.002

Hagedorn, M.G., 2004. Contexto geotectônico da Serra do Espinhaço e domínios adjacentes a leste (Minas Gerais) com ênfase em aspectos geoquímicos e geocronológicos (doctoral dissertation). [s.n.], Rio Claro.

Harnois, L., 1988. The CIW index: A new chemical index of weathering. Sediment. Geol. 55, 319–322. https://doi.org/10.1016/0037-0738(88)90137-6

Harris, N.B.W., Pearce, J.A., Tindle, A.G., 1986. Geochemical characteristics of collision-zone magmatism. Geol. Soc. Spec. Publ. 19, 67–81. https://doi.org/10.1144/GSL.SP.1986.019.01.04

Hastie, A.R., Kerr, A.C., Pearce, J.A., Mitchell, S.F., 2007. Classification of altered volcanic island arc rocks using immobile trace elements: Development of the Th-Co discrimination diagram. J. Petrol. 48, 2341–2357. https://doi.org/10.1093/petrology/egm062

Heilbron, M., Cordani, U.G., Alkmim, F.F., 2017. The São Francisco Craton and Its Margins, in: Heilbron, M., Cordani, U.G., Alkmim, F.F. (Eds.), São Francisco Craton, Eastern Brazil: Tectonic Genealogy of a Miniature Continent. Springer International Publishing, Cham, pp. 3–13. https://doi.org/10.1007/978-3-319-01715-0_1

Heilbron, M., Duarte, B.P., Valeriano, C. de M., Simonetti, A., Machado, N., Nogueira, J.R., 2010. Evolution of reworked Paleoproterozoic basement rocks within the Ribeira belt (Neoproterozoic), SE-Brazil, based on U-Pb geochronology: Implications for paleogeographic reconstructions of the São Francisco-Congo paleocontinent. Precambrian Res. 178, 136–148. https://doi.org/10.1016/j.precamres.2010.02.002

Heilbron, M., Eirado, L.G., Almeida, J., 2016. Mapa geológico e de recursos minerais do estado do Rio de Janeiro.

Heineck, C.A., Leite, C.A.S., Silva, M.A. da, Vieira, V.S., 2003. Mapa Geológico de Minas Gerais, Escala 1: 1.000. 000. CPRM-Serviço Geológico do Bras. Belo Horiz.

Henry, D.J., Dutrow, B.L., 1996. Reviews in Mineralogy and Geochemistry. Rev. Mineral. Geochemistry 33, 503–557.

Henry, D.J., Dutrow, B.L., 2018. Tourmaline studies through time: Contributions to scientific advancements. J. Geosci. (Czech Republic) 63, 77–98. https://doi.org/10.3190/jgeosci.255

Henry, D.J., Sun, H., Slack, J.F., Dutrow, B.L., 2008. Tourmaline in meta-evaporites and highly magnesian rocks: perspectives from Namibian tourmalinites. Eur. J. Mineral. 20, 889–904. https://doi.org/10.1127/0935-1221/2008/0020-1879

Hensler, A.S., Hagemann, S.G., Rosière, C.A., Angerer, T., Gilbert, S., 2015. Hydrothermal and metamorphic fluid-rock interaction associated with hypogene “hard” iron ore mineralisation in the Quadrilátero Ferrífero, Brazil: Implications from in-situ laser ablation ICP-MS iron oxide chemistry. Ore Geol. Rev. 69, 325–351. https://doi.org/10.1016/j.oregeorev.2015.02.023

Hettich, M., 1973. Zur Stratigraphie und Genese des Macaúbas nördlich der Serra Negra, Espinhaço - Zone (Minas Geraes, Brasilien). Freiburg University.

Hoffmann, C., 1983a. The Archean Peraluminous Gouveia Granite, its structure, geochemistry, and phase petrology (Serra do Espinhaço, Minas Gerais, Brazil). Neues Jarhbvh Miner.Abh. 146, 151–169.

Hoffmann, C., 1983b. The Costa Sena Group - an early proterozoic supracrustal sucession and the evolution of the Southern Serra do Espinhaço, Minas Gerais, Brazil. Zbl. Geol. Paläont. Teil I, 446–458.

Holland, H.D., 2006. The oxygenation of the atmosphere and oceans. Philos. Trans. R. Soc. B Biol. Sci. 361, 903–915. https://doi.org/10.1098/rstb.2006.1838

Hsi, C.-K.D., Langmur, D., 1985. Adsorption of uranyl onto ferric oxyhydroxides: Application of the surface complexation site-binding model. Geochim. Cosmochim. Acta 49, 1931–1941.

Jackson, S.E., Pearson, N.J., Griffin, W.L., Belousova, E.A., 2004. The application of laser ablation-inductively coupled plasma-mass spectrometry to in situ U-Pb zircon geochronology. Chem. Geol. 211, 47–69. https://doi.org/10.1016/j.chemgeo.2004.06.017

Kato, Y., Kano, T., Kunugiza, K., 2002. Negative Ce Anomaly in the Indian Banded Iron Formations: Evidence for the Emergence of Oxygenated Deep-Sea at 2.9-2.7 Ga. Resour. Geol. 52, 101–110. https://doi.org/10.1111/j.1751-3928.2002.tb00123.x

Kato, Y., Yamaguchi, K.E., Ohmoto, H., 2006. Rare earth elements in Precambrian banded iron formations: Secular changes of Ce and Eu anomalies and evolution of atmospheric oxygen, in: Evolution of Early Earth's Atmosphere, Hydrosphere, and Biosphere - Constraints from Ore Deposits. Geological Society of America, pp. 269–289. https://doi.org/10.1130/2006.1198(16)

Knauer, L.G., 1990. Evolução geológica do Precambriano da porção centro-leste da Serra do Espinhaço Meridional e metalogênese associada. Unicamp, Campinas.

Knauer, L.G., 1999. Aspectos estratigráficos e estruturais das unidades proterozóicas da Serra do Espinhaço Meridional e suas implicações para a caracterização do Evento Uruaçuano. Universidade Estadual Paulista.

Knauer, L.G., 2007. O Supergrupo Espinhaço Em Minas Gerais : Considerações Sobre Sua Estratigrafia E Seu Arranjo Estrutural. Geonomos 15, 81–90.

Knauer, L.G., da Silva, L.L., Souza, F. de B.B., Silva, L.R., do Carmo, R.C., 2007. Monte Azul- SD.23-Z-D-II, escala 1:100.000: nota explicativa. CPRM.

Knauer, L.G., Grossi-Sad, J.H., 1997. Geologia da Folha Presidente Kubitschek, in: Grossi-Sad, J.H., Lobato, L.M., Pedrosa-Soares, A.C., Soares-Filho, B.S. (Eds.), Projeto Espinhaço Em CD-ROM (Textos, Mapas e Anexos). COMIG - Companhia Mineradora de Minas Gerais, Belo Horizonte, pp. 1901–2055.

Koehler, M.C., Buick, R., Kipp, M.A., Stüeken, E.E., Zaloumis, J., 2018. Transient surface ocean oxygenation recorded in the ∼2.66-Ga Jeerinah Formation, Australia. Proc. Natl. Acad. Sci. 115, 7711–7716. https://doi.org/10.1073/pnas.1720820115

Konhauser, K.O., Planavsky, N.J., Hardisty, D.S., Robbins, L.J., Warchola, T.J., Haugaard, R., Lalonde, S. V., Partin, C.A., Oonk, P.B.H., Tsikos, H., Lyons, T.W., Bekker, A., Johnson, C.M., 2017. Iron formations: A global record of Neoarchaean to Palaeoproterozoic environmental history. Earth-Science Rev. 172, 140–177. https://doi.org/10.1016/j.earscirev.2017.06.012

Kresse, C., Lobato, L.M., Figueiredo e Silva, R.C., Hagemann, S.G., Banks, D., Vitorino, A.L.A., 2020. Fluid signature of the shear zone–controlled Veio de Quartzo ore body in the world-class BIF-hosted Cuiabá gold deposit, Archaean Rio das Velhas greenstone belt, Brazil: a fluid inclusion study. Miner. Depos. 55, 1441–1466. https://doi.org/10.1007/s00126-019-00941-0

Kuchenbecker, M., Barbuena, D., 2023. Basement inliers of the Araçuaí-West Congo orogen: key pieces for understanding the evolution of the São Francisco-Congo paleocontinent. J. South Am. Earth Sci. 125. https://doi.org/10.1016/j.jsames.2023.104299

Kuchenbecker, M., Reis, H.L.S., Silva, L.C. da, Costa, R.D. da, Fragoso, D.G.C., Knauer, L.G., Dussin, I.A., Soares, A.C.P., 2015. Age Constraints for Deposition and Sedimentary Provenance of Espinhaço Supergroup and Bambuí Group in Eastern São Francisco Craton. Geonomos 23, 14–28. https://doi.org/10.18285/geonomos.v23i2.708

Kuchenbecker, M., Sanglard, J.C.D., 2018. The role of detachment and interlayer shear zones in the structural evolution of the southern Espinhaço range, eastern Brazil. J. South Am. Earth Sci. 84, 343–350. https://doi.org/10.1016/j.jsames.2018.04.010

Lana, C., Alkmim, F.F., Armstrong, R., Scholz, R., Romano, R., Nalini, H.A., 2013. The ancestry and magmatic evolution of Archaean TTG rocks of the Quadrilátero Ferrífero province, southeast Brazil. Precambrian Res. 231, 157–173. https://doi.org/10.1016/j.precamres.2013.03.008

Le Bas, M.J., Le Maitre, R.N., Streckeisen, A., Zanettin, B., 1986. A chemical classification of volcanic rock based on total silica diagram. J. Petrol. 27, 745–750.

Leal, V.L.S., Kuchenbecker, M., Barbuena, D., Queiroga, G., Pinheiro, M.A.P., Freimann, M. de A., 2021. Geochemistry and U–Pb zircon ages of the metamafic-ultramafic rocks of the Riacho dos Machados metavolcanosedimentary sequence: Evidence of a late Rhyacian back-arc basin during the assembly of São Francisco-Congo paleocontinent. J. South Am. Earth Sci. 105, 102972. https://doi.org/10.1016/j.jsames.2020.102972

Lerouge, C., Cocherie, A., Toteu, S.F., Penaye, J., Milési, J.P., Tchameni, R., Nsifa, E.N., Mark Fanning, C., Deloule, E., 2006. Shrimp U-Pb zircon age evidence for Paleoproterozoic sedimentation and 2.05 Ga syntectonic plutonism in the Nyong Group, South-Western Cameroon: consequences for the Eburnean-Transamazonian belt of NE Brazil and Central Africa. J. African Earth Sci. 44, 413–427. https://doi.org/10.1016/j.jafrearsci.2005.11.010

Li, J., Kusky, T., 2007. A Late Archean foreland fold and thrust belt in the North China Craton: Implications for early collisional tectonics. Gondwana Res. 12, 47–66. https://doi.org/10.1016/j.gr.2006.10.020

Lin, M., Peng, S., Jiang, X., Polat, A., Kusky, T., Wang, Q., Deng, H., 2016. Geochemistry, petrogenesis and tectonic setting of Neoproterozoic mafic-ultramafic rocks from the western Jiangnan orogen, South China. Gondwana Res. 35, 338–356. https://doi.org/10.1016/j.gr.2015.05.015

Lobato, L.M., Ribeiro-Rodrigues, L.C., Vieira, F.W.R., 2001. Brazil's premier gold province. Part 11: Geology and genesis of gold deposits in the Archean rio das velhas greenstone belt, Quadrilátero ferrifero. Miner. Depos. 36, 249–277. https://doi.org/10.1007/s001260100180

Lopes-Silva, L., Knauer, L.G., 2011. Posicionamento Estratigráfico da Formação Bandeirinha na Região de Diamantina , Minas Gerais : Grupo Costa Sena ou Supergrupo Espinhaço ? 19, 131–151.

Ludwig, K.R., 2003. Using Isoplot/Ex, version 3.00, a geochronological toolkit for Microsoft Excel. Berkeley Geochronol. Center, Spec. Publ. 1a, 43.

Machado, N., Noce, C.M., Ladeira, E.A., Belo De Oliveira, O., 1992. U-Pb geochronology of Archean magmatism and Proterozoic metamorphism in the Quadrilatero Ferrifero, southern Sao Francisco Craton, Brazil. Geol. Soc. Am. Bull. 104, 1221–1227. https://doi.org/10.1130/0016-7606(1992)104<1221:UPGOAM>2.3.CO;2

Machado, N., Schrank, A., Abreu, F.R. de, Knauer, L.G., Almeida-Abreu, P.Â., 1989. Resultados preliminares da geocronologia UPb na Serra do Espinhaço Meridional, in: Anais Do Quinto Simpósio de Geologia Núcleo MG.

Machado, N., Schrank, A., Noce, C.M., Gauthier, G., 1996. Ages of detrital zircon from archean - Paleoproterozoic sequences: Implications for greenstone belt setting and evolution of a transamazonian foreland basin in Quadrilátero Ferrífero, southeast Brazil. Earth Planet. Sci. Lett. 141, 259–276. https://doi.org/10.1016/0012-821x(96)00054-4

Martin, J.-M., Whitfield, M., 1983. The Significance of the River Input of Chemical Elements to the Ocean, in: Trace Metals in Sea Water. Springer US, Boston, MA, pp. 265–296. https://doi.org/10.1007/978-1-4757-6864-0_16

Martínez Dopico, C.I., Lana, C., Moreira, H.S., Cassino, L.F., Alkmim, F.F., 2017. U–Pb ages and Hf-isotope data of detrital zircons from the late Neoarchean-Paleoproterozoic Minas Basin, SE Brazil. Precambrian Res. 291, 143–161. https://doi.org/10.1016/j.precamres.2017.01.026

Martins-Ferreira, M.A.C., Dias, A.N.C., Chemale, F., Campos, J.*E.G.*, Seraine, M., Novais-Rodrigues, E., 2020. Multi-stage crustal accretion by magmatic flare-up and quiescence intervals in the western margin of the São Francisco Craton: U-Pb-Hf and geochemical constraints from the Almas Terrane. Gondwana Res. 85, 32–54. https://doi.org/10.1016/j.gr.2020.04.005

Martins-neto, M. a., 2000. Tectonics and sedimentation in a paleo / mesoproterozoic rift-sag basin (Espinhac ¸ o basin , southeastern Brazil). Precambrian Res. 103, 147–173.

Martins de Sousa, D.F., Oliveira, E.P., Amaral, W.S., Baldim, M.R., 2020. The Itabuna-Salvador-Curaçá Orogen revisited, São Francisco Craton, Brazil: New zircon U–Pb ages and Hf data support evolution from archean continental arc to paleoproterozoic crustal reworking during block collision. J. South Am. Earth Sci. 104, 102826. https://doi.org/10.1016/j.jsames.2020.102826

Mascarenhas, J. de F., Silva, E.F.A. da, 1994. Greenstone Belt de Mundo Novo: caracterização e implicações metalogenéticas e geotectônicas no Cráton do São Francisco. Série Arq. Abertos 5, 1–31.

Melo-Silva, P. de, Amaral, W. da S., Oliveira, E.P., 2020. Geochronological evolution of the Pitangui greenstone belt, southern São Francisco Craton, Brazil: Constraints from U-Pb zircon age, geochemistry and field relationships. J. South Am. Earth Sci. 99, 102380. https://doi.org/10.1016/j.jsames.2019.102380

Menezes Leal, A.B. de, Santos, A.L.D., Bastos Leal, L.R., Cunha, J.C., 2015. Geochemistry of contaminated komatiites from the Umburanas greenstone belt, Bahia State, Brazil. J. South Am. Earth Sci. 61, 1–13. https://doi.org/10.1016/j.jsames.2015.03.006

Michard, A., Albarède, F., 1986. The REE content of some hydrothermal fluids. Chem. Geol. 55, 51–60. https://doi.org/10.1016/0009-2541(86)90127-0

Miranda, D.A., Chaves, A. de O., Dussin, I.A., Porcher, C.C., 2020. Paleoproterozoic khondalites in Brazil: a case study of metamorphism and anatexis in khondalites from Itapecerica supracrustal succession of the southern São Francisco Craton. Int. Geol. Rev. 00, 1–25. https://doi.org/10.1080/00206814.2020.1716273

Morteani, G., Ackermand, D., Horn, A.H., 2001. Aluminium-phosphates and borosilicates in muscovite-kyanite metaquartzites near Diamantina (Minas Gerais , Brazil): Petrogenetic implications The rocks studied in this paper are examples of the rather rare cases of sedimentary phosphate-rich rocks of Mi 111–129.

Moteiro, B.A.A., Silva, V.C. de S. e, Oliveira, V. de P., 2019. Mapeamento geológico em escala 1:25.000 e caracterização de minerais do grupo da turmalina a sudoeste de Diamantina.

Nesbitt, H.W., Young, G.M., 1982. Early Proterozoic climates and plate motions inferred from major element chemistry of lutites. Nature 299, 715–717. https://doi.org/10.1038/299715a0

Nesbitt, H.W., Young, G.M., 1984. Prediction of Some Weathering Trends of Plutonic and Volcanic-Rocks Based on Thermodynamic and Kinetic Considerations. Geochim. Cosmochim. Acta 48, 1523–1534. https://doi.org/10.1016/0016-7037(84)90408-3

Neves, B.D.E.B., Kawashita, K., Delhal, J., 1979. CORDILHElRA DO ESPINHA ~ O ; DADOS NOVOS. Rev. Bras. Geociencias 9.

Noce, C.M., Pedrosa-Soares, A.C., Silva, L.C. da, Alkmim, F.F. de, 2007. O Embasamento Arqueano E Paleoproterozóico Do Orógeno Araçuaí. Rev. Geonomos 15, 17–23. https://doi.org/10.18285/geonomos.v15i1.104

Noce, C.M., Zuccheti, M., Baltazar, O.F., Armstrong, R., Dantas, E., Renger, F.E., Lobato, L.M., 2005. Age of felsic volcanism and the role of ancient continental crust in the evolution of the Neoarchean Rio das Velhas Greenstone belt (Quadrilátero Ferrífero, Brazil): U-Pb zircon dating of volcaniclastic graywackes. Precambrian Res. 141, 67–82. https://doi.org/10.1016/j.precamres.2005.08.002

Novo, T.A., Noce, C.M., Pedrosa-Soares, A.C., Batista, G.A.P., 2013. Rochas Granulíticas Da Suíte Caparaó Na Região Do Pico Da Bandeira: Embasamento Oriental Do Orógeno Araçuaí. Geonomos 19, 70–77. https://doi.org/10.18285/geonomos.v19i2.42

Nozaki, Y., Zhang, J., Amakawa, H., 1997. The fractionation between Y and Ho in the marine environment. Earth Planet. Sci. Lett. 148, 329–340. https://doi.org/10.1016/s0012-821x(97)00034-4

Nutman, A.P., Friend, C.R.L., Bennett, V.C., Van Kranendonk, M., Chivas, A.R., 2019. Reconstruction of a 3700 Ma transgressive marine environment from Isua (Greenland): Sedimentology, stratigraphy and geochemical signatures. Lithos 346–347, 105164. https://doi.org/10.1016/j.lithos.2019.105164

Olson, S.L., Kump, L.R., Kasting, J.F., 2013. Quantifying the areal extent and dissolved oxygen concentrations of Archean oxygen oases. Chem. Geol. 362, 35–43. https://doi.org/10.1016/j.chemgeo.2013.08.012

Ossa, F.O., Hofmann, A., Spangenberg, J.E., Poulton, S.W., Stüeken, E.E., Schoenberg, R., Eickmann, B., Wille, M., Butler, M., Bekker, A., 2019. Limited oxygen production in the Mesoarchean ocean. Proc. Natl. Acad. Sci. U. S. A. 116, 6647–6652. https://doi.org/10.1073/pnas.1818762116

Pasyanos, M.E., Nyblade, A.A., 2007. A top to bottom lithospheric study of Africa and Arabia. Tectonophysics 444, 27–44. https://doi.org/10.1016/j.tecto.2007.07.008

Pearce, J.A., 1982. Trace element characteristics of lavas from destructive plate boundaries. Orog. Andesites Relat. Rocks 525–548.

Pearce, J.A., Harris, N.B.W., Tindle, A.G., 1984. Trace Element Discrimination Diagrams for the Tectonic Interpretation of Granitic Rocks. J. Petrol. 25, 956–983. https://doi.org/10.1093/petrology/25.4.956

Pedrosa-Soares, A.C., Deluca, C., Araujo, C.S., Gradim, C., Lana, C. de C., Dussin, I., Silva, L.C. da, Babinski, M., 2020. O Orógeno Araçuaí à luz da geocronologia: um tributo a Umberto Cordani, in: Geocronologia e Evolução Tectônica Do Continente Sul-Americano: A Contribuição de Umberto Giuseppe Cordani. Solaris Edições Culturais.

Pedrosa-Soares, A.C., Noce, C.M., Alkmim, F.F. De, Silva, L.C. da, Babinski, M., Cordani, U., Castañeda, C., 2007. ORÓGENO ARAÇUAÍ: SÍNTESE DO CONHECIMENTO 30 ANOS APÓS ALMEIDA 1977. Geonomos 15, 1–16. https://doi.org/10.18285/geonomos.v15i1.103

Pedrosa-Soares, A.C., Noce, C.M., Wiedemann, C.M., Pinto, C.P., 2001. The Araçuaí-West-Congo Orogen in Brazil: An overview of a confined orogen formed during Gondwanaland assembly. Precambrian Res. 110, 307–323. https://doi.org/10.1016/S0301-9268(01)00174-7

Peng, P., Bleeker, W., Ernst, R.E., Söderlund, U., McNicoll, V., 2011. U-Pb baddeleyite ages, distribution and geochemistry of 925Ma mafic dykes and 900Ma sills in the North China craton: Evidence for a Neoproterozoic mantle plume. Lithos 127, 210–221. https://doi.org/10.1016/j.lithos.2011.08.018

Pesquera, A., Velasco, F., 1997. Mineralogy, geochemistry and geological significance of tourmaline-rich rocks from the Paleozoic Cinco Villas Massif (western Pyrenees, Spain). Contrib. to Mineral. Petrol. 129, 53–74. https://doi.org/10.1007/s004100050323

Pflug, R., 1965. A geologia da parte meridional da Serra do Espinhaço e zonas adjacentes, Minas Gerais, Div.Geol.Min., Bol.

Pidgeon, R.T., 1992. Recrystallisation of oscillatory zoned zircon: some geochronological and petrological implications. Contrib. to Mineral. Petrol. 110, 463–472. https://doi.org/10.1007/BF00344081

Pinto, C.P., Silva, M.A. da, 2014. Mapa geológico do estado de Minas Gerais, escala 1: 1.000. 000. Belo Horizonte, CPRM-Serviço Geológico do Bras.

Pirouz, M., Simpson, G., Bahroudi, A., Azhdari, A., 2011. Neogene sediments and modern depositional environments of the Zagros foreland basin system. Geol. Mag. 148, 838–853. https://doi.org/10.1017/S0016756811000392

Planavsky, N., Bekker, A., Rouxel, O.J., Kamber, B., Hofmann, A., Knudsen, A., Lyons, T.W., 2010. Rare Earth Element and yttrium compositions of Archean and Paleoproterozoic Fe formations revisited: New perspectives on the significance and mechanisms of deposition. Geochim. Cosmochim. Acta 74, 6387–6405. https://doi.org/10.1016/j.gca.2010.07.021

Planavsky, N., Rouxel, O.J., Bekker, A., Hofmann, A., Little, C.T.S., Lyons, T.W., 2012. Iron isotope composition of some Archean and Proterozoic iron formations. Geochim. Cosmochim. Acta 80, 158–169. https://doi.org/10.1016/j.gca.2011.12.001

Priestley, K., Mckenzie, D., Debayle, E., Pilidou, S., 2008. The African upper mantle and its relationship to tectonics and surface geology. Geophys. J. Int. 175, 1108–1126. https://doi.org/10.1111/j.1365-246X.2008.03951.x

Reis, H.L.S., Suss, J.F., Fonseca, R.C.S., Alkmim, F.F., 2017. Ediacaran forebulge grabens of the southern São Francisco basin, SE Brazil: Craton interior dynamics during West Gondwana assembly. Precambrian Res. 302, 150–170. https://doi.org/10.1016/j.precamres.2017.09.023

Rogers, J.J.W., Santosh, M., 2004. Continents and Supercontinents. Gondwana Res. 7, 653. https://doi.org/10.1016/s1342-937x(05)70827-3

Rolim, V.K., 1992. Uma interpretação das estruturas tectônicas do Supergrupo Espinhaço, baseada na geometria dos falhamentos de empurrão. Rev. da Esc. Minas 45, 75–77.

Roser, B.P., Korsch, R.J., 1988. Provenance signatures of sandstone-mudstone suites determined using discriminant function analysis of major-element data. Chem. Geol. 67, 119–139. https://doi.org/10.1016/0009-2541(88)90010-1

Rosière, C.A., Bekker, A., Rolim, V.K., Santos, J.O.S., 2019. Post-Great Oxidation Event Orosirian–Statherian iron formations on the São Francisco craton: Geotectonic implications. Isl. Arc 28, 1–10. https://doi.org/10.1111/iar.12300

Rudnick, R.L., Gao, S., 2003. Composition of the Continental Crust, in: Treatise on Geochemistry. Elsevier, pp. 1–64. https://doi.org/10.1016/B0-08-043751-6/03016-4

Sampaio, G.M.S., Pufahl, P.K., Raye, U., Kyser, K.T., Abreu, A.T., Alkmim, A.R., Nalini, H.A., 2018. Influence of weathering and hydrothermal alteration on the REE and δ56Fe composition of iron formation, Cauê Formation, Iron Quadrangle, Brazil. Chem. Geol. 497, 27–40. https://doi.org/10.1016/j.chemgeo.2018.08.014

Santos, M.N. Dos, 2015. GEOCRONOLOGIA U/PB EM ZIRCÕES DETRÍTICOS E A EVOLUÇÃO TECTÔNICA E ESTRATIGRÁFICA DA BACIA ESPINHAÇO NO SETOR MERIDIONAL. Universidade de Brasília.

Santos, M.N. dos, Chemale Jr, F., Dussin, I.A., Martins, M.S., Queiroga, G., Pinto, R.T.R., Santos, A.N., Armstrong, R., 2015. Provenance and paleogeographic reconstruction of a mesoproterozoic intracratonic sag basin (Upper Espinhaço Basin, Brazil). Sediment. Geol. 318, 40–57. https://doi.org/10.1016/j.sedgeo.2014.12.006

Santos, M.M., Lana, C., Scholz, R., Buick, I., Schmitz, M.D., Kamo, S.L., Gerdes, A., Corfu, F., Tapster, S., Lancaster, P., Storey, C.D., Basei, M.A.S., Tohver, E., Alkmim, A., Nalini, H., Krambrock, K., Fantini, C., Wiedenbeck, M., 2017. A New Appraisal of Sri Lankan BB Zircon as a Reference Material for LA-ICP-MS U-Pb Geochronology and Lu-Hf Isotope Tracing. Geostand. Geoanalytical Res. 41, 335–358. https://doi.org/10.1111/ggr.12167

Santos, M.N., Chemale, F., Dussin, I.A., Martins, M., Assis, T.A.R., Jelinek, A.R., Guadagnin, F., Armstrong, R., 2013. Sedimentological and paleoenvironmental constraints of the Statherian and Stenian Espinhaço rift system, Brazil. Sediment. Geol. 290, 47–59. https://doi.org/10.1016/j.sedgeo.2013.03.002

Schöll, W.U., Fogaça, A.C.C., 1979. SCHÖLL, W.U. & FOGAÇA, A.C.C. (1979). Estratigrafia da Serra do Espinhaço na região de Diamantina (MG)..pdf.pdf, in: Atas Do I Simpósio de Geologia de Minas Gerais, Diamantina. Diamantina, pp. 55–73.

Schöll, W.U., Fogaça, A.C.C., 1981. Mapeamento geológico das quadrículas Guinda e Gouveia (MG), Projeto Mapeamento Espinhaço, Conv. DNPM/UFMG, Rel. inédito.

Sepulveda, G.O., Novo, T.A., Roncato, J., 2021. Characterization and geochronology of Archean metasedimentary sequences in the eastern portion of Rio das Velhas greenstone belt, Quadrilátero Ferrífero, Brazil. J. South Am. Earth Sci. 105. https://doi.org/10.1016/j.jsames.2020.102962

Siga Junior, O., 1986. A evolução geotectônica da porção nordeste de Minas Gerais, com base em interpretações geocronológicas.

Silva, L.C. Da, Armstrong, R., Noce, C.M., Carneiro, M.A., Pimentel, M., Pedrosa-Soares, A.C., Leite, C.A., Vieira, V.S., Silva, M.A. Da, Paes, V.J.D.C., Cardoso Filho, J.M., 2002a. Reavaliação da evolução geológica em terrenos pré-cambrianos brasileiros com base em novos dados U-PB Shrimp, parte II: orógeno araçuaí, Cinturão Mineiro e cráton São Francisco Meridional. Rev. Bras. Geociências 32, 513–528. https://doi.org/10.25249/0375-7536.2002324513528

Silva, L.C. Da, Armstrong, R., Noce, C.M., Carneiro, M.A., Pimentel, M., Pedrosa-Soares, A.C., Leite, C.A., Vieira, V.S., Silva, M.A. Da, Paes, V.J.D.C., Cardoso Filho, J.M., 2002b. Reavaliação da evolução geológica em terrenos pré-cambrianos brasileiros com base em novos dados U-Pb shrimp, parte II: Orógeno Araçuaí, Cinturão Mineiro e Cráton São Francisco Meridional. Rev. Bras. Geociências 32, 513–528. https://doi.org/10.25249/0375-7536.2002324513528

Silva, L.C. da, McNaughton, N.J., Armstrong, R., Hartmann, L.A., Fletcher, I.R., 2005. The neoproterozoic Mantiqueira Province and its African connections: A zircon-based U-Pb geochronologic subdivision for the Brasiliano/Pan-African systems of orogens. Precambrian Res. 136, 203–240. https://doi.org/10.1016/j.precamres.2004.10.004

Silva, L.C. da, Pedrosa-Soares, A.C., Armstrong, R., Pinto, C.P., Magalhães, J.T.R., Pinheiro, M.A.P., Santos, G.G., 2015. Disclosing the Paleoarchean to Ediacaran history of the São Francisco craton basement: The Porteirinha domain (northern Araçuaí orogen, Brazil). J. South Am. Earth Sci. 68, 50–67. https://doi.org/10.1016/j.jsames.2015.12.002

Silva, M.C.R., Chaves, M.L.D.S.C., Andrade, K.W., 2015. Clastos de formação ferrífera bandada no conglomerado diamantífero Sopa em Extração. Geociências 34, 153–168.

Silva, R.R., 1995. Sequence stratigraphy and depositional systems of the lower Espinhaço in the region between Diamantina and Gouveia, Minas Gerais, Brazil. Freiberg Universität.

Simplicio, F., Basilici, G., 2015. Unusual thick eolian sand sheet sedimentary succession: Paleoproterozoic Bandeirinha Formation, Minas Gerais. Brazilian J. Geol. 45, 3–11. https://doi.org/10.1590/2317-4889201530133

Sláma, J., Košler, J., Condon, D.J., Crowley, J.L., Gerdes, A., Hanchar, J.M., Horstwood, M.S.A., Morris, G.A., Nasdala, L., Norberg, N., Schaltegger, U., Schoene, B., Tubrett, M.N., Whitehouse, M.J., 2008. Plešovice zircon - A new natural reference material for U-Pb and Hf isotopic microanalysis. Chem. Geol. 249, 1–35. https://doi.org/10.1016/j.chemgeo.2007.11.005

Souza, M.A.T.A., Grossi-Sad, J.H., 1997. Geologia da Folha Rio Vermelho, in: Grossi-Sad, J.H., Lobato, L.M., Pedrosa-Soares, A.C., S, S.-F.B. (Eds.), Projeto Espinhaço Em Cd-Rom (Textos, Mapas e Anexos). COMIG, Belo Horizonte, pp. 1667–1806.

Spencer, C.J., Roberts, N.M.W., Santosh, M., 2017. Growth, destruction, and preservation of Earth’s continental crust. Earth-Science Rev. 172, 87–106. https://doi.org/10.1016/j.earscirev.2017.07.013

Spier, C.A., de Oliveira, S.M.B., Sial, A.N., Rios, F.J., 2007. Geochemistry and genesis of the banded iron formations of the Cauê Formation, Quadrilátero Ferrífero, Minas Gerais, Brazil. Precambrian Res. 152, 170–206. https://doi.org/10.1016/j.precamres.2006.10.003

Spier, C.A., Levett, A., Rosière, C.A., 2019. Geochemistry of canga (ferricrete) and evolution of the weathering profile developed on itabirite and iron ore in the Quadrilátero Ferrífero, Minas Gerais, Brazil. Miner. Depos. 54, 983–1010. https://doi.org/10.1007/s00126-018-0856-7

Spreafico, R.R., Figueiredo Barbosa, J.S., Barbosa, N.S., Vitória de Moraes, A.M., 2019. Tectonic evolution of the Neoarchean Mundo Novo greenstone belt, eastern São Francisco Craton, NE Brazil: Petrology, U-Pb geochronology, and Nd and Sr isotopic constraints. J. South Am. Earth Sci. 95, 102296. https://doi.org/10.1016/j.jsames.2019.102296

Strecker, M.R., Alonso, R.N., Bookhagen, B., Carrapa, B., Hilley, G.E., Sobel, E.R., Trauth, M.H., 2007. Tectonics and climate of the southern central Andes. Annu. Rev. Earth Planet. Sci. 35, 747–787. https://doi.org/10.1146/annurev.earth.35.031306.140158

Tack, L., Wingate, M.T.D., Liégeois, J.P., Fernandez-Alonso, M., Deblond, A., 2001. Early Neoproterozoic magmatism (1000-910 Ma) of the Zadinian and Mayumbian groups (Bas-Congo): Onset of Rodinia rifting at the western edge of the Congo craton. Precambrian Res. 110, 277–306. https://doi.org/10.1016/S0301-9268(01)00192-9

Tapponnier, P., Molnar, P., 1976. Slip-line field theory and large-scale continental tectonics. Nature 264, 319–324. https://doi.org/10.1038/264319a0

Tassinari, C.C.G., Mateus, A.M., Velásquez, M.E., Munhá, J.M.U., Lobato, L.M., Bello, R.M., Chiquini, A.P., Campos, W.F., 2015. Geochronology and thermochronology of gold mineralization in the Turmalina deposit, NE of the Quadrilátero Ferrífero Region, Brazil. Ore Geol. Rev. 67, 368–381. https://doi.org/10.1016/j.oregeorev.2014.12.013

Taylor, S.R., McLennan, S.M., 1985. The Continental Crust: Its composition and evolution: and examination of the geochemical record preserved in sedimentary rocks. Oxford.

Taylor, S.R., McLennan, S.M., 1995. The geochemical evolution of the continental crust. Rev. Geophys. 33, 241. https://doi.org/10.1029/95RG00262

Teixeira, W., Ernst, R.E., Hamilton, M.A., Lima, G., Ruiz, A.S., Geraldes, M.C., 2016. Widespread ca. 1.4 Ga intraplate magmatism and tectonics in a growing Amazonia. Gff 138, 241–254. https://doi.org/10.1080/11035897.2015.1042033

Teixeira, W., Oliveira, E.P., Marques, L.S., 2017a. Nature and Evolution of the Archean Crust of the São Francisco Craton, in: São Francisco Craton, Eastern Brazil: Tectonic Genealogy of a Miniature Continent. p. 326. https://doi.org/10.1007/978-3-319-01715-0

Teixeira, W., Oliveira, E.P., Peng, P., Dantas, E.L., Hollanda, M.H.B.M., 2017b. U-Pb geochronology of the 2.0 Ga Itapecerica graphite-rich supracrustal succession in the São Francisco Craton: Tectonic matches with the North China Craton and paleogeographic inferences. Precambrian Res. 293, 91–111. https://doi.org/10.1016/j.precamres.2017.02.021

Teixeira, W., Sabaté, P., Barbosa, J., Noce, C.M., Carneiro, M.A., 2000. Archean and Paleoproterozoic tectonic evolution of the São Francisco craton, Brazil, in: Tectonic Evolution of South America. SBG Rio de Janeiro, Brazil, pp. 101–137.

Toloczyki, M., 1982. Der Granitaufbruch von Senador Modestino Gonçalves und sein geologischer Rahmen (Präkambrium, Minas Gerais, Brasilien). Freiburg University.

Uhlein, A., 1991. Transição cráton-faixa dobrada: exemplo do Cráton do São Francisco e da Faixa Aracuai (ciclo brasiliano) no estado de Minas Gerais: aspectos estratigráficos e estruturais. Universidade de São Pauilo. https://doi.org/DOI10.11606/T.44.1991.tde-27102015-092630

Van Achterbergh, E., Ryan, C.G., Jackson, S.E., Griffin, W.L., 2001. Data reduction software for LA-ICPMS, in: Sylvester, P. (Ed.), Laser Ablation ICPMS in the Earth Sciences: Mineralogical Association of Canada Short Course. pp. 239–243.

Van Hinsberg, V.J., Schumacher, J.C., 2011. Tourmaline as a petrogenetic indicator mineral in the haut-allier metamorphic suite, Massif Central, France. Can. Mineral. 49, 177–194. https://doi.org/10.3749/canmin.49.1.177

Verma, S.K., Oliveira, E.P., Silva, P.M., Moreno, J.A., Amaral, W.S., 2017. Geochemistry of komatiites and basalts from the Rio das Velhas and Pitangui greenstone belts, São Francisco Craton, Brazil: Implications for the origin, evolution, and tectonic setting. Lithos 284–285, 560–577. https://doi.org/10.1016/j.lithos.2017.04.024

Vermeesch, P., 2012. On the visualisation of detrital age distributions. Chem. Geol. 312–313, 190–194. https://doi.org/10.1016/j.chemgeo.2012.04.021

Vicat, J.P., Pouclet, A., 2000. Palæo- and Neoproterozoic granitoids and rhyolites from the West Congolian Belt (Gabon, Congo, Cabinda, north Angola): Chemical composition and geotectonic implications. J. African Earth Sci. 31, 597–617. https://doi.org/10.1016/S0899-5362(00)80009-3

Viehmann, S., Bau, M., Hoffmann, J.E., Münker, C., 2015. Geochemistry of the Krivoy Rog Banded Iron Formation, Ukraine, and the impact of peak episodes of increased global magmatic activity on the trace element composition of Precambrian seawater. Precambrian Res. 270, 165–180. https://doi.org/10.1016/j.precamres.2015.09.015

Vieira, V.S., Silva, M.A., Corrêa, T.R., Lopes, N.H.B., 2018. Mapa geológico do estado do Espírito Santo.

Vitorino, A.L.A., Figueiredo e Silva, R.C., Lobato, L.M., 2020. Shear-zone-related gold mineralization in quartz-carbonate veins from metamafic rocks of the BIF-hosted world-class Cuiabá deposit, Rio das Velhas greenstone belt, Quadrilátero Ferrífero, Brazil: Vein classification and structural control. Ore Geol. Rev. 127, 103789. https://doi.org/10.1016/j.oregeorev.2020.103789

Von Goerne, G., Franz, G., Robert, J.L., 1999. Upper thermal stability of tourmaline + quartz in the system MgO-Al2O3-SiO2-B2O3-H2O and Na2O-MgO-Al2O3-SiO2-B2O3-H2O-HCl in hydrothermal solutions and siliceous melts. Can. Mineral. 37, 1025–1039.

Williams, N.C., Davidson, G.J., 2004. Possible submarine Advanced Argillic Alteration at the basin lake prospect, western Tasmania, Australia. Econ. Geol. 99, 987–1002. https://doi.org/10.2113/gsecongeo.99.5.987

Yuan, F., Cai, Y., Yang, S., Liu, Z., Chen, L., Lang, Y., Wang, X., Wang, S., 2017. Simultaneous sequestration of uranyl and arsenate at the goethite/water interface. J. Radioanal. Nucl. Chem. 311, 815–831. https://doi.org/10.1007/s10967-016-5086-9

Zincone, S.A., Barbuena, D., Oliveira, E.P., Baldim, M.R., 2017. Detrital zircon U-Pb ages as evidence for deposition of the Saúde Complex in a Paleoproterozoic foreland basin, northern São Francisco Craton, Brazil. J. South Am. Earth Sci. 79, 537–548. https://doi.org/10.1016/j.jsames.2017.09.009

Zincone, S.A., Oliveira, E.P., 2017. Field and geochronological evidence for origin of the Contendas-Mirante supracrustal Belt, São Francisco Craton, Brazil, as a Paleoproterozoic foreland basin. Precambrian Res. 299, 117–131. https://doi.org/10.1016/j.precamres.2017.07.031

APÊNDICE A – dados isotópicos dos padrões utilizados

Table 3: Standards

											Ratios b								Ratios c												Dates c						
Identifier	Comments	f206c	206Pb	207Pb	U (µg g-1)	Th/U	206Pb/204Pb	207Pb/206Pb	1s	206Pb/238U	1s	207Pb/235U	1s	208Pb/232Th	1s	207Pb/206Pb	2s (%)	207Pb/235U	2s (%)	206Pb/238U	2s (%)	Rho	208Pb/232Th	2s (%)	207Pb/206Pb	2s	2ssys	206Pb/238U	2s	2ssys	207Pb/235U	2s	2ssys	208Pb/232Th	2s	2ssys	% conc d
			CPS	CPS															Data for Wetherill plot c							abs	abs		abs	abs		abs	abs		abs	abs	
PRIMARY REF. MAT. (BLUEBERRY)																																					
1.sSMPABC001		0.07017	168621.3	9901.236	446.8704	0.444277	108.8048	0.05876	0.00065	0.09148	0.0006	0.74195	0.000885	0.02791	0.0004	0.058719	2.226805	0.740635	2.588999	0.09148	1.320702	0.510121	0.02791	2.866356	556.6847	48.56528	53.27372	564.2841	7.139598	10.81809	562.7762	11.24764	13.73373	556.4	15.84	16.68034	100.2679
1.sSMPABC002		0	162770	9596.919	428.1343	0.456135	9596.919	0.05896	0.00065	0.09217	0.00061	0.75011	0.000891	0.02827	0.00042	0.05896	2.204885	0.749287	2.571681	0.09217	1.323641	0.514699	0.02827	2.971348	565.6194	48.0146	52.75849	568.3581	7.204942	10.90345	567.8107	11.24701	13.76354	563.5	16.38	17.46417	100.0964
1.sSMPABC021		0	151737	8985.865	407.1088	0.45879	109.5837	0.05922	0.00068	0.09036	0.0006	0.73856	0.000907	0.02834	0.00047	0.05922	2.296521	0.737812	2.652857	0.09036	1.328021	0.5006	0.02834	3.316867	575.1934	49.92939	91.71056	557.6659	7.098533	9.264427	561.1281	11.50123	14.33666	564.9	18.38	35.08538	99.38298
1.sSMPABC022		0	147725	8658.162	390.6807	0.457977	8658.162	0.05861	0.00067	0.09167	0.00061	0.74156	0.000906	0.02835	0.00047	0.05861	2.286299	0.740799	2.64544	0.09167	1.330861	0.503077	0.02835	3.315697	552.6396	49.89699	63.8412	565.4062	7.208243	6.608452	562.8716	11.49571	9.964543	565	18.6	23.2661	100.4503
1.sSMPABC041		0	151043	8864.714	401.3383	0.471051	8864.714	0.05869	0.00071	0.09124	0.00062	0.73919	0.000943	0.0274	0.00054	0.05869	2.419492	0.73833	2.775062	0.09124	1.359053	0.489738	0.0274	3.941606	555.6157	52.77722	67.28892	562.8665	7.329367	12.26949	561.4307	12.03907	17.36238	546.4	21.1	165.5317	100.2557
1.sSMPABC042		0.18004	151016.9	8922.597	397.8676	0.460753	86.62715	0.05919	0.00072	0.09202	0.00063	0.75176	0.000957	0.02901	0.00058	0.059083	2.512276	0.749634	2.887828	0.09202	1.424085	0.493134	0.02901	3.998621	570.1717	54.66646	75.1669	567.4726	7.740456	12.81967	568.012	12.64165	19.00459	578	22.62	207.8475	99.90505
											Ratios b								Ratios c												Dates c						
Identifier	Comments	f206c	206Pb	207Pb	U (µg g-1)	Th/U	206Pb/204Pb	207Pb/206Pb	1s	206Pb/238U	1s	207Pb/235U	1s	208Pb/232Th	1s	207Pb/206Pb	2s (%)	207Pb/235U	2s (%)	206Pb/238U	2s (%)	Rho	208Pb/232Th	2s (%)	207Pb/206Pb	2s	2ssys	206Pb/238U	2s	2ssys	207Pb/235U	2s	2ssys	208Pb/232Th	2s	2ssys	% conc d
			CPS	CPS															Data for Wetherill plot c							abs	abs		abs	abs		abs	abs		abs	abs	
SECONDARY REF. MAT. (PLESOVICE)																																					
1.sSMPABC003		0.48065	74718.13	3984.899	334.5205	0.217114	25.22088	0.05359	0.00093	0.054216	0.00042	0.400598	0.00102	0.01728	0.00088	0.053332	3.925809	0.398672	4.579287	0.054216	2.35752	0.514822	0.01728	10.18519	342.9655	88.85071	91.71056	340.3506	7.811469	9.264427	340.6848	13.32907	14.33666	346.2	34.84	35.08538	99.88688
1.sSMPABC004		0	59083	3142.034	267.6342	0.205931	3142.034	0.05318	0.0007	0.053585	0.00036	0.392908	0.000787	0.01592	0.00058	0.05318	2.632569	0.392908	2.956387	0.053585	1.345291	0.455046	0.01592	7.286432	336.4843	59.65008	63.8412	336.4924	4.407135	6.608452	336.4914	8.495681	9.964543	319.2	23.26	23.2661	99.98542
1.sSMPABC023		0	59926	3194.056	271.1995	0.191163	20.0884	0.0533	0.00126	0.053635	0.0005	0.394162	0.001356	0.01796	0.00146	0.0533	4.727955	0.394162	5.083128	0.053635	1.866716	0.367238	0.01796	16.25835	341.5891	107.0314	109.4182	336.7987	6.121544	7.859599	337.4055	14.6853	15.59282	359.7	57.9	58.08221	99.80527
1.sSMPABC024		0	72330	3846.509	327.0905	0.218174	21.3695	0.05318	0.0009	0.053675	0.00041	0.393569	0.000989	0.01886	0.00086	0.05318	3.384731	0.393569	3.714293	0.053675	1.529565	0.411805	0.01886	9.11983	336.4843	76.69296	79.99611	337.0437	5.019047	7.037041	336.9729	10.69811	11.90435	377.6	34	34.3044	100.0061
1.sSMPABC043		0	73107	3890.755	328.6425	0.229955	3890.755	0.05322	0.00074	0.053995	0.00038	0.396216	0.000832	0.01806	0.00059	0.05322	2.780909	0.396216	3.117595	0.053995	1.409234	0.452026	0.01806	6.533776	338.1877	62.99221	66.97217	339.0036	4.650254	6.799166	338.8998	9.015279	10.42778	361.8	23.6	23.74048	100.0157
1.sSMPABC044		0	81403	4326.569	367.9831	0.258213	4326.569	0.05315	0.001	0.053695	0.00045	0.393493	0.001097	0.01597	0.00081	0.05315	3.762935	0.393493	4.120184	0.053695	1.678165	0.407303	0.01597	10.14402	335.2056	85.28187	88.2655	337.1662	5.508814	7.395656	336.9181	11.87241	12.97133	320.3	32.36	32.47364	100.0587
											Ratios b								Ratios c												Dates c						
Identifier	Comments	f206c	206Pb	207Pb	U (µg g-1)	Th/U	206Pb/204Pb	207Pb/206Pb	1s	206Pb/238U	1s	207Pb/235U	1s	208Pb/232Th	1s	207Pb/206Pb	2s (%)	207Pb/235U	2s (%)	206Pb/238U	2s (%)	Rho	208Pb/232Th	2s (%)	207Pb/206Pb	2s	2ssys	206Pb/238U	2s	2ssys	207Pb/235U	2s	2ssys	208Pb/232Th	2s	2ssys	% conc d
			CPS	CPS															Data for Wetherill plot c							abs	abs		abs	abs		abs	abs		abs	abs	
TERCIARY REF. MAT. (GJ-1)																																					
1.sSMPABC005		0	88688	5351.434	219.3987	0.039597	57.5423	0.06034	0.00089	0.098119	0.00074	0.816315	0.001157	0.03822	0.00423	0.06034	2.94995	0.816315	3.314049	0.098119	1.510204	0.455698	0.03822	22.13501	615.7889	63.70034	67.28892	603.3734	8.695017	12.26949	605.9904	15.22715	17.36238	758.1	164.58	165.5317	99.5439
1.sSMPABC006		0	93108	5595.791	228.3986	0.036995	5595.791	0.0601	0.001	0.09895	0.0008	0.819954	0.001281	0.03854	0.00531	0.0601	3.327787	0.819954	3.700694	0.09895	1.618942	0.43747	0.03854	27.55579	607.1768	71.96279	75.1669	608.2499	9.393427	12.81967	608.0229	17.06071	19.00459	764.3	206.84	207.8475	100.0129
1.sSMPABC025		0	80207	4824.451	198.6208	0.035734	4824.451	0.06015	0.00075	0.098018	0.00067	0.812914	0.001006	0.04239	0.00334	0.06015	2.493766	0.812914	2.844701	0.098018	1.368744	0.481155	0.04239	15.75843	608.9749	53.911	58.11655	602.7856	7.87273	11.6947	604.0874	13.02648	15.45144	839.2	129.44	130.2742	99.76027
1.sSMPABC026		0	74789	4472.382	183.74	0.048703	4472.382	0.0598	0.00083	0.098799	0.0007	0.814623	0.001086	0.03437	0.00302	0.0598	2.77592	0.814623	3.117454	0.098799	1.418727	0.455092	0.03437	17.57347	596.3455	60.13781	63.9507	607.3689	8.219622	11.97674	605.0441	14.30097	16.5486	683.1	118.12	118.6422	100.3599
1.sSMPABC045		0	77336	4647.894	191.5504	0.040431	516.4326	0.0601	0.00099	0.097998	0.00074	0.812072	0.001236	0.03929	0.00422	0.0601	3.294509	0.812072	3.624928	0.097998	1.512056	0.417127	0.03929	21.48129	607.1768	71.24316	74.47824	602.6681	8.695968	12.26335	603.6159	16.61912	18.58805	778.9	164.28	164.9583	99.81874
1.sSMPABC046		0	71650	4301.15	177.1773	0.039338	4301.15	0.06003	0.00098	0.098159	0.00073	0.812452	0.001222	0.0381	0.0044	0.06003	3.265034	0.812452	3.588611	0.098159	1.489188	0.414976	0.0381	23.09711	604.6561	70.63557	73.89995	603.6085	8.577126	12.18844	603.8289	16.45554	18.44249	755.8	171.16	172.2551	99.93925

a concentration uncertainty ca. 10%

b data not corrected for common-Pb

c data corrected/not corrected for common-Pb

*d Concordance calculated as (206Pb-238U age/207Pb-235U age)*100.*

Decay constants of Jaffey et al. (1971) used

bd = below detection; #N/A = not available

Uncertainties quoted without components related to systematic error unless otherwise stated

Total systematic uncertainties (ssys): 206Pb/238U = 2.0%, 207Pb/206Pb = 0.55% (2s)

APÊNDICE B - tabela com os dados geoquímicos das bifs e metariolito da sequência Pedro Pereira

Table 1: PPMS iron formation and metarhyolite whole-rock geochemistry

	PP14*	PP15*	PP16*	PP18*	PP42*	PP54*	PP14**	PP15B**	PP16**	PP42**	CSLC-17*
Rock type	BIF	BIF	BIF	BIF	MIF	BIF	BIF	BIF	BIF	MIF	Meta rhyolite
SiO2	47.44	49.44	40.15	40.76	13.37	38.07	48.96	41.2	45.93	19.06	73.66
Al2O3	1.11	0.25	0.1	1.05	0.4	0.58	3.08	1.09	0.42	0.53	11.1
Fe2O3	47.17	49.5	54.78	53.89	>75	56.17	45.47	56.62	53.23	79.64	4.81
TiO2	0.03	<0,01	<0,01	0.04	0.02	0.02	0.08	0.02	<0.01	0.02	0.3
K2O	0.44	0.1	0.03	0.2	0.11	0.18	1.21	0.34	0.09	0.13	2.34
Na2O	<0,01	<0,01	<0,01	<0,01	0.01	<0,01	0.01	0.02	<0.01	0.01	0.09
CaO	0.02	0.02	0.03	0.02	0.04	0.03	0.08	0.05	0.03	0.02	0.01
MgO	0.13	0.03	0.03	0.06	0.1	0.05	0.27	0.02	<0.01	0.1	3.45
MnO	0.01	0.03	0.02	0.07	0.04	0.01	0.01	0.02	0.02	0.05	0.04
P2O5	<0,01	0.02	0.02	0.03	<0,01	<0,01	<0.01	0.03	<0.01	<0.01	0.06
Cr2O3	<0,01	<0,01	<0,01	<0,01	<0,01	<0,01	0.006	0.003	0.005	0.004	<0,01
LOI	0.04	-0.08	0	1.33	0.11	0.07	0.8	0.5	0.2	0.4	2.92
Ba	<10	<10	83	<10	<10	26	62	183	70	47	196
La	8.5	17.7	76.4	4.4	57	20.8	21.5	114.2	35.2	61.2	118.9
Ce	13.3	12.2	18.4	4.2	9.3	17.9	22.7	36	14	8.5	198.4
Pr	1.11	3.23	14.29	0.46	8.01	1.86	2.72	14.63	3.78	8.5	25.54
Nd	3.5	10.3	41.8	1.4	20.4	5	9.4	43.5	11.9	29	82.2
Sm	0.7	1.5	6.6	0.3	4.8	0.7	1.86	5.93	1.98	6.57	15.9
Eu	0.11	0.2	0.49	0.06	0.58	0.09	0.4	0.91	0.31	0.91	0.71
Gd	0.64	1.24	3.91	0.29	5.67	0.57	2.69	5.08	1.86	9.63	14.86
Tb	0.13	0.23	0.47	0.07	1.36	0.11	0.46	0.75	0.23	1.46	2.43
Dy	0.88	1.21	2	0.38	8.58	0.64	2.72	4.23	1.01	8.14	13.42
Y	6.91	3.56	8.64	2.26	42.36	2.66	15	15	3.7	60.8	63.09
Ho	0.22	0.19	0.31	0.11	1.79	0.11	0.54	0.71	0.13	1.78	2.44
Er	0.73	0.47	0.83	0.29	4.94	0.29	1.82	1.88	0.39	5.06	6.5
Tm	0.13	0.08	0.1	0.05	0.7	<0,05	0.33	0.22	0.06	0.63	0.89
Yb	1	0.4	0.7	0.4	4.2	0.2	2.54	1.6	0.38	3.46	5.4
Lu	0.15	<0,05	0.11	0.06	0.55	0.05	0.43	0.17	0.06	0.49	0.76
REEY_Sum	38.01	52.51	175.05	14.73	170.24	50.98	85.11	244.81	74.99	206.13	-
V	36	20	25	43	52	42	17	<8	<8	<8	<5
Zr	<10	<10	13	<10	<10	<10	25.7	4.6	6.8	5.7	407
Sr	<10	<10	13	<10	<10	11	7.2	8.7	13.1	2.2	18
Co	1.4	20.1	3	21.6	26.7	11.7	1.4	4.2	1.7	3.8	5.4
Cs	0.13	0.08	0.07	0.15	0.07	0.1	0.3	<0.1	<0.1	<0.1	1.69
Ga	5.4	2	2	10.4	4.4	4.4	7.1	5.1	0.6	4.2	26.1
Ni	6	15	<5	18	21	11	<20	<20	<20	<20	11

Table 1: PPMS iron formation and metarhyolite whole-rock geochemistry

	PP14*	PP15*	PP16*	PP18*	PP42*	PP54*	PP14**	PP15B**	PP16**	PP42**	CSLC-17*
Hf	0.27	0.19	0.54	0.33	0.23	0.21	0.7	<0.1	<0.1	0.2	13.99
Rb	17.6	5.6	2.7	12.7	4.8	9.3	47.8	14.3	5.5	10.2	194.2
Nb	1.9	2.16	0.38	8.77	1.98	2.61	3.6	3.6	0.7	1.8	62.21
Sn	19.5	0.3	<0,3	19	48.4	0.3	33	21	2	95	4.3
Ta	0.06	0.69	<0,05	1.05	0.05	0.13	0.6	0.5	0.1	<0.1	4.95
Th	3.4	2.7	3.3	2.8	1.8	3.7	2.2	1.4	1.5	1.8	45.7
U	1.95	1.45	0.81	7.79	11.38	4.02	4.4	3.3	0.8	6.3	8.73
W	0.8	11.2	1.6	0.5	109.6	3.1	2.2	3.7	2	22.5	0.6
Sc	-	-	-	-	-	-	3	<1	<1	1	-
Be	-	-	-	-	-	-	<1	<1	<1	<1	-
TOT/C	-	-	-	-	-	-	<0.02	<0.02	<0.02	<0.02	-
TOT/S	-	-	-	-	-	-	<0.02	<0.02	<0.02	<0.02	-
Zn	21	20	11	85	35	41	-	-	-	-	73
Tl	<0,5	<0,5	<0,5	<0,5	<0,5	<0,5	-	-	-	-	0.9
Mo	<2	<2	4	6	7	<2	-	-	-	-	<2
Cu	6	<5	7	32	<5	87	-	-	-	-	<5
Y/Ho	31.40909	18.73684	27.87097	20.54545	23.6648	24.18182	27.77778	21.12676	28.46154	34.1573	-
Zr/Hf	-	-	24.07407	-	-	-	36.71429	-	-	28.5	-
Ce(SN)/Ce*(SN)	1.186964	0.377505	0.120736	0.880565	0.1	0.854897	0.89374	0.23337	0.366444	0.105841	-

Those samples labeled with an identical number are from the same outcrop, however, from distinct sectors of it.

* Samples analyzed at SGS GEOSOL, Brazil.

** Samples analyzed at Bureau Veritas Commodities Canada Ltd.

APÊNDICE C - tabela de medições isotópicas do metariolito CSLC-16

Table 2 - Zircon LA-ICP-MS U-Pb data - Metarhyolite

Spot #	207Pb^{a} (cps)	U (ppm)^{b}	Th/U^{b}	206Pb^{c} (%)	Isotope ratios							Ages (Ma)						% Conc.^{f}
					^{206}Pb/^{238}U^{d}	2s (%)	^{207}Pb/^{235}U^{d}	2s (%)	^{207}Pb/^{206}Pb^{d}	2s (%)	Rho^{e}	^{206}Pb/^{238}U	2s	^{207}Pb/^{235}U	2s	^{207}Pb/^{206}Pb	2s	
PP.7	30571	71	1.39	b.d.	0.5378	1.4	14.38	2.6	0.1939	2.3	0.52	2774	31	2775	25	2775	37	99.9
PP.8	36872	87	1.3	0.0986	0.531	1.4	14.12	2.6	0.1929	2.3	0.52	2745	30	2758	25	2767	37	99.5
PP.9	77198	187	1.75	b.d.	0.5152	1.4	13.79	2.5	0.1942	2.1	0.54	2679	30	2735	24	2778	35	97.9
PP.10	26727	63	1.17	0.1401	0.5358	1.4	14.2	2.6	0.1922	2.3	0.52	2766	31	2763	25	2761	37	100
PP.12	26642	69	1.53	b.d.	0.4845	1.3	12.87	2.5	0.1927	2.2	0.52	2547	28	2670	24	2765	36	95.3
PP.13	58303	191	1.8	0.9077	0.3916	1.5	10.21	3.3	0.1891	3	0.46	2130	28	2454	31	2735	49	86.8
PP.14	65875	153	1.37	0.1019	0.5383	1.3	14.38	2.4	0.1938	2.1	0.53	2776	29	2775	24	2774	34	100
PP.15	33303	76	1.27	b.d.	0.5456	1.6	14.71	3	0.1956	2.6	0.51	2807	35	2797	29	2789	43	100.3
PP.16	18006	42	1.01	b.d.	0.5365	1.6	14.31	3.8	0.1935	3.4	0.43	2769	36	2771	36	2772	56	99.9
PP.17	24305	56	1.25	b.d.	0.5368	1.7	14.57	3.3	0.1969	2.9	0.51	2770	38	2788	32	2800	47	99.3
PP.19	25703	93	1.97	0.1626	0.3493	1.3	9.26	2.6	0.1922	2.2	0.52	1931	22	2364	24	2761	36	81.7
PP.20	13576	32	1.51	b.d.	0.5394	1.8	14.39	3.6	0.1935	3.1	0.51	2781	42	2776	35	2772	51	100.1
PP.27	18825	43	1.16	b.d.	0.5486	1.5	14.73	2.9	0.1948	2.5	0.51	2819	34	2798	28	2783	41	100.7
PP.28	31016	106	1.6	0.5362	0.3655	1.4	9.76	2.7	0.1938	2.3	0.53	2008	25	2413	25	2774	38	83.2
PP.29	32491	127	1.37	b.d.	0.3317	1.4	8.54	2.7	0.1868	2.3	0.53	1847	23	2290	25	2714	38	80.6
PP.30	24041	55	1.21	0.4377	0.545	1.5	14.62	3	0.1946	2.6	0.5	2804	34	2791	29	2781	42	100.4
PP.31	38523	94	1.34	b.d.	0.5146	1.4	13.78	2.6	0.1943	2.2	0.53	2676	30	2735	25	2779	36	97.8
PP.32	25138	63	1.16	b.d.	0.5026	1.5	13.41	3	0.1935	2.6	0.5	2625	33	2709	29	2772	43	96.8
PP.33	65285	157	1.31	0.2352	0.5197	1.5	13.88	3	0.1937	2.6	0.49	2698	33	2742	29	2774	43	98.4
PP.34	30563	72	1.26	b.d.	0.5353	1.5	14.28	3.2	0.1935	2.8	0.46	2764	33	2768	31	2772	46	99.8
PP.35	23544	71	1.19	b.d.	0.4259	1.6	11.15	3.5	0.1899	3.1	0.45	2287	31	2536	33	2741	51	90.1

Table 2 - Zircon LA-ICP-MS U-Pb data - Metarhyolite

Spot #	**207Pb[a] (cps)**	**U (ppm)[b]**	**Th/U[b]**	**206Pb[c] (%)**	Isotope ratios							Ages (Ma)						**% Conc. [f]**
					^{206}Pb/^{238}U[d]	**2s (%)**	**^{207}Pb/^{235}U[d]**	**2s (%)**	**^{207}Pb/^{206}Pb[d]**	**2s (%)**	**Rho[e]**	**^{206}Pb/^{238}U**	**2s**	**^{207}Pb/^{235}U**	**2s**	**^{207}Pb/^{206}Pb**	**2s**	
PP.36	31018	73	1.4	b.d.	0.531	1.6	14.28	3.6	0.195	3.2	0.46	2746	37	2768	35	2785	52	99.1
PP.37	67975	347	1.6	b.d.	0.2642	1.3	6.56	2.5	0.1801	2.2	0.52	1512	18	2054	23	2654	36	73.5
PP.39	45932	111	1.38	b.d.	0.5153	1.5	13.83	3.1	0.1946	2.7	0.49	2679	34	2738	30	2781	45	97.8
PP.40	79279	1140	0.28	0.5256	0.1504	1.6	2.33	3.1	0.1122	2.6	0.52	903	13	1220	22	1835	48	74
PP.47	27901	64	1.44	b.d.	0.5415	1.7	14.58	3.7	0.1953	3.3	0.46	2790	38	2788	35	2787	53	100
PP.48	49253	228	0.93	0.4743	0.2796	1.5	7.25	3.2	0.188	2.8	0.48	1589	21	2142	29	2724	46	74.1
PP.49	34630	80	1.3	b.d.	0.5412	1.4	14.56	2.8	0.1952	2.5	0.49	2789	32	2787	27	2786	40	100
PP.11	69894	220	1.75	b.d.	0.4289	1.3	10.65	2.6	0.1801	2.3	0.51	2301	26	2493	25	2653	37	92.2
PP.18	39340	123	0.96	0.1381	0.4266	1.5	10.67	3.4	0.1814	3.1	0.45	2290	30	2495	32	2666	51	91.8
PP.38	75903	270	1.66	0.0096	0.3988	1.5	9.41	2.9	0.1712	2.5	0.5	2163	27	2379	27	2569	42	90.9

Spot size = 30 µm; ^{206}Pb/^{238}U error is the quadratic addition of the within-run precision (2 SE) and the external reproducibility (2 SD) of the reference zircon. ^{207}Pb/^{206}Pb error propagation (^{207}Pb signal dependent) following (Gerdes and Zeh, 2009); ^{207}Pb/^{235}U error is the quadratic addition of the ^{207}Pb/^{206}Pb and ^{206}Pb/^{238}U uncertainty.

[a] Within run background-corrected mean ^{207}Pb signal in cps (counts per second).

[b] U content and Th/U ratio were corrected relatively to Blueberry reference zircon.

[c] Percentage of common Pb on the ^{206}Pb; b.d. = below detection limit.

[d] Corrected for background, within-run Pb/U fractionation (in case of ^{206}Pb/^{238}U) and common Pb using (Stacey and Kramers, 1975) model for Pb composition and subsequently normalized to Blueberry (ID- IMS value/measured value); ^{207}Pb/^{235}U calculated using ^{207}Pb/^{206}Pb/(^{238}U/^{206}Pb*1/137.88).

[e] Rho is the ^{206}Pb/^{238}U/^{207}Pb/^{235}U error correlation coefficient.

[f] Concordance calculated as (^{206}Pb-^{238}U age/^{207}Pb-^{235}U age)*100.

References:

Stacey, J.S., Kramers, J.D., 1975. Approximation of terrestrial lead isotope evolution by a two-stage model. Earth Planet. Sci. Lett. 26, 207–221. https://doi.org/10.1016/0012-821X(75)90088-6

Gerdes, A., Zeh, A., 2009. Zircon formation versus zircon alteration - New insights from combined U-Pb and Lu-Hf in-situ LA-ICP-MS analyses, and consequences for the interpretation of Archean zircon from the Central Zone of the Limpopo Belt. Chem. Geol. 261, 230–243. https://doi.org/10.1016/j.chemgeo.2008.03.005

APÊNDICE D - tabela com os dados geoquímicos dos xistos e quartzitos do Grupo Costa Sena

Sample	CSOV-07	CSOV-08	PE-BD-88*	CSLC 23	CSOV-09	MCS004	MCS010	MCS012	CS 005	CS 012	CSLC 35	PE-SM-04*	CSLC 31	CS 002	CS 017	DMF-003	PE-BD-87*	CSOV-06A	CSOV-04	CSLC 26	CS 023	PE- GO-01*
Group	High SiO_2 sedimentary rock			Highly weathered schist	Porphyroclastic facies								Type I schist						Type II schist			
X_UTMWGS84	638577	646994	-	628927	637101	640072	635570	636530	628529	626364	646233	-	647358	628496	636252	638235	-	628819	627341	633359	632272	-
Y_UTMWGS84	7975980	7980090	-	7968130	7978800	7935080	7936530	7934840	7946150	7968080	7964674	-	7966350	7950390	7950120	7976085	-	7967250	7962100	7969180	7938370	-
Al2O3	2.33	3.36	0.03	21.86	15.50	16.18	12.64	14.96	14.15	17.33	27.72	0.07	15.06	25.20	9.06	14.92	0.1	15.60	13.36	12.79	23.60	0.09
Ba	95.00	158.00	0.59	<10	371.00	352.00	334.00	62.00	139.00	62.00	864.00	1.48	363.00	348.00	269.00	172.00	1.13	1146.00	936.00	217.00	1114.00	1.99
CaO	0.01	0.01	2.05	0.02	<0.01	<0.01	<0.01	<0.01	<0.01	<0.01	<0.01	14.08	<0.01	1.04	<0.01	<0.01	17.63	0.03	0.02	0.02	<0.01	16.47
Cr2O3	<0.01	<0.01	0.02	<0.01	<0.01	<0.01	<0.01	<0.01	<0.01	<0.01	0.04	0	0.02	0.01	0.05	<0.01	0	0.01	<0.01	0.01	0.04	0.01
Fe2O3	1.33	1.13	0.02	31.79	1.96	3.12	1.80	1.36	2.39	2.81	12.15	0.04	3.26	5.21	8.11	2.81	0.02	3.79	3.54	4.92	11.33	0.11
K2O	0.71	0.45	0.07	<0.01	5.04	6.02	4.80	1.18	4.55	5.18	9.54	0.04	6.19	7.49	3.84	2.57	0.07	6.28	5.62	1.27	7.64	0.34
MgO	0.10	0.03	0.02	0.05	0.84	0.84	1.11	0.01	0.22	0.07	0.89	0.16	1.54	0.14	1.08	0.02	0.26	1.32	1.29	0.26	3.04	0.11
MnO	0.02	0.03	0.08	0.01	0.02	<0.01	<0.01	<0.01	<0.01	<0.01	<0.01	0.18	0.02	<0.01	0.02	<0.01	0.67	0.02	0.02	<0.01	0.11	0.78
Na2O	0.03	0.03	95.88	0.01	0.18	0.09	0.07	0.05	0.13	0.12	0.31	81.08	0.08	0.54	0.04	0.18	74.02	0.10	0.08	0.18	0.22	68.49
P2O5	<0.01	0.03	0.36	0.06	0.02	0.02	0.03	0.04	0.01	0.04	0.06	1.68	0.05	0.92	0.04	0.17	4.59	0.12	0.10	0.06	0.07	8.15
SiO2	95.26	94.70	0.001	32.62	78.24	72.24	78.60	82.52	78.48	73.79	42.06	0.001	70.52	56.08	72.36	77.28	0.007	68.92	76.64	79.71	50.54	0.023
Sr	15.00	101.00	0.53	<10	31.00	13.00	<10	21.00	21.00	104.00	80.00	1.17	16.00	149.00	<10	516.00	1.26	88.00	110.00	90.00	30.00	1.84
TiO2	0.05	0.09	11.8	0.44	0.03	0.14	0.17	0.04	0.12	0.18	1.27	47.3	0.39	0.55	0.73	0.50	96.7	0.56	0.09	0.48	1.04	25.8
Zn	<5	<5	25.2	273.00	34.00	39.00	<5	17.00	<5	9.00	7.00	91.5	35.00	11.00	21.00	<5	290	44.00	32.00	13.00	133.00	52.5
Zr	66.00	73.00	2.51	296.00	46.00	156.00	121.00	57.00	83.00	146.00	211.00	10.5	175.00	1085.00	218.00	342.00	22.7	191.00	32.00	103.00	157.00	5.33
V	11.00	38.00	8.52	66.00	29.00	10.00	7.00	12.00	<5	6.00	166.00	33.6	9.00	66.00	25.00	33.00	85.6	80.00	17.00	37.00	175.00	20.7
LOI	0.16	0.17	1.31	9.73	2.14	2.37	1.95	0.62	1.88	2.34	4.26	7.03	2.45	3.45	1.55	1.41	18.1	2.75	2.19	1.25	4.41	4.56
Ce	15.40	28.60	0.23	27.90	27.20	112.50	57.50	45.90	39.90	65.00	128.60	0.77	123.30	387.60	165.40	251.70	3.23	265.00	25.20	83.20	53.20	1.3
Co	0.70	1.10	1.03	6.60	28.90	2.20	2.40	0.60	1.10	<0.5	9.70	5.78	12.00	1.80	18.10	1.00	14.4	6.60	5.50	8.60	38.30	5.26
Cs	0.23	0.17	0.17	0.11	0.91	1.09	0.50	<0.05	0.43	0.78	2.97	1.04	2.71	1.08	1.48	1.64	1.82	8.06	5.83	1.45	1.90	1.08
Cu	<5	<5	1.09	5.00	<5	<5	14.00	<5	<5	<5	6.00	5.84	<5	6.00	67.00	<5	8.31	7.00	10.00	<5	124.00	6.16
Dy	0.62	1.65	0.23	4.18	4.87	30.91	7.14	3.73	4.63	3.96	12.73	1.27	2.57	10.72	5.19	4.81	1.29	5.17	1.83	5.46	3.20	1.07
Er	0.44	0.80	0.73	3.24	4.80	22.22	4.40	2.34	2.55	3.01	7.37	4.19	1.18	5.39	2.86	2.14	3.12	2.09	0.77	2.70	1.70	3.77
Eu	0.08	0.28	0.12	0.58	0.48	1.24	0.31	0.29	0.31	0.46	1.97	0.66	1.13	4.02	1.88	3.50	0.41	2.66	0.56	1.86	0.99	0.5

Sample	**CSOV-07**	**CSOV-08**	**PE-BD-88***	**CSLC 23**	**CSOV-09**	**MCS004**	**MCS010**	**MCS012**	**CS 005**	**CS 012**	**CSLC 35**	**PE-SM-04***	**CSLC 31**	**CS 002**	**CS 017**	**DMF-003**	**PE-BD-87***	**CSOV-06A**	**CSOV-04**	**CSLC 26**	**CS 023**	**PE- GO-01***
Group	**High SiO_2 sedimentary rock**			**Highly weathered schist**	**Porphyroclastic facies**								**Type I schist**						**Type II schist**			
Ga	2.40	3.20	0.91	32.80	21.10	25.00	17.60	14.60	17.80	25.20	37.90	4.1	20.00	41.00	13.30	15.10	2.51	18.10	14.60	10.70	35.30	3.25
Gd	0.51	1.99	0.162	3.27	2.27	21.55	5.05	2.45	3.96	3.44	10.06	0.54	3.59	15.60	7.17	13.98	0.373	8.89	2.38	7.99	3.34	0.512
Hf	2.05	2.31	155	9.78	1.55	5.79	4.38	2.41	2.89	4.43	6.29	47	4.74	28.99	5.86	9.45	90	5.21	1.48	3.15	4.54	358
Ho	0.10	0.26	9	1.01	1.26	6.73	1.47	0.73	0.85	0.98	2.71	12	0.49	2.03	1.00	0.78	39	0.84	0.33	0.93	0.63	44
La	12.50	22.00	10	8.80	25.30	60.10	28.80	28.20	22.70	34.90	72.10	10	57.90	175.40	104.80	122.50	20	154.20	20.10	44.70	32.80	60
Lu	0.08	0.12	5	0.42	0.68	3.64	0.63	0.38	0.37	0.47	0.97	5	0.17	0.69	0.31	0.30	5	0.30	0.09	0.33	0.27	5
Mo	<2	<2	15	<2	<2	<2	<2	<2	<2	<2	<2	15	<2	<2	<2	<2	15	<2	<2	<2	<2	50
Nb	2.50	4.35	8	17.41	4.27	2.58	36.09	3.94	15.00	22.32	15.97	56	8.44	31.78	18.05	29.12	24	8.69	4.48	7.28	11.80	86
Nd	5.40	11.40	25	5.70	7.80	45.80	22.20	17.40	15.10	22.10	54.60	621	30.70	175.50	83.80	124.30	949	106.30	10.40	33.00	24.30	167
Ni	6.00	5.00	7.5	69.00	15.00	<5	<5	<5	7.00	<5	57.00	35.6	29.00	21.00	63.00	10.00	39	26.00	24.00	42.00	138.00	37.7
Pr	1.76	3.35	198	1.52	2.66	12.65	6.16	5.11	4.41	6.89	14.77	190	9.06	44.09	22.00	29.42	479	32.68	2.90	8.80	6.40	193
Rb	10.10	9.50	2.3	0.90	67.70	215.40	100.50	27.20	128.50	101.80	292.40	33.9	176.80	295.70	82.30	51.80	34.5	183.00	162.20	40.90	237.20	7.7
Sm	1.00	2.50	3.9	2.30	1.90	12.10	4.80	3.50	4.10	4.00	10.80	6.1	4.50	27.80	13.20	24.00	11.2	16.70	2.50	7.50	4.50	4.9
Sn	1.00	0.50	5.45	<0.3	3.90	2.80	3.50	1.90	3.10	15.80	7.50	25	1.20	11.10	3.60	6.80	80.5	9.60	1.60	1.40	20.30	9.13
Ta	0.32	0.43	1.63	1.49	0.76	0.42	1.39	0.43	0.94	2.56	1.59	2.47	0.86	3.40	0.95	2.70	4.23	0.97	3.56	0.85	0.75	2.51
Tb	0.13	0.24	90	0.61	0.58	4.60	1.03	0.47	0.69	0.57	1.90	43	0.40	1.94	0.99	1.28	44	1.12	0.38	1.10	0.53	38
Th	1.80	8.70	0.05	105.00	4.30	40.40	43.20	22.30	16.40	26.90	29.30	0.3	30.30	73.70	25.00	61.00	0.05	23.70	4.10	7.00	14.80	5.4
Tl	<0.5	<0.5	0.5	<0.5	<0.5	0.50	<0.5	<0.5	<0.5	<0.5	0.60	5	0.50	0.60	<0.5	<0.5	10	0.90	0.90	<0.5	<0.5	0.5
Tm	0.07	0.10	1.16	0.47	0.74	3.68	0.66	0.36	0.38	0.48	1.12	7.04	0.19	0.85	0.37	0.34	3.29	0.29	0.11	0.38	0.27	1
U	0.47	1.10	893	12.32	1.51	6.21	3.68	3.15	5.05	1.88	4.10	358	1.96	58.81	3.77	3.38	429	3.09	1.54	1.11	3.76	225
W	1.90	1.50	-	0.20	3.40	2.70	0.90	1.10	0.20	2.80	2.10	-	4.00	4.00	0.30	3.20	-	5.10	3.60	2.80	5.50	-
Y	3.78	7.39	-	28.74	35.03	198.72	43.22	20.64	25.43	23.84	76.29	-	13.56	60.68	29.81	19.66	-	21.25	8.57	25.43	16.83	-
Yb	0.40	1.00	-	3.10	4.90	24.90	4.70	2.70	2.60	3.30	6.80	-	1.10	5.10	2.40	2.00	-	1.90	0.50	2.30	1.90	-

*** Samples compiled from Dussin and Chemale (2012)**

References: Dussin, I.A., Chemale Jr, F., 2012. Geologia estrutural e estratigrafia do Sistema Espinhaço-Chapada Diamantina e sua aplicação nas bacias mesocenozoicas da margem passiva brasileira, Authors ed. ed. Belo Horizonte.

APÊNDICE E - medições isotópicas U-Pb em zircões da amostra CSOV-07 (Formação Bandeirinha)

Spot #	207Pb[a] (cps)	U (ppm)[b]	Th/U[b]	206Pb[c] (%)	Isotope ratios							Ages (Ma)						% Conc. [f]
					^{206}Pb/^{238}U[d]	2s (%)	^{207}Pb/^{235}U[d]	2s (%)	^{207}Pb/^{206}Pb[d]	2s (%)	Rho[e]	^{206}Pb/^{238}U	2s	^{207}Pb/^{235}U	2s	^{207}Pb/^{206}Pb	2s	
BD.1	39449	139	0.45	0.0000	0.5020	1.6	12.16	2.6	0.1757	2.1	0.60	2622	34	2617	25	2613	35	99.9
BD.2	39764	151	0.29	0.2133	0.4870	1.5	11.33	2.6	0.1687	2.2	0.57	2558	31	2551	25	2545	36	100.0
BD.3	74087	340	0.37	3.9472	0.2438	3.6	9.35	4.9	0.2780	3.4	0.72	1406	45	2372	46	3352	53	59.1
BD.4	8138	51	0.33	0.0000	0.3819	1.7	6.79	2.9	0.1290	2.4	0.58	2085	30	2085	26	2084	42	99.8
BD.5	23077	101	0.46	0.0000	0.3553	1.5	9.82	2.6	0.2003	2.1	0.58	1960	25	2418	24	2829	34	80.8
BD.6	24631	89	0.37	0.0000	0.4862	1.5	11.87	2.7	0.1770	2.3	0.56	2554	32	2594	26	2625	38	98.2
BD.7	100042	360	0.51	0.0000	0.2291	1.5	11.92	2.5	0.3772	1.9	0.62	1330	18	2598	23	3821	29	51.0
BD.8	38110	133	0.49	0.0587	0.5055	1.5	12.30	2.5	0.1765	2.0	0.62	2638	33	2628	24	2620	33	100.1
BD.9	31716	54	0.44	0.0000	0.6726	1.5	24.97	2.5	0.2693	2.0	0.60	3316	39	3307	25	3302	31	100.0
BD.10	14649	95	0.46	0.4125	0.3856	1.6	6.64	3.0	0.1249	2.5	0.54	2102	29	2065	26	2027	44	101.6
BD.11	105282	297	0.83	7.0240	0.2841	5.2	15.20	6.7	0.3881	4.2	0.78	1612	74	2828	66	3864	63	56.8
BD.12	17372	104	0.51	0.0000	0.3919	1.5	7.18	2.6	0.1329	2.2	0.57	2132	27	2134	24	2137	38	99.6
BD.13	27243	192	0.36	1.6994	0.2646	2.1	6.07	3.6	0.1664	3.0	0.57	1513	28	1986	32	2522	50	76.0
BD.14	45772	88	0.57	0.2488	0.6306	1.6	22.40	2.9	0.2576	2.4	0.55	3152	39	3201	28	3232	38	98.2
BD.15	15082	78	0.55	0.6164	0.4003	1.5	8.34	2.6	0.1511	2.1	0.59	2170	28	2268	24	2358	36	95.4
BD.16	8430	58	0.41	0.4828	0.3321	1.8	6.25	3.2	0.1365	2.6	0.57	1849	29	2011	28	2183	45	91.7
BD.17	27713	90	0.78	0.0497	0.5193	1.5	13.19	2.5	0.1843	2.0	0.59	2696	32	2694	24	2692	33	99.8
BD.18	12129	77	0.25	1.0000	0.3820	1.6	6.78	3.3	0.1287	2.8	0.50	2086	29	2083	29	2080	50	99.9
BD.19	18113	127	0.54	0.4263	0.3119	1.6	6.11	2.9	0.1420	2.4	0.54	1750	24	1991	26	2252	42	87.7
BD.20	13128	72	0.33	0.0000	0.4105	1.5	7.84	2.5	0.1385	2.0	0.59	2217	28	2213	23	2208	35	100.0
BD.21	29683	86	0.76	0.0000	0.5478	1.6	14.88	2.6	0.1970	2.0	0.61	2816	36	2807	25	2801	33	100.0
BD.22	14503	96	0.58	0.0000	0.3730	1.5	6.49	2.5	0.1262	1.9	0.62	2044	27	2044	22	2045	34	99.7
BD.23	11501	72	0.53	0.0169	0.3847	1.5	6.85	2.5	0.1291	2.0	0.61	2098	27	2092	22	2086	34	100.0

Spot #	207Pb[a] (cps)	U (ppm)[b]	Th/U[b]	206Pb[c] (%)	Isotope ratios							Ages (Ma)						% Conc. [f]
					^{206}Pb/^{238}U[d]	2s (%)	^{207}Pb/^{235}U[d]	2s (%)	^{207}Pb/^{206}Pb[d]	2s (%)	Rho[e]	^{206}Pb/^{238}U	2s	^{207}Pb/^{235}U	2s	^{207}Pb/^{206}Pb	2s	
BD.24	34560	106	0.98	0.0000	0.3166	1.6	13.98	2.7	0.3203	2.2	0.57	1773	24	2749	26	3571	35	64.3
BD.25	23686	131	0.63	0.0224	0.3798	1.5	7.73	2.6	0.1476	2.1	0.57	2075	26	2200	23	2318	36	94.1
BD.26	35924	193	0.35	0.0000	0.3000	1.5	8.00	2.6	0.1935	2.1	0.57	1691	22	2232	24	2772	35	75.6
BD.27	43955	176	0.45	0.0000	0.4255	1.6	10.68	2.7	0.1821	2.2	0.60	2285	31	2496	25	2672	36	91.3
BD.28	18513	131	0.61	0.3668	0.3104	1.6	6.06	2.7	0.1415	2.2	0.59	1743	25	1984	24	2246	38	87.6
BD.29	29852	127	0.40	1.7834	0.3738	1.8	10.11	3.2	0.1962	2.6	0.56	2047	31	2445	30	2795	43	83.5
BD.30	27370	91	0.40	0.0000	0.5158	1.8	12.93	3.6	0.1818	3.1	0.50	2681	39	2675	34	2670	51	100.0
BD.31	19833	73	0.67	0.3607	0.4944	1.7	11.67	3.6	0.1712	3.2	0.48	2590	37	2578	34	2570	53	100.2
BD.32	27860	95	0.43	0.0000	0.5104	1.5	12.64	2.6	0.1797	2.1	0.57	2658	32	2653	24	2650	35	99.9
BD.33	41772	135	0.41	0.1056	0.5239	1.6	13.25	2.9	0.1834	2.4	0.55	2716	35	2697	27	2684	40	100.4
BD.34	38518	133	0.42	0.0000	0.5090	1.5	12.44	2.7	0.1773	2.3	0.56	2652	33	2639	26	2628	38	100.2
BD.35	32407	91	0.64	0.1419	0.5533	1.5	15.23	2.4	0.1996	1.9	0.61	2839	34	2830	23	2823	31	100.0
BD.36	34100	121	0.36	0.0000	0.5011	1.5	12.07	2.5	0.1748	2.0	0.61	2619	33	2610	24	2604	34	100.0
BD.37	31170	89	0.54	0.0000	0.5489	1.7	14.98	2.9	0.1979	2.4	0.58	2821	39	2814	28	2809	38	100.0
BD.38	91724	268	0.43	4.3591	0.3500	3.0	14.70	4.7	0.3048	3.7	0.63	1934	50	2796	46	3495	57	69.0
BD.39	17278	115	0.14	0.1287	0.3668	1.7	6.45	2.9	0.1275	2.3	0.58	2014	29	2039	26	2063	41	98.6
BD.40	3795	23	0.79	1.0000	0.3883	2.3	7.00	4.4	0.1307	3.8	0.52	2115	41	2111	40	2107	66	99.9
BD.41	54733	245	0.13	0.0000	0.2988	1.6	9.60	2.6	0.2329	2.0	0.61	1686	23	2397	24	3072	33	70.1
BD.42	11106	33	0.75	0.0000	0.5383	2.1	14.23	3.7	0.1917	3.1	0.56	2777	47	2765	36	2757	51	100.1
BD.43	29947	104	0.43	0.0000	0.5063	1.5	12.31	2.4	0.1764	1.9	0.61	2641	32	2628	23	2619	32	100.2
BD.44	16792	73	0.39	0.0980	0.4578	1.6	9.87	2.8	0.1564	2.4	0.55	2430	31	2423	27	2417	40	100.0
BD.45	23449	150	0.81	0.0000	0.3792	1.5	6.69	2.5	0.1279	2.0	0.61	2073	27	2071	22	2070	35	99.8
BD.46	16307	92	0.28	0.5202	0.3836	1.9	7.57	3.6	0.1432	3.1	0.52	2093	34	2182	33	2266	53	95.7
BD.47	15955	94	0.36	0.2307	0.3965	1.6	7.27	2.8	0.1330	2.3	0.58	2153	30	2145	25	2137	40	100.1
BD.48	36015	161	0.62	2.2948	0.3377	2.1	9.62	4.0	0.2066	3.4	0.52	1876	34	2399	38	2879	56	78.0

Spot #	207Pb[a] (cps)	U (ppm)[b]	Th/U[b]	206Pb[c] (%)	Isotope ratios							Ages (Ma)						% Conc. [f]
					^{206}Pb/^{238}U[d]	2s (%)	^{207}Pb/^{235}U[d]	2s (%)	^{207}Pb/^{206}Pb[d]	2s (%)	Rho[e]	^{206}Pb/^{238}U	2s	^{207}Pb/^{235}U	2s	^{207}Pb/^{206}Pb	2s	
BD.49	36244	125	0.54	0.0779	0.5069	1.6	12.43	2.7	0.1779	2.1	0.60	2643	35	2638	25	2633	36	99.9
BD.50	22835	79	0.38	0.0000	0.5067	1.8	12.38	4.0	0.1771	3.6	0.45	2643	39	2633	38	2626	60	100.1
BD.51	36761	124	0.41	0.0000	0.5128	1.5	12.72	2.5	0.1799	2.0	0.58	2669	32	2659	24	2652	34	100.1
BD.52	32510	110	0.88	0.0000	0.5118	1.5	12.70	2.7	0.1800	2.3	0.55	2664	33	2658	26	2653	37	100.0
BD.53	13562	54	0.18	0.1069	0.4748	1.8	10.69	3.6	0.1634	3.1	0.51	2504	37	2497	34	2491	52	100.0
BD.54	21841	142	0.38	0.5511	0.3376	1.8	6.58	3.3	0.1415	2.8	0.54	1875	29	2057	30	2245	48	90.9
BD.55	45338	155	0.43	0.1410	0.5094	1.5	12.57	2.4	0.1790	1.9	0.62	2654	32	2648	23	2643	31	99.9
BD.56	69310	235	0.30	0.0000	0.3629	1.6	12.66	2.8	0.2531	2.3	0.58	1996	28	2655	27	3204	37	75.0
BD.57	15142	101	0.30	0.0000	0.3728	1.7	6.45	2.9	0.1255	2.4	0.57	2043	29	2039	26	2036	42	99.9
BD.58	94462	195	0.55	0.0000	0.4610	1.6	20.74	2.7	0.3262	2.2	0.59	2444	33	3126	27	3599	34	77.9
BD.59	40718	162	0.49	0.0000	0.4226	1.6	10.76	2.7	0.1846	2.2	0.59	2272	31	2503	26	2695	36	90.6
BD.60	34559	167	0.30	1.6156	0.3390	1.9	8.89	3.8	0.1901	3.3	0.50	1882	31	2326	35	2743	54	80.7
BD.61	145202	1152	0.33	0.0657	0.3188	1.6	5.41	2.8	0.1230	2.2	0.58	1784	25	1886	24	2000	40	94.4
BD.62	20050	70	0.39	0.0000	0.5072	1.7	12.34	2.8	0.1765	2.3	0.59	2645	36	2631	27	2620	38	100.2
BD.63	37751	132	0.44	0.7637	0.4287	1.6	12.27	3.1	0.2076	2.6	0.52	2300	31	2625	29	2887	43	87.4
BD.64	48527	208	0.42	0.0000	0.3778	1.6	10.03	2.9	0.1925	2.3	0.57	2066	29	2437	27	2764	38	84.5
BD.65	53992	191	0.34	1.0000	0.4996	1.7	12.13	3.1	0.1761	2.6	0.54	2612	36	2615	30	2617	44	99.6
BD.66	9904	53	0.51	0.0000	0.4151	1.6	8.01	2.8	0.1399	2.3	0.57	2238	30	2232	26	2225	40	100.0
BD.67	38815	137	0.48	1.0000	0.4987	1.5	12.17	2.9	0.1769	2.5	0.53	2608	33	2617	28	2624	41	99.4
BD.68	40848	138	0.42	0.1495	0.5106	1.5	12.66	2.6	0.1798	2.2	0.57	2659	33	2654	25	2651	36	99.9
BD.69	47660	160	0.47	0.0000	0.5124	1.5	12.80	2.6	0.1812	2.1	0.58	2667	33	2665	25	2664	35	99.8
BD.70	31878	86	0.68	0.0347	0.5630	1.5	15.98	2.6	0.2059	2.1	0.57	2879	35	2876	25	2873	35	99.8
BD.71	33332	167	0.37	1.3948	0.3586	1.8	8.56	3.3	0.1731	2.8	0.54	1976	30	2292	30	2588	46	86.0
BD.72	12751	65	0.57	0.2098	0.4280	1.5	8.45	2.5	0.1433	2.0	0.60	2297	29	2281	23	2267	35	100.4
BD.73	11164	73	0.43	0.0000	0.3780	1.6	6.57	3.1	0.1260	2.7	0.52	2067	28	2055	28	2043	47	100.3

Spot #	207Pb[a] (cps)	U (ppm)[b]	Th/U[b]	206Pb[c] (%)	Isotope ratios							Ages (Ma)						% Conc. [f]
					^{206}Pb/^{238}U[d]	2s (%)	^{207}Pb/^{235}U[d]	2s (%)	^{207}Pb/^{206}Pb[d]	2s (%)	Rho[e]	^{206}Pb/^{238}U	2s	^{207}Pb/^{235}U	2s	^{207}Pb/^{206}Pb	2s	
BD.74	50641	175	0.37	0.0000	0.5050	1.6	12.38	2.9	0.1778	2.4	0.57	2635	35	2633	28	2632	40	99.8
BD.75	109118	126	0.79	0.4643	0.3968	2.0	7.22	2.9	0.1320	2.0	0.71	2154	37	2139	26	2124	35	100.1
BD.76	210348	139	0.40	0.0149	0.5141	1.9	12.71	2.7	0.1793	1.9	0.72	2674	42	2658	25	2646	31	100.0
BD.77	294262	208	0.39	1.2727	0.3814	1.9	11.81	3.0	0.2245	2.3	0.64	2083	34	2589	28	3014	37	79.9
BD.78	197576	124	0.39	0.0000	0.5243	1.9	13.30	2.7	0.1839	1.9	0.70	2717	41	2701	26	2689	32	100.0
BD.79	301292	166	0.20	0.0000	0.5544	1.9	15.17	2.7	0.1984	1.9	0.71	2843	44	2826	26	2813	31	100.0
BD.80	105001	127	0.32	1.0000	0.3861	2.0	6.91	3.2	0.1297	2.5	0.63	2105	36	2099	29	2095	44	99.7
BD.81	186879	117	0.38	0.1060	0.5222	1.8	13.39	2.7	0.1860	2.0	0.67	2709	40	2708	26	2707	33	99.4
BD.82	240705	152	0.44	0.0000	0.5227	2.0	13.23	2.7	0.1836	1.9	0.73	2711	44	2696	26	2686	31	99.9
BD.83	66541	104	0.63	0.0000	0.2544	2.0	5.36	2.8	0.1527	2.0	0.71	1461	26	1878	24	2377	33	77.3
BD.84	604088	289	0.26	4.9156	0.3571	3.4	17.50	4.8	0.3554	3.4	0.71	1968	58	2963	48	3730	52	66.0
BD.85	109988	73	0.51	0.3402	0.5157	1.9	12.58	2.8	0.1769	2.0	0.69	2681	42	2649	26	2624	33	100.6
BD.86	372626	374	0.42	4.0771	0.2176	4.3	8.34	5.6	0.2781	3.6	0.77	1269	49	2269	52	3352	56	55.5
BD.87	323558	106	0.61	0.0588	0.6843	1.9	25.53	2.8	0.2705	2.0	0.68	3361	50	3329	28	3309	32	100.3
BD.88	286395	184	0.40	0.1366	0.5194	1.9	13.04	2.7	0.1821	1.9	0.71	2697	43	2683	26	2672	32	99.9
BD.89	216222	146	0.36	0.4320	0.4822	1.9	12.39	2.7	0.1863	2.0	0.69	2537	40	2634	26	2710	33	95.7
BD.90	121108	142	0.28	0.0000	0.3975	1.9	7.14	2.8	0.1304	2.1	0.68	2157	35	2130	26	2103	37	100.7
BD.91	115181	102	0.74	1.6467	0.3656	2.2	9.48	3.5	0.1880	2.7	0.64	2008	38	2385	32	2725	44	83.7
BD.92	215180	136	0.59	0.0000	0.5209	1.9	13.22	2.7	0.1840	1.9	0.70	2703	42	2695	26	2689	32	99.6
BD.93	247136	88	0.47	0.0807	0.6604	1.9	23.47	2.8	0.2577	2.0	0.70	3269	50	3247	27	3233	31	100.0
BD.94	97430	60	0.42	0.1746	0.5323	1.8	13.64	2.7	0.1858	2.1	0.66	2751	40	2725	26	2705	34	100.3
BD.95	211967	143	0.41	0.2727	0.4942	1.9	12.38	2.7	0.1817	1.9	0.70	2589	40	2633	26	2668	32	97.7
BD.96	219571	166	0.58	0.5148	0.4326	2.0	11.09	2.9	0.1859	2.0	0.71	2317	39	2531	27	2706	33	91.0
BD.97	170816	120	0.46	0.1215	0.5003	2.0	11.88	2.8	0.1722	1.9	0.72	2615	43	2595	26	2579	32	100.1
BD.98	95901	110	0.37	0.3038	0.3804	2.0	7.30	2.9	0.1392	2.1	0.69	2078	35	2149	26	2217	36	96.1

Spot #	207Pb^a (cps)	U (ppm)^b	Th/U^b	206Pb^c (%)	Isotope ratios							Ages (Ma)						% Conc. ^{f}
					^{206}Pb/^{238}U^d	2s (%)	^{207}Pb/^{235}U^d	2s (%)	^{207}Pb/^{206}Pb^d	2s (%)	Rho^e	^{206}Pb/^{238}U	2s	^{207}Pb/^{235}U	2s	^{207}Pb/^{206}Pb	2s	
BD.99	63971	82	0.49	0.8060	0.3294	1.9	6.51	3.0	0.1432	2.4	0.61	1836	30	2047	27	2267	41	89.1
BD.100	356343	242	0.24	4.7043	0.2922	3.8	12.34	5.3	0.3065	3.7	0.72	1652	56	2631	51	3503	57	62.4
BD.101	272431	223	0.34	3.4021	0.2968	3.1	10.21	4.6	0.2493	3.4	0.67	1676	45	2454	43	3181	53	67.8
BD.102	77702	90	0.81	0.0000	0.3954	2.0	7.21	2.8	0.1323	2.0	0.71	2148	37	2138	26	2128	35	99.9
BD.103	216145	215	0.27	1.9398	0.3114	2.4	8.40	3.7	0.1955	2.8	0.65	1748	36	2275	34	2789	46	76.3
BD.104	206285	129	0.41	0.0000	0.5262	1.9	13.38	2.7	0.1845	2.0	0.69	2725	42	2707	26	2693	33	100.0
BD.105	193246	137	0.46	1.0000	0.4758	2.1	11.80	3.1	0.1799	2.3	0.67	2509	43	2589	30	2652	39	96.3
BD.106	157146	99	0.37	0.0000	0.5236	1.8	13.27	2.7	0.1839	2.0	0.68	2714	41	2699	26	2688	33	99.9
BD.107	172920	114	0.36	0.0000	0.5137	2.0	12.65	2.8	0.1786	2.0	0.71	2672	43	2654	27	2640	33	100.1
BD.108	242352	115	0.26	0.0000	0.5336	2.0	17.67	2.8	0.2402	2.0	0.71	2757	45	2972	28	3121	32	92.1
BD.109	31045	37	0.46	0.0000	0.3822	1.9	7.00	3.0	0.1329	2.3	0.62	2086	33	2112	27	2137	41	98.2
BD.110	233028	151	0.43	1.0000	0.5175	1.9	12.93	3.0	0.1812	2.3	0.64	2689	42	2675	28	2664	37	99.9
BD.111	133810	83	0.47	0.0000	0.5277	1.9	13.54	2.8	0.1861	2.0	0.67	2732	41	2718	26	2708	34	99.9
BD.112	129681	119	0.60	0.7717	0.3810	2.0	9.09	2.9	0.1730	2.2	0.68	2081	35	2347	27	2587	36	88.1
BD.113	226433	143	0.37	0.0724	0.5309	1.9	13.23	2.7	0.1807	2.0	0.70	2745	42	2696	26	2660	32	101.2
BD.114	101246	119	0.49	0.0000	0.3936	1.9	7.13	2.7	0.1314	2.0	0.69	2140	34	2128	25	2116	35	100.0
BD.115	201058	130	0.39	0.0000	0.5183	1.9	12.93	2.8	0.1810	2.1	0.66	2692	41	2675	27	2662	35	100.0
BD.116	210287	180	0.35	0.3320	0.3638	1.8	9.80	2.8	0.1954	2.1	0.65	2000	31	2416	26	2788	35	82.2
BD.117	289759	275	0.55	0.8247	0.3302	2.1	8.83	3.0	0.1939	2.2	0.69	1839	33	2320	28	2776	36	78.7
BD.118	57785	69	0.49	0.0000	0.3908	2.0	7.03	3.0	0.1304	2.1	0.69	2126	37	2115	27	2103	38	100.0
BD.119	143790	190	0.36	0.9850	0.2912	2.0	6.34	3.2	0.1579	2.5	0.61	1647	29	2024	29	2433	43	80.9
BD.120	928619	387	0.42	9.1182	0.3049	6.4	20.07	7.7	0.4775	4.4	0.82	1715	96	3095	78	4173	65	55.0
BD.121	152017	163	0.24	0.7911	0.3457	2.1	7.81	3.1	0.1638	2.3	0.66	1914	34	2209	29	2495	39	86.1
BD.122	122238	141	0.28	0.8134	0.3230	2.0	7.27	3.0	0.1633	2.2	0.67	1804	31	2145	27	2490	37	83.6
BD.123	155862	97	0.37	0.1194	0.5269	1.9	13.49	2.9	0.1856	2.2	0.66	2728	42	2714	28	2704	36	99.9

Spot #	207Pb[a] (cps)	U (ppm)[b]	Th/U[b]	206Pb[c] (%)	Isotope ratios							Ages (Ma)						% Conc. [f]
					^{206}Pb/^{238}U[d]	2s (%)	^{207}Pb/^{235}U[d]	2s (%)	^{207}Pb/^{206}Pb[d]	2s (%)	Rho[e]	^{206}Pb/^{238}U	2s	^{207}Pb/^{235}U	2s	^{207}Pb/^{206}Pb	2s	
BD.124	63085	65	0.20	0.0000	0.3780	2.1	8.15	3.1	0.1564	2.3	0.67	2067	37	2248	28	2417	39	91.4
BD.125	222034	76	0.07	1.0000	0.6689	1.9	24.44	2.9	0.2650	2.2	0.64	3302	48	3286	29	3277	35	99.8
BD.126	98589	67	0.58	0.0000	0.4632	1.9	12.26	2.8	0.1920	2.0	0.70	2454	39	2625	26	2759	32	92.9
BD.127	54923	64	0.19	0.0000	0.3954	1.9	7.23	2.8	0.1325	2.0	0.68	2148	34	2140	25	2132	35	99.8
BD.128	211549	157	0.42	0.1537	0.4595	2.0	11.30	2.9	0.1783	2.0	0.70	2438	40	2548	27	2637	34	95.1
BD.129	119245	82	0.34	0.2358	0.5042	2.0	12.11	2.8	0.1741	2.0	0.70	2632	43	2613	27	2598	34	100.1
BD.130	156118	60	1.02	1.0000	0.6398	1.9	21.65	3.1	0.2454	2.4	0.61	3188	47	3168	30	3156	38	100.0
BD.131	66869	83	0.48	0.0000	0.3844	2.0	6.71	2.8	0.1265	2.0	0.70	2097	35	2073	25	2050	36	100.5
BD.132	93894	117	0.56	0.0767	0.3819	2.0	6.70	2.8	0.1272	2.0	0.71	2085	35	2073	25	2060	35	100.0
BD.133	183531	115	0.41	0.0000	0.5241	1.9	13.38	2.8	0.1851	2.1	0.67	2716	41	2707	27	2699	34	99.7

Spot size = 30 µm; ^{206}Pb/^{238}U error is the quadratic addition of the within-run precision (2 SE) and the external reproducibility (2 SD) of the reference zircon. ^{207}Pb/^{206}Pb error propagation (^{207}Pb signal dependent) following (Gerdes and Zeh, 2009); ^{207}Pb/^{235}U error is the quadratic addition of the ^{207}Pb/^{206}Pb and ^{206}Pb/^{238}U uncertainty.

[a] Within run background-corrected mean ^{207}Pb signal in cps (counts per second).

[b] U content and Th/U ratio were corrected relatively to Blueberry reference zircon.

[c] Percentage of common Pb on the ^{206}Pb; b.d. = below detection limit.

[d] Corrected for background, within-run Pb/U fractionation (in case of ^{206}Pb/^{238}U) and common Pb using (Stacey and Kramers, 1975) model for Pb composition and subsequently normalized to Blueberry (ID- IMS value/measured value); ^{207}Pb/^{235}U calculated using ^{207}Pb/^{206}Pb/(^{238}U/^{206}Pb*1/137.88).

[e] Rho is the ^{206}Pb/^{238}U/^{207}Pb/^{235}U error correlation coefficient.

[f] Concordance calculated as (^{206}Pb-^{238}U age/^{207}Pb-^{235}U age)*100.

References:

Stacey, J.S., Kramers, J.D., 1975. Approximation of terrestrial lead isotope evolution by a two-stage model. Earth Planet. Sci. Lett. 26, 207–221. https://doi.org/10.1016/0012-821X(75)90088-6

Gerdes, A., Zeh, A., 2009. Zircon formation versus zircon alteration - New insights from combined U-Pb and Lu-Hf in-situ LA-ICP-MS analyses, and consequences for the interpretation of Archean zircon from the Central Zone of the Limpopo Belt. Chem. Geol. 261, 230–243. https://doi.org/10.1016/j.chemgeo.2008.03.005

APÊNDICE F - medições isotópicas U-Pb em zircões da amostra CSOV-06A (xisto Fm. Barão do Guaicuí)

Spot #	207Pb[a] (cps)	U (ppm)[b]	Th/U[b]	206Pb[c] (%)	Isotope ratios							Ages (Ma)						% Conc.[f]
					^{206}Pb/^{238}U[d]	2s (%)	^{207}Pb/^{235}U[d]	2s (%)	^{207}Pb/^{206}Pb[d]	2s (%)	Rho[e]	^{206}Pb/^{238}U	2s	^{207}Pb/^{235}U	2s	^{207}Pb/^{206}Pb	2s	
C6.32	156687	329	15.29	0.4639	0.1874	1.5	3.78	2.5	0.1462	2.0	0.61	1107	16	1588	20	2302	34	69.6
C6.31	226620	1154	23.40	0.6379	0.0773	2.2	1.05	3.2	0.0986	2.3	0.70	480	10	730	17	1598	42	65.7
C6.28	232403	345	13.53	0.0000	0.2652	1.7	5.35	2.8	0.1462	2.2	0.60	1517	22	1876	24	2302	38	80.7
C6.20	216556	422	7.50	0.0000	0.2023	1.5	3.96	2.4	0.1419	1.8	0.64	1188	17	1626	20	2251	32	72.9
C6.19	125343	133	31.14	0.0000	0.3705	2.0	8.08	3.4	0.1582	2.8	0.58	2032	35	2240	31	2436	47	90.5
C6.7	144086	348	19.65	0.1791	0.1633	1.5	2.43	2.8	0.1077	2.3	0.55	975	14	1250	20	1761	42	77.9
C6.8	241663	1093	25.02	0.0000	0.0871	1.5	1.10	2.4	0.0915	1.9	0.63	538	8	753	13	1458	36	71.4
C6.9	189777	886	24.97	0.0000	0.0844	1.7	1.12	2.8	0.0961	2.3	0.59	522	8	762	15	1550	43	68.5
C6.10	265667	1512	20.92	0.0000	0.0692	1.7	0.85	2.8	0.0886	2.3	0.58	431	7	622	13	1396	44	69.3
C6.11	196336	309	18.54	1.0000	0.2502	1.7	4.15	3.0	0.1202	2.5	0.55	1440	21	1664	25	1959	45	86.4
C6.12	164118	523	17.92	0.5630	0.1237	1.7	1.78	2.8	0.1046	2.2	0.61	752	12	1040	19	1708	41	72.2
C6.13	159334	254	24.56	0.0000	0.2466	1.6	4.09	2.6	0.1201	2.0	0.62	1421	20	1651	21	1958	36	85.9
C6.14	227151	396	9.34	0.3862	0.2259	1.6	3.66	2.5	0.1174	2.0	0.62	1313	19	1562	20	1916	35	83.9
C6.15	190697	679	21.14	0.0000	0.1106	1.6	1.72	2.6	0.1125	2.1	0.61	676	10	1014	17	1840	38	66.6
C6.16	198725	456	16.82	0.0000	0.1717	1.6	2.72	2.5	0.1148	2.0	0.62	1021	15	1333	19	1877	36	76.5
C6.17	200752	403	22.70	0.0425	0.1964	1.6	3.14	2.5	0.1162	2.0	0.62	1156	16	1444	19	1898	35	79.9
C6.18	202516	423	26.99	0.0990	0.1885	1.5	3.01	2.3	0.1159	1.8	0.62	1113	15	1411	18	1894	33	78.8
C6.27	187839	484	19.61	0.6969	0.1529	1.8	2.41	3.0	0.1143	2.4	0.61	917	16	1245	22	1868	43	73.5
C6.36	206654	796	5.12	0.9993	0.1023	2.5	1.48	3.8	0.1050	2.8	0.67	628	15	923	23	1715	52	68.0
C6.39	103999	425	32.16	0.8657	0.0965	2.4	1.37	3.8	0.1028	3.0	0.63	594	13	875	22	1675	55	67.8
C6.40	238547	708	17.03	0.0000	0.1327	1.6	2.07	2.6	0.1130	2.0	0.62	803	12	1138	18	1848	36	70.5
C6.151	158394	165	21.36	0.0000	0.3785	1.7	6.65	2.9	0.1273	2.4	0.57	2069	29	2065	26	2062	42	100.0
C6.29	242782	205	12.25	0.0000	0.4673	1.7	10.34	2.7	0.1605	2.1	0.62	2472	34	2466	25	2461	35	100.1

Spot #	207Pb[a] (cps)	U (ppm)[b]	Th/U[b]	206Pb[c] (%)	Isotope ratios							Ages (Ma)						% Conc.[f]
					^{206}Pb/^{238}U[d]	2s (%)	^{207}Pb/^{235}U[d]	2s (%)	^{207}Pb/^{206}Pb[d]	2s (%)	Rho[e]	^{206}Pb/^{238}U	2s	^{207}Pb/^{235}U	2s	^{207}Pb/^{206}Pb	2s	
C6.30	138576	167	22.54	2.1790	0.3266	2.0	10.53	3.3	0.2338	2.6	0.61	1822	32	2482	31	3078	42	73.3
C6.34	117315	564	18.69	0.7163	0.0820	2.3	1.05	3.7	0.0931	2.9	0.63	508	11	730	19	1490	54	69.5
C6.35	223404	789	7.65	0.0000	0.1115	1.5	1.44	2.5	0.0937	1.9	0.62	681	10	906	15	1502	37	75.1
C6.38	152210	1529	47.89	1.2268	0.0392	6.5	0.68	7.0	0.1263	2.7	0.92	248	16	529	29	2047	48	46.9
C6.33	191260	1346	45.78	0.5941	0.0560	2.6	0.77	3.5	0.1003	2.3	0.75	351	9	582	16	1630	43	60.3
C6.37	40819	258	18.55	0.0000	0.0622	2.3	0.79	5.2	0.0923	4.7	0.44	389	9	593	24	1474	89	65.6
~~C6.157~~	~~469~~	~~0~~	~~-356.20~~	~~0.0000~~	~~-0.8049~~	~~-94.2~~	~~18.88~~	~~192.2~~	~~-0.1702~~	~~-167.5~~	~~-0.49~~	~~-10535~~	-	~~3036~~	-	-	-	~~-343.9~~
C6.147	122124	163	12.81	0.0000	0.2959	1.9	4.85	4.2	0.1190	3.7	0.46	1671	28	1794	36	1941	66	93.0
C6.148	118810	300	46.89	0.0000	0.1558	1.7	2.47	3.3	0.1151	2.8	0.51	933	15	1264	24	1881	51	73.7
C6.149	5977	34	20.51	3.5565	0.0692	11.1	1.00	14.5	0.1045	9.4	0.76	431	46	703	76	1706	173	61.3
C6.150	4778	10	868.45	0.0000	0.1875	7.9	2.54	16.2	0.0984	14.1	0.49	1108	81	1285	125	1594	263	86.1
C6.152	145274	185	21.31	0.0000	0.3101	1.8	7.12	3.6	0.1665	3.1	0.50	1741	28	2126	33	2522	52	81.7
C6.153	14989	35	28.18	0.0000	0.1693	2.8	2.61	5.7	0.1119	5.0	0.50	1008	27	1304	43	1831	90	77.2
C6.154	180577	401	14.22	0.0000	0.1776	1.6	2.69	3.0	0.1098	2.5	0.55	1054	16	1325	22	1795	45	79.4
C6.155	240394	1679	3.73	0.4663	0.0564	2.2	0.64	3.2	0.0829	2.3	0.69	354	8	505	13	1267	46	70.0
C6.156	179537	942	45.96	0.6778	0.0751	2.4	1.05	3.5	0.1013	2.5	0.69	467	11	728	18	1648	47	64.0
C6.158	285227	723	17.43	0.2174	0.1553	1.6	2.15	2.8	0.1002	2.3	0.57	931	14	1163	20	1627	43	79.9
C6.159	166669	231	10.07	0.0000	0.2838	1.8	5.15	3.2	0.1315	2.7	0.54	1611	25	1844	28	2118	48	87.2
C6.160	122642	992	18.37	0.0000	0.0487	1.8	0.86	3.3	0.1285	2.7	0.55	306	5	631	15	2077	48	48.5
C6.16	198725	456	16.82	0.0000	0.1717	1.6	2.72	2.5	0.1148	2.0	0.62	1021	15	1333	19	1877	36	76.5

Spot size = 30 µm; ^{206}Pb/^{238}U error is the quadratic addition of the within-run precision (2 SE) and the external reproducibility (2 SD) of the reference zircon. ^{207}Pb/^{206}Pb error propagation (^{207}Pb signal dependent) following (Gerdes and Zeh, 2009); ^{207}Pb/^{235}U error is the quadratic addition of the ^{207}Pb/^{206}Pb and ^{206}Pb/^{238}U uncertainty.

[a] Within run background-corrected mean ^{207}Pb signal in cps (counts per second).

[b] U content and Th/U ratio were corrected relatively to Blueberry reference zircon.

[c] Percentage of common Pb on the ^{206}Pb; b.d. = below detection limit.

[d] Corrected for background, within-run Pb/U fractionation (in case of $^{206}Pb/^{238}U$) and common Pb using (Stacey and Kramers, 1975) model for Pb composition and subsequently normalized to Blueberry (ID- IMS value/measured value); $^{207}Pb/^{235}U$ calculated using $^{207}Pb/^{206}Pb/(^{238}U/^{206}Pb*1/137.88)$.

[e] Rho is the $^{206}Pb/^{238}U/^{207}Pb/^{235}U$ error correlation coefficient.

[f] Concordance calculated as (^{206}Pb-^{238}U age/^{207}Pb-^{235}U age)*100.

References:

Stacey, J.S., Kramers, J.D., 1975. Approximation of terrestrial lead isotope evolution by a two-stage model. Earth Planet. Sci. Lett. 26, 207–221. https://doi.org/10.1016/0012-821X(75)90088-6

Gerdes, A., Zeh, A., 2009. Zircon formation versus zircon alteration - New insights from combined U-Pb and Lu-Hf in-situ LA-ICP-MS analyses, and consequences for the interpretation of Archean zircon from the Central Zone of the Limpopo Belt. Chem. Geol. 261, 230–243. https://doi.org/10.1016/j.chemgeo.2008.03.005

APÊNDICE G - medições isotópicas U-Pb em zircões da amostra CSOV-08 (metaconglomerado da Fm. Barão do Guaicuí)

Spot #	207Pb[a] (cps)	U (ppm)[b]	Th/U[b]	206Pb[c] (%)	Isotope ratios							Ages (Ma)						% Conc.[f]
					^{206}Pb/^{238}U[d]	2s (%)	^{207}Pb/^{235}U[d]	2s (%)	207Pb/^{206}Pb[d]	2s (%)	Rho[e]	^{206}Pb/^{238}U	2s	^{207}Pb/^{235}U	2s	^{207}Pb/^{206}Pb	2s	
FF.99	91287	68	22.75	0.0000	0.5259	1.8	12.95	3.18	0.1786	2.6	0.57	2724	41	2676	30	2640	43	101.6
FF.74	102145	74	19.14	0.1685	0.5413	1.6	14.06	2.80	0.1884	2.3	0.56	2789	36	2754	27	2728	38	101.1
FF.107	106303	108	22.61	0.0000	0.3869	1.5	6.87	2.53	0.1288	2.0	0.61	2108	28	2095	23	2082	35	100.5
FF.78	114518	120	7.64	0.0000	0.3773	1.5	6.60	2.52	0.1269	2.0	0.60	2064	27	2060	22	2056	36	100.0
FF.60	65096	48	17.15	0.0000	0.5359	2.2	14.18	4.74	0.1919	4.2	0.47	2766	50	2762	46	2758	69	100.0
FF.59	112593	120	11.60	0.2414	0.3697	1.5	6.35	2.60	0.1246	2.1	0.58	2028	26	2025	23	2023	37	100.0
FF.67	102654	108	6.68	0.0000	0.3760	1.6	6.57	2.95	0.1268	2.5	0.54	2057	28	2056	26	2054	44	99.9
FF.79	128816	141	17.86	0.0000	0.3600	1.6	6.04	2.59	0.1216	2.0	0.61	1982	27	1981	23	1980	36	99.9
FF.108	90358	95	21.51	0.0000	0.3750	1.9	6.58	3.49	0.1272	2.9	0.54	2053	33	2056	31	2059	52	99.7
FF.132	114595	94	12.22	0.0000	0.4808	1.7	11.81	3.37	0.1781	2.9	0.51	2531	36	2589	32	2635	48	97.5
FF.110	79617	67	36.22	0.0000	0.4671	1.7	11.11	2.95	0.1725	2.4	0.59	2471	36	2532	28	2582	40	97.4
FF.72	122348	104	25.66	0.0000	0.4616	1.7	10.83	3.00	0.1701	2.5	0.57	2447	35	2509	28	2559	41	97.3
FF.88	185749	260	26.49	0.0000	0.2817	1.6	4.60	2.67	0.1184	2.1	0.61	1600	23	1749	23	1932	38	91.3
FF.97	176530	177	25.16	0.1487	0.3927	1.7	8.98	2.98	0.1659	2.5	0.55	2135	30	2336	28	2516	42	91.2
FF.116	104995	593	17.65	0.3527	0.0697	1.9	0.62	3.71	0.0640	3.2	0.52	435	8	487	14	741	67	89.2
FF.49	323080	2382	29.22	0.0602	0.0534	1.6	0.45	2.59	0.0613	2.1	0.60	336	5	378	8	648	44	88.7
FF.80	124095	128	29.96	0.0000	0.3831	1.7	9.69	2.73	0.1835	2.2	0.61	2091	30	2406	25	2685	36	86.7
FF.109	173308	271	10.04	0.0000	0.2516	1.7	4.20	3.09	0.1212	2.6	0.55	1447	22	1675	26	1974	46	86.2
FF.93	155116	275	28.48	0.0000	0.2225	1.7	3.45	2.89	0.1124	2.3	0.58	1295	20	1516	23	1838	43	85.3
FF.58	221129	425	21.32	0.1449	0.2049	1.6	3.09	2.69	0.1093	2.1	0.61	1201	18	1429	21	1787	39	83.9
FF.92	70729	86	23.94	0.0000	0.3248	1.7	7.50	3.08	0.1675	2.6	0.55	1813	27	2173	28	2533	43	83.3
FF.139	308074	1366	11.03	0.2029	0.0889	1.6	0.91	2.73	0.0745	2.2	0.60	549	9	659	13	1056	44	83.2

Spot #	207Pb^{a} (cps)	U (ppm)^{b}	Th/U^{b}	206Pb^{c} (%)	Isotope ratios							Ages (Ma)						% Conc.^{f}
					^{206}Pb/^{238}U^{d}	2s (%)	^{207}Pb/^{235}U^{d}	2s (%)	207Pb/^{206}Pb^{d}	2s (%)	Rho^{e}	^{206}Pb/^{238}U	2s	^{207}Pb/^{235}U	2s	^{207}Pb/^{206}Pb	2s	
FF.100	158170	280	23.31	0.1541	0.2228	1.5	3.73	2.70	0.1215	2.2	0.57	1297	18	1578	22	1978	40	82.0
FF.56	295305	1336	18.78	0.3244	0.0870	1.7	0.92	2.70	0.0768	2.1	0.63	538	9	663	13	1115	42	81.1
FF.134	417024	1566	3.88	0.1220	0.1049	1.7	1.19	3.21	0.0821	2.7	0.54	643	11	795	18	1249	53	80.8
FF.48	273350	329	17.04	0.0000	0.3278	1.6	8.38	2.69	0.1854	2.2	0.58	1828	25	2273	25	2702	36	80.2
FF.111	194124	364	13.90	0.1569	0.2100	1.7	3.51	2.83	0.1212	2.3	0.58	1229	18	1529	23	1973	41	80.2
FF.54	195167	397	11.61	0.0000	0.1938	1.6	3.10	2.66	0.1161	2.1	0.61	1142	17	1433	21	1897	38	79.5
FF.138	108692	592	26.62	0.3237	0.0724	1.8	0.78	3.10	0.0780	2.5	0.57	451	8	585	14	1148	51	77.0
FF.136	141270	1550	24.12	0.2063	0.0359	1.9	0.34	2.84	0.0693	2.1	0.67	227	4	300	7	908	43	75.9
FF.131	164256	235	19.78	0.4950	0.2757	1.6	6.67	3.06	0.1754	2.6	0.54	1570	23	2068	27	2609	43	75.8
FF.51	144669	358	15.88	0.0000	0.1591	1.7	2.49	2.76	0.1134	2.2	0.60	952	15	1268	20	1854	40	74.9
FF.120	256006	961	21.61	0.2120	0.1050	1.7	1.35	2.82	0.0929	2.3	0.59	643	10	865	17	1487	43	74.3
FF.128	201337	1392	28.64	0.0711	0.0570	1.6	0.61	2.72	0.0776	2.2	0.59	357	6	483	10	1136	44	73.9
FF.76	196377	305	24.86	0.0000	0.2533	1.6	6.27	2.59	0.1795	2.0	0.62	1455	21	2014	23	2648	34	72.1
FF.87	138745	158	40.10	0.0000	0.3467	18.5	13.46	60.71	0.2817	57.8	0.30	1919	314	2713	845	3372	902	70.6
FF.68	13663	267	43.48	0.8303	0.0201	8.6	0.20	10.07	0.0713	5.2	0.86	128	11	183	17	966	106	70.1
FF.129	301950	2178	21.26	0.3028	0.0546	1.9	0.63	2.94	0.0830	2.2	0.65	343	6	493	12	1269	44	69.5
FF.77	157865	280	38.46	0.0934	0.2218	1.6	5.25	2.59	0.1717	2.1	0.61	1291	19	1861	22	2574	34	69.3
FF.112	221344	1312	20.53	0.2459	0.0665	1.7	0.81	2.95	0.0879	2.4	0.58	415	7	600	13	1380	46	69.1
FF.50	243409	2281	24.97	0.0000	0.0420	1.6	0.47	2.58	0.0803	2.0	0.61	265	4	388	8	1205	40	68.3
FF.113	317223	1225	16.64	0.0000	0.1020	1.6	1.49	2.62	0.1057	2.1	0.60	626	9	925	16	1727	39	67.6
FF.119	243888	881	19.17	0.0000	0.1090	1.5	1.65	2.79	0.1095	2.3	0.55	667	10	988	18	1792	43	67.4
FF.55	155062	618	19.49	1.0000	0.0989	2.5	1.44	4.00	0.1053	3.1	0.64	608	15	904	24	1719	57	67.2
FF.118	56273	269	17.23	1.0000	0.0825	3.0	1.12	4.83	0.0985	3.8	0.63	511	15	764	26	1596	70	66.9
FF.91	171840	905	31.12	0.0000	0.0748	1.7	0.99	3.04	0.0959	2.5	0.57	465	8	698	15	1545	47	66.5
FF.95	226091	610	18.64	0.0000	0.1460	1.5	2.67	2.40	0.1325	1.9	0.63	878	12	1319	18	2131	33	66.5

Spot #	207Pb[a] (cps)	U (ppm)[b]	Th/U[b]	206Pb[c] (%)	Isotope ratios							Ages (Ma)						% Conc.[f]
					^{206}Pb/^{238}U[d]	2s (%)	^{207}Pb/^{235}U[d]	2s (%)	207Pb/^{206}Pb[d]	2s (%)	Rho[e]	^{206}Pb/^{238}U	2s	^{207}Pb/^{235}U	2s	^{207}Pb/^{206}Pb	2s	
FF.98	162979	401	19.00	0.1571	0.1602	1.5	3.13	2.55	0.1415	2.1	0.59	958	13	1439	20	2246	36	66.5
FF.133	232250	446	26.30	0.0000	0.2051	1.8	4.97	3.25	0.1759	2.7	0.54	1203	19	1815	28	2615	45	66.1
FF.52	389381	3494	9.11	0.3270	0.0439	2.2	0.51	3.24	0.0846	2.4	0.69	277	6	420	11	1307	46	65.9
FF.71	357910	970	12.26	0.0000	0.1453	1.6	2.70	2.51	0.1345	2.0	0.62	875	13	1327	19	2158	34	65.8
FF.75	251591	546	21.46	0.0000	0.1817	1.5	4.02	2.35	0.1606	1.8	0.63	1076	15	1639	19	2462	31	65.6
FF.70	259115	825	24.24	0.3677	0.1237	1.7	2.09	2.64	0.1226	2.0	0.63	752	12	1146	18	1995	36	65.5
FF.94	293574	872	15.08	0.2268	0.1326	1.6	2.36	2.55	0.1289	2.0	0.62	803	12	1229	18	2082	35	65.2
FF.117	181989	1280	16.66	0.2829	0.0560	1.8	0.71	2.69	0.0918	2.0	0.66	351	6	544	11	1462	38	64.5
FF.69	280725	1672	20.18	0.0000	0.0662	1.6	0.89	2.60	0.0978	2.1	0.61	413	6	647	12	1582	39	63.7
FF.114	242275	822	14.26	0.0000	0.1162	1.6	1.99	2.68	0.1245	2.2	0.59	709	11	1113	18	2021	38	63.5
FF.90	24495	84	19.17	0.0000	0.1147	1.7	1.99	3.02	0.1258	2.5	0.57	700	11	1111	21	2039	44	62.9
FF.57	190975	505	15.21	0.0711	0.1489	1.5	3.06	2.55	0.1488	2.1	0.58	895	12	1422	20	2332	36	62.9
FF.127	25006	184	17.66	0.9613	0.0537	4.1	0.72	5.68	0.0978	3.9	0.72	337	13	553	24	1583	74	60.9
FF.115	225587	607	21.29	0.2745	0.1464	1.5	3.28	2.44	0.1626	1.9	0.63	881	13	1477	19	2483	32	59.5
FF.137	214459	626	38.49	0.2674	0.1350	2.0	2.86	3.91	0.1537	3.4	0.50	817	15	1372	30	2387	57	59.4
FF.73	155933	379	32.10	0.0000	0.1621	1.6	4.32	2.80	0.1935	2.3	0.56	968	14	1698	23	2772	38	56.9
FF.89	153448	384	21.61	0.0289	0.1575	1.5	4.32	2.58	0.1988	2.1	0.58	943	13	1696	21	2816	34	55.5
FF.140	39191	335	18.12	0.0000	0.0460	1.8	0.71	3.63	0.1112	3.1	0.51	290	5	542	15	1820	57	53.4
FF.135	8450	109	44.31	0.0000	0.0307	3.4	0.44	6.76	0.1041	5.8	0.50	195	7	370	21	1698	108	52.5
FF.130	13612	188	31.15	4.0680	0.0286	28.7	0.43	30.04	0.1088	8.8	0.96	182	51	362	96	1780	161	50.1
FF.96	115446	1214	17.46	0.0000	0.0375	1.5	0.61	2.73	0.1182	2.3	0.55	237	3	484	11	1929	41	49.0
FF.53	24484	785	37.53	0.0030	0.0123	2.0	0.18	3.71	0.1036	3.1	0.53	79	2	164	6	1689	58	47.9
FF.47	23164	257	20.83	0.2687	0.0355	2.8	0.92	4.55	0.1890	3.6	0.61	225	6	664	22	2733	59	33.8

Spot size = 30 µm; ^{206}Pb/^{238}U error is the quadratic addition of the within-run precision (2 SE) and the external reproducibility (2 SD) of the reference zircon. ^{207}Pb/^{206}Pb error propagation (^{207}Pb signal dependent) following (Gerdes and Zeh, 2009); ^{207}Pb/^{235}U error is the quadratic addition of the ^{207}Pb/^{206}Pb and ^{206}Pb/^{238}U uncertainty.

[a] Within run background-corrected mean ^{207}Pb signal in cps (counts per second).

[b] U content and Th/U ratio were corrected relatively to Blueberry reference zircon.

[c] Percentage of common Pb on the ^{206}Pb; b.d. = below detection limit.

[d] Corrected for background, within-run Pb/U fractionation (in case of ^{206}Pb/^{238}U) and common Pb using (Stacey and Kramers, 1975) model for Pb composition and subsequently normalized to Blueberry (ID- IMS value/measured value); ^{207}Pb/^{235}U calculated using ^{207}Pb/^{206}Pb/(^{238}U/^{206}Pb*1/137.88).

[e] Rho is the ^{206}Pb/^{238}U/^{207}Pb/^{235}U error correlation coefficient.

[f] Concordance calculated as (^{206}Pb-^{238}U age/^{207}Pb-^{235}U age)*100.

References:

Stacey, J.S., Kramers, J.D., 1975. Approximation of terrestrial lead isotope evolution by a two-stage model. Earth Planet. Sci. Lett. 26, 207–221. https://doi.org/10.1016/0012-821X(75)90088-6

Gerdes, A., Zeh, A., 2009. Zircon formation versus zircon alteration - New insights from combined U-Pb and Lu-Hf in-situ LA-ICP-MS analyses, and consequences for the interpretation of Archean zircon from the Central Zone of the Limpopo Belt. Chem. Geol. 261, 230–243. https://doi.org/10.1016/j.chemgeo.2008.03.005

APÊNDICE H - dados isotópicos U-Pb em zircão da amostra CSOV-04 (metavulcanica ácida da região de Cuiabá?)

Table 2 - Zircon LA-ICP-MS U-Pb data from sample CSOV-04 (metavolcanite from Barão do Guaicuí Formation?)

Spot #	207Pb[a] (cps)	U (ppm)[b]	Th/U[b]	206Pb[c] (%)	Isotope ratios							Ages (Ma)						% Conc. [f]
					^{206}Pb/^{238}U[d]	2s (%)	^{207}Pb/^{235}U[d]	2s (%)	^{207}Pb/^{206}Pb[d]	2s (%)	Rho[e]	^{206}Pb/^{238}U	2s	^{207}Pb/^{235}U	2s	^{207}Pb/^{206}Pb	2s	
1.sSMPABC013	31412	1360	0.01	0.2075	0.0989	1.5	0.99	2.5	0.0726	1.9	0.62	608	9	699	12	1003	39	86.9
1.sSMPABC038	33946	1428	0.13	0.2799	0.1000	1.6	1.02	2.5	0.0740	2.0	0.62	614	9	714	13	1041	40	85.9
1.sSMPABC018	26841	1206	0.03	0.0000	0.0940	1.4	0.96	2.3	0.0737	1.8	0.62	579	8	681	12	1032	37	85.0
1.sSMPABC060	39259	1873	0.06	0.2433	0.0883	1.6	0.90	2.5	0.0739	2.0	0.62	545	8	651	12	1038	39	83.6
1.sSMPABC058	26760	1734	0.13	0.2142	0.0689	1.6	0.66	2.5	0.0697	1.9	0.63	430	6	516	10	919	40	83.2
1.sSMPABC037	36288	1442	0.33	0.2599	0.0987	1.6	1.08	2.6	0.0793	2.0	0.62	607	9	743	14	1181	40	81.5
1.sSMPABC048	31445	1512	0.27	0.4623	0.0851	1.9	0.89	3.1	0.0760	2.5	0.61	527	10	648	15	1096	49	81.2
1.sSMPABC053	27443	1246	0.56	0.0000	0.0889	1.4	0.94	2.3	0.0771	1.8	0.62	549	8	675	12	1124	37	81.1
1.sSMPABC008	37348	1784	0.25	0.2906	0.0854	1.6	0.90	2.6	0.0763	2.0	0.64	528	8	651	12	1102	39	81.1
1.sSMPABC007	32565	1658	0.48	0.3050	0.0812	1.7	0.84	2.7	0.0752	2.1	0.64	503	8	620	12	1074	41	81.0
1.sSMPABC035	34715	1292	0.18	0.0000	0.1028	1.5	1.15	2.4	0.0813	1.8	0.63	631	9	779	13	1229	36	80.9
1.sSMPABC011	26203	1360	0.27	0.1862	0.0797	1.5	0.83	2.4	0.0752	1.9	0.63	494	7	612	11	1073	38	80.8
1.sSMPABC055	27066	1081	0.08	0.3642	0.0972	1.6	1.07	2.6	0.0802	2.1	0.62	598	9	741	14	1202	41	80.6
1.sSMPABC032	42421	1546	0.60	0.0959	0.1038	1.5	1.18	2.3	0.0822	1.8	0.63	637	9	790	13	1251	36	80.5
1.sSMPABC009	39434	1676	0.23	0.4133	0.0925	1.8	1.01	2.8	0.0791	2.2	0.63	571	10	708	14	1175	43	80.4
1.sSMPABC014	26811	1167	0.22	0.0000	0.0900	1.4	0.99	2.3	0.0794	1.8	0.62	556	8	696	12	1181	36	79.7
1.sSMPABC028	14617	1189	0.49	0.1892	0.0544	1.6	0.53	2.5	0.0703	2.0	0.63	341	5	430	9	938	40	79.3
1.sSMPABC057	30226	1854	1.62	0.1695	0.0685	1.7	0.70	2.9	0.0740	2.4	0.57	427	7	538	12	1043	48	79.2
1.sSMPABC052	19197	781	0.20	0.2324	0.0940	1.7	1.05	2.8	0.0813	2.3	0.59	579	9	731	15	1230	45	79.1
1.sSMPABC059	26487	1037	0.08	0.4155	0.0966	1.7	1.10	2.7	0.0822	2.1	0.62	594	9	751	14	1251	41	79.0
1.sSMPABC039	31543	1212	0.33	0.3576	0.0976	1.6	1.12	2.6	0.0829	2.0	0.63	601	9	761	14	1267	39	78.8
1.sSMPABC012	30029	1408	0.15	0.4368	0.0836	1.8	0.92	2.8	0.0794	2.1	0.65	517	9	660	13	1182	41	78.3
1.sSMPABC054	16362	3133	0.14	0.5007	0.0252	4.2	0.22	4.9	0.0644	2.5	0.86	161	7	205	9	756	52	78.186201

1.sSMPABC019	13072	642	0.32	0.4187	0.0802	1.8	0.87	2.8	0.0789	2.2	0.64	498	9	637	13	1171	43	77.960574
1.sSMPABC033	26097	1078	0.43	0.4291	0.0912	1.7	1.04	2.7	0.0826	2.1	0.63	563	9	723	14	1259	41	77.701462
1.sSMPABC036	28294	1078	0.05	0.5209	0.0966	1.8	1.13	2.8	0.0845	2.2	0.64	595	10	766	15	1304	42	77.544148
1.sSMPABC015	26768	1270	1.09	0.5029	0.0818	1.9	0.90	2.9	0.0802	2.2	0.65	507	9	654	14	1201	44	77.406091
1.sSMPABC040	24636	1043	0.25	0.0000	0.0888	1.4	1.01	2.3	0.0828	1.8	0.62	549	8	711	12	1264	36	77.073365
1.sSMPABC031	31345	980	1.44	0.0000	0.1099	1.5	1.37	2.4	0.0905	1.9	0.63	672	10	877	14	1437	35	76.537966
1.sSMPABC030	18042	959	0.49	0.1517	0.0738	1.5	0.81	2.4	0.0793	1.9	0.62	459	7	601	11	1180	37	76.301941
1.sSMPABC050	24450	1014	0.97	0.3710	0.0892	1.7	1.03	2.7	0.0841	2.1	0.63	551	9	721	14	1295	40	76.289051
1.sSMPABC017	22473	1052	0.87	0.3362	0.0813	1.6	0.92	2.6	0.0818	2.0	0.63	504	8	660	13	1241	39	76.150189
1.sSMPABC029	18612	1243	0.39	0.1567	0.0613	1.6	0.64	2.6	0.0760	2.0	0.62	384	6	504	10	1094	40	76.090696
1.sSMPABC027	23335	1233	0.52	0.3276	0.0736	1.7	0.81	2.6	0.0800	2.0	0.64	458	7	604	12	1196	40	75.787753
1.sSMPABC049	18721	828	0.33	0.2963	0.0840	1.6	0.97	2.6	0.0837	2.0	0.63	520	8	688	13	1285	40	75.461844
1.sSMPABC056	12379	1873	0.34	0.5891	0.0292	4.3	0.28	5.0	0.0704	2.6	0.86	186	8	253	11	940	52	73.200924
1.sSMPABC051	19133	982	0.67	0.3474	0.0723	1.7	0.84	2.7	0.0839	2.1	0.63	450	7	617	13	1289	41	72.845477
1.sSMPABC034	8599	440	2.24	0.4267	0.0695	1.9	0.84	2.9	0.0875	2.2	0.67	433	8	618	13	1371	41	69.991741
1.sSMPABC047	15056	942	4.14	0.0000	0.0584	1.5	0.69	2.9	0.0852	2.5	0.52	366	5	530	12	1320	48	68.902238
1.sSMPABC020	18807	2339	0.16	0.3877	0.0319	2.8	0.34	3.5	0.0785	2.1	0.80	202	6	301	9	1160	42	67.158034
1.sSMPABC010	11583	361	1.76	0.3892	0.0935	1.7	1.38	2.7	0.1069	2.1	0.62	576	9	880	16	1747	39	65.404663
1.sSMPABC016	16198	1770	0.29	0.3963	0.0346	2.7	0.39	3.4	0.0822	2.1	0.79	219	6	336	10	1251	41	65.218895

ANEXO – artigo de coautoria sobre a sequência metavulcanossedimentar Riacho dos Machados

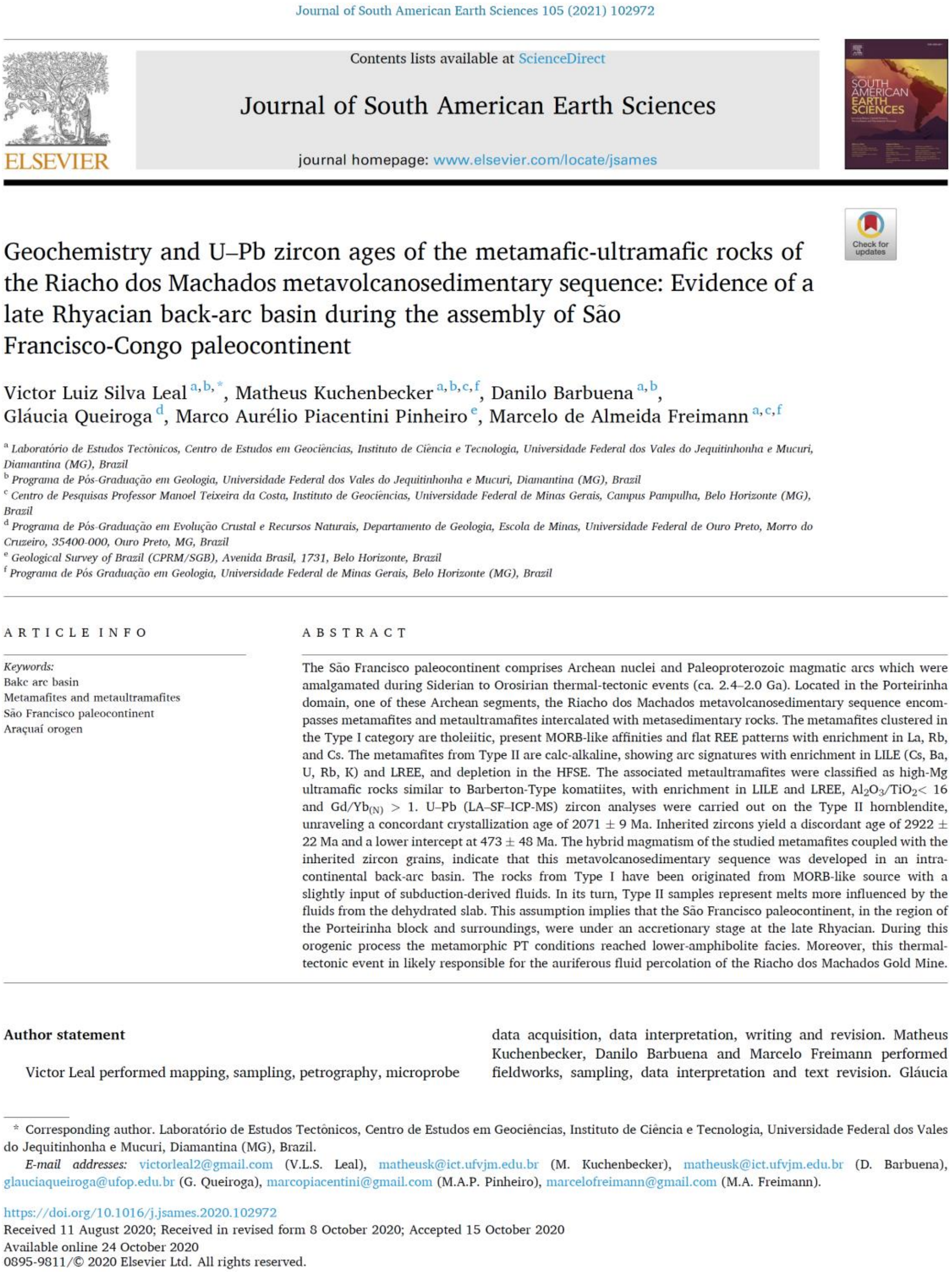

Journal of South American Earth Sciences 105 (2021) 102972

Contents lists available at ScienceDirect

Journal of South American Earth Sciences

journal homepage: www.elsevier.com/locate/jsames

Geochemistry and U–Pb zircon ages of the metamafic-ultramafic rocks of the Riacho dos Machados metavolcanosedimentary sequence: Evidence of a late Rhyacian back-arc basin during the assembly of São Francisco-Congo paleocontinent

Victor Luiz Silva Leal[a,b,*], Matheus Kuchenbecker[a,b,c,f], Danilo Barbuena[a,b],
Gláucia Queiroga[d], Marco Aurélio Piacentini Pinheiro[e], Marcelo de Almeida Freimann[a,c,f]

[a] *Laboratório de Estudos Tectônicos, Centro de Estudos em Geociências, Instituto de Ciência e Tecnologia, Universidade Federal dos Vales do Jequitinhonha e Mucuri, Diamantina (MG), Brazil*
[b] *Programa de Pós-Graduação em Geologia, Universidade Federal dos Vales do Jequitinhonha e Mucuri, Diamantina (MG), Brazil*
[c] *Centro de Pesquisas Professor Manoel Teixeira da Costa, Instituto de Geociências, Universidade Federal de Minas Gerais, Campus Pampulha, Belo Horizonte (MG), Brazil*
[d] *Programa de Pós-Graduação em Evolução Crustal e Recursos Naturais, Departamento de Geologia, Escola de Minas, Universidade Federal de Ouro Preto, Morro do Cruzeiro, 35400-000, Ouro Preto, MG, Brazil*
[e] *Geological Survey of Brazil (CPRM/SGB), Avenida Brasil, 1731, Belo Horizonte, Brazil*
[f] *Programa de Pós Graduação em Geologia, Universidade Federal de Minas Gerais, Belo Horizonte (MG), Brazil*

ARTICLE INFO

Keywords:
Bakc arc basin
Metamafites and metaultramafites
São Francisco paleocontinent
Araçuaí orogen

ABSTRACT

The São Francisco paleocontinent comprises Archean nuclei and Paleoproterozoic magmatic arcs which were amalgamated during Siderian to Orosirian thermal-tectonic events (ca. 2.4–2.0 Ga). Located in the Porteirinha domain, one of these Archean segments, the Riacho dos Machados metavolcanosedimentary sequence encompasses metamafites and metaultramafites intercalated with metasedimentary rocks. The metamafites clustered in the Type I category are tholeiitic, present MORB-like affinities and flat REE patterns with enrichment in La, Rb, and Cs. The metamafites from Type II are calc-alkaline, showing arc signatures with enrichment in LILE (Cs, Ba, U, Rb, K) and LREE, and depletion in the HFSE. The associated metaultramafites were classified as high-Mg ultramafic rocks similar to Barberton-Type komatiites, with enrichment in LILE and LREE, $Al_2O_3/TiO_2 < 16$ and $Gd/Yb_{(N)} > 1$. U–Pb (LA–SF–ICP-MS) zircon analyses were carried out on the Type II hornblendite, unraveling a concordant crystallization age of 2071 ± 9 Ma. Inherited zircons yield a discordant age of 2922 ± 22 Ma and a lower intercept at 473 ± 48 Ma. The hybrid magmatism of the studied metamafites coupled with the inherited zircon grains, indicate that this metavolcanosedimentary sequence was developed in an intracontinental back-arc basin. The rocks from Type I have been originated from MORB-like source with a slightly input of subduction-derived fluids. In its turn, Type II samples represent melts more influenced by the fluids from the dehydrated slab. This assumption implies that the São Francisco paleocontinent, in the region of the Porteirinha block and surroundings, were under an accretionary stage at the late Rhyacian. During this orogenic process the metamorphic PT conditions reached lower-amphibolite facies. Moreover, this thermal-tectonic event in likely responsible for the auriferous fluid percolation of the Riacho dos Machados Gold Mine.

Author statement

Victor Leal performed mapping, sampling, petrography, microprobe data acquisition, data interpretation, writing and revision. Matheus Kuchenbecker, Danilo Barbuena and Marcelo Freimann performed fieldworks, sampling, data interpretation and text revision. Gláucia

---

* Corresponding author. Laboratório de Estudos Tectônicos, Centro de Estudos em Geociências, Instituto de Ciência e Tecnologia, Universidade Federal dos Vales do Jequitinhonha e Mucuri, Diamantina (MG), Brazil.

E-mail addresses: victorleal2@gmail.com (V.L.S. Leal), matheusk@ict.ufvjm.edu.br (M. Kuchenbecker), matheusk@ict.ufvjm.edu.br (D. Barbuena), glauciaqueiroga@ufop.edu.br (G. Queiroga), marcopiacentini@gmail.com (M.A.P. Pinheiro), marcelofreimann@gmail.com (M.A. Freimann).

https://doi.org/10.1016/j.jsames.2020.102972
Received 11 August 2020; Received in revised form 8 October 2020; Accepted 15 October 2020

Fonte: Science Direct https://www.sciencedirect.com/science/article/pii/S0895981120305150